MICROPLASTICS TRANSPORT IN TURBULENT FLOW: INVESTIGATING THE EFFECTS OF PHYSICAL CHARACTERISTICS AND FLOW DYNAMICS

AREFEH SHAMSKHANY

A DISSERTATION SUBMITTED TO THE FACULTY OF GRADUATE STUDIES
IN PARTIAL FULFILMENT OF THE REQUIREMENTS
FOR THE DEGREE OF
DOCTOR OF PHILOSOPHY

GRADUATE PROGRAM IN CIVIL ENGINEERING
YORK UNIVERSITY
TORONTO, ONTARIO

OCTOBER, 2024

Abstract

The surge in global plastic production has led to increasing plastic pollution in aquatic environments, where plastic debris fragments into microplastics (MPs), particles smaller than 5 mm, through weathering processes. MPs are transported by ambient flow across different aquatic compartments, posing ubiquitous risks to the ecosystem health. Effective mitigation of MPs' risks requires a comprehensive understanding of MPs' transport and mobility. Turbulence and the natural settling or rising movements of MPs are fundamental transport mechanisms, yet many aspects of how MPs' diverse physical properties affect these processes remain underexplored. Density, size, and shape are amongst critical physical properties of MPs that shape their transport and affect flow interactions. This PhD dissertation investigates the effects of MPs' physical properties on their transport and mixing in turbulent flows using numerical and experimental approaches. The findings of this research elucidate how density, size, and shape affect the behaviour of MPs, providing explanations for their selective abundance and distribution in aquatic environments. Results of this PhD dissertation illustrate that lower marginal densities relative to the ambient fluid, smaller sizes, and non-spherical shapes make MPs more susceptible to the transient dynamics of the ambient flow as such MPs deviate significantly from their terminal behaviours. The findings explain the distant transport of smaller non-spherical MPs and the absence of smaller MPs of common polymers in offshore surface layers, as such particles are more likely transported to deeper water columns by in-depth currents. This research also explores the advantages of dynamic Lagrangian modelling over commonly used kinematic approaches, emphasizing the importance of particle acceleration for MPs with higher mixing levels, particularly those with smaller

sizes, lower marginal densities, and non-spherical shapes. These findings contribute to understanding MPs' transport and distribution based on their physical properties and flow dynamics and offer a foundation for developing effective strategies to mitigate the ecological impacts of MPs.

Dedication

I humbly dedicate my PhD dissertation to all compassionate women who devoted their lives to protecting our environment and the fragile balance of our planet... many of whom might remain unsung but are held in the deepest admiration and respect in our hearts.

Arefeh Shamskhany
Fall 2024

Acknowledgements

This dissertation would not exist without the guidance, support, and empathy of my supervisor, Dr. Shooka Karimpour. I begin by expressing my deepest gratitude to her, as she supported and believed in me throughout this journey, with all its ups and downs.

I cannot find words strong enough to convey my appreciation and love for my family—Baba, Maman, Reza, and Bahareh—who have been "the wind beneath my wings" all these years. This PhD thesis, and I myself, would not exist without them! Love you forever, and "thank you" from here to the end of the world.

I also want to thank my dearest friends and colleagues, who gave me love and faith. Without their support, I could never have come this far. I wish I could write about each of them here, but that would fill hundreds of pages! To all of you, I am forever thankful and love you dearly.

Finally, I am grateful to the community of York University and Lassonde School of Engineering for their kindness and assistance throughout these years. Thank you all for being a part of this journey.

Arefeh Shamskhany,
Fall 2024

Table of Contents

List of Tables

List of Figures

Abbreviations

WWTP	Wastewater Treatment Plant
MP	Microplastic
BFS	Backward-Facing Step
LES	Large Eddy Simulation
PE	Polyethylene
LDPE	Light-Density Polyethylene
HDPE	High-Density Polyethylene
PP	Polypropylene
PS	Polystyrene
PVC	Polyvinyl Chloride
PUR	Polyurethane
PET	Polyethylene Terephthalate
AR	Aspect Ratio
S1	Size of 0.1 mm
S2	Size of 0.2 mm (0.5 mm in Chapter 7)
S3	Size of 0.5 mm
S4	Size of 2.0 mm
E	Elongated (fibre)
F	Flattened (film)
E1	Fibres with aspect ratio of 8
E1	Films with aspect ratio of 8
E2	Fibres with aspect ratio of 24
E2	Films with aspect ratio of 24

List of symbols

Roman Symbols

a_p	Particle acceleration
a_y	Particle acceleration in y-direction
A_p	Projected area
AR	Aspect Ratio
C_D	Drag coefficient
C_s, C_e, C_k	LES subgrid scale model coefficients
D_{50}	Particle size corresponding to the cumulative frequency of 50%
d_{eq}	The diameter of the equivalent sphere with an identical volume
d_p	Particle diameter
d_s	Sediment particle diameter
FE	Fractional computational error
f	Frequency
F_B	Buoyancy
F_D	Drag
F_G	Gravity
F_{VM}	Virtual mass
g	Gravitational acceleration
h	Step height
k	Turbulent kinetic energy

M	Mesh opening size
m_p	Particle mass
P	Pressure
P_k	Order of convergence
Q	Discharge
r	Refinement ratio
r_{ET}	Radius of eddy trapping
Re	Reynolds number of the ambient flow
Re_*	Boundary layer Reynolds number
Re_p	Particle Reynolds number
S_{ij}	Strain rate tensor
S_ν	Settling parameter
St	Stokes number
St_l	Stokes number based on integral time scale
St_ν	Stokes number based on Kolmogorov's time scale
Str	Strouhal number
T	Period of intermittent eddy-detachment/reattachment
t	Time
U_o	Inlet velocity
u	Instantaneous velocity of the flow in x-direction
u_*	Shear velocity
u'	fluctuating velocity components in x-direction
$\bar{U}$	Mean velocity in x-direction
v	Instantaneous velocity of the flow in y-direction
v'	fluctuating velocity components in y-direction
V, V_p	Particle volume
V_s	Stokes settling velocity of the particle
V_T	Terminal velocity of the particle

V_{slip}	Slip velocity of the particle
$\bar{V}$	Mean velocity in y-direction
w	Instantaneous velocity of the flow in z-direction
w'	fluctuating velocity components in z-direction
w_p	Steady state particle velocity (terminal velocity)
$\bar{W}$	Mean velocity in z-direction
x	Position in the streamwise direction
y	Position in the depthwise direction
z	Position in the spanwise direction

Greek Symbols

Δ	Filter size of the LES model
δ	Thickness of the viscous sublayer
δ_{ij}	Kronecker delta tensor
η	Length scale
ε	Dissipation rate per unit mass
μ	Dynamic viscosity of the ambient fluid
μ_t, μ_{SGS}	Subgrid scale turbulent dynamic viscosity
ν	Kinematic viscosity of the ambient fluid
ν_t, ν_{SGS}	Subgrid scale turbulent kinematic viscosity
ϕ	Sphericity
ρ	Density
ρ_f	Density of the ambient fluid
ρ_p	Particle density
ρ_s	Density of the sediment particle
ρ_w	Density of the water
σ (in Chapter 6)	Grid solidity
σ (in other Chapters)	Flow velocity scale
θ	Shields number

τ^{SGS}	Subgrid-scale turbulent stresses
τ_l	Turnover time scale
τ_o	Shear stress
τ_p	Particle relaxation time
τ_ν	Kolmogorov's time
ζ, Ω	Vorticity

Index notation

x	Streamwise direction
y	Depthwise direction
z	Spanwise direction
i	x-direction
j	y-direction
k	z-direction

Chapter 1

Introduction

1.1 Background and motivation

Access to safe and clean water is essential for human health and well-being, as highlighted by the 6th Sustainable Development Goal [1]. Water pollution, caused by introducing harmful substances such as chemicals, microorganisms, and waste materials, degrades water quality and disrupts aquatic ecosystems [2, 3]. Plastic debris, which constitutes approximately 75% of marine litter, has become a major environmental issue [4]. Since the commercialization of plastic polymers in the 1950s, global plastic production has surged by about 620% [5, 6]. This increase in plastic production, along with the surge in demand for single-use plastics due to the COVID-19 pandemic, has significantly worsened plastic pollution. For instance, more than three billion single-use plastic face coverings were disposed of globally each day during the COVID-19 pandemic [7].

Approximately half of the plastic generated is disposed of immediately after single-use applications, such as plastic bags, water bottles, single-use cutlery, and packaging [8, 9]. This short-lived plastic waste is often mismanaged, entering aquatic environments through various pathways, including rivers, wind, wastewater treatment plants, stormwater run-off, and waste disposal across coastal areas, as demonstrated in Figure 1.1 [10]. Rivers play a significant role in transporting land-based plastic waste to the aquatic environment, as they

transport between 1.15 and 2.41 million tonnes of plastic litter annually to the oceans [11]. Without proper end-of-life management, plastic litter accumulates in aquatic environments, fragmenting into smaller pieces due to UV radiation and particle erosion [12].

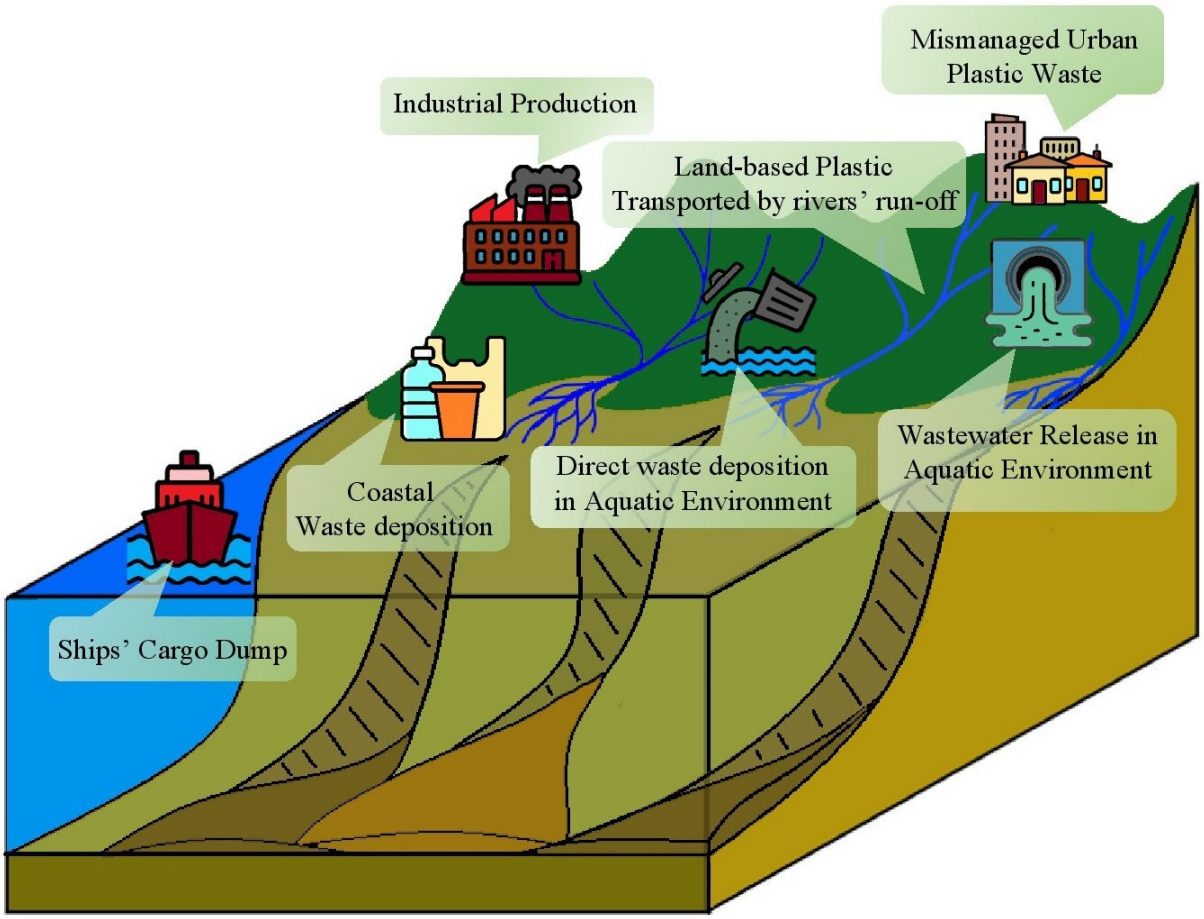

Figure 1.1: Different pathways through which mismanaged plastic waste enters the aquatic environment.

Plastic particles are classified into macroplastics (larger than 5 mm) and Microplastics (MPs) (10 μm to 5 mm), with some classifications also including mesoplastics (5 to 20 mm). MPs can be manufactured in factories for various commercial purposes, known as primary MPs, or can be generated from the degradation of larger plastic particles, referred to as secondary MPs. Even if the release of larger plastic items were to cease immediately, the number of

MPs would likely continue to increase due to the ongoing fragmentation of existing debris [12]. Since the first reports of MP abundance in aquatic environments in 1972 [13], MP pollution has drawn growing concern.

The presence of MPs in aquatic environments poses a significant threat to aquatic species and ecosystem health. Numerous studies have documented the ingestion of MPs by marine organisms and birds [14, 15, 16, 17, 18]. Based on a recent study, MPs are even detected in the human placenta [19]. MP particles absorb various additives, such as chemicals, metals, and antibiotics, transferring them into the bodies of species that ingest them [20, 21, 22, 23, 24]. Despite some recent advances in removing MPs from aquatic environments, challenges persist, including high costs, difficulties in removing very small particles, and dealing with the diverse types of MPs [25, 26, 27]. In order to understand the selective presence of MPs in different aquatic compartments and to develop effective risk management and mitigation strategies, a thorough understanding of the behaviour, transport, and fate of MPs is required. For instance, based on recent studies, the physical properties of MPs, such as size and shape, affect their ingestion rate by aquatic species [16, 28]. Therefore, understanding the selective abundance and accumulation of MPs based on their physical properties in different aquatic regions can help build a foundation for the future risk assessment of MPs ingestion by aquatic species.

Continued research is needed to enhance the existing knowledge on MPs' mixing and transport in aquatic environments and to develop more efficient techniques for their removal. This dissertation will explore various aspects of MPs' behaviour and distribution in turbulent flow, focusing on the effect of their physical properties as well as the flow dynamics. The outcomes of this research can improve the understanding of unexplored aspects of MP pollution, such as different transport mechanisms and the effects of their physical properties on their distribution and fate, thereby aiding future mitigation efforts.

1.2 Questions and research gaps

In recent decades, MP pollution in aquatic environments has become an increasingly severe problem, prompting numerous studies to explore various aspects of MPs. Once released into water bodies, MPs exhibit diverse behaviours regarding their transport with the ambient flow and their eventual destinations. Almost no environment on Earth has remained untouched by MP pollution. MPs have been detected throughout aquatic environments, from coastal areas [29, 30] to remote Arctic and Antarctic marine systems [31, 32], and at varying water depths and compartments, from surface waters to deep sediments [33, 34]. This wide distribution of aquatic MPs is influenced by several factors, including their physical properties, weathering processes, biofilm growth, and ambient flow dynamics.

The multifaceted nature of these particles creates innumerable combinations of physical characteristics, making the comprehension of their transport and distribution very challenging compared to other natural particles. MPs comprise various polymers with densities ranging from 0.88 to 2.30 g/cm^3 [35]. Biofouling, the accumulation of microorganisms and algae on MP surfaces, further alters their density and impacts their sinking or rising behaviour based on their buoyancy [36]. This mechanism is recognized as one of the possible reasons for the abundance of naturally buoyant MPs, such as polyethylene and polypropylene, in the sediment layers of aquatic compartments [37, 38]. MPs are found in a wide size range, from 10 μm to 5 mm, across different aquatic compartments [39, 40]. Most MPs originate from the fragmentation of larger plastic items (Duis and Coors [41]), resulting in diverse shapes [42]. These diverse physical properties significantly influence MPs' transport and distribution in aquatic environments. Moreover, weathering processes and UV irradiation constantly modify MPs' size and shape, adding to the complexity of predicting their behaviour in natural water bodies [12].

In addition to particle characteristics, turbulent flow dynamics can significantly alter the behaviour of particles. Turbulent regimes are quite common in aquatic environments, driven

by mechanisms such as density or temperature gradients, wind forces on surface layers, and abrupt topographical changes. Turbulent eddies influence the transport and mixing of natural suspended particles, like sediments, as well as emerging contaminants like MPs, often overriding their natural vertical movements governed by buoyancy or gravity. Consequently, the properties of MPs—such as size, shape, and density—combined with turbulence dictate their vertical and horizontal distribution throughout the aquatic system. A notable example of how turbulence can alter the natural fate and behaviour of MPs is the observed absence of millimetre-sized plastic debris from the ocean's surface layer, first reported by Thompson et al. [43]. Although most abundant plastic polymers in aquatic environments, such as polyethylene and polypropylene (as reported by Schwarz et al. [35]), are less dense than water and are expected to remain in surface layers, multiple field investigations have documented the absence of buoyant MPs from surface waters and highlighted their distribution at greater depths [34, 44, 45]. The combination of various physical characteristics and turbulent flows has made the transport and mixing behaviour of MPs in aquatic environments very diverse and complex compared to other natural particles.

Despite the fast-growing body of research on MP pollution in aquatic environments, several factors affect their distribution and fate. Still, significant gaps remain in comprehending their mobility in the aquatic environment. Numerous site-specific studies have examined the abundance and characteristics of MPs in various aquatic regions. However, a comprehensive discussion of their transport mechanisms—and the relationship between their physical properties, travel distances, and accumulation hotspots in marine environments—is still lacking. At the start of this PhD research in 2019, several challenging and unresolved questions were identified, including:

- What is the relationship between particle physical properties and their selective abundance across different aquatic compartments?
- How do particle physical properties, such as density, size, and shape, influence the transport, mobility, and fate of MPs?

- Given that turbulence is a frequent flow regime in many aquatic compartments, what effect does turbulent mixing have on MPs' trajectories and dispersion?
- What is the impact of MP properties and turbulent mixing on their proximity to source regions?
- What are the most suitable computational modelling approaches for simulating the transport and mobility of MPs in aquatic environments? Is a more detailed approach, such as advanced turbulence models or a dynamic Lagrangian particle tracking method that considers active forces and particle acceleration, required for accurately simulating the transport and turbulent mixing of MPs?

This PhD research addresses the questions above to bridge fundamental gaps in understanding the hydrodynamic aspects of aquatic MPs distribution and fate using numerical and empirical investigations. The chapters of this dissertation examine the interactions between the physical properties of MPs and the dynamics of ambient turbulent flow. Several numerical experiments were conducted to explore the complexities of MPs' interactions with turbulent flow based on their diverse physical properties to achieve this. Additionally, multiple preliminary laboratory experiments were designed and performed to validate our understanding of the effects of MPs' size and shape on their turbulent mixing and to assess their tendency for deposition versus long-range transport. This research also highlights the importance of particle acceleration in various scenarios and evaluates the suitability of dynamic versus kinematic modelling approaches. The following sections provide a detailed discussion of the identified research gaps and explain how each chapter of this dissertation addresses them.

1.2.1 Linkage between MPs physical properties and their distribution in the aquatic environment

Among the various physical characteristics of MPs, polymer density is a well-recognized factor influencing their abundance and distribution across aquatic environments [27, 35]. Polymer density directly affects the gravitational forces acting on MPs, determining whether they will

sink or float. Particle size is another critical factor that governs the transport and mobility of MPs by affecting forces such as gravity, buoyancy, and drag. Although many site-based studies have documented the size range of abundant MPs in various marine and freshwater systems [30, 32, 34, 46], a gap remains in understanding how particle size, in combination with polymer densities and shapes, influences the spatial distribution and selective presence of MPs. To address this gap, evidence was collected on the most common properties of MPs, with a primary focus on size, in an effort to link these properties to the final destinations of MPs. Chapter 3 of this dissertation presents a comprehensive review of the key particle properties, examining their distribution from surface waters to deeper layers and across coastal, near-shore, offshore, and remote areas, with a particular focus on particle size. This review provides beneficial insights into the approximate distribution and behaviour of MPs of various sizes, laying the groundwork for the subsequent analysis of how particle size, along with other properties, impacts the specific behaviour of MPs.

1.2.2 Investigation of microplastics entrainment with turbulent flow based on their physical properties

Understanding the effect of turbulence on MP behaviour is crucial for predicting their distribution and potential accumulation zones within aquatic environments. To date, most studies investigating the impact of turbulence on MP transport have focused on large-scale circulations in oceans, such as thermohaline currents. While this approach is valuable for simulating the long-term transport of MPs and identifying potential accumulation hotspots, it overlooks the impact of smaller-scale turbulent perturbations, particularly at depth. This dissertation, however, aims to investigate the effect of different turbulent flow scales on the vertical entrainment and transport of MPs with various physical properties using a Large Eddy Simulation (LES) turbulence model. The LES model resolves the majority of large, energy-containing eddies while modelling only the smallest scales through sub-grid approaches. This enables a more accurate representation of the effect of turbulent scales compared to the random-walk technique commonly used to incorporate the effect of turbulent dispersion

on MP transport in aquatic environments. LES strikes a balance between computational efficiency and the resolution of turbulence scales, enabling a more accurate capture of the entrainment and mixing behaviour of MPs in turbulent flows.

This research incorporates the effect of density, size, and shape as the most important physical characteristics of MPs. Three primary polymers are considered: Polyethylene (PE), Polystyrene (PS), and Polyethylene Terephthalate (PET), which were chosen due to their abundance in the aquatic environment. MPs possess a wide range of particle sizes, from micron-sized particles barely visible to the naked eye to millimetre-sized particles comparable to small gravel, as illustrated in Figure 1.2. The wide range of MP sizes can result in diverse behaviours and entrainment of these particles, especially in turbulent flow configurations. Using computational fluid dynamics, we conducted several numerical experiments to understand the effect of MP size and polymer density on the mixing behaviour and distribution of these particles in response to turbulent flow, which is provided in Chapter 4 of this dissertation. The results of this section show that MPs' mixing levels in turbulent flow can vary significantly based on their size and polymer density. Large particles are more influenced by gravity, while fine MPs are primarily driven by turbulent entrainment, explaining their presence in remote areas, as reported in the literature.

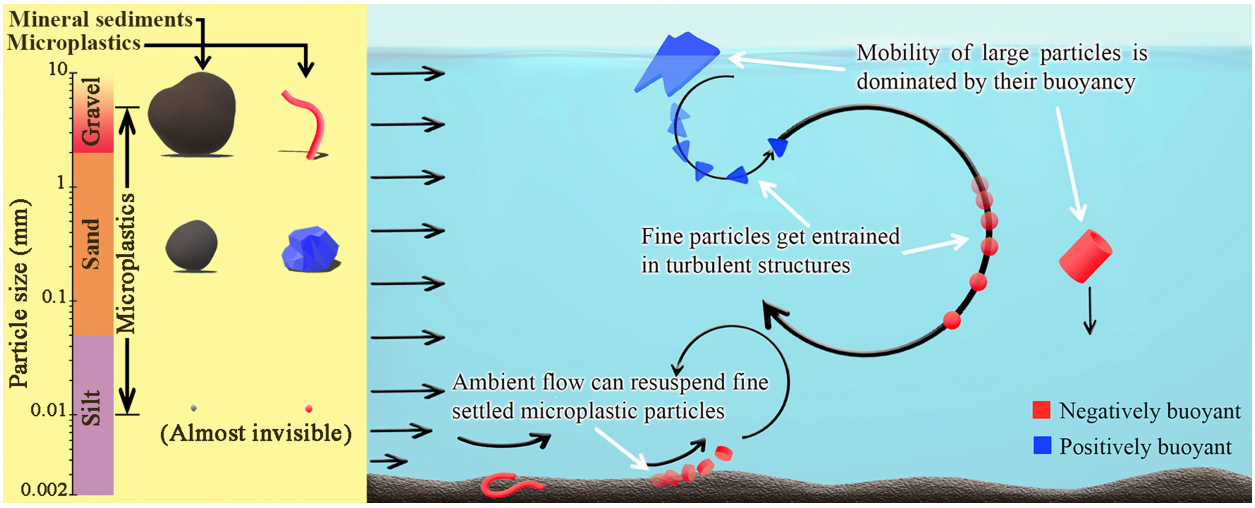

Figure 1.2: A comparison of the range of MPs sizes and sediments (left panel). The schematic turbulent-mixing of MPs of different physical characteristics (right panel).

MPs exhibit a wide variety of shapes, from spheres and isometric forms found in manufactured primary MPs to irregular shapes like fragments and fibres, which result from the degradation of larger particles through various weathering processes. Among the physical characteristics of MPs, understanding how their diverse shapes, particularly irregular ones, influence turbulent entrainment is one of the most complex aspects. These varying shapes significantly affect a particle's drag coefficient, which in turn impacts MPs' mixing and transport. However, the effect of MP shapes—especially irregular ones—on the drag-driven behaviour of MPs remains an unresolved question and still faces many challenging questions [47, 48, 49]. To address this gap, we conducted a vast series of numerical experiments examining the impact of particle shape on MPs' turbulent mixing and entrainment. These experiments considered both spherical and non-spherical MPs with varying aspect ratios. A detailed discussion of this aspect of our research can be found in Chapter 5 of this dissertation.

Furthermore, to deepen our understanding of the effects of MP size and shape, we designed and conducted a series of preliminary laboratory experiments. These experiments assessed the impact of size and shape on the entrainment and long-range transport of MPs in a grid-generated turbulent flow. The details and results of these experiments are discussed in Chapter 6 of this dissertation. Our findings indicate that smaller MPs and those with non-spherical shapes have a higher likelihood of remaining suspended in the turbulent flow, allowing them to be transported to farther distant locations.

1.2.3 Impact of modelling approach for the transport of MP in ambient turbulent conditions

Modelling has become an essential tool for understanding and predicting the complex behaviour of MPs in aquatic environments, particularly in large systems like lakes, seas, and oceans. It improves time and cost efficiency by reducing the need for extensive field investigations, which are resource-intensive and logistically challenging. Modelling techniques offer insights into MP transport and distribution across various compartments, enabling better

resource allocation for sampling and mitigation efforts [50]. Additionally, numerical models help establish relationships between existing site-based data and provide predictions about MPs' behaviour, allowing researchers to experiment with different scenarios and accelerate research compared to physical experiments or fieldwork.

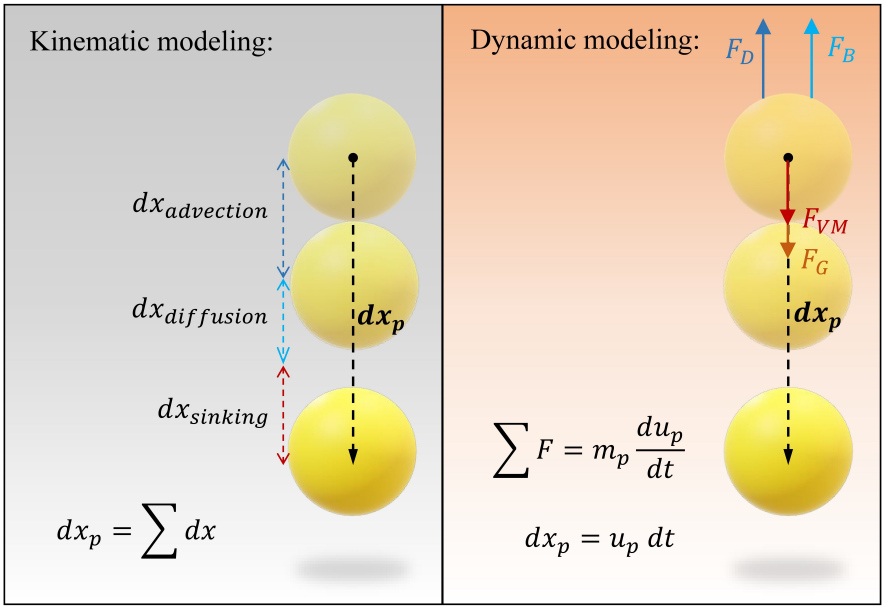

Figure 1.3: A comparison kinematic and dynamic approach in Lagrangian particle-tracking models.

Many Lagrangian particle-tracking models used in recent studies on MP transport in aquatic environments adopt a kinematic modelling approach [30, 51, 52]. In this approach, it is assumed that the net force acting on the particle is negligible (dynamic equilibrium), and the particle experiences no acceleration relative to the ambient flow. As a result, kinematic Lagrangian particle-tracking models do not explicitly account for the primary active forces that initiate transport mechanisms such as advection, turbulent diffusion, or sinking/rising. Instead, a corresponding displacement is used to represent these mechanisms. One key assumption in kinematic Lagrangian modelling is that the slip velocity of the MP relative to the ambient flow equals its terminal velocity in a quiescent fluid. However, this assumption may become inaccurate when the particle undergoes significant acceleration or deceleration

in the ambient flow, causing the instantaneous slip velocity to deviate substantially from its terminal velocity.

Figure 1.3 shows a schematic comparison of kinematic and dynamic Lagrangian particle-tracking models. In this study, we investigate the transport and instantaneous mobility of MPs using a dynamic Lagrangian particle-tracking model that accounts for Newton's second law and incorporates active forces such as gravity, buoyancy, drag, and virtual mass. The inclusion of virtual mass is particularly important when the acceleration of particles in the flow is significant. Our findings show that, under turbulent flow conditions, the physical properties of MPs, such as lower specific gravity, fine particle sizes, and non-spherical shapes with high aspect ratios, result in significant particle acceleration and substantial deviations in slip velocity compared to terminal velocity. This highlights the limitations of kinematic models in accurately predicting MP transport and trajectories. Chapter 7 of this dissertation presents the results of our 3D numerical simulations, detailing the ranges of particle acceleration and slip velocity for MPs with varying densities, sizes, and shapes.

1.3 Research objectives

To achieve the overall goals of this project, five specific objectives have been established, with each forming the foundation of a chapter in this dissertation:

- Objective 1: Study the relationship between the physical properties of MPs and their selective abundance across different aquatic compartments, with a focus on particle size (Chapter 3).
- Objective 2: Perform a numerical investigation into the effect of particle physical properties (density and size) on MP transport and fate in turbulent flow (Chapter 4).
- Objective 3: Conduct a numerical investigation into the combined effects of particle physical properties, with a primary focus on shape, in conjunction with size and density, on MPs' entrainment and turbulent mixing (Chapter 5).

- Objective 4: Carry out an experimental investigation into the impact of MP properties, focusing on size and shape, on their distribution and long-range transport (Chapter 6).
- Objective 5: Evaluate the advantages of dynamic modelling approaches in Lagrangian particle tracking for MPs, emphasizing the critical role of particle acceleration in accurately capturing their transport and distribution in a turbulent structure (Chapter 7).

1.4 Dissertation structure

This dissertation is organised into eight chapters, each addressing specific objectives:

- Chapter 2 provides a comprehensive literature review focusing on the physical properties of aquatic MPs, their distribution in different compartments, and previous studies on MP transport based on both numerical and experimental methods used in MP research, highlighting areas that require further investigation.
- Chapter 3 examines the distribution of MPs across various aquatic environments, from surface waters to deep sediments and coastal to remote areas, focusing on their reported sizes and other properties. This chapter addresses Objective 1 outlined in Section 1.3.

  Shamskhany, A., Li, Z., Patel, P., & Karimpour, S. (2021). Evidence of microplastic size impact on mobility and transport in the marine environment: a review and synthesis of recent research. Frontiers in Marine Science, 8, 760649.
- Chapter 4 details the 2D numerical investigation of MP transport and mixing, focusing on the effect of particle size and density on their behaviour in turbulent flow. This chapter addresses Objective 2 outlined in Section 1.3.

  Shamskhany, A., & Karimpour, S. (2022). Entrainment and vertical mixing of aquatic microplastics in turbulent flow: the coupled role of particle size and density. Marine Pollution Bulletin, 184, 114160.

- Chapter 5 builds upon the findings of Chapter 3 by expanding the investigation to include the impact of particle shape. This chapter presents simulations exploring the effect of MPs' sphericity and aspect ratios, in addition to their sizes and densities, on their turbulent entrainment. This chapter addresses Objective 3 outlined in Section 1.3.

  Shamskhany, A., & Karimpour, S. (2024). Microplastics Entrainment in Turbulent Flow: A Numerical Study on the Effect of Shape and Other Physical Particle Properties. Submitted.

- Chapter 6 describes the experimental investigations designed to evaluate and complement the numerical findings, focusing on the impact of MP size and shape on their long-range transport and entrainment in turbulent flow. This chapter addresses Objective 4 outlined in Section 1.3.

  Shamskhany, A., & Karimpour, S. (2024). Experimental Investigation of Microplastics Entrainment in Grid-Generated Turbulence: Effect of Size and Shape. Submitted.

- Chapter 7 presents the 3D numerical investigations, evaluating the advantages of dynamic versus kinematic modelling approaches in predicting MP behaviour under turbulent conditions. This chapter highlights the critical role of particle acceleration and active forces in accurately capturing MP transport and distribution within turbulent structures. This chapter addresses Objective 5 outlined in Section 1.3.

  Shamskhany, A., & Karimpour, S. (2024). Microplastics Entrainment in Turbulent Flow: A Three-Dimensional Numerical Investigation. Draft for submission.

- Chapter 8 concludes the dissertation by summarizing the key findings and discussing their implications for future research and MP mitigation. The chapter also outlines potential strategies for improving MP transport models and suggests areas for further investigation.

Chapter 2

Literature Review

2.1 Sources and pathways of microplastics

Microplastics (MPs), plastic debris ranging from 10 μm to 5 mm [53], are emerging contaminants in different aquatic compartments. Aquatic MPs can be classified into two general groups based on the source of emanation:

- Primary MPs: manufactured for different industrial purposes, such as cosmetic products like cleansers/exfoliators, textile industry, air-blasting, and etc [54, 55, 56]. These MPs usually have regular shapes, and are released to the aquatic environment through wastewater treatment plants (WWTPs) [55].
- Secondary MPs: emerge from the degradation of larger plastic debris over time, due to different causes, such as physical abrasion due to different weathering procedures, photo-oxidation, and UV irradiation [55, 57, 58, 59, 60, 61].

MPs predominantly enter aquatic environments from land-based sources, accounting for approximately 80% of marine MPs [62, 63, 64]. These sources include WWTPs [65, 66], waste landfills, and coastal waste deposition [6]. WWTPs play a crucial role in filtering MPs, with retention rates exceeding 98% for particles larger than 300 µm; however, smaller particles often escape into aquatic systems via treated effluent [67]. Wind and atmospheric transport

also plays a role in delivering MPs to water bodies[68]. Another major pathway for MPs to aquatic systems is stormwater runoff [69]. Urban activities, such as street traffic that causes the erosion of tires [70], and construction and industrial activities that primarily use expanded polystyrene and polyvinyl chloride, which are brittle materials [71], contribute to the breakdown of larger plastic debris into MPs. These particles are then carried by stormwater into nearby rivers or water bodies [72, 73]. Rivers are a major pathway for MPs to the aquatic environment, contributing between 1.15 and 2.41 million tonnes of plastic annually [11].

The behaviour, transport, and fate of aquatic MPs significantly depend on their physical characteristics. The size, shape, and density of MPs, in particular, play a critical role in determining their movement, interaction with the ambient flow, and their preferential accumulation or transport regions. In the following section, we will explore the diverse physical properties of MPs in aquatic systems.

2.2 Review of the selected MP physical properties

2.2.1 Size

Similar to sediment particles, size is one of the most effective physical properties influencing the motion of MPs. A comprehensive literature review about the effect of size on the distribution and fate of MPs in the aquatic environment was conducted as part of this research, and the results are published as a review paper in the Journal of Frontiers in Marine Science. This review study is presented in Chapter 3 of this manuscript.

2.2.2 Density

There are many different synthetic polymers used for commercial purposes, each chosen based on characteristics such as flexibility, strength, heat resistance, cost, and density. While the majority of plastic polymers are made from oil-based materials, there are also polymer types

derived from non-oil-based sources such as rayon and cellulose [35]. In general, high-demand polymers can be classified into Polyethylene (PE), Polypropylene (PP), Polystyrene (PS), Polyethylene Terephthalate (PET), Polyvinyl chloride (PVC), and Polyurethane (PUR) [74, 75, 76]. Other common polymer types, such as Acrylic, Nylon or Polyimide, Acetal, Polyvinyl acetate, and Poly(methyl methacrylate)—here categorized as others—are typically associated with densities higher than that of water [74, 75]. The density of the most common polymer types is represented in Table 2.1. According to global plastic production records [5, 76, 77, 78], PE, PP, and PS account for approximately 60% of total plastic production, as shown in Table 2.1, while less than 3% of the plastic waste made from these polymers is recovered, with the remainder disposed in the environment [12]. This contributes to the fact that the majority of MPs detected in aquatic environments are composed of PE, PP, and PS, respectively [35, 79].

MPs are associated with a wide range of densities, depending on their original polymer type. Additionally, the density of MPs can be influenced by additives introduced during the commercial production process, physical processes such as biofouling and aggregation, and the particle's retention history, including deterioration due to UV irradiation and exposure to chemicals as they travel through the aquatic environment [80]. Density plays a significant role in determining the mobility and distribution of MPs in aquatic environments, as it governs the gravitational forces acting on the particles. The vertical movement of a suspended MP particle, whether rising upward or sinking downward, is dependent on its marginal density—the difference between the particle's density, ρ_p, and the density of the surrounding flow, ρ_f. The marginal density of aquatic MPs, $(\rho_p - \rho_f)$, as shown in Table 2.1, governs the balance between gravity and buoyancy, indicating whether MPs naturally rise ($(\rho_p - \rho_f)<0$) or settle ($(\rho_p - \rho_f)>0$).

Marginal density plays a significant role in determining how particles mix with the flow. When marginal density is close to zero, MPs experience higher levels of mixing, leading to significant deviations from their terminal behaviour observed in quiescent conditions. This trend is evident in the distribution of MPs across various aquatic environments, which

Table 2.1: Properties of the common high-demand polymers [35, 74, 80].

Polymer	Density ρ_p (g/cm^3)	Marginal density* $(\rho_p - \rho_f)$ (g/cm^3)	Frequent site [35, 46, 79, 81]	Global demand** [5, 76, 77, 78]
PE	[0.88, 0.97]	[-0.14, -0.05]	Epipelagic zone, Beach,Deep-sea sediment,Water-column	29.14%
PP	[0.90, 0.92]	[-0.12, -0.10]	Epipelagic zone, Beach, Deep-sea sediment	19.73%
PS	[1.04, 1.10]	[0.02, 0.08]	Epipelagic zone, Beach, Deep-sea sediment	6.25%
PET	[1.37, 1.45]	[0.35, 0.43]	Deep-sea sediment, Water-column	7.30%
PVC	[1.15, 1.58]	[0.13, 0.56]	Deep-sea sediment, Water-column	11.66%
PUR	[0.01, 1.26]	[-1.01, 0.24]	Epipelagic zone, Beach, Deep-sea sediment, Water-column	6.96%
Others	[0.10, 2.20]	[-0.92, 1.18]	Beach, Deep-sea sediment, Water-column	18.95%

$*$ Based on the seawater density at a temperature of $25°C$, salinity of 35 g/kg, and 1 atm pressure, $\rho_f = 1020$ kg/m^3.

$**$ The plastic demand by resin type is averaged over 2020 to 2023.

correlates with their polymer densities. Recent global reviews based on field measurements have documented the widespread presence of PE, PP, and PS, which have marginal densities close to zero, throughout marine environments—from surface layers to water columns and deep-sea sediments, as shown in Table 2.1. Furthermore, the vertical movement of MPs in flow is heavily influenced by flow dynamics, which can significantly alter their natural behaviour in still water and entrain them into the flow. This dynamic interaction between MPs' natural vertical movements and ambient flow motions explains the presence of naturally buoyant particles, with densities lower than the surrounding fluid, in sediment samples [32, 33, 79]. It also accounts for the reported abundance of heavier polymer types in surface waters

[30, 34, 82, 83, 84]. However, as marginal density increases, MPs tend to follow their natural sinking or rising behaviour more closely. Therefore, MPs with higher marginal densities, such as PET and PVC, are more likely to resist weaker ambient flow dynamics. This may explain the predominant presence of such polymers in sediment samples and water columns [35, 46, 79, 81]. In contrast, MPs with lower marginal densities, such as PE, PP, and PS, are more sensitive to ambient flow dynamics compared to polymers with higher marginal densities, such as PUR or PVC. Nonetheless, several factors, in addition to marginal density, influence the transport and fate of aquatic MPs, potentially overriding their natural motion based on marginal density.

Additionally, marginal density can enhance long-range transport of particles to remote regions from their initial source of entry, as it increases particle mixing with the ambient flow. This mixing prevents natural rising or sinking motions, keeping the particles suspended in the flow. The dominant presence of PE, PP, and PS MPs in offshore surface waters confirms that densities closer to that of the ambient water are associated with higher levels of flow mixing, and thus a greater potential for distant transport from their source in the aquatic environment [30, 79, 82]. However, as previously noted, the original density of plastic polymers can significantly change due to chemical processes and exposure to UV irradiation. As a result, discrepancies exist among the reported properties of abundant MPs in different aquatic compartments. For example, heavy MPs with high densities, such as heavy-PUR and polyamide, have been found in the ocean surface and around the Antarctic Peninsula, with UV irradiation and oxidation suggested as possible causes for this unusual behaviour [12, 81, 82]. Moreover, the diversity of sampling methods used to detect and quantify aquatic MPs has likely influenced the results, contributing to the inconsistencies observed in various studies [85].

2.2.3 Shape

Shape is a key factor influencing particle motion in flow, as it directly affects the drag coefficient and, consequently, the settling behaviour of suspended particles. Aquatic MPs

exhibit a wide range of shapes, from regular forms such as spheres, cylinders, pellets, and disks, to highly irregular shapes such as fragments, sheets, fibres, and films, as shown in Figure 2.1. Duis and Coors [41] identified fragmentation and the breakdown of larger plastic pieces as the primary sources of aquatic MPs. However, fragmentation predominantly produces irregular shapes, leading to a higher abundance of irregularly shaped MPs in aquatic environments [42, 79, 82]. The characteristics of different shapes of MPs depend on their source and retention time in the aquatic environment. MPs that have been present in the environment for extended periods tend to exhibit more rounded shapes due to erosion and weathering processes, whereas newly introduced MP fragments often display sharp edges and corners [79].

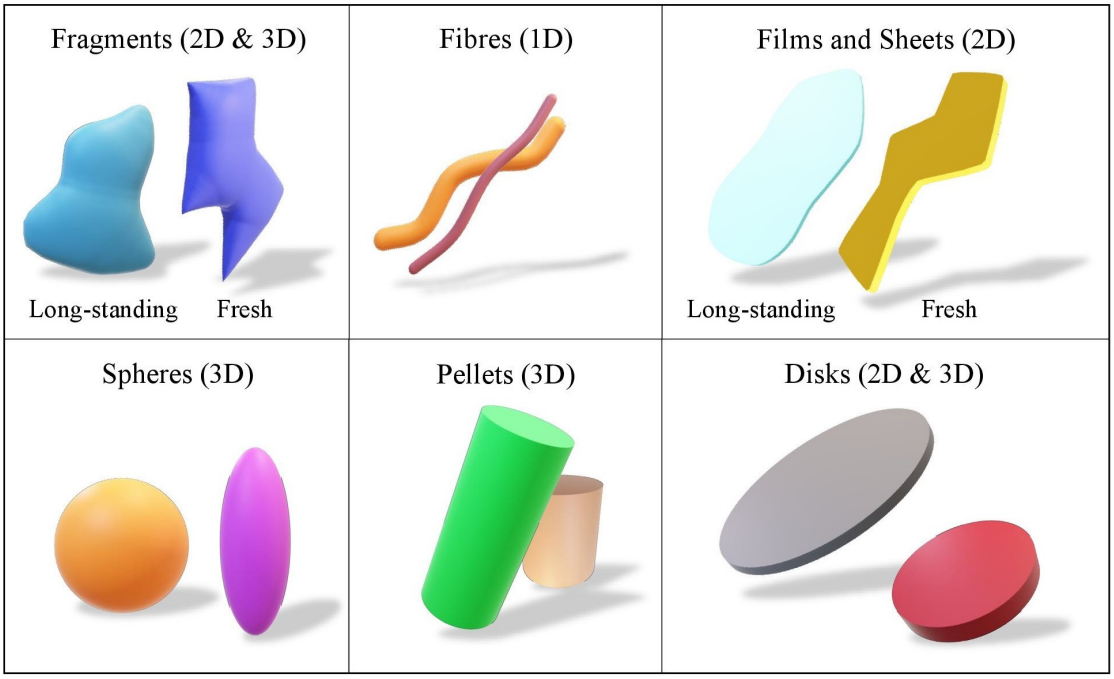

Figure 2.1: Typical shapes of aquatic MPs; the top row shows irregular shapes resulting from the fragmentation of larger plastic pieces, while the bottom row depicts regular shapes of manufactured MPs.

Many sediment transport investigations recommend using the equivalent or nominal diameter-defined as the diameter of a sphere with the same volume-for analysing the particle-flow interaction of non-spherical shapes, such as drag coefficient calculation [86, 87, 88]. However,

MP non-spherical shapes are usually anisodiametric, meaning they might have considerably different dimensions along different axes. For such particle shapes, approximating the drag calculation and predicting behaviour using an equivalent sphere can lead to significant errors. Experimental observations suggest that these approximations often introduce deviations to some extent from the actual behaviour of non-spherical particles. For instance, Chubarenko et al. [85] reported that the retention time of naturally buoyant MPs in surface layers depends on particle shape, and for a similar range of sizes, spherical MPs had retention periods up to 20 times longer than non-spherical shapes. Similarly, Kowalski et al. [89] identified shape as a key factor influencing the vertical distribution of MPs, as non-spherical MPs show a more dispersed distribution compared to spherical particles.Rosal [90] described the diverse morphology of MPs using three dimensionless parameters based on the particle dimensions, and represented that for MPs associated with high aspect ratios, the equivalent diameter cannot adequately predict the behaviour of the particle. Therefore, while using the equivalent diameter can help investigate the effect of size, it is important to consider a suitable criterion to also incorporate the effect of shape.

Finding an accurate definition and assessment criteria for the diverse shapes of MPs, especially irregular ones, remains challenging [91]. However, based on natural particles and sediment analogy, multiple methods have been developed to classify different shapes and quantify their effects. Wadell [87] introduced the sphericity of a particle of any shape as the ratio of the surface area of the equivalent sphere-with the same volume as that of the particle-to the surface area of the particle. Shape factor is another common parameter that is used by many sediment transport studies to distinguish the effect of particle shape [92]. One of the most common shape factor equations is proposed by Corey [93], based on the assumption that particles fall with the maximum projection area. Janke [94] introduced a shape measurement criterion based on a surface area coefficient and a form coefficient, which both have a value of one for a perfect sphere. Aspect ratio of a particle, defined as the ratio of the longest axis to its shortest one, is another well-known parameter for characterizing non-spherical shapes. The aspect ratio can indicate the level of anisotropy of a shape and is therefore a useful

parameter for describing MP shapes such as fibres and films. Finding the aspect ratio of MPs of irregular shapes is quite challenging, as most of the existing studies reported particle dimension in one direction solely. However, based on the reported diameter of synthetic fibres [95, 96, 97, 98] and thickness of the plastic films and sheets [99], as well as several field investigations that reported the average length of MP particles in different regions of the marine environment [79, 96, 100, 101, 102], the aspect ratio, AR, of MPs of irregular shapes, such as fibres and films, is in the range of $1 < AR < 60$, while a value of 25 ± 10 seems the most repeated based on the mentioned different studies at different regions.

During the past decades, several field investigations presented evidence of the distribution of MPs in the aquatic environment based on their shapes. However, it is important to note that the field sampling technique has a significant effect on the reported abundance of MPs of different properties. For instance, using the Neuston net can lead to significant underestimation of the abundance of MP fibres, as they can escape the net due to high aspect ratios [96, 103, 104, 105]. Despite the sampling limitations, several field investigations reported MP fibres as one of the most abundant shapes in different aquatic compartments [100, 101, 106, 107]. Moreover, fibres are reported as the most prevalent shape of MPs in sediment samples [37, 106, 108, 109, 110, 111]. Fragments and beads or spheroids are also dominantly reported among abundant shapes of MPs in WWTPs samples [112]. Cordova and Wahyudi [113] also reported granule shapes as the most dominant form of MPs in sediment samples from the eastern Indian Ocean. MP fragments are also recognized as the most abundant shape, especially in water surface [34, 114, 115]. According to observations by Cózar et al. [31], both shape and size play significant roles in the distant transport of MPs, where smaller non-spherical shapes more likely to be found in distant and deep layers of the aquatic environment. It is evident that the distribution of aquatic MPs based on their abundant shapes is quite diverse, and understanding the effect of particle shape on MP transport and fate is a very important step toward future mitigation protocols. However, it is important to note that the combined effect of different particle properties dominates the behaviour of MPs, and it is still not quite clear which properties have a more significant

impact on the transport and fate of MPs [28, 48].

2.3 Transport mechanisms of MPs and effective physical processes

Plastics from land, rivers, and marine sources follow various pathways and enter the marine environment, where they ultimately accumulate in beaches, tidal wetlands, and marine sediments. According to a recent analytical modelling study on the vertical distribution of MPs in the marine environment, by 2016, 99.8% of the global plastic input to the ocean since 1950 had settled below the surface, with an additional 9.4 million tons settling each year [116]. Multiple factors affect the transport and mobility of aquatic MPs, including terminal movements, physical processes such as degradation and biofouling, windage, surface and subsurface turbulent currents, and sediment-laden flow, as demonstrated in Figure 2.2. In the following section, the effect of these processes on the transport, deposition, and entrainment of MPs is discussed.

2.3.1 Movements of MPs under quiescent condition

Similar to any natural suspended particle, under quiescent conditions, MPs move in the vertical direction with a terminal settling or rising velocity, as demonstrated in Figure 2.3. The terminal velocity of a suspended particle in still fluid is derived based on the vertical forces equilibrium and, thus, depends on the particle and the ambient flow physical properties, such as density of the particle and the flow, particle shape and size, and flow viscosity. MPs have diverse physical properties compared to sediment and other naturally suspended particles, which affects their vertical movements.

In contrast to sediment particles commonly associated with regular and isometric shapes, MPs are quite diverse in shapes, including irregular and non-spherical shapes such as fibres and films. MP shapes, particularly non-spherical ones, significantly impacts the settling

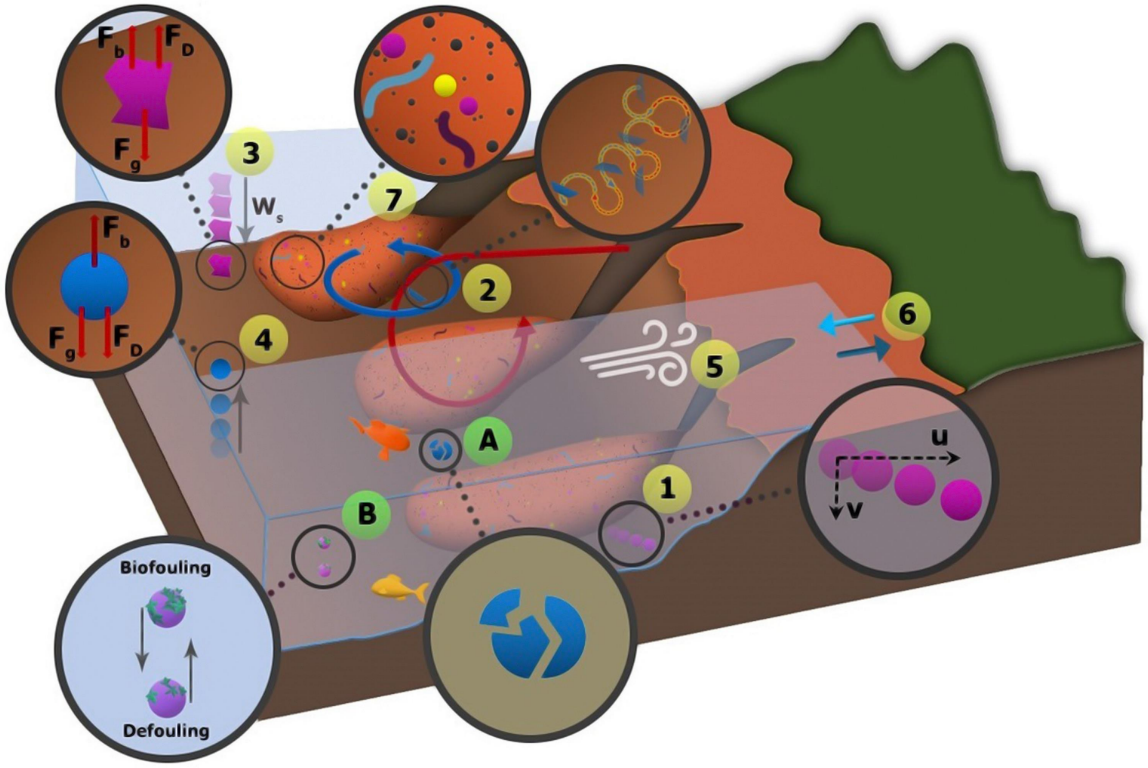

Figure 2.2: Physical processes and transport mechanisms affecting the transport and distribution of marine MPs: (1) advection; (2) turbulent dispersion; (3) and (4) terminal settling and rising movements, respectively; (5) transport by wind; (6) coastal beaching and wash off; (7) transport with sediment gravity flow; A and B present fragmentation and biofouling, respectively.

velocity of MPs, making some of the original sediment-based theoretical methods associated with high errors for calculating the MPs settling velocity [117]. The effect of non-spherical shapes on the settling behaviour of particles is highlighted in multiple pioneering studies, for instance, Willmarth et al. [118] and Jayaweera and Mason [119] who discussed the oscillations and complex settling dynamics of particles with non-spherical shapes at different Reynolds numbers, further establishing the importance of shape. Yang et al. [120] conducted similar experiments on the settling behaviour of MP disks with both positively and negatively buoyant densities. They demonstrated that the rising trajectory of buoyant particles is linear, while the settling trajectory of heavier MP disks exhibits oscillations and zigzag patterns.

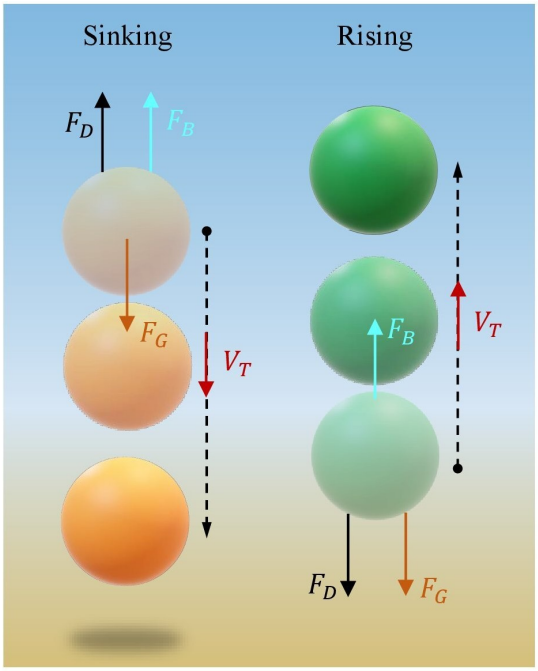

Figure 2.3: The terminal vertical movement of a positively buoyant MP (Right) and a negatively buoyant one (Left); F_G, F_B, and F_D represent Gravity, buoyancy, and the drag force; The terminal velocity of the particle, V_T, can be upward for a rising particle (Right), or downward for a sinking one (Left).

The effect of shape on the settling behaviour of MPs is further supported by recent experimental investigations, demonstrating that the settling behaviour of MPs is complex and highly dependent on their morphology. Wang et al. [49] reported that irregularly shaped MPs experience considerably lower terminal velocities compared to spherical counterparts at different flow regimes. Similar results are reported by Kaiser et al. [121], indicating that terminal velocities of irregularly shaped particles are considerably lower than theoretical values for spheres of the same size range. The various and oscillatory settling behaviour of non-spherical MPs can be due to their rotation and orientation angles in the ambient flow. Bagaev et al. [122] and Khatmullina and Isachenko [47] have shown that smaller fibres' settling velocities vary significantly based on their orientation relative to the flow, and the shape of MPs substantially affects their drag coefficient, complicating settling dynamics. Goral et al. [123] found that MPs tend to settle with their largest projected area perpendicular

to their direction of motion, maximizing the effect of drag.

In addition to the complex effect of particle shape, MPs are associated with a wide range of marginal densities, which makes their natural settling behaviour very different from that of heavy sediment particles. The most abundant reported polymer types in the aquatic environment, such as PE, PP, and PS [117], are associated with marginal densities close to zero, which makes these particles, especially for small sizes, very sensitive to the ambient flow movements. Recent studies highlighted the effect of density, size, and shape of MPs on the deviations in their settling velocity under quiescent and dynamic flow conditions [49, 117, 124]. Despite the recent advancements in understanding the settling behaviour of MPs, challenges remain in elucidating their dynamics in complex scenarios such as mixing and transport in turbulent flows. Additionally, ongoing physical and chemical processes, such as fragmentation, deterioration, photo-oxidation, and biofouling, affect the physical properties of aquatic MPs over time. Such physical mechanisms make the prediction of the settling behaviour of MPs in the aquatic environment even more complex.

2.3.2 Fragmentation and deterioration

Plastic particles continuously fracture and break down into smaller pieces through fragmentation due to various weathering and chemical processes [59]. Fragmentation affects the physical properties of the particles and, therefore, their transport and distribution. For instance, the fragmentation of MPs in aquatic environments enhances their mixing and transport within the water column and deeper parts of water bodies [44]. Erosion is a primary cause of fragmentation and degradation, resulting from the abrasion or collision of plastic particles with one another or with sediment and other natural particles, for instance in density currents. Approximately two-thirds of the global MP input to the oceans originates from the erosion of synthetic textiles and tires during driving [10]. A recent study indicates that different polymers respond differently to erosion in water, with PP exhibiting significant rates of surface erosion [125]. PE seems to be one of the most resistant polymers to mechanical erosion [44, 126].

Moreover, oxidation and UV irradiation (or photodegradation) are recognized as primary causes of the deterioration and fragmentation of plastic debris [58, 59, 127]. The rate at which polymers deteriorate influences the abundance of MPs derived from them, as different polymers respond differently to UV irradiation and oxidation over time. PS, widely used for single-use packaging, is identified as the most sensitive polymer to UV light and oxidation [128], and PE fragmentation due to photo-oxidation is also reported repeatedly in the literature [44, 126, 129, 130]. As a result, rapid deterioration may be a key factor contributing to the significant abundance of PE and PS MPs in the aquatic environment [80, 128]. Oxidation and photodegradation can further alter the original molecular constitution of MP polymers and increase their original density [128, 131]. On the other hand, biofouling—discussed in detail in the next subsection—adds complexity to the fragmentation process of MPs during their ageing, as it creates a protective layer around the particles, thereby altering the rate of fragmentation [129, 132].

2.3.3 Biofouling

In addition to MPs' wide range of physical properties, the accumulation of microorganisms and algae on the surfaces of these particles, known as biofouling, modifies their density and enhances their settling behaviour. When the net density of biofouled particles becomes greater than that of the surrounding fluid, the particles begin to sink. The density increase of light plastic particles, such as PE and PP, due to biofouling has been reported in multiple experimental studies [82, 132]. However, biofouling significantly depends on the properties of the surrounding environment, such as sunlight exposure, nutrient availability, temperature, competing algal growth, and salinity [132, 133]. It can reverse when the sinking particles descend to greater depths with limited light exposure or unsuitable conditions for biofilm growth. In such cases, the rate of biofilm growth decreases through a phenomenon called defouling, and MP particles may rise back to the surface layers, where they are once again exposed to sunlight and other favourable conditions for biofouling. Consequently, these particles may sink again, repeating the cycle. Kooi et al. [133] investigated the effect of

biofilm growth on MPs' up and down vertical transport in water columns, showing that the effect of biofouling is more pronounced on the vertical movement of smaller MPs.

The rate of biofouling increase rapidly on small non-spherical MPs, due to their higher surface area-to-volume ratio. While the buoyancy and weight of a particle are proportional to its volume, its susceptibility to biofouling largely depends on its surface area, and thus, smaller particles lose buoyancy much faster than larger ones [134]. Chubarenko et al. [85] conducted an analytical study on the biofouling of MPs of different shapes, showing that biofouling rates are influenced by the particle's surface area and the time required for its net density to reach that of the surrounding fluid, with fibres being affected more quickly than fragments due to their higher surface area-to-volume ratio. Van Melkebeke et al. [135] further discussed the potential effect of biofouling on the polarity of MPs, which in turn affects its sinking behaviour and may potentially impact the effectiveness of remediation techniques designed for particle separation.

2.3.4 Windage and the wind-driven Ekman currents

The effect of wind on the transport of plastic debris is determined by the ratio of afloat to submerged volume, which depends on the polymer density relative to the density of the surrounding fluid [85, 136]. consequently, low-density plastic debris, such as polyethylene and polypropylene, is particularly sensitive to transport by wind. This wind-driven transport, often resulting from direct drift, is known as windage or leeway drift. [136, 137, 138]. As the density of a polymer decreases, the effect of windage becomes more dominant, intensifying the mobility and transport of very light MPs, such as polyethylene and light foam, in surface layer currents, which can explain their dispersed abundance in the oceans [85]. Additionally, strong winds and the resulting Ekman currents can induce vertical mixing within the water column, leading to the resuspension of plastics from the seabed [39, 52, 139, 140]. Brignac et al. [141] field investigations in Main Hawaiian Islands showed that windward beaches, despite smaller human populations, had about two orders of magnitude more plastic pollution compared to leeward beaches, with the former dominated by light floating polymers such as PE and PP,

while the latter and sediment debris were mainly composed of dense polymers such as PS, Nylon, and PET. However, biofouling can increase the density of the buoyant particles, and as the particles sink in the water column, the leeway effect becomes less pronounced [85].

2.3.5 Tidal movements and beaching

Coastal regions are one of the major sources of land-based plastic waste, and the plastic concentration in these regions has a direct relationship with the population [12, 80, 105, 142]. Some field investigations reported the highest concentration of MPs in coastal regions with industrial and commercial activities [100, 110]. Tidal moves and wind-driven waves can transport coastal plastic waste to the aquatic environment [143, 144]. Zhang [145] reported the significant effect of tidal currents on the residence duration and remote transport of MPs in the coastal regions through flood-ebb and spring-neap tidal currents. Similar to the effect of windage, the role of waves and tidal movements also becomes more effective for light-density polymers, which are abundant in the surface layers of the marine environment [146].

2.3.6 Flow mixing and turbulent entrainment

The ambient flow patterns and regime affect suspended particles' behaviour. The Reynolds number, Re, is a dimensionless parameter that characterizes the flow regime from laminar (Re <2000) to transient (2000<Re <4000) and turbulent (Re >4000) regimes. Turbulent conditions are prevalent in aquatic compartments generated by density currents, tidal forces, wind-driven mixing in surface layers, or topographic changes, including along continental shelves and estuaries. The scales of turbulence vary in size, ranging from smaller scales in vertically stratified flows (centimetres to meters) to large oceanic gyres and thermohaline (tens to hundreds of kilometres) [147, 148]. The Reynolds number in highly turbulent regions of the aquatic environment, for instance, due to the effect of the large-scale thermohaline circulations, can reach up to 10^8 Bray [149]. In the deeper layers of the ocean or below the thermocline, where the temperature and density gradients are reduced, the turbulent mixing

is weaker, and the Reynolds number can range from 10^3 to 10^5 [147, 148]. Still, the turbulent regime in these regions can significantly impact the suspended particle transport, particularly those associated with low marginal densities, such as MPs [150]. Various field observations and computational studies indicate that ocean circulation and bottom currents are among the main transport processes driving the distribution of aquatic MPs [52, 108, 150, 151, 152].

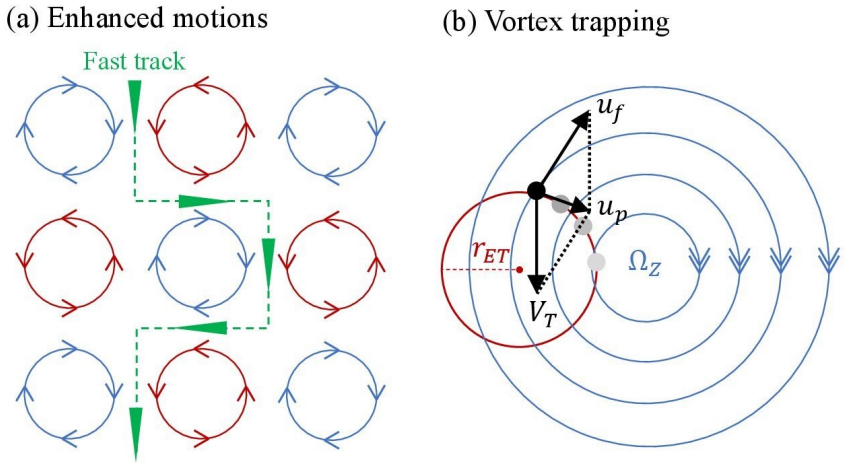

Figure 2.4: Schematic of the (a) enhanced motions track and (b) the vortex trapping, where Ω_z is the vorticity in z-direction, u_f is the velocity of the ambient flow, V_T is the terminal velocity of the particle in still fluid, u_P is the velocity of the particle, and r_{ET} is the radius of eddy trapping (regenerated based on Dey et al. 2019).

Turbulence has been recognized as a major driver of particle mobility and transport since early studies on the settling trajectories of heavy particles in convection cells [153]. Since then, several studies have investigated the effect of turbulence on the settling velocity of suspended particles, describing different phenomena such as sweeping and enhanced settling [154, 155, 156, 157, 158], vortex trapping [159, 160], and the loitering effect on accelerated or decelerated settling of particles passing through turbulent eddies [161, 162, 163, 164, 165]. A schematic of these transport phenomena under the influence of turbulent eddies is shown in Figure 2.4.

Primary discussions on the effect of particle size on the settling behaviour of suspended inertial particles in turbulent flow date back to Nielsen [159], who introduced the concept of

loitering, which has since been explored further in several studies [160, 162, 166]. Loitering refers to the settling behaviour of larger particles that are more likely to deviate from ambient flow trajectories and become trapped in low-vorticity regions. The occurrence of loitering depends on turbulence intensity, which can keep particles suspended longer than expected based on their size. Stout et al. [154], another key investigation into the settling behaviour of heavy particles, demonstrated that particles with small to moderate inertia—defined as when the ratio of the ambient flow velocity scale to the particle's terminal velocity is approximately unity—experience accelerated settling due to preferential sweeping into downdraft regions. Similar findings were reported in a more recent Direct Numerical Simulation (DNS) study by Good et al. [162], who showed that when particles are large enough to be comparable to the Kolmogorov scale of the turbulent flow, they tend to over-sample the downward-moving motions of the flow—referred to as preferential sweeping—leading to an increase in their settling velocity. Furthermore, the experimental study by Wang et al. [158] on sub-millimetre-sized inertial particles revealed that when the ratio of particle diameter to the Kolmogorov length scale is less than 0.5, settling is hindered rather than enhanced. For MPs, turbulence can play a key role in transporting MPs from upper layers of the aquatic environment to deeper parts of the water column and bed sediment [30, 109, 110, 146, 167] and theoretical models developed based on experimental results have demonstrated that smaller MPs experience greater vertical dispersion [30, 89].

The effect of shape on particles settling behaviour becomes very significant in turbulent flow. Vaseleski and Metzner [168] experimented the drag reduction for suspended Asbestos fibres of different high aspect ratios (above 70) in the turbulent flow. Wang et al. [49] performed a series of experiments to examine the settling velocity of MPs with irregular shapes under the effect of turbulence and indicated that the irregularity of MPs shapes substantially reduces their settling velocities compared to spherical MPs. Similarly, Goral et al. [123] investigates the settling velocities of MPs with both regular and irregular shapes under transient regimes, highlighting the importance of orientation angles of non-spherical particles on their settling behaviour. Bagaev et al. [122] conducted empirical studies to establish a precise correlation

for the settling velocity of non-spherical MPs, also demonstrating that the settling velocity of smaller fibres varies significantly depending on their orientation relative to the flow. Turbulent entrainment and vortex trapping instantaneously affects particles rotations in the flow, and therefore, the effect of particle shapes, particularly for high aspect ratios, is very important [121, 122].

2.4 Particle interaction with the ambient flow

2.4.1 Regimes of particles motion

Drag force is the flow resistance to an immersed moving object which is generated by pressure and viscous stresses acting on the surface of the object, opposing its relative velocity with respect to the ambient flow. Drag has a crucial role in dominating the settling behaviour and transport of suspended particles, and governing the settling velocity. Calculation of the drag depends on the flow regime around the particle, which is characterized by the particle Reynolds number, which under quiescent conditions is calculated as:

$$Re_p = \frac{\rho_f V_T d_p}{\mu} \tag{2.1}$$

where μ is the dynamic viscosity of the flow, V_T is the terminal velocity of the particle under vertical force equilibrium, and d_p is the particle diameter. Based on the Stokes law, the drag force, F_D, on any immersed object can be calculated as:

$$F_D = 3\pi\mu V_T d_p \tag{2.2}$$

The equation of Stokes, however, is only valid for Stokesian regimes of the flow around the submerged particle, where $Re_p < 0.1$. In case the particle Reynolds number does not fall in

the Stokesian regime, the drag force (under vertical force equilibrium) is calculated as:

$$F_D = \frac{1}{2}\rho_f C_D A_p V_T^2 \tag{2.3}$$

where C_D is the drag coefficient, and A_p is the projected area. Drag coefficient of a particle significantly depends on its size and shape. Calculation of the drag coefficient for spherical particles is very clear and there are several existing methods to determine the drag coefficient of spherical particles, which is a prevalent shape among sediment and other natural particles.

Early attempts to understand particle motion in ambient flow can be traced back to Oseen (1927) [169], focusing on laminar flow regimes where $Re_p < 1$, and the drag coefficient was calculated using Stokes' law. Later, Schiller and Naumann (1933) developed a more comprehensive empirical model that extended beyond the Stokesian regime, applicable for particle Reynolds numbers in the range of $0.1 < Re_p < 1000$. Putnam [170] was one of the first studies that introduced a correction to drag coefficient models, accounting for all regimes of particle motion, from transitional to turbulent. Similarly, Flemmer and Banks [171] proposed one of the most widely used drag coefficient correlations, applicable across a broad range of flow regimes, from Stokesian to turbulent, with $Re < 10^5$. Table 2.2 provides a summary of the most common drag coefficient correlations used in particle-laden flow studies.

Multiple studies compared the common empirical drag coefficient correlations for spherical shapes and demonstrated that the results of different equations have minimal differences Aggarwal and Peng [169], Flemmer and Banks [171], Hartman and Yates [172], and Clift et al. [173]. The drag force on non-spherical particles is affected by both the shape properties and the orientation angle of the particle relative to the flow. Drag calculation for irregular shapes poses significant challenges due to difficulties in accurately measuring the orientation angle and projected area, the scarcity of experimental data under creeping flow conditions, the insufficient documentation of their shape characteristics, and the random orientations of their protrusions, which result in large statistical variations in drag forces [174].

The non-spherical shapes of particles can be classified as regular shapes-such as cylinders,

Table 2.2: Most common empirical drag coefficient correlations for spherical particles.

Author(s)	Equation	Range of applicability
Oseen (1927) [171]	$C_D = \frac{24}{Re_p}(1 + \frac{3}{16}Re_p)$	$Re_p < 1$
Schiller & Naumann (1933) [171]	$C_D = \frac{24}{Re_p} + \frac{3.6}{Re_p^{0.313}}$	$0.1 < Re_p < 10^3$
Putnam (1961) [170]	$C_D = \frac{24}{Re_p}(1 + \frac{Re_p^{2/3}}{6})$	$Re_p < 10^3$
	$C_D = 0.424$	$Re_p > 10^3$
Flemmer & Banks (1986) [171]	$C_D = \frac{24}{Re_p}10^E$ $E = 0.261Re_p^{0.369} - 0.105Re_p^{0.431}$	$Re_p < 3 \times 10^5$

cuboids, cones-and irregular and anisometric shapes, like MP fragments and fibres. Several studies focused on understanding the effect of particular non-spherical shapes on the drag coefficient. Table 2.3 presents some of the most well-known studies which developed empirical correlations for the drag coefficient of non-spherical shapes. Each of these empirical investigations uses a parameter that defines the shape characteristics of the particle, like sphericity, nominal diameter, aspect ratio, etc., to incorporate the effect of non-spherical shapes on the drag coefficient. Among the listed correlations, Haider and Levenspiel [175] is one of the most popular equations, which includes a wide range of non-spherical shapes, from regular to irregular ones, for a vast range of particle Reynolds numbers, from Stokesian to turbulent regimes.

Loth [174] compared different empirical correlations for calculating the drag of non-spherical shapes across different regimes and found that aspect ratio is the most suitable shape parameter for cylinders, as well as prolate and oblate spheroids, while sphericity is more suitable for other regular shapes. For irregular shapes, the ratio of maximum, medium, and minimum surface areas is suggested as the most suitable parameter to incorporate shape effects

Table 2.3: Most common empirical investigations on the drag coefficient of non-spherical shapes.

Author(s)	Shape	Shape parameter	Range of applicability
Marchildon et. al. (1964) [176]	Cylinders	Front-surface centre of pressure	$70 < Re_p < 2400$
Willmarth et. al. (1964)[118]	Disks	Moment of inertia	$Re_p < 10000$
Jayaweera & Mason (1965) [119]	Cylinders	Aspect ratio	$0.01 < Re_p < 1000$
Haider & Levenspiel (1989) [175]	Isometric and anisometric shapes	Sphericity	$Re_p < 25000$
Tran-Cong et. al. (2004) [177]	Isometric and anisometric shapes	Sphericity, nominal diameter, roundness	$0.05 < Re_p < 1500$

[174]. Non-spherical and irregular shapes exhibit significantly different settling behaviours compared to spherical particles, where drag force is affected by more complex processes [47, 158]. For example at sufficiently high particle Reynolds numbers, turbulence can add to this complexity by causing non-spherical particles to rotate and oscillate continuously, which further complicates drag calculations. Further investigation is essential to understand the hydrodynamics of MPs, especially those with non-spherical shapes, in turbulent flows.

2.4.2 Coupling systems

Another fundamental step toward understanding particle hydrodynamics is clarifying the interaction between particles and the ambient flow, as well as potential interactions between particles. Elghobashi [178] categorized the interaction between particles and turbulent flow into three groups based on the volume fraction of particles in the flow:

- One-way coupling: This occurs when the particle concentration is dilute in the ambient turbulent flow, with a volume fraction smaller than 10^{-6}. In this case, the effect of particles on the ambient flow and on each other is negligible, and the particle-flow interaction is unidirectional, meaning only the flow impacts the particles' motion.
- Two-way coupling: This occurs when the particle concentration spans between 10^{-6} and 10^{-3}, leading to a bi-directional interaction. In such conditions, the energy dissipation in the flow increases due to the concentration of particles.
- Four-way coupling: This occurs when the particle volume fraction exceeds 10^{-3}. In addition to the bi-directional interaction between particles and the turbulent flow, the effect of particle collisions also becomes significant.

In sediment-laden flows and density currents the particle volume fraction is usually considerable, and most studies recommend a two-way or four-way coupling approach. Aliseda et al. [156] and Bosse et al. [157] conducted experimental and numerical investigations, respectively, showing that in homogeneous turbulence, the settling velocity of inertial particles is enhanced as particle concentration increases. This enhancement is due to the preferential accumulation of particles in low-vorticity regions, with the dissipation of turbulent energy becoming more significant as particle concentration rises. However, based on the literature, the reported concentration of MPs—defined as the ratio of MPs' volume to the total volume of the sample—in different aquatic compartments never exceeds 10^{-6} [34, 100, 101, 179, 180]. This concentration falls within the range recommended for a one-way coupling approach to model the interactions between the particle and the ambient turbulent flow, as proposed by

Elghobashi [178] (see Figure 2.5).

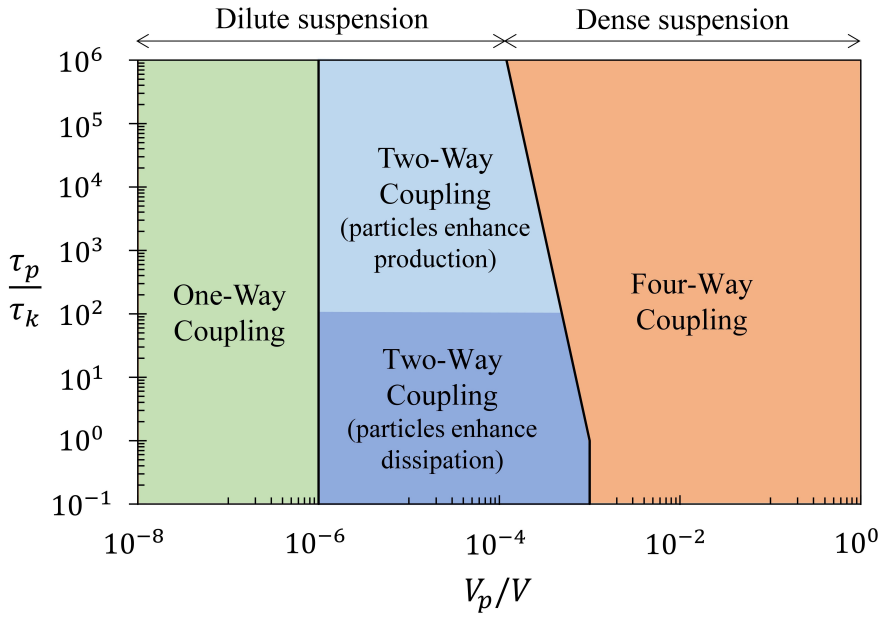

Figure 2.5: Classification of coupling mechanisms for turbulent suspensions; τ_p/τ_k is the ratio of the particle relaxation time, which is the response time-scale of the particle, to the Kolmogorov time scale of the turbulent flow, when molecular viscosity affects the coherent structure, and V_p/V is the volume fraction of the particle in the ambient flow (regenerated based on Elghobashi, 1994).

2.5 Numerical modelling and computational fluid dynamics

Based on the discussion so far, understanding the behaviour of MPs in aquatic environments presents unique challenges due to their varied physical properties compared to natural particles, as well as their complex interactions with flow dynamics. Computational Fluid Dynamics (CFD) modelling has become a vital tool for examining the intricate behaviour and transport of MPs, particularly in turbulent environments, offering significant time and cost advantages over field investigations. Numerical simulations of MP transport in marine environments are relatively recent, with most studies emerging over the past few decades

[181]. Different CFD models have been employed in the literature to explore various aspects of MP transport and the role of flow dynamics. These numerical studies can be classified into two categories of Eulerian and Lagrangian, based on their particle modelling approach.

2.5.1 Eulerian models

Eulerian frameworks model the transport of particles in the flow from a fixed spatial reference point. This approach considers a particular control volume and calculates the concentration of particles within the domain based on the advection-both by terminal settling/rising and ambient flow-and diffusion of the particles. This model is useful for gaining a general understanding of MPs' dispersion and accumulation concentration when the trajectory and behaviour of individual particles are not the primary focus. Mountford and Morales Maqueda [182] developed the first Eulerian model for a large-scale, coarse-resolution simulation of MP distribution in aquatic environments. Their results highlight the significant role of vertical transport and the abundance of MPs in water columns. Guerrini et al. [183] used an Eulerian framework to model the advection and diffusion of plastic-related organic pollutants, carried with MPs in the aquatic environment, in the surface layer of the Mediterranean sea.

In an Eulerian model, representing various MP characteristics—such as variations in settling or rising velocities due to differences in density and size—requires the definition of discrete classes. Nordam et al. [184] compared the Eulerian and Lagrangian approaches for simulating the advection-diffusion of MPs in the water column and demonstrated that increasing the number of settling/rising classes improves the convergence of the Eulerian model's results with those of the Lagrangian model. However, to balance the computational efficiency and accuracy of the simulation, only a limited number of specified classes can be applied in an Eulerian model. Therefore, given the versatile physical properties of MPs and their varied settling and rising behaviours, developing a comprehensive Eulerian model that accurately simulates the specific transport and behaviour of MPs in aquatic environments is challenging.

2.5.2 Lagrangian particle-tracking models

On the other hand, the Lagrangian modelling approach also called the particle-tracking method, calculates the trajectories of individual particles. This method is advantageous for understanding the behaviour of individual MPs rather than the MP concentration and is commonly used for particle tracking in turbulence flow. Lagrangian particle tracking models can be categorized to two main groups of kinematic and dynamic approaches. In a kinematic Lagrangian approach, the displacement of the particles is calculated as the superposition of displacements due to different transport mechanisms. Dynamic modelling, on the other hand, consider the active forces on the particle which dominate its transport and displacement. The detailed definition of these two Lagrangian modelling approaches are provided in Section 1.2.3. This section delves to the existing literature on each of these modelling approaches.

Kinematic modelling approach

Kinematic modelling studies typically focus on the long-range transport of MPs governed by large-scale ocean dynamics. These modelling frameworks are often linked to hydrodynamic models that represent major averaged oceanic circulations, such as thermohaline and Ekman currents. Consequently, although they often employ schemes such as the random-walk method to approximate small-scale perturbations in the ambient flow, they may still lack accuracy in studying fine-scale fluctuations that impact MP transport [185]. Lebreton et al. [186] was among the first to model the long-term planar transport of large floating plastic debris using a global ocean circulation model, identifying the formation of garbage patches. Ballent et al. [152] examined the distribution of MPs in European waters, analysing both surface and subsurface levels, and studied the transport of non-buoyant particles under the influence of large-scale turbulence. Kukulka et al. [140] investigated the impact of wind-driven mixing within the upper layers of the water column on the vertical distribution of MPs. Isobe et al. [52] developed a simplified Lagrangian particle tracking model using a kinematic approach, simulating MP transport in coastal regions as a combination of displacement due to Stokes

drift in finite ocean depth and a random walk model to represent turbulent perturbations. Similar studies on the transport of MPs in large water bodies are conducted using existing hydrodynamic modelling software [187, 188].

In addition to simulating the transport of MPs in the aquatic environment, the kinematic approach is also used to study the influential factors on the preferential accumulation of MPs in aquatic environments [189]. Bagaev et al. [122] used the kinematic approach to model the effect of irregular shapes on the transport, settling, and distribution of MPs. Studies such as Kane et al. [150] and Shiravani et al. [190] also contributed to understanding MP distribution, emphasizing the role of deep-sea sediment currents and the effect of particle proprieties, such as density, size, and shape. Jalón-Rojas et al. [51] and Pilechi et al. [191] developed 3D kinematic models for the transport and fate of MPs, integrating the effect of turbulent dispersion with ocean circulation and random-walk models.

Overall, kinematic models are cost-effective tools that facilitate the large-scale modelling of the long-term transport of MPs and their widespread distribution across aquatic environments, from surface waters to deep-sea sediments. Based on the results of these models, turbulence has a critical role in the transport and distribution of MPs in aquatic environments [52, 122, 140]. However, kinematic models assume that particles move at their terminal velocity relative to the ambient flow, which may not be accurate under the influence of turbulence or certain particle properties. These models neglect particle acceleration due to active forces and their nonlinear effects on particle motion. A clear understanding of MPs transport and mobility, as well as the effect of their various physical characteristics, requires further detailed numerical investigation.

Dynamic modelling approach

Dynamic modelling studies usually focus on specific aspects of MP transport, such as settling, resuspension, and turbulent dispersion, within a more confined region. These numerical models elucidate the complexities of MP transport and their interactions with the flow. A

prime example of small-scale modelling is the study of MP settling behaviour, an intricate process discussed in Sections 2.3.1 and 2.4.1. A common assumption in kinematic modelling studies is that the settling velocity of MPs sinking through the water column or resuspended from bed sediments is equivalent to their terminal velocity in still water. However, the settling velocity of MPs in turbulent flow, particularly for non-spherical particles, can deviate considerably from their terminal velocity [122, 123, 158]. Multiple studies used a dynamic approach to model the settling behaviour of MPs with various regular and irregular shapes, accounting for the equilibrium of active forces [145, 192, 193, 194].

Quyen et al. [195] implemented a dynamic Lagrangian particle-tracking model to investigate the impact of wave breakers on the distribution and accumulation of MPs. Fatahi et al. [196] employed a turbulence model with a dynamic approach in Ansys-Fluent to examine how particle properties, including size, shape, and density, affect MP accumulation and distribution. Quyen et al. [197] used dynamic approach to investigate the effect of different transport mechanisms, such as deposition and accumulation, resuspension, and turbulent dispersion, on the distribution of MPs near artificial structures. Dynamic Lagrangian modelling utilization for understanding the transport, mixing, and entrainment of MPs in turbulent flow is a relatively recent topic, and significant research gaps still exist that need further investigations, such as understanding the effects of various particle properties, as well as the interplay of different transport mechanisms and physical processes.

Nabi et al. [198] Used a Large Eddy Simulation (LES) model to investigate the turbulent mixing of spherical sediment particles of varying sizes. The study revealed that smaller particles are more likely to be resuspended and undergo turbulent mixing. Similarly, Wang et al. [199] conducted an LES study to explore the preferential distribution of suspended sediments with different sizes and densities in a partially vegetated channel flow. Their findings indicated an uneven distribution of particles and centrifugal ejection from the vortex core for spherical sands with Stokes numbers greater than unity [199]. Despite the effective use of LES turbulence models in sediment transport studies, comprehensive numerical investigations into the entrainment of MPs in large-scale turbulent configurations remain lacking. This gap

presents a significant opportunity for future research on the transport of MPs under turbulent conditions. The insights gained from sediment transport studies can serve as a framework for developing analogous models to investigate the transport and mixing behaviour of MPs in turbulent flows.

Chapter 3

Evidence of Microplastic Size Impact on Mobility and Transport in the Marine Environment: A Review and Synthesis of Recent Research

A. Shamskhany, Z. Li, P. Patel, & S. Karimpour (2021), Evidence of Microplastic Size Impact on Mobility and Transport in the Marine Environment: A Review and Synthesis of Recent Research, Frontiers in Marine Science, 8, 760649 [200].

3.1 Abstract

Marine Microplastics (MPs) exhibit a wide range of properties due to their variable origins and the weathering processes to which they are exposed. MP's versatile properties are connected to their dispersal, accumulation, and deposition in the marine environment. MP transport and dispersion are often explained by analogy with sediments. For natural sediments, one of the key features linked to transport and marine morphology is particle size. There is, however, no size classification defined for MP particles and MPs constitute all plastic particles sized smaller than the threshold of 5mm. In this study, based on existing knowledge in hydrodynamics and natural sediment transport, the impact of MP size on turbulent entrainment, particle settling, and resuspension is described. Moreover, by analyzing several

quantitative studies that have provided size distribution, size-selective accumulation of MPs in various regions of the marine environment is reported on. The preferential presence of MPs based on their size in different marine compartments is discussed based on the governing hydrodynamic parameters. Furthermore, the linkage between polymer properties and MP shape and size is explored. Despite the evident connection between hydrodynamic transport and MP size presented, classification of MP size presents challenges. MP size, shape, and density appear simultaneously in the definition of many hydrodynamic parameters described in this study. Unlike mineral sediments that possess a narrow range of density and shape, plastics are manufactured in a wide variety of densities and marine MPs are versatile in shape. Classification for MP size should incorporate particle variability in terms of polymer density and shape.

3.2 Introduction

Plastics are used for a wide spectrum of products and their production has increased drastically over the past decades. Due to improper or lack of end-of-life plastic management, plastic wastes appear globally from mountaintops [4] to seafloors (e.g., Van Cauwenberghe et al. [33]). Plastic emission to freshwater and marine environments occurs through various pathways such as stormwater runoffs, rivers, wastewater discharge, and wind. Once plastic debris reaches a body of water, water acts as a transport vehicle and distributes and spreads the particles. Due to their slow decomposition processes, plastics can last in aquatic environments for centuries, if not millennia. In the past decade, concerns about Microplastics (MPs), plastic debris sized smaller than 5mm, have emerged due to MP pollution impacts on the health of aquatic animals and humans. MPs can be ingested by various animals, ranging from micro-sized zooplankton [201] to whales [202], and move up into the food chain. Furthermore, once ingested, toxins and microbes absorbed by MPs or accumulated on the surface can affect the host organism's health [21, 203].

In marine and freshwater ecosystems, MPs have been reported in high concentrations both in

the vicinity of their emission source, for instance, downstream of wastewater treatment plants [204, 205], as well as in remote areas distant from the source [206]. Quantitative site-based studies in different water bodies have shown a varied assembly of MP properties in terms of their polymer, density, shape, and size (e.g., Morét-Ferguson et al. [82] and Naidoo et al. [207]). Many studies have identified the preferential presence of MPs based on their numerous properties in different compartments of aquatic systems [31, 35, 43, 208, 209]. Marine and freshwater MP particles are transported and dispersed by physical hydrodynamic processes. The importance and role of each process in MP mobility and deposition vary from site to site and are also dependent on MP properties (e.g., Zhang [145] and Van Sebille et al. [210]).

One of the physical properties frequently associated with the distribution and mobility of MPs is density. Plastic density in freshwater and marine environments depends on the type of polymers and can be significantly affected by biofouling, that is the formation of biofilms on particles' surfaces (e.g., Lagarde et al. [211] and Long et al. [212]). Plastics with densities higher than the density of the ambient water are negatively buoyant and tend to sink, while plastics lighter than the ambient fluid are positively buoyant and tend to rise and float in a quiescent fluid (see Figure 3.1). For accumulation in surface water, for instance, some studies have found substantial quantities of polyethylene (PE) and polypropylene (PP) (e.g., Suaria et al. [213]), whereas others have identified polymers such as polystyrene (PS) to be abundantly present (e.g., Di and Wang [214]). Review studies by Erni-Cassola et al. [46] and Schwarz et al. [35] have found PE and PP to be predominant in surface water, followed by PS. The overall data suggests that low-density polymers, PE and PP, both lighter than water, and PS, with densities only marginally different from that of water (Table 3.1), are predominant in surface water.

Similarly, MP shape is also linked to its mobility. MPs are either engineered as small-sized plastics, primary MPs, or they are the by-product of fragmentation of larger plastic debris, secondary MPs. While primary MPs are often in the form of spheres or pellets, secondary aquatic MPs exist in different shapes depending on their origin and exposure to fragmentation processes [79]. Tanaka and Takada [16], among others, presented shapes for MPs, from

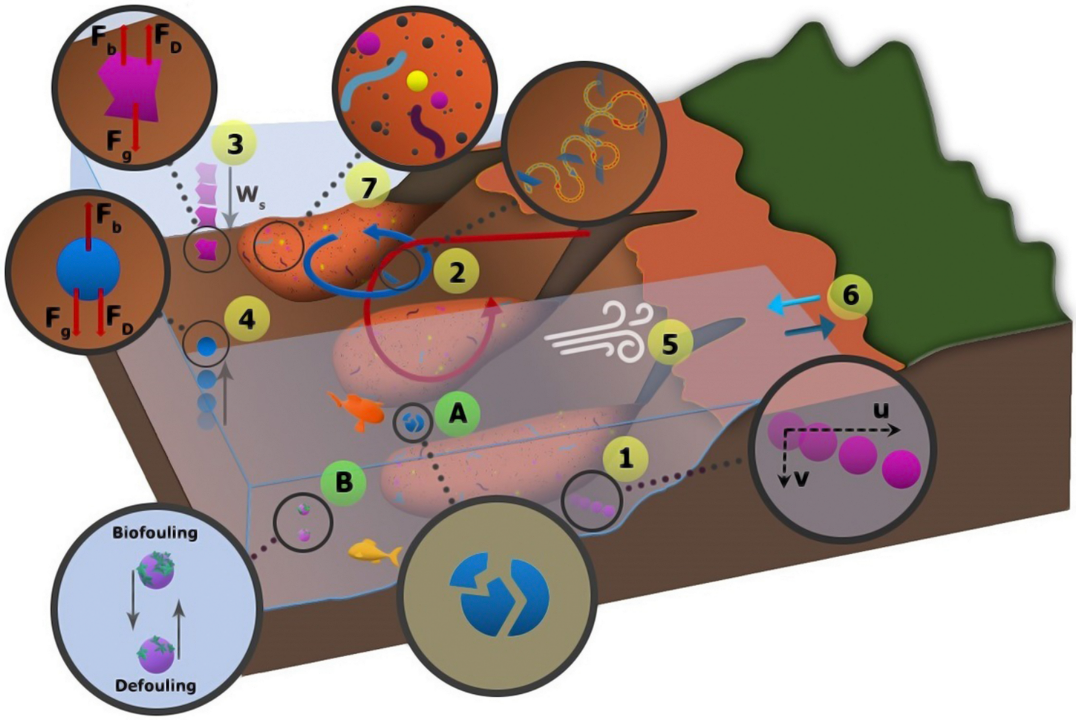

Figure 3.1: Range of physical processes that affect the transport and distribution of marine MPs (modified from Karimpour et al. (2021): 1) advection; 2) entrainment by turbulent structures; 3) sinking of negatively buoyant or biofouled MPs, and vertical forces including drag force, F_D, gravity, F_G, and buoyant force, F_b; 4) rising of positively buoyant or defouled MPs; 5) transport by wind; 6) coastal beaching and wash off; 7) transport with sediment gravity flow. A and B present fragmentation and biofouling, respectively. These two processes are assumed to play significant roles in altering MP transport [215].

fragments and microbeads to sheets, films, and fibres. MP shape affects the particle's drag force, F_D, shown in Figure 3.1, and their rise and fall velocity [47, 89]. The biofouling rate is also strongly linked to particle shape and the particles' exterior surface to volume ratio [133, 216]. Furthermore, sedimentary records have shown a higher presence of a specific MP shape, microfibres [217].

Another characteristic that can strongly impact MP dispersal is size. MPs are reported in a wide range of sizes across freshwater and marine compartments, varying from 10 μm to 5 mm (e.g., Reisser et al. [39] and Bergmann et al. [40]). Compared to natural sediments, the particle size of 5 mm, the upper size limit for MPs, is equivalent to the size of fine

gravel, while the size of 10 μm is equivalent to that of silt. Among sediment properties, size classification is one of the most important sediment features affecting hydrodynamic transport and aquatic morphology (e.g., Yang and Shi [218] and Heitmuller and Hudson [219]). Despite its importance, a limited number of quantitative studies have sorted MPs based on size. In addition, in site-based quantitative studies that have provided size distributions, size classification and categories are inconsistent due to varying objectives, sampling locations and techniques, preparation, and analytical limitations. Filella [104] has first highlighted the lack of attention to standardized size classification and its importance, using the sediment analogy. MP ingestion and ecological impacts are also tied to their size. Lehtiniemi et al. [28] suggested that the size of MP fragments is a crucial factor, influencing the number of plastic particles ingested by small predators. In their study off the coast of South Africa for larger plastic debris, Ryan [208] stressed the importance of plastic size in their long-distance transport. Furthermore, Kooi et al. [133] noted the importance of size in MP biofouling and defouling. They have attributed size-dependent biofouling to the absence of finer MPs from the surface layers, reported by Cózar et al. [34]. Although the impact of MP size on some transport mechanisms has been discussed in several recent studies, a comprehensive understanding of this MP feature and its role in the mobility of MPs is still required.

In this study, some of the hydro-environmental factors that affect the transport of MPs are critically discussed. The impact of particle size and its linkage to these physical processes are explored in-depth. Furthermore, by consolidating the data on MP size distribution from different regions of the marine environment including sediments, the interconnections of size to transport process and accumulation are assessed. Evidence based on plastic composition and polymer types is also presented when reviewing the impact of polymer type and associated fragmentation rate on MP mobility. The objective is to provide a new narrative for MP size based on existing knowledge in sedimentology and to identify existing gaps in this area.

3.3 Microplastic size impact on hydrodynamic parameters

Owing to the unique set of characteristics including their density, range, shape and morphology, MPs' behaviour is different from that of natural sediments and other contaminants. Knowledge regarding the transport of natural sediments, however, can be utilized to formulate the unique hydrodynamic behaviour of MP particles. In this section, the role of selected hydrodynamic processes in MP transport and their relation to particle size are discussed. Figure 3.3 illustrates the role of particle size in MP response to the physical processes discussed in this section.

3.3.1 Effect of size on turbulent mixing and MP entrainment

In turbulent flow, the particle entrainment process is an interplay of turbulence features, gravitational effects, and particle morphology. This interaction between the turbulent flow and gravitational effects of particles appears in different scales of the flow, from larger integral-scale eddies to small dissipative Kolmogorov's scale. The energy-containing eddies are presented by the integral scale, while the viscous range is presented by the Kolmogorov's scale. In formulating this interaction, parameters associated with turbulence length and time scales must be accounted for. The larger scale of turbulence is presented by integral length, l, and turnover time scale, τ_l. The small Kolmogorov's time, τ_ν, and length scale, η, are defined as (e.g., Good et al. [162]):

$$\tau_\nu = (\frac{\nu}{\varepsilon})^{1/2} \tag{3.1}$$

$$\eta = (\frac{\nu^3}{\varepsilon})^{1/4} \tag{3.2}$$

where ν is the kinematic viscosity of the fluid and ε is the dissipation rate per unit mass. Particle engagement also depends on particle size and density, as well as the density of the

ambient fluid [160]. These factors are reflected in particle relaxation time, τ_p:

$$\tau_p = \frac{d_p^2(\rho_p - \rho_w)}{18\mu} \tag{3.3}$$

where d_p is the particle diameter, ρ_p is the particle density, ρ_w the density of the ambient water, and μ is the dynamic viscosity of fluid. The particle relaxation time is sometimes defined by the absolute density (e.g., Wang and Maxey [220]); however, the more general equation considers the density difference between the particle and the ambient fluid, as demonstrated in Eq. 3.3 [158]. Two dimensionless parameters, based on turbulent time scales and particle relaxation time, can be defined to describe the relative significance of natural vertical movements of particles due to gravity and buoyancy, compared to turbulent-induced particle entrainment. The effects of small-scale turbulence on particle motion are ascertained by the Stokes number as defined by Kolmogorov's time scale:

$$St_\nu = \frac{\tau_p}{\tau_\nu} \tag{3.4}$$

The integral time and length scale are dependent on the magnitude of the geometry of the problem, as well as the initial instability conditions (e.g., Karimpour et al. [221] and Karimpour and Chu [222]). The effect of integral scale eddies on entrainment is formulated using the integral time scale:

$$St_l = \frac{\tau_p}{\tau_l} \tag{3.5}$$

Large Stokes numbers associate with higher particle relaxation time or smaller turbulence time scales. In such conditions, particle engagement with the ambient structure lags, and particles move following their natural sinking or rising behaviour. For suspended sediments, large Stokes numbers lead to sinking and deposition to bed. On the contrary, for small Stokes numbers, particles are entrained in the flow and when the Stokes number is very low, particle behaviour will be similar to that of a passive scalar. The relevance of these two dimensionless Stokes numbers depends on the particle's size compared to integral and Kolmogorov's length

scales (e.g., Gorokhovski and Zamansky [223]).

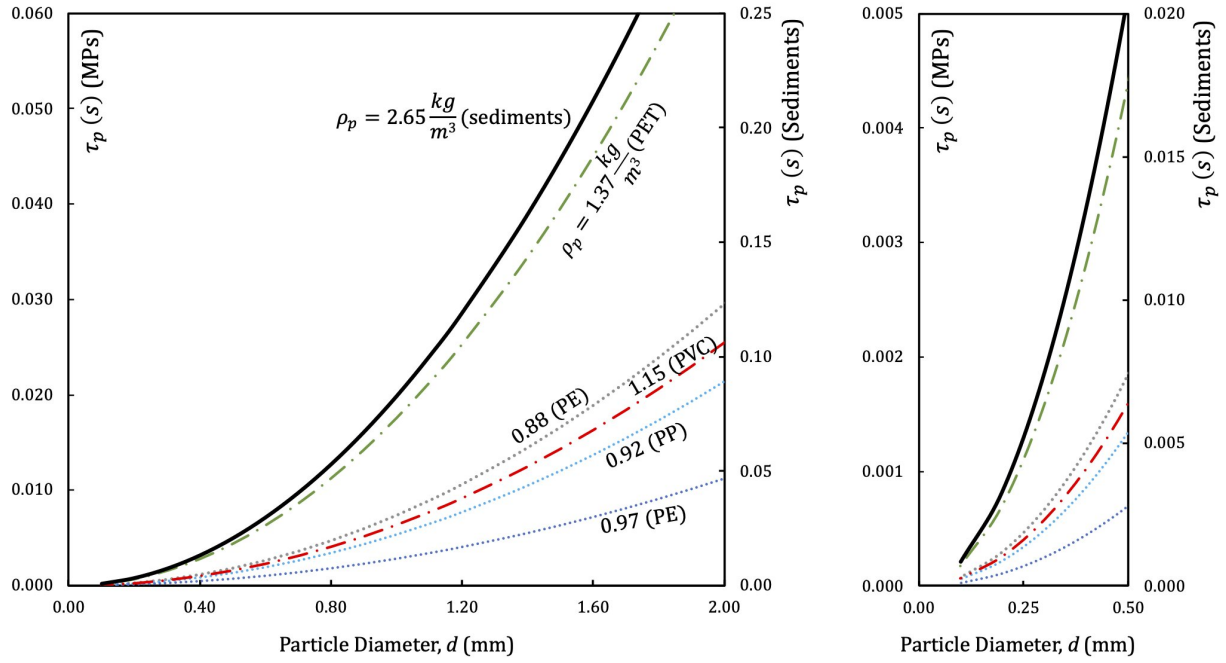

Figure 3.2: Relaxation time, τ_p, for sediment particles (ρ_p =2.65 g/cm^3) and microplastic particles (ρ_p=0.88 to 1.37 g/cm^3). Figure on the left shows τ_p for particle sizes ranging from 0.1 to 2 mm, whereas figure on the right highlights the range for smaller sizes of 0.1 to 0.5 mm.

As can be seen in Eq. 3.3, particle relaxation time, τ_p, is a function of the particle size, d_p, as well as the particle's marginal density from that of ambient water, $(\rho_p - \rho_w)$. Sediment particle density, composed of minerals, is typically between 2.50 to 2.80 g/cm^3. Plastics, on the other hand, possess a wide range of densities: density of foamed PS is a fraction of the density of water, PS can be marginally heavier or lighter than water, whereas PVC can be up to 60% heavier than seawater and freshwater. About 50% of plastics have densities within the 20% margin of seawater and freshwater densities (Table 3.1). The most common polymer types, PE and PP, are marginally lighter than seawater. Figure 3.2 is the plot of relaxation time for sediment particles with density of ρ_p= 2.65 g/cm^3, positively buoyant plastics with densities between 0.88 and 0.97 g/cm^3, and negatively buoyant plastics with densities of 1.15

and 1.37 g/cm^3. These densities are selected as they represent the minimum and maximum ranges of some of the most common polymer types listed in Table 3.1. Particles with smaller marginal density compared to that of seawater, e.g., 0.97 g/cm^3, correspondingly have a very low overall relaxation time.

Table 3.1: Density of high-demand plastics [74], seawater, freshwater, and common range for mineral sediments. The last column provides the global demand for each plastic polymer.

Polymer type	Min (g/cm^3)	Max (g/cm^3)	Global plastic demand and distribution, 2019 [5]
Polyethylene (PE: LDPE, HDPE, LLDPE, MDPE)	0.88	0.97	29.8%
Polypropylene (PP)	0.90	0.92	19.4%
Polyvinyl Chloride (PVC)	1.15	1.58	10.0%
Polyurethane (PUR)	0.01	1.26	7.9%
Polyethylene Terephthalate (PET/PETE)	1.37	1.45	7.9%
Polystyrene (PS/EPS)	1.04	1.10	6.2%
Others	0.10	2.20	18.8%
Freshwater*	1.000		-
Seawater**	1.025		-
Mineral sand/silt/clay	2.50	2.80	-

$*$ 4 °C.

$**$ 25 °C, salinity of 35 g/kg, 1 atm pressure.

A sand particle with a diameter of 0.2 mm, has a relaxation time of about τ_p= 0.0036 s. This relaxation time is attributed to the small particle diameter and marginal density, $(\rho_p - \rho_w)$. Particles smaller than fine sands (including silt and clay) are often entrained with the ambient flow and are transported to distant areas where samples from deep sediments often include silt, clay, and fine sands (e.g., Cunningham et al. [224]). However, MPs have a lower marginal density compared to natural sediments. Therefore, for a turbulent flow with an integral time scale of τ_l and Kolmogorov's time scale of τ_ν, MP particles identical to sediments in terms

of size and shape exhibit lower Stokes numbers. Due to the lower marginal density of MPs, larger MP particles may entrain in various scales of the turbulent flow. For instance, for a density of 0.88 g/cm^3 and 1.37 g/cm^3, MPs with diameters of 0.7 and 0.4 mm respectively, exhibit the same relaxation time as sand particles with a diameter of 0.2 mm. For a MP particle, made of heavy PE with a density of 0.97 g/cm^3, particles with a diameter of 1.15 mm exhibit a similar range of relaxation time as fine sand particles. Due to their smaller marginal density in turbulent flow, MP particles deviate from their natural sinking or rising behaviours as defined by their density. A combination of MP's marginal density and size will govern the process. As demonstrated in Figure 3.3, small size MP particles with small marginal density can be entrained and transported to areas distant from MP emission sources.

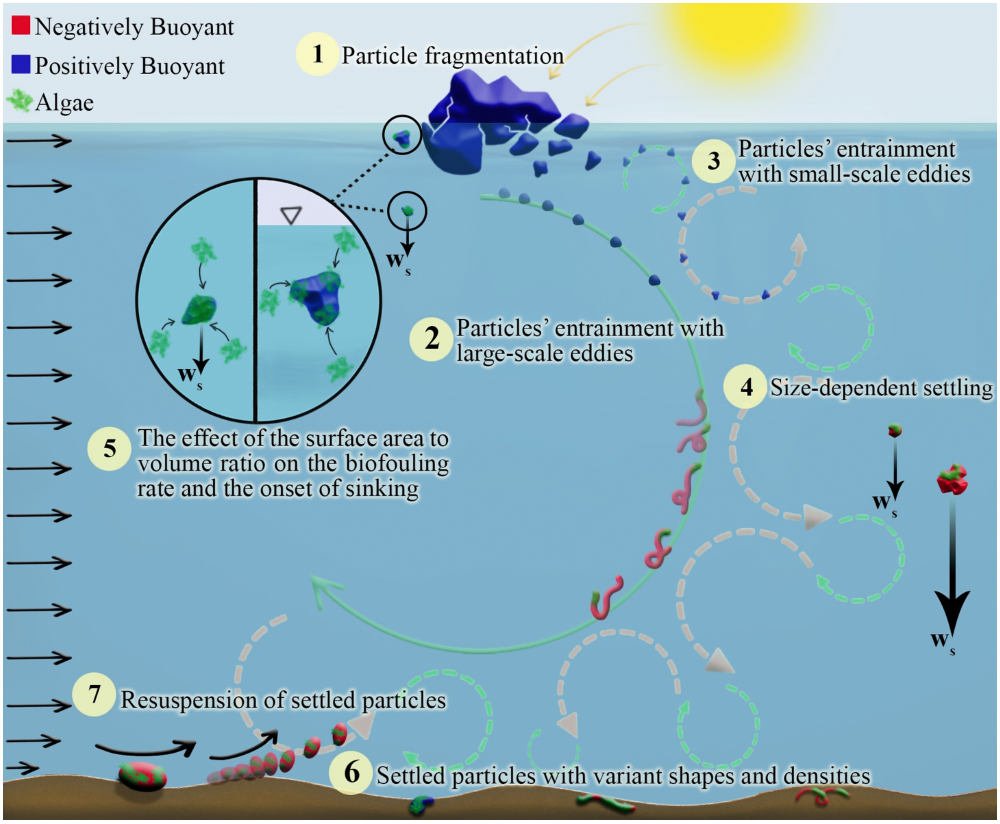

Figure 3.3: Schematic representation of MP size linkage to different processes: from entrainment and sinking to resuspension. In this figure, MPs of different shapes are illustrated, where red and blue colours present negatively and positively buoyant plastics, respectively.

3.3.2 Rising and settling velocities of microplastics

MP particles can either be positively or negatively buoyant, leading to the rising or settling of these contaminants in a motionless water column (Figure 3.1). The rising and settling velocities of MP particles are often assumed to be calculated similarly to those of natural sediments with similar characteristics (e.g., Waldschlager and Schuttrumpf [117]). However, MP particles have shapes that exhibit complex sinking or rising behaviours [16]. In motionless fluid, assuming that vertical forces are limited to gravity, buoyancy, and drag, the steady state particle velocity, w_p, can be estimated based on the following equation:

$$\frac{1}{2}C_D\rho_w A_p w_p^2 = |\rho_p - \rho_w|gV \tag{3.6}$$

where C_D is the drag coefficient and depends on particle shape and flow regime (e.g., Chubarenko et al. [80] and Clift et al. [225]), A_p is the particle projected area resisting the relative fluid motion, and V is the volume of the particle. Re-arranging Eq. 3.7 yields:

$$w_p = \sqrt{\frac{2g}{C_D}\frac{|\rho_p - \rho_w|}{\rho_w}\frac{V}{A_p}} \tag{3.7}$$

In Eq. 3.7, the volume to projected area ratio, V/A_p, is affected by particle shape which plays a key role in the settling pattern of MPs as it influences the drag coefficient as well as the volume to projected area ratio. MP shape can further affect the sinking or rising behaviour of particles in favourable biofouling conditions (see Section 3.3.3). The volume to projected area ratio additionally signifies the role of particle size on settling and rising velocities. The particle size also affects the flow regime that is surrounding the MP particle by impacting the particle's Reynolds number:

$$Re_p = \frac{w_p d_p}{\nu} \tag{3.8}$$

For laminar particle Reynolds number, the drag coefficient is larger for smaller particles. Along with a smaller volume to projected area ratio, V/A_p, this leads to a smaller steady

state rising or settling velocity for finer particles. For MPs, Kooi et al. [133] have shown the sinking velocity variability with size. Similar to Eq. 3.3 for particle relaxation time, Eq. 3.7 for settling and rising velocity is derived from the particle's force balance, therefore, marginal density, $(\rho_p - \rho_w)$, also appears in this equation. Due to a smaller marginal density in comparison to mineral sediment particles, MPs exhibit smaller settling velocities. The settling velocity of an MP particle with a density of 1.30 g/cm^3 is about 2.3 times slower than the settling velocity of a similarly sized and shaped sediment particle. The ratio for an MP particle of a density of 1.10 g/cm^3 is about 4.0. This leads to longer exposure of small MP particles to in-depth currents and mixing induced by waves, roller, and other wind-induced structures, as well as structures such as thermohaline circulations. Such entrainment and mixing of MP particles, as evidenced by the Stokes number, results in inhibited sinking and rising.

3.3.3 Biofouling

Biofouling is an important mechanism that impacts the buoyancy of MPs in aquatic systems. The growth and accumulation of microbes, algae, and invertebrates alter the density of MPs, affecting their buoyancy and sinking or rising patterns [36, 212]. Some of the environmental parameters that affect biofilm formation, growth rate, and composition are depth profiles of light extinction, salinity, density, and viscosity [133]. Due to the variability of these environmental factors, the biofouling effect on MP vertical transport is reported to vary in different marine regions and seasons (e.g., Kaiser et al. [226] and Artham et al. [227]). Biofouling formation also depends on polymer composition, surface energy, and the particle's surface roughness [63, 227].

For naturally buoyant particles, biofouling results in an increase in apparent density and ultimate sinking. Biofouling also affects the settling behaviour of negatively buoyant and naturally sinking particles [228]. The change in apparent density of biofouled MPs is directly related to the exterior surface area to volume ratio. This exterior surface area to volume ratio is affected by MP shape (e.g., Fazey and Ryan [134] and Ballent et al. [229]) and size

[133]. Based on the exterior surface to volume ratio analysis, Chubarenko et al. [85] suggested that, for MP shapes of smaller characteristic length in similar environmental conditions, the impact of biofouling progression on density appears faster. Therefore, among different MP shape categories, those with a larger exterior surface area to volume ratio, such as fibres and filaments, will sink faster when exposed to biofouling in contrast to fragments and beads which are slower to respond to biofouling. Kaiser et al. [226], however, that even in similar environments, the biofilm composition may be dependent on MP shape. Especially in microfibres, small exterior surface areas and characteristic length may prevent the attachment of some macro-foulants.

For MP particles of similar shapes, when particles are small, due to their large exterior surface area to volume ratio, the buoyancy changes immediately after the particle is exposed to biofouling. On the other hand, for larger particles, the impact of biofouling on particles' buoyancy only emerges after longer exposure, as illustrated in Figure 3.3. Kooi et al. [133] evaluated settling onset time with different particle radii and densities. For spherical particles of different buoyant polymer types, the sinking onset was estimated at about 26 days for those with a radius of 1 to 10 mm, while the onset for smaller particles was estimated to occur more rapidly.

Moreover, the impact of biofouling on MP sinking behaviour is complex and not solely due to the change in the particle's density. The accumulation of biofilm may alter the overall shape of the particles and affect their roughness. Furthermore, biofilm aggregates can be permeable, affecting the vertical transport patterns [212, 230]. Change of buoyancy due to biofouling is evidently affected by the plastic size, where smaller buoyant MPs change buoyancy faster. However, further studies will be required to examine the sinking behaviours of various sized and shaped MPs with different fouling conditions.

3.3.4 Critical velocity for resuspension

Negatively buoyant particles that have settled experience shear stress caused by flow velocity. The shear stress exerted on settled particles eventually reaches a value that will force the particles to resuspend, get entrained with the ambient flow, and be transported. A major advancement in sediment resuspension threshold determination was provided by the Shields diagram (Shields, 1936). The threshold developed by Shields (1936) is based on dimensional analysis where:

$$\text{Threshold} = f(\nu, d_s, \tau_o, \rho_s, \rho_w, g) \tag{3.9}$$

which yields:

$$\frac{\tau_o}{(\rho_s - \rho_w)gd_s} = f(\frac{u_* d_s}{\nu}) = f(\frac{d_s}{\delta}) \tag{3.10}$$

where δ is the thickness of the viscous sublayer, d_s is the sediment size, ρ_s is sediment particle density, and τ_o is the shear stress. The ratio of particle to viscous sub-layer thickness on the right-hand side of Eq. 3.10, d_s/δ, is defined as the boundary layer Reynolds number, Re_*. Based on the shear stress, τ_o, shear velocity is defined as $u_* = \sqrt{(\tau_o/\rho_w)}$, which is a measure of the shear stress in the flow. The dimensionless variable on the left-hand-side denotes the ratio of forces acting on a particle affecting its motion and is recognized as Shields number, θ. The Shields diagram identifies the motion threshold based on the Shields number, θ, as a function of the boundary layer Reynolds number, Re_*. The Shields diagram and its variants are discussed in Miller et al. [231]. Similar to sediment particles, MPs that have settled in sediments are prone to resuspension. Chubarenko et al. [80] have plotted experiments by Ballent et al. [152] for MP pellets on the Shields diagram and identified the discrepancies in behaviour observed between Shields material and MPs. Kane et al. [150] have used the Shields number to assess the mobility of sedimentary MPs. Re-writing dimensional analysis and incorporating MP particle density, ρ_p, and size, d_p, the MP resuspension threshold becomes:

$$\text{Threshold} = f(\nu, d_s, \tau_o, \rho_s, \rho_w, g, d_p, \rho_p) \tag{3.11}$$

which yields:

$$\frac{\tau_o}{(\rho_p - \rho_w)gd_p} = g(\frac{u_* d_s}{\nu}, \frac{d_s}{d_p}) \tag{3.12}$$

In Eq. 3.12, the Shields number, θ, is defined based on MP density, ρ_p, and size, d_p, as this dimensionless number denotes the forces on a MP particle. On the other hand, the boundary layer Reynolds number, Re_*, is governed by bed roughness size, for sediments denoted by d_s, and δ that is the thickness of the viscous sublayer. The impact of sediment to settled MP particle size ratio, d_s/d_p, on boundary layer development is not clear. However, in a few studies on sedimentary MPs, authors have reported sediment aggregate size and alluded to its potential impact on boundary layer development and resuspension thresholds [150, 224]. The impact of MP size on resuspension is clearly demonstrated in Eq. 3.12. MPs with a smaller characterized dimension, d_p, possess a higher Shields number, and are of greater probability to exceed the threshold of motion. The fine settled particles are more likely to resuspend in a weak flow field and surrender to long-distance transport. The particle's marginal density, $(\rho_p - \rho_w)$, also appears in the definition of this hydrodynamic parameter. With a marginal density difference between the ambient water and MP, smaller shear stresses and shear velocities lead to the resuspension of MPs.

3.4 Evidence of size-selective distribution and transport

For this section, literature on marine MP presence and detection is systematically reviewed, focusing on studies that have investigated size and density in various marine compartments. Among more than 200 reviewed studies, although many have reported the size range, only 15 provided size distribution for MP particles. These studies are summarized in Table 3.2 and categorized on the basis of the region of the study and vicinity to nearshore for both sediments and surface water. The depth of the sampling is governed by the sampling method. In studies listed for surface water, a variety of sampling techniques, including bulk and volume-reduced sampling methods, were used. In volume-reduced methods employing manta and neuston nets listed in Table 3.2, the depth of the sampling did not exceed 75 cm from the

free surface. While for the bulk sampling employed by Enders et al. [30], the inlet of the pump was submerged to a depth of 3.0 m below the free surface. For studies in sediments, the depth of sampling was measured from the bed and was limited to 65 cm. The reported abundance, concentration, and polymer type depend on source vicinity, discharge routes, and locally used plastics. The size distribution, however, is an indication of flow hydrodynamics dominating the MP spread and dispersal. Despite the provision of the size range in many reviewed studies, the size distribution is not widely available. In studies that have provided size distribution, there is no standardized size classification as observed by Filella [104]. Furthermore, the lower and upper size limits are bounded by sampling and analytical methods, as well as the objective of the study (see Table 3.2 for size range). The lack of a unified and standardized approach amongst different studies has limited the analysis presented in this paper. However, the size distribution in these studies provides insight into the frequency and concentration of various size categories and qualitative descriptions of size distribution profiles.

3.4.1 Impact of MP size on surface water presence

Waves and currents in coastal regions are the most important factors in the transport, erosion, and deposition of sediments [232]. In nearshore areas, the effect of breaking waves along with the presence of longitudinal currents generated by waves creates a size-selective distribution of sediments. This leads to a heterogeneous sediment distribution, with coarse material remaining on the beach and fine material being washed away. Inman and Bagnold [233] were among the first to examine nearshore sand distribution based on their size. Finn et al. [234] analysed the motion of coarse and fine sand particles under passing surface waves, and found strong spatio-temporal particle size sorting patterns, where vertical size sorting of grains in suspension has been reported. Correspondingly, for microplastics, transport and entrainment induced by coastal sub-surface currents and vortices are size-dependent.

Table 3.2: Studies that have identified the size distribution of MPs in nearshore (NS) and offshore (OS) surface water (SW) and offshore sediments (Sed.). In surface water sampling, depth indicates the depth from the free surface, while in sediments, depth is measured from the bed. Size limitation indicates the minimum threshold dictated by sampling and/or characterization method. Square brackets in size range indicate that the size range is limited to the endpoint, whereas round parentheses mean size range contains values beyond the endpoint.

	Location	Sampling depth (cm)	Sampling technique	Size range (μm)	Dominant shape
SW - NS	Coastal waters of China [235]	not available	Volumetric steel samplers	[20 5000]	Fibres
	Hiroshima Bay, Japan [236]	0.00-75.00[A]	Neuston net; 75×75×300 cm^3	(355 5000)	-
	Korean West Coast [237]	0.00-0.04	Stainless steel sieve; 20 cm diameter	[50 1000)	-
	Atlantic European Coastal [30]	0.00-300.00	Volumetric sampling using pump	[10 10000]	Other than fibres
SW - OS	Mediterranean Sea, Arctic Ocean, Subtropical Gyres [31]	0.00-15.00	Manta net; 86 cm width	[320 860]	Fragments
	North Atlantic Subtropical Gyre, Atlantic Open Ocean, Atlantic European offshore [30]	0.00-300.00	Volumetric sampling using pump	[10 10000]	Other than fibres
	North Atlantic sub-tropical gyre [39]	0.00-50.00	Filter net	[500 5500)	Fragments
	Malaspina Circumnavigation [34]	0.00-50.00[A]	Neuston net; 50×100 cm^2	[200 10000]	Fragments and Sheets
	Atlantic Ocean [82]	0.00-25.00	Neuston net; 50×100 cm^2	[335 15000)	Fragments
	North Pacific Central Gyre [238]	0.00-15.00[A]	Manta trawl; 15×90×350 cm^3	[355 4760]	Fragments
Sed. – OS	Rockall Trough North Atlantic Ocean [83]	0.00-60.00	Sediment core samples;60 cm height & 10 cm diameter	[52 6500)	Fibres
	Western Pacific Ocean [239]	0.00-5.00	Stainless-steel box corer	[100 5000)	Fibres
	Eastern Indian Ocean [113]	0.00-60.00[B]	Main samples: box corer; 60×40×50 cm^3; Sub-samples: stainless steel shovel	(20 500)	Granules
Arctic Sed. – OS	Arctic Ocean [32]	0.00-5.00	Video-guided multiple corer; 8 cores (100 mm diameter)	[11 100)	Fibres
	Arctic Ocean [106]	0.00-65.00[B]	Stainless-steel box corer; 50×50×65 cm^3	[100 2000)	Fibres
	Arctic Ocean [40]	0.00-5.00	A video-guided multiple corer with eight cores of 100 mm diameter	[11 500)	-

A Water depth was not explicitly provided. Therefore, the maximum net mouth dimension is assumed as the depth.
B Sediment depth was not available. Therefore, the maximum core dimension is assumed as the depth.

Ryan [208] has reported the size distribution for plastic debris in nearshore and offshore sites for plastic pieces sized smaller than 60 cm. In the coastal areas, the results indicate that about 60% of plastic pieces were sized smaller than 5 cm. While in offshore regions, about 65% of plastics were sized between 5 to 30 cm. This shows a preferential abundance of larger floating plastic pieces offshore in surface water.

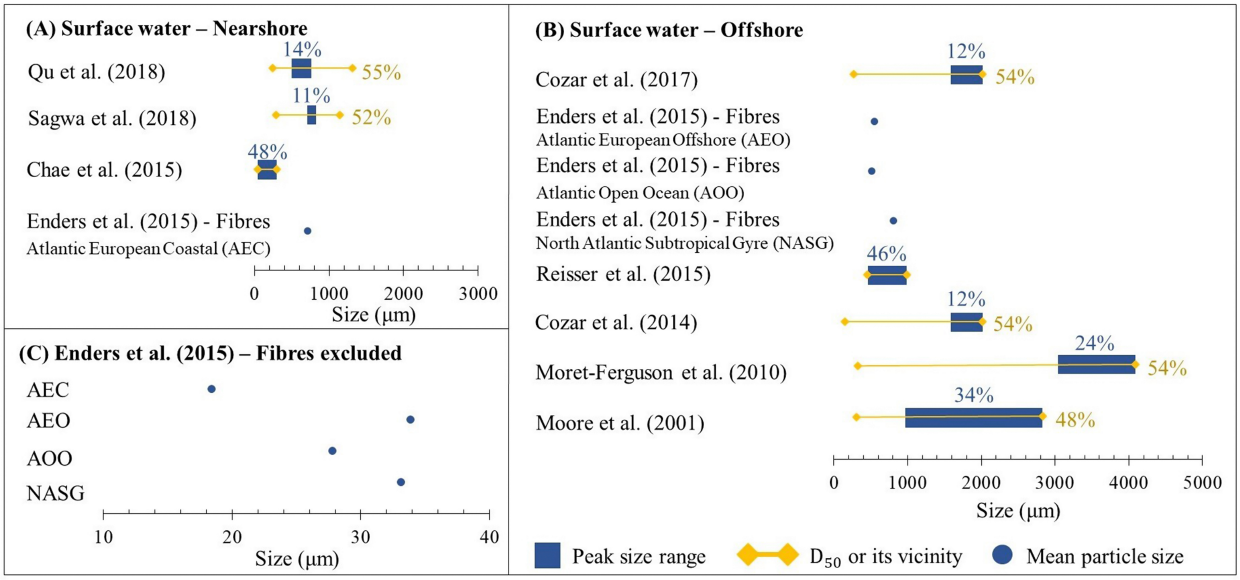

Figure 3.4: Size distribution characteristics for surface water sample (A) nearshore and (B) offshore. (c) The mean size for MP particles excluding fibres by Enders et al. (2015). The box in each study identifies the size bin with the highest concentration. The size of the box is unique in each study and is consistent with the bin size reported. The horizontal bar in each study is the D_{50} or its proximity. Since bin sizes vary among these studies, D_{50} is determined within $\pm 5\%$. The circles are the average MP size presented by selected studies, where size distribution was available but could not be extracted.

Figure 3.4 reports the size characteristics for studies in Table 3.2 that provided size distribution for surface water in nearshore and offshore regions. In this figure a few features are extracted from the size distribution reported in the original studies: peak size distribution and D_{50}, or vicinity thereof. The peak size boxes in Figure 3.4 have variable sizes as the bin sizes vary in different studies. D_{50} is the particle diameter at 50% in the cumulative distribution, demonstrated by a horizontal line for each study. Sagawa et al. [236], Chae et al. [237], and Qu et al. [235] are among the studies that investigated the size distribution of microplastics

in coastal areas. The peak size bins in all three studies lie between 100-750 μm, whereas D_{50} is approximately smaller than 1200 μm as shown in Figure 3.4 (A).

Offshore studies, shown in Figure 3.4 (B), reported peak frequency or concentration at larger size categories. The peak size bin varies from Reisser et al. [39], who have reported a peak size of 500-1000 μm, to Morét-Ferguson et al. [82] with a peak of 3000-4000 μm. Morét-Ferguson et al. [82] have also used larger bin sizes to provide size distribution. The peak of the distribution, however, lies at a larger size. Furthermore, the vicinity of D_{50} is also identified at a larger size range. Enders et al. [30] have looked at individual MP particle and fibre size. The mean size reported for particles with shapes other than fibres was notably smaller for both nearshore and offshore regions compared to other studies, as demonstrated in Figure 3.4 (C). They, however, reported mean size values from nearshore samples that were smaller compared to samples extracted from offshore, open ocean, and subtropical gyres.

For low-density buoyant MPs, with apparent density lower than that of seawater, particle size affects the relaxation time. Smaller MPs have smaller particle relaxation times. Therefore, as buoyant plastics and MPs reach coastal areas, small-sized particles are more likely to separate from the surface layer and get entrained with wave-, wind-, or thermal-induced currents and subsequently get advected and transported offshore. Additionally, small MPs have a larger exterior surface area to volume ratio and therefore, when exposed to biofouling, their onset of sinking is shorter. Due to the combined influence of biofouling effect and higher potential for entrainment, they appear less abundant in offshore surface water samples.

Similarly, for fine negatively buoyant MPs, biofouled or pristine, entrainment with in-depth vortices and their offshore transport can be induced by weaker currents. This is further reinforced as smaller negatively buoyant particles sink gradually. Therefore, the presence of small-sized high-density MPs, both biofouled and pristine, in the water column is prolonged. This increases the likelihood of entrainment over time. While, for larger sinking MPs, only strong currents can entrain the particles and lead to offshore transport. Furthermore, the resuspension and mobility of settled MPs are also size dependant. Smaller sized MPs that

have settled have a higher Shields number, θ, which leads to a lower resuspension threshold, and a higher likelihood of resuspension.

3.4.2 Deep-sea MP presence

Once sediments are transported by fluvial means into marine environments, larger sediments, such as sand, settle in shallower marine environments in nearshore areas. Smaller sediments, such as silt and clay, remain entrained in the currents and are transported offshore. These particles are carried to regions with lower velocity currents and, with a very slow rate, are deposited to the bed. Another main mechanism leading to the bed deposition of sediments is turbidity currents. Turbidity currents originate over continental shelves, where high-density sediment-laden flow plunges down to the seabed. These currents are the primary processes for carrying fine sand to deep-sea sediments. Similarly, MP debris accumulates in seafloor sediments either directly by sinking through the water column, or via currents and sediments transported from the fluvial regions [217, 240]. Some studies suggest that deep-sea sediments can be the sink for lost MPs (e.g., Anderson et al. [241] and Chiba et al. [242]). However, Barrett et al. [243] have shown the contrary, where the sedimentary deep-sea MPs account for only a small portion of lost MPs. Nevertheless, our analysis of the existing studies on size distribution in nearshore and offshore areas on surface water shows that smaller MPs are missing from the water surface. This corroborates findings by Cózar et al. [34] that have shown a size-selective absence of MPs from the ocean surface.

Figure 3.5 (A) shows the peak bin size with the highest concentration and D_{50}, or its proximity, for deep-sea sediments. D_{50} in all cases falls below 1000 μm, and this value never exceeds the peak bin size. This signifies the abundance of narrow particle size distribution that is limited to very fine MPs in deep-sea sediments. For nearshore surface water samples, although the peak size bin was also reported to be small, D_{50} extended beyond this size showing a wider spread of size distribution. This is attributed to the impact of size in hydrodynamic processes outlined in Section 3.3. Intrusion of fine MPs in deep-sea sediments can partly explain the absence of these MPs from the water surface in offshore regions.

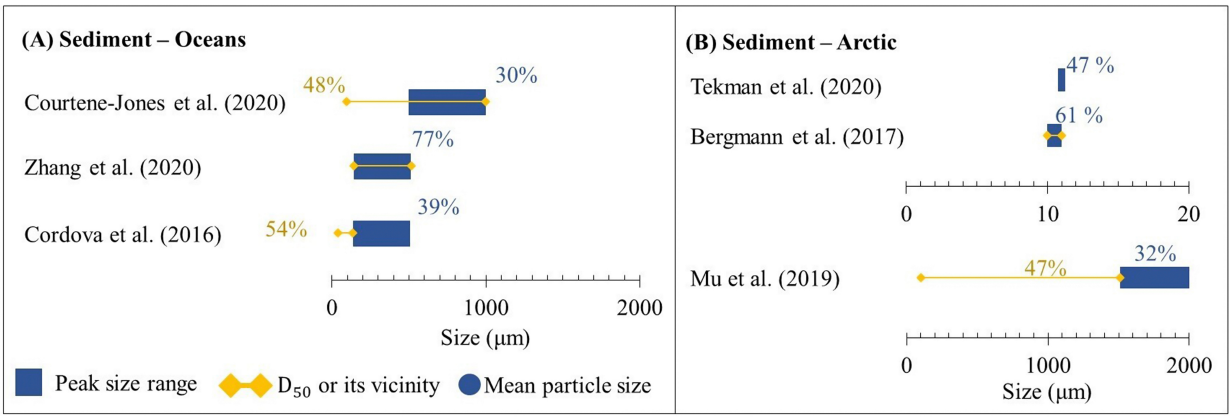

Figure 3.5: Size distribution characteristics for sediment samples for (A) offshore and (B) the Arctic. The box in each study identifies the size bin with the highest concentration. The horizontal bar in each study is the D_{50}, or its proximity. The circles are the average MP size presented by selected studies, where size distribution was available but could not be extracted.

3.4.3 Remote areas and size distribution

In recent years, the prevalence of MPs in remote Arctic and Antarctic regions has drawn the attention of researchers around the world. MP particles have been found in Arctic and Antarctic surface water [31, 32, 206] as well as in deep-sea sediment samples [32, 40, 106, 206, 244]. The high abundance reported had no correlation with upstream population and was associated with long-distance transport from remote sources [206]. Thermohaline currents are among the important processes in the transport of deep fine sediments [245], and Cózar et al. [31] attributed the prevalence of MPs in Arctic remote areas to these global currents. The shallow thermohaline currents can redistribute floating plastics from different latitudes [31]. On the other hand, deep thermohaline currents will interact with deep-sea sediments and sediment currents, and transport settled, settling, and neutrally buoyant MP pieces [121].

A few studies have provided the size distribution of MPs in the sediments extracted from Arctic regions (Figure 3.5). All these studies have noted the abundance of fine MPs in sediment samples. In fact, Bergmann et al. [40] have reported that about 80% of MP particles were sized smaller than 25 μm. The mobility of MP particles induced by the thermohaline

currents is dependent on their size. The shear velocity imposed by deep thermohaline currents can lead to resuspension of fine sediments, as well as fine MPs. The turbulent structures induced by this velocity gradient in a thermohaline current [246] can lead to the entrainment and long-distance transport of sediment and MP particles, depending on their size and relaxation time.

3.5 Polymer type and relation to particle size and shape

Plastics are made of different polymers with a wide variety of properties. Plastic density has been highlighted as one of the important properties affecting transport and distribution. Density evidently impacts aquatic MP distribution as it affects the buoyancy of the particle in quiescent fluid. In recent years, Schwarz et al. [35] and Erni-Cassola et al. [46] have looked at plastic distribution in different freshwater and marine regions. Schwarz et al. [35] have consolidated literature on marine sediments, while Erni-Cassola et al. [46] have gathered evidence on polymer type accumulation in intertidal, subtidal, and deep-sea sediments separately. Both studies have discussed the selectiveness of MP distribution based on density.

Table 3.3: Young's Modulus of elasticity and elongation for selected polymer types [74].

Polymer type	Young's Modulus (MPa)	Elongation (%)
Polyethylene HDPE	1069 – 1089	10 – 1200
Polyethylene LDPE	172 – 282	100 – 650
Polypropylene (PP)	1138 – 1551	100 – 600
Polyvinyl Chloride (PVC), hard	2413 – 4137	40 – 80
Polyurethane (PUR)	0.17 – 34.47	250 – 800
Polyethylene Terephthalate (PET/PETE)	2758 – 4137	30 – 300
Polystyrene (PS/EPS)	2275 – 3275	1.2 – 2.5
Polyamide (PA6)	2000	65 – 150
Polyamide (PA66)	1586 – 3447	150 – 300

Plastics, however, possess other properties that affect their distribution; among these properties are brittleness and flexibility. Table 3.3 presents two material properties: Young's

Modulus of elasticity, in MPa, and Elongation, in percentage. Young's Modulus is a measure of the ability of a material, plastics in this case, to withstand changes in length when it undergoes tension or compression. Elongation, on the other hand, is a measure of deformation before a material breaks if subjected to a tensile load. Plastic polymers such as HDPE, LDPE, PUR, and PP, have high elongation and can be categorized as ductile, while hard plastics such as PVC, PS, and PET have relatively lower elongation. All three polymers also have high Young's Modulus of elasticity and are more brittle than other plastics listed. This is consistent with the study by Efimova et al. [247] that examined the fragmentation rate for PS, PS foam, LDPE, and PP. They reported that PS, listed with the lowest elongation in Table 3.3, has the highest fragmentation rate and after 15-18 days of mixing with sediment and water it reached about 80% fragmentation in the form of MPs, in terms of its original mass. Whereas, for PP, a ductile plastic polymer, only 0.07% of the original mass was fragmented into MPs after about 24 days of mixing. Due to their low brittleness, HDPE, LDP, PUR, and PP are resistant to fragmentation. Whereas fast fragmentation to smaller plastics and eventually to smaller-sized MPs is anticipated for PVC, PS, and PET.

As described in Section 3.3, long-distance transport is size-selective. Given that PVC, PS, and PET are fragmented rapidly, under favourable conditions, they will most likely be entrained and transported farther. The meta-analysis by Erni-Cassola et al. [46], clearly demonstrated this polymer selectiveness, established by a combination of fast fragmentation, density, and impact of size on transport. In their analysis for subtidal and intertidal sediments, they reported a concentration of between 25-40% for polyester, polyamide, and acrylic. Whereas, in deep-sea marine sediments their compilation yielded a higher concentration of roughly 75% for polyester, polyamide, and acrylic. The demand for polyester, made of PET, is about 8% and demand for polyamide is 2%. If the density is considered as the sole plastic property governing the distribution, all land-based debris pieces composed of PET, polyamide, and acrylic should settle nearshore as these polymers have densities higher than those of both seawater and freshwater. Due to their high fragmentation rate and smaller size, particles made of these polymers can be transported offshore and settle in areas with slow ambient

velocities. The high concentration of polyester, polyamide, and acrylic in deep-sea sediment is due to the combination of polymer properties, including their brittleness, measured by elongation and density, as well as particle's shape. The presence of small-sized MPs, based on the evidence presented in this paper, along with the abundance of polyester, polyamide, and acrylic in deep-sea sediments conform with observations reported for MP shape in this compartment. All the studies listed in Table 3.2 for deep-sea sediments have reported MP shape categories. Courtene-Jones et al. [83] and Zhang et al. [239] have distinctly reported fibres as the dominant shape. Microfibres are also found in higher percentages in other studies conducted for deep-sea sediments (e.g., Woodall et al. [111]). The abundance of microfibres is consistent with the reported polymer types, as microfibres used in textiles are commonly made of polyester, polyamide, and acrylic [56]. Other factors have also been linked with the abundance of microfibres in deep-sea sediments. Owing to their distinct shape, Kane and Clare [217] suggested that microfibres can be transported by gravity currents to deeper sediments. Furthermore, as discussed in this paper, microfibres possess a larger exterior surface to volume ratio, which would lead to fast alteration in buoyancy if exposed to biofouling. The combination of brittleness and density of these polymers with the unique shape of microfibres leads to their intrusion into deep-sea sediments.

For offshore surface water, a compilation by Erni-Cassola et al. [46] shows that more than 75% of polymers present are either PP or PE, while the demand for these 2 polymers combined is about 50%. These polymers are ductile and are not easily fragmented. As described in this study, in this compartment, MPs have a larger mean particle size. Due to their size, stemming from their slow fragmentation, these plastics remain afloat as they are associated with larger Stokes numbers. Moreover, among the studies compiled here for surface water offshore, all have provided shape categories. Aside from Enders et al. [30], all studies in this category have identified fragments as the dominant shape which was also reported by Woodall et al. [111], among others. The combination of buoyancy and slow fragmentation rate leads to the presence of PP and PE particles in the surface, which is also related to a higher concentration of larger fragments in this compartment.

In nearshore surface water, however, authors did not find a consistently dominant shape in various studies. While Qu et al. [235] reported fibres as the dominant shape, other studies such as Song et al. [42] have reported fragments to be dominant. Furthermore, polymer analysis, conducted by Erni-Cassola et al. [46] in the intertidal region, has shown the presence of multiple polymer types. This is likely due to the closer proximity of nearshore water to both marine and terrestrial plastic sources. Due to source variability in different geographical regions, plastic shapes and polymers found in studies conducted in the nearshore water are diverse.

As noted by Schwarz et al. [35], the abundance of PVC in all freshwater and marine compartments is very low, while its production comprises about 10% of plastic demand. PVC is mainly used in building and construction [5] and, due to its extended life-cycle and better end-of-life waste management, provides a smaller contribution to freshwater and marine plastic pollution. Similarly, PUR is highly used in automotive and building and construction sectors, hence they also have not been reported in high concentrations in aquatic systems. PS is the polymer with the smallest elongation listed in Table 3.3. This polymer has been reported in various environmental compartments in both freshwater and marine surface and sediment samples [35, 46]. This is due to the small marginal density of this polymer, $(\rho_p - \rho_w)$, combined with fast fragmentation. Once broken down into fine MPs, PS particles behave similarly to a passive scalar and disperse easily with the flow.

3.6 Discussion and recommendation for future work

Aside from hydrodynamic and environmental factors, MPS' mobility is affected by their properties. These properties include polymer density, particle shape, and size. Motion of a MP particle, even in a quiescent fluid, is affected by all three properties: density dominates the buoyancy of the particle, shape affects the drag force, and size affects the magnitude of buoyant and gravitational forces as well as the magnitude of the drag force. Significant emphasis has been put on plastic density in the literature, as it is undeniably a critical factor

in the distribution of plastics. Furthermore, to understand the mobility of MPs in terms of natural sediment particles, efforts have been made to define MPs by shape categories and, accordingly, define shape factors [89, 248]. MP shape is also strongly linked to biofouling. The analogy with sediment particles infers that MP size is another important driver in MP distribution and mobility. Our assessment of several hydrodynamic factors, namely relaxation time, settling and rise velocity, and Shields parameter indicates that MP particle size is directly tied to these parameters. Smaller-sized MPs exhibit lower relaxation time, lower settling velocity, faster onset of sinking if exposed to biofouling, and a lower Shields number.

These parameters affect the mobility of MP particles and their transport to regions distant from their source of emission. Our analysis of 15 studies that have provided size distribution for different regions of marine systems, also confirms this correlation. Nearshore surface water samples that are often closer to the emission source have exhibited a smaller D_{50}, while offshore surface water samples have shown a larger D_{50}, where aged plastics have undergone weathering and smaller MPs should be more abundant. This trend has been previously attributed to biofouling and faster onset of sinking for small MPs [133]. Our analysis suggests that other factors may contribute to the absence of small-sized MPs from the surface in offshore areas. Entrainment and in-depth mixing lead to the entrainment and long-distance transport of fine MPs. Similarly, small MPs can be entrained and advected with thermohaline circulation resulting in their deposit in remote Arctic areas. Furthermore, polymer fragmentation rates affect plastic size and, ultimately, its transport. Brittle polymers are fragmented into smaller MPs and are more abundant in far and remote areas. Along with microfibres' unique shape, this supports the presence of fibres in deep-sea sediments. On the other hand, polymers with slow fragmentation rates are found in larger fragment shapes in the offshore water surface. The studies that were presented in Table 3.2 and analysed in Figures 3.4 and 3.5 were selected based on size distribution availability. However, these studies did not employ a standardized sampling, separation, and identification method or protocol. For in-depth and meaningful comparison and monitoring, it is critical to define and implement a standard method for all three steps to estimate the abundance, distribution,

and composition of MPs. The size distribution range and bin sizes reported, therefore, were different since authors used different approaches. This has limited our analysis of existing literature and adds uncertainty to the analysis. Hence, we have limited our discussion and examination of these studies to qualitative analysis and have not provided aggregated size ranges herein.

This study highlights the importance of MP size, along with polymer composition and shape, in their mobility. Given the lack of data in size distribution, future quantitative studies should carefully examine the size distribution and limitations imposed by sampling and analysis. In using the analogy with natural sediments in terms of MP size, further research is required to investigate the linkage between MP shape, size, and density. Unlike mineral sediments, MPs are versatile in terms of their density and shape. As outlined in this study, marginal density, shape, and size appear in most hydrodynamic parameters, therefore, the definition of size categories for MPs should include consideration for other MP properties.

Chapter 4

Entrainment and Vertical Mixing of Aquatic Microplastics in Turbulent Flow: the Coupled Role of Particle Size and Density

A. Shamskhany & S. Karimpour (2022), Entrainment and Vertical Mixing of Aquatic Microplastics in Turbulent Flow: the Coupled Role of Particle Size and Density, Marine Pollution Bulletin, 184, 114160 [249].

4.1 Abstract

Diversity in microplastics' characteristics, including their size, affects their transport and distribution in aquatic systems. Furthermore, turbulent induced mixing is often considered dominant in the dispersion of sediments and contaminants in marine and freshwater systems, which is also affected by particle size. The aim of this study is to investigate the effect of microplastics' size and polymer density on their mixing behaviour in response to turbulent structures. Using sediment analogy, several parameters are defined to describe entrainment patterns of microplastic particles of common polymers. Our results indicate that the level of mixing of microplastics in turbulent flow can vary several orders of magnitude. While large particles' vertical motion may be dominated by the gravitational settling or rising, the

motion of fine microplastics is highly affected by the ambient turbulent flow. Our findings provide a plausible explanation for the abundance of fine microplastics in remote areas.

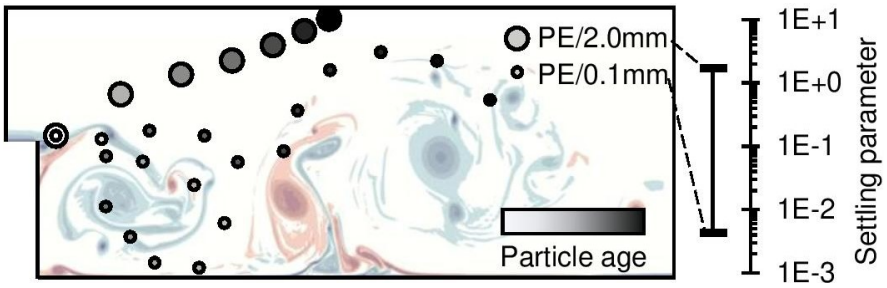

Figure 4.1: Graphical abstract.

4.2 Introduction

Features such as strength, durability, low cost, and versatility have led to plastic proliferation over the last few decades. Along with their benefits, the exponential growth of mismanaged plastic waste has brought catastrophic pressure upon the environment. Plastic debris enters freshwater and marine environments through different pathways such as rivers, wind, wastewater treatment plants, stormwater run-off, waste disposal across coastal areas, and surge waves [10]. Due to slow degradation, plastic debris can remain in the aquatic environment for decades, if not centuries, turning into ever smaller pieces through various weathering processes [12]. Therefore, the presence of Microplastics (MPs), plastic debris sized smaller than 5 mm, grows exponentially over the years. MP pollution in aquatic environments has drawn significant attention due to its adverse impact on aquatic health. Numerous studies have documented the ingestion, assimilation, and accumulation of MPs in aquatic species [250, 251]. MPs are found in various aquatic compartments, from deep-sea sediments [33] to the remote Arctic and Antarctic areas [32, 40].

MPs in aquatic environments are exceptionally diverse in terms of their properties. They possess a wide range of shapes, from spheres to completely irregular shapes, such as fragments and fibres. In addition, MPs are made of various polymers with densities ranging from 0.88 to

2.80 g/cm^3 [200]. Moreover, biofouling, the accumulation and growth of micro-organisms and algae on MP's surface, affects the density of the particle and its sinking behaviour [36, 133]. Aquatic MPs are also reported in different size ranges, varying from 10 μm to 5 mm, in various aquatic compartments [39, 40]. Similar to sediments, particle size affects MPs' transport and fate in the aquatic environment significantly. Evidence on MPs' size distribution corroborates the preferential presence of MPs in different aquatic compartments based on their size [200].

The distribution and fate of MPs in freshwater and marine environments are dominated by characteristics of both the MPs and the ambient flow [35, 46, 200]. Most abundant plastic polymers in aquatic environments, such as polyethylene and polypropylene, have densities lower than the density of water. Therefore, based on the buoyancy alone, the majority of MPs are expected to be present in surface layers of aquatic environments. However, Cózar et al. [34] first observed the absence of millimetre-sized plastic debris from the ocean's surface layer. Other studies have also supported the absence of buoyant MPs from surface layers and discussed their in-depth distribution [44]. The absence of MPs from the surface layer has been attributed to many factors, including biofouling followed by settling [133] and vertical mixing [39]. The latter is mainly induced by turbulent flow, induced by different mechanisms, such as temperature or density gradient, wind, and sudden topography changes, which can potentially affect transport and vertical distribution of MPs [200].

Studies on the hydrodynamics of aquatic MPs have mainly been undertaken since 2010. The impact of vertical mixing and the role of turbulence on the settling/rising behaviours of MPs have been barely studied so far. However, sediment analogy has been widely used to describe the behaviour of MPs, both in quiescent and dynamic ambient fluids [47, 49, 51]. Decades of research in sediment transport have demonstrated the undeniable effect of size on particle's entrainment and sinking [154, 159, 162, 166]. For instance, both silt (0.004 – 0.062 mm) and sand (0.06 – 2 mm) are heavy particles, but their behaviour in turbulent flow can be entirely different [200]. Similarly, MPs' behaviour in turbulent flow can be quite diverse due to their size. Filella [104] was the first to highlight the lack of attention to standardized size classification and its importance, using the sediment analogy. The question arising is

the role of particle size on MPs' entrainment and transport. Similar to other contaminants and natural sediments, distribution, accumulation, and overall fate of MPs are rooted in fluid dynamics. This paper, therefore, aims to investigate the response of MP particles of different sizes and densities to turbulent flow using computational fluid dynamics. For this purpose, we conducted multiple numerical experiments with various particle sizes ranging from 100 μm to 2 mm, and densities associated with abundantly found polymers, from Polyethylene and Polypropylene to Polyester and Polyvinyl Chloride [35]. We exposed these particles to fully developed two-dimensional (2D) turbulent structures of different intensities and observed particle mixing and mobility. Well-established hydrodynamic and sediment transport parameters are employed to quantify the combined effect of size and density on MPs' entrainment and their vertical mixing based on the results of the present study.

4.3 Methodology

A backward-facing step (BFS) geometry is selected in this study to investigate the entrainment behaviour of MPs in a turbulent flow. Flow over a BFS creates self-sustained oscillations and vortex shedding, initiating from the corner of the step. BFS is among the most fundamental benchmark configurations in turbulent flow and has been historically studied for decades [252]. This flow exhibits many features of a mixing layer, from shear layer formation, re-circulation, detachment, and reattachment (see e.g., Driver and Seegmiller [253]). Current simulations are 2D and transverse averaged. Observations made in this paper exclude any additional three-dimensional effects and rather focus on the formation of 2D structures. This approximation eliminates turbulent dissipation in the lateral direction. However, the formation of the vortex shedding originated at the corner of the BFS is a 2D feature of this three-dimensional flow [252]. Furthermore, this study is a pragmatic study and aims to investigate the effect of particle properties on MPs' vertical mixing in an induced turbulent flow. Thus, transverse averaging does not affect the role of MPs' size and density on their in-depth entrainment and transport.

Open Source Field Operation and Manipulation (OpenFOAM-v6) is used to simulate the numerical experiments in the present research. This computational hydraulic package contains several pre-developed solvers for single- and multi-phase flow simulations, with Eulerian and Lagrangian approaches. Here, a modified single-phase flow solver is employed to create a hybrid Eulerian-Lagrangian computational model with a two-stage process. In the first step, the Eulerian sub-model calculates the hydrodynamics of the turbulent structure behind the BFS. Next, MP particles are injected into the fully developed turbulent ambient flow, and their trajectories and distribution are modelled through the particle-tracking Lagrangian sub-model.

4.3.1 Eulerian sub-model

Direct Numerical Simulation (DNS) and Large Eddy Simulation (LES) turbulent flow modelling combined with Lagrangian particle tracking is known as one of the most accurate numerical solutions for particle mixing and transport [254]. Due to the extreme computational cost of DNS [255], here we resorted to LES modelling for the simulation of the induced turbulent flow over the BFS. First, the turbulent ambient flow is simulated using the Eulerian sub-model. For this purpose, conservation of mass and momentum equations are discretized using a finite volume scheme. The continuity and momentum equations for an incompressible flow in the index notation are [256]:

$$\frac{\partial(\rho_f u_i)}{\partial x_i} = 0 \tag{4.1}$$

$$\frac{\partial u_i}{\partial t} + \frac{\partial(u_i u_j)}{\partial x_j} = -\frac{1}{\rho_f}\frac{\partial p}{\partial x_i} + \nu\frac{\partial^2 u_i}{\partial x_j \partial x_j} - \frac{1}{\rho_f}\frac{\partial \tau_{ij}^{SGS}}{\partial x_j} \tag{4.2}$$

where ρ_f is the density of the ambient fluid, and here it is assumed to be 1020 kg/m^3 as a representative for density of seawater, P is the pressure, ν is the kinematic viscosity of the fluid, g is the gravitational acceleration, u_i is the larger than scale instantaneous velocity of the flow, and τ_{ij}^{SGS} represents the subgrid-scale turbulent stresses. In the index notation, i, j

= 1, 2 present x-, y-directions, respectively. The governing equations for LES are derived by applying a convolution filter to the unsteady Navier-Stokes equations. The Smagorinsky subgrid-scale viscosity, which is the pioneer subgrid-scale model, is implemented in this study [257].

$$\tau_{ij}^{SGS} - \frac{1}{3}\tau_{kk}\delta_{ij} = 2\nu_t S_{ij} \tag{4.3}$$

$$\nu_t = C_s \Delta^2 \sqrt{2S_{ij}S_{ij}} \tag{4.4}$$

$$S_{ij} = \frac{1}{2}(\frac{\partial u_i}{\partial x_j} + \frac{\partial u_j}{\partial x_i}) \tag{4.5}$$

where ν_t is the turbulent viscosity, S_{ij} is the strain rate tensor, δ_{ij} is the Kronecker delta tensor, $\Delta = \sqrt{dxdy} = dx$ is the filter size, and C_s is the Smagorinsky constant considered as a default value of $C_s = 0.094$.

4.3.2 Lagrangian sub-model

Lagrangian models are classified into four groups based on the coupling scheme, which dictates the interaction between particles, and particles and the ambient flow [178]. In the current simulation, the solid phase concentration of MPs is dilute and dispersed. Therefore, a one-way coupling scheme is applied to describe the interaction between particles and the ambient flow. In a one-way coupling system, only the ambient flow affects the behaviour and trajectories of particles, and MPs collision and their effect on the surrounding flow are deemed negligible. In this Lagrangian solver, MP's displacement is computed after each Eulerian time step using the following equation:

$$\frac{dx_{i_p}}{dt_p} = u_{i_p} \tag{4.6}$$

where u_{i_p} and x_{i_p} are the velocity and the position of the particle, respectively, and dt_p is the Lagrangian time step. Each particle's instantaneous velocity is based on the active forces equilibrium,

$$m_p \frac{du_{i_p}}{dt_p} = F_D + F_G + F_B \tag{4.7}$$

where, m_p is the particle's mass, and F_D, F_G, and F_B are drag, gravitational, and buoyancy force components, respectively. The Basset history force and the forces due to added mass effects are neglected, as the implementation of these forces makes the simulation more complex and computationally expensive [258]. The active force components are calculated as:

$$F_D = \frac{1}{2}\rho_f C_D A_p |u_i - u_{i_p}|(u_i - u_{i_p}) \tag{4.8}$$

$$F_G = \rho_p g V_p \tag{4.9}$$

$$F_B = \rho_f g V_p \tag{4.10}$$

where A_p is the particle's projected area, ρ_p is the density of the particle, V_p is the volume of the particle, and C_D is the drag coefficient. The drag coefficient affects particles' settling/rising velocity and is a fundamental parameter in MP simulations. However, quantifying MPs' drag force is challenging due to variability in particles' shapes. So far, few studies have investigated settling/rising velocities of irregular-shaped MPs [47, 49]. Since the drag coefficient, and thus the settling/rising behaviour of an idealized sphere is well studied, we focused on spherical MP particles. In the present study, the drag coefficient is calculated using the Putnam [170] method for spherical MP particles.

$$C_D = \begin{cases} \frac{24}{Re_p}(1 + \frac{1}{6}Re_p^{\frac{2}{3}}), & Re_p \leq 1000 \\ 0.424, & Re_p > 1000 \end{cases} \tag{4.11}$$

where Re_p is the particle Reynolds number, and is defined based on the particle diameter, d_p, kinematic viscosity of the ambient fluid, ν, and the relative velocity of the particle with respect to the ambient flow, $u_i - u_{i_p}$, as:

$$Re_p = \frac{d_p |u_i - u_{i_p}|}{\nu} \tag{4.12}$$

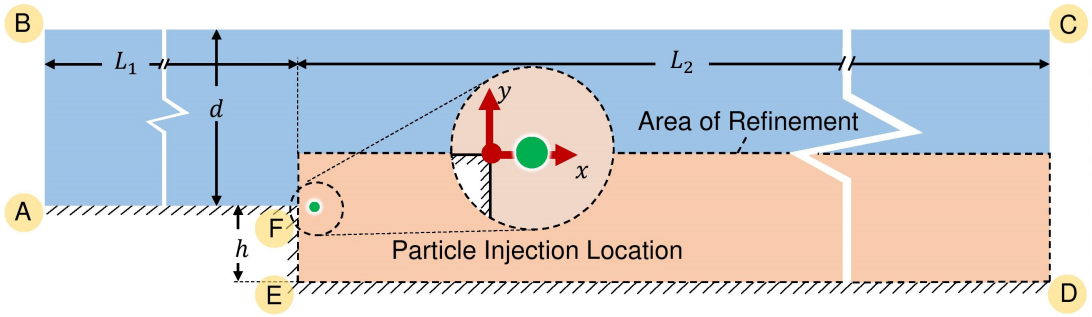

Figure 4.2: Geometry of the BFS; $L_1 = 20.0$, $L_2 = 30.0$, $d = 7.0$, and $h = 3.0$ m with sequential multiple injections of MPs every 10 s at $x = 0.5$ m and, $y = 0.0$ m. The coordinate system is located at the corner of the BFS.

4.3.3 Numerical model set-up

Current simulations are based on the PimpleFoam solver, which employs the PIMPLE algorithm to solve the pressure equation in an unsteady flow. The temporal and spatial discretization schemes are Backward Euler and Gauss Linear, respectively. Here the solver is implicit in time. The computational grid size in the current simulations is always greater than the particle size. Therefore, in each time step, the ambient flow characteristics need to be interpolated at the location of the particle inside a grid. However, there is a significant difference between the particle and the grid size, and relatively large Eulerian time steps create significant gaps in the particle's updated position and velocity. Thus, in order to increase the accuracy of particle tracking, a Courant cap is used to limit the time steps in Eulerian phase calculations. Furthermore, the Courant number is also employed to regulate the Lagrangian time marching in the particle tracking sub-model. Based on the maximum particle Courant number, the Lagrangian time step, dt_P, is defined as the time the particle needs to exit the containing cell, and is a fraction of the Eulerian time step.

The simulation's geometry is demonstrated in Figure 4.2, where d is the inlet water depth, h is the step height, and L_1 and L_2 are lengths of the domain in the x-direction before and after the step, respectively. Boundary conditions used in this study are uniform flow with an inlet velocity of U_o at the upstream inlet boundary (A-B), zero-gradient at the outlet, and

Table 4.1: MP properties and IDs. These cases are studied at three inlet velocities of U_o = 0.025, 0.100, and 0.400 m/s

Density, ρ_p	Particle diameter, d_p (mm)			
(kg/m^3)	0.1	0.2	0.5	2.0
PE:940	PE-S1	PE-S2	PE-S3	PE-S4
PS:1100	PS-S1	PS-S2	PS-S3	PS-S4
PET:1410	PET-S1	PET-S2	PET-S3	PET-S4

free surface boundaries (C-D and B-C, respectively), and no-slip at the lower wall boundary (A-F-E-D). Particle injection into the ambient flow starts at $t = t_q$, when the turbulent flow is fully developed and reaches the quasi-steady state. The location of MP injection is illustrated in Figure 4.2.

Table 4.1 summarizes particle parameters included in numerical simulations. PE with an average density of 940 Kg/m^3 renders a representation for Polyethylene with a density range of 880 to 970 Kg/m^3. Mobility and entrainment of Polypropylene MPs with a density ranging from 900 to 920 kg/m^3 will be similar to the behaviour of PE [200]. PS presents Polystyrene, with a density ranging from 1040 to 1100 kg/m^3. PET presents the average density range for Polyethylene Terephthalate, which has a similar density range to Polyvinyl Chloride. We have opted for these polymers and associated densities due to their reported abundance in the aquatic environment [35]. These densities can also represent the overall density of aquatic MP particles, considering both polymer and biofilm accumulation. Furthermore, among these densities, PE has a lower density compared to the ambient fluid, whereas PS and PET have densities higher than that of the ambient fluid, ρ_f. Four size classes are considered in the present study, in the range of 2 mm to 100 μm. The selected size classes are based on the MPs' size abundance reported by Cózar et al. [34] for the sea surface, and the smaller size range reported by Courtene-Jones et al. [83], Zhang et al. [239], and Cordova and Wahyudi [113] for sediments. Three inlet velocities are considered to reproduce recirculating zone and turbulent perturbations of different intensities [259].

In the computational setup, grid resolution impacts the truncation error and accuracy of the

numerical scheme [260]. Also, in LES modelling, the grid size affects the fraction of resolved turbulent scales [256]. Here we used structured orthogonal square grids in the computational domain. A series of sensitivity and convergence analyses is conducted to establish the optimal grid resolution in terms of computational cost and accuracy. This includes analysis of ambient flow characteristics as well as particles' trajectories to gauge the appropriate grid resolution for the Eulerian-Lagrangian solver. Results included in the paper are based on the optimal grid resolution of $dx = dy = 5.00$ cm in the exterior area, shown in blue in Figure 4.2. However, an area of refinement spans downstream of the BFS in order to further resolve the 2D turbulent coherent structures of smaller than scale perturbations in the LES modelling. In this area (shown in orange in Figure 4.2), the grid size is refined to $dx = dy = 1.25$ cm. Further information and discussion on sensitivity and convergence analysis and criteria are available in Appendix A.

4.4 Results

4.4.1 Hydrodynamics of a two-dimensional backward-facing step

Flow separation over a 2D BFS is illustrated in Figure 4.3. This figure shows the contour plot of instantaneous velocity in the x-direction, u, and vorticity, ζ, in the spanwise direction. As described earlier, 2D flow over a BFS is an established benchmark, in this study generated to gauge the vertical entrainment and transport of MP particles.

In this set-up, turbulent circulations induced by the step corner exhibit detachment and reattachment. As shown in Figure 4.3(b), vortices start to develop behind the BFS at $t = t_q$+150 s, pushing against existing vortical structures, which subsequently detach as shown in Figure 4.3(b) at $t = t_q$+250 s and $t = t_q$+350 s. The coherent detached vortices are then convected in the streamwise direction and move downstream. During this reattachment and detachment period, vortices coalesce and interact. In each simulation, we used the Fourier transform to find the dominant frequency and associated period, T, of the self-sustained

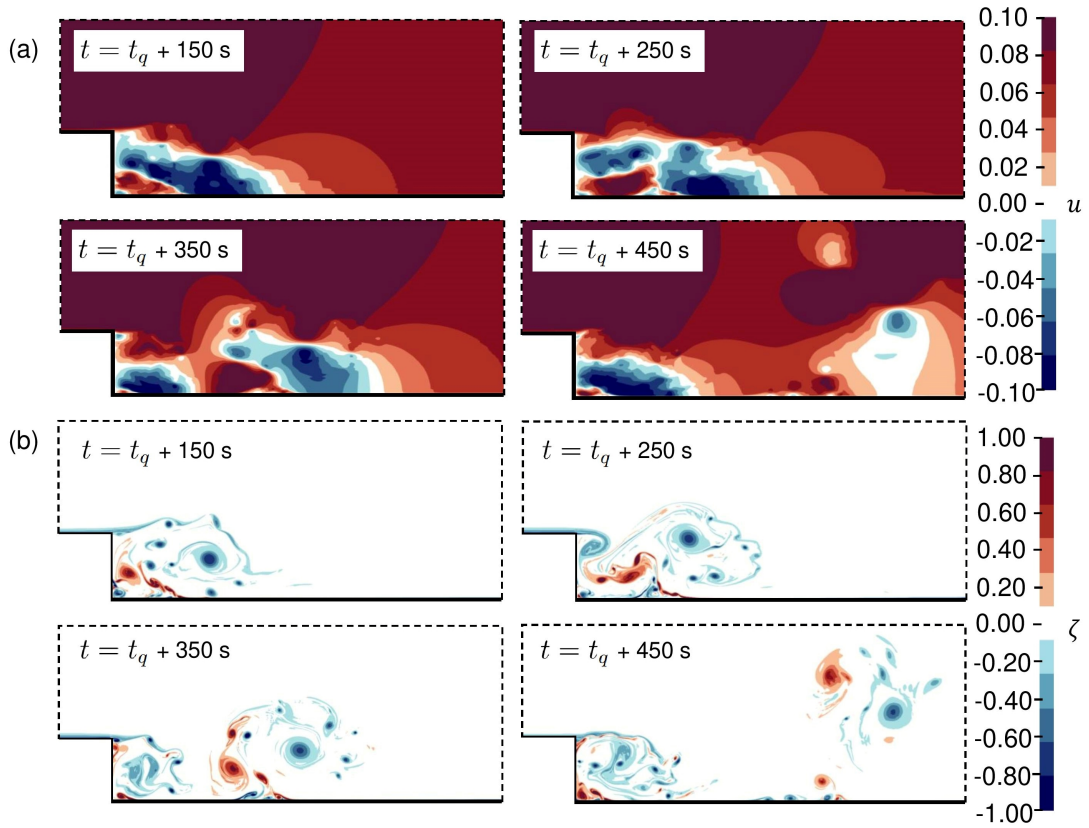

Figure 4.3: An example of the detachment and reattachment of circulations behind the BFS for inlet velocity of $U_o = 0.1$ m/s; (a) is the ambient flow $x-$ velocity component, u, and (b) is the spanwise vorticity in the z-direction, $\zeta = \frac{\partial v}{\partial y} - \frac{\partial u}{\partial x}$.

oscillations behind the BFS. The frequency analysis and comparison with literature are presented in Appendix B. In a turbulent flow, instantaneous velocity can be decomposed into a mean and a fluctuating component:

$$u = \bar{U} + u', \quad v = \bar{V} + v' \tag{4.13}$$

where u and v are the instantaneous velocity components, $\bar{U}$ and $\bar{V}$ are the mean velocity components, and u' and v' are the fluctuating velocity components in x- and y-directions, respectively. To determine the mean and fluctuating components, time-averaging with an interval of $1s$, as a means of ensemble averaging, is conducted over the period of oscillation, once the flow has reached the quasi-steady state at t_q. Turbulent kinetic energy, k, is the

parameter frequently used to quantify turbulent intensity, and in a 2D flow is defined as:

$$k = \frac{1}{2}(\overline{u'^2} + \overline{v'^2}) \tag{4.14}$$

Table 4.2 summarizes the range of maximum mean velocities, $\bar{U}$ and $\bar{V}$ and turbulent kinetic energy, k, for different ambient flow inlet velocities of U_o= 0.025, 0.1, and 0.4 m/s. As shown in Table 4.2, the maximum and minimum velocity range for $\bar{U}$ and $\bar{V}$ grow with the inlet velocity magnitude. In the current BFS turbulent flow simulation, the turbulent fluctuations, presented by $\sqrt{k_{max}}$ in Table 4.2, also grow with the inlet velocity and have the same order of magnitude as the mean velocity components. Figure 4.4 demonstrates contours of the turbulent kinetic energy, k, and mean velocity components, $\bar{U}$ and $\bar{V}$, behind the step. While the coherent turbulent structure behind the BFS has a similar pattern, the turbulent intensity increases with the inlet velocity enhancement.

Table 4.2: The range of mean velocities, $\bar{U}$ and $\bar{V}$, and the maximum turbulent kinetic energy, k_{max}, at different inlet velocities, U_o, in the present simulations

U_o	$\bar{U}_{min}$	$\bar{U}_{max}$	$\bar{V}_{min}$	$\bar{V}_{max}$	$\sqrt{k_{max}}$
			(m/s)		
0.025	-0.013	0.027	-0.008	0.0104	0.016
0.100	-0.048	0.105	-0.038	0.032	0.062
0.400	-0.193	0.428	-0.120	0.158	0.234

To study the exposure of MPs to the temporal variation of turbulent coherent structures, particles are injected with intervals of 10 s, once the flow has reached a quasi-steady state at t_q. Figure 4.5 demonstrates the time-lapse of MP movement up to 40 s after the onset of injection, focusing on the recirculating zone immediately downstream of the BFS. This sequential injection enables us to study the entrainment behaviour over an entire detachment and reattachment cycle. As demonstrated in Figure 4.5, the instantaneous behaviour of the turbulent flow affects particle mixing and transport, i.e., particles with the same properties have different trajectories based on the injection time.

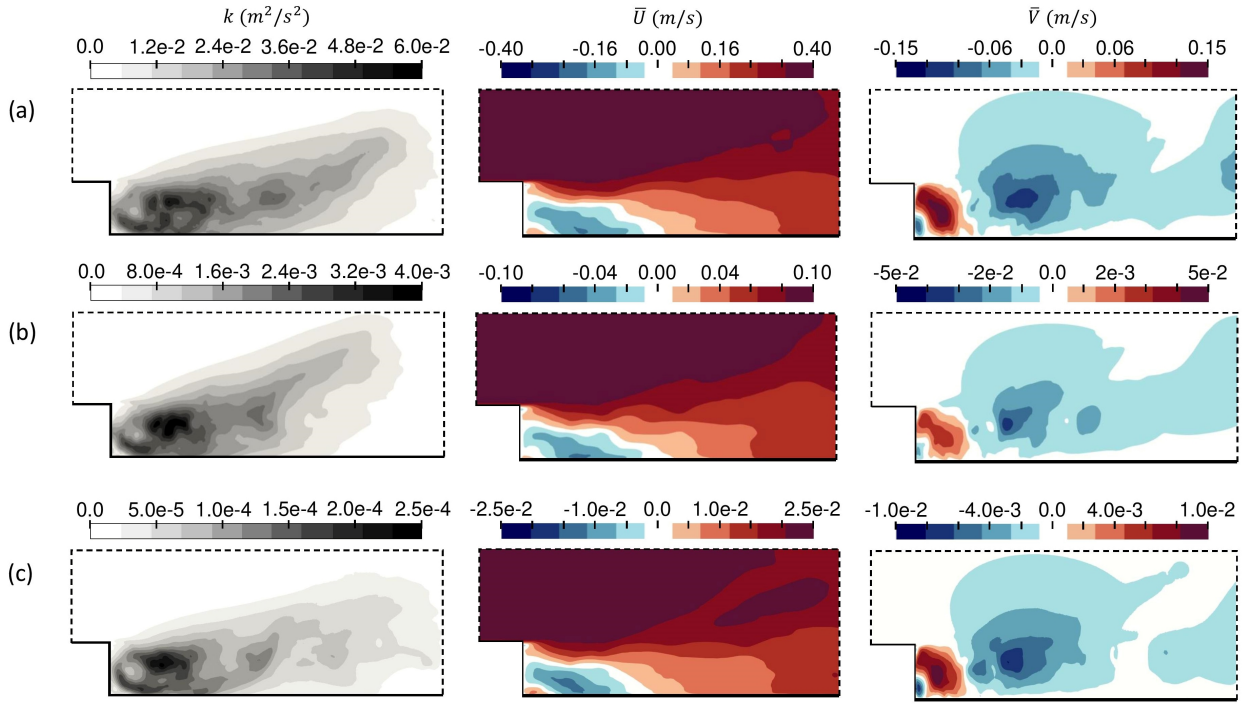

Figure 4.4: Turbulent kinetic energy, k, and mean velocity in x- and y-directions, $\bar{U}$ and $\bar{V}$. (a), (b), and (c) demonstrate results for inlet velocities of $U_o = 0.4$, 0.1, and 0.025 m/s, respectively.

4.4.2 Particle relaxation time and settling parameter

Existing studies on sediment particles have established several parameters to describe their motion in a turbulent flow. The entrainment regime depends on particle characteristics as well as those of the ambient flow. As one key parameter, particle relaxation time, τ_p, is often used to describe a particle's response to the ambient flow [158, 200], which is defined as:

$$\tau_p = \frac{|\rho_p - \rho_f| {d_p}^2}{18\mu} \tag{4.15}$$

Due to the wide spectrum of size and density for MPs, the range of their relaxation time is correspondingly broad. Larger particles or particles with high marginal density from the ambient fluid, $\rho_p - \rho_f$, possess a higher relaxation time, and small-sized particles or particles with low marginal density, have a lower relaxation time. In the Stokes realm for low particle

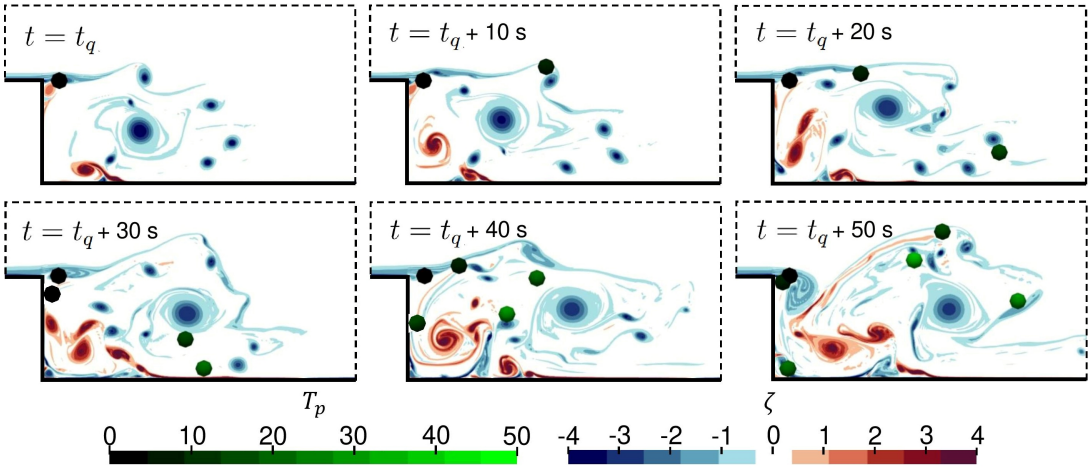

Figure 4.5: MP trajectory of PET-S3 case at inlet velocity of $U_o = 0.4$ m/s. The age of particles after the injection, T_p, and the vorticity in z-direction, ζ, are used to represent particles' and turbulent ambient flow characteristics, respectively.

Reynolds numbers of $Re_p < 1$, the relaxation time is related to the particle's settling velocity. Stokes settling velocity, V_s, in a quiescent fluid is defined as $V_s = g\tau_p$, which can be simply derived from Eq. 4.7. Historically, to assess the entrainment of the particle, the velocity scale of the particle, i.e. its Stokes settling velocity V_s, is compared to the flow vertical velocity scale, σ [154]. This ratio, $S_\nu = V_s/\sigma$, has been described by Good et al. [162], among others, as the settling parameter. As shown in Table 4.2, in the present study, the range of mean vertical velocity, $\bar{V}$, proportionally changes with the magnitude of the incoming velocity, U_o. Similarly, the maximum resolved turbulent kinetic energy, k_{max}, also grows with the magnitude of the incoming velocity. Hence, the incoming velocity, U_o, is adopted as the flow velocity scale, leading to the following definition for the settling parameter in this study:

$$S_\nu = \frac{g\tau_p}{U_o} \tag{4.16}$$

The settling parameter defined by Eq. 4.16 describes the combined effect of the gravitational settling and turbulence on a particle's mobility. However, it does not demonstrate the effect of varying turbulent scales on particle entrainment [162]. Figure 4.6 illustrates the settling

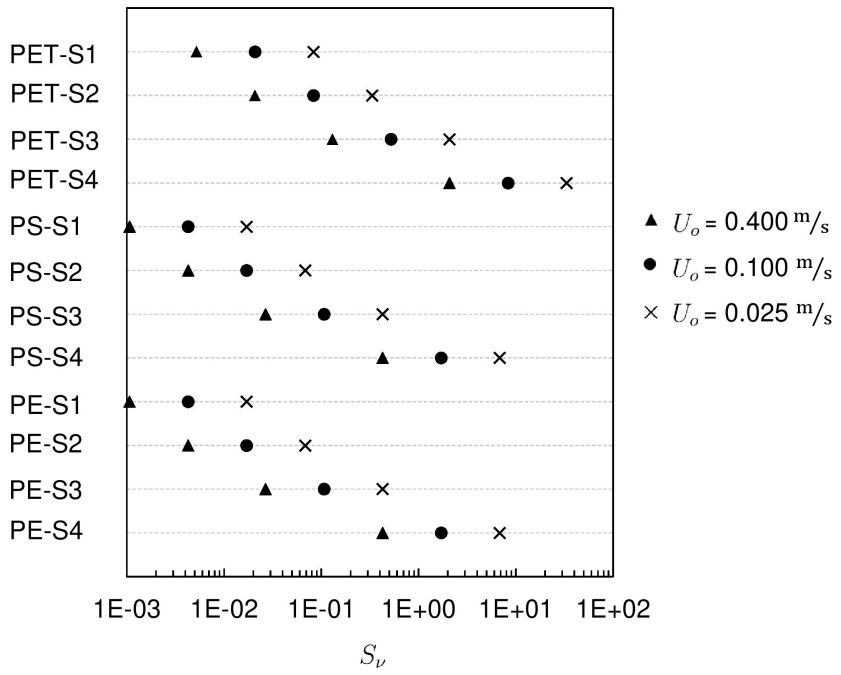

Figure 4.6: The range of settling parameters, S_ν, for different particle properties at inlet velocities of $U_o = 0.025$, 0.1, and 0.4 m/s.

parameters, S_ν, for particle properties (size and density) presented in Table 4.1, exposed to three inlet velocities of $U_o = 0.025$, 0.1, and 0.4 m/s. The marginal density is the same for PE and PS particles, with densities above and below that of ambient water, respectively.

The minimum settling parameter in Figure 4.6 is $S_\nu = 0.0011$, which is obtained for PE-S1 and PS-S1 in the inlet velocity of $U_o = 0.4$ m/s. On the other hand, the maximum settling parameter is $S_\nu = 33.341$, which is associated with PET-S4, for an inlet velocity of $U_o = 0.025$ m/s. The range of settling parameters for these three polymers, with sizes ranging from 2.0 to 0.1 mm, varies more than four orders of magnitude. This has a significant impact on MPs' response to the ambient flow, and thus, the behaviour of MPs with different sizes differs in a turbulent flow, as described in the following sections.

4.4.3 Coupled impact of size and density on entrainment

Figure 4.7 demonstrates size-classified trajectories of selected MPs of different densities, exposed to a range of turbulent intensities. As demonstrated in Figure 4.7(a), for the inlet velocity of $U_o = 0.025$ m/s, S4 MPs with a diameter of $d_p = 2$ mm are not engaged with the ambient turbulent flow. In a flow with such low turbulent intensity, the behaviour of large S4 MPs is dominated by buoyancy and resembles their behaviour in quiescent fluid. At the inlet velocity of $U_o = 0.025$ m/s, the range of S4 particles' settling parameter is from $S_\nu = 6.84$, for PE and PS, to 33.34, for PET. As we progressively refined the particle size, the particles' response at this inlet velocity gradually changed. For S3 particles, $d_p = 0.5$ mm shown in Figure 4.7(b), the movement of particles is mainly dominated by their buoyancy. However, during settling or rising, their pathways are slightly altered by the turbulent ambient flow. This is specifically visible for the PS particle in Figure 4.7(b) at $U_o = 0.025$ m/s, where the particle meanders from its linear settling path. For the finest size classes, S2 and S1 with $d_p = 0.2$ and 0.1 mm, the effect of gravitational settling or rising becomes smaller and particles are entrained with the ambient flow. For the inlet velocity of $U_o = 0.025$ m/s, the settling parameter for S2 and S1 particles ranges from $S_\nu = 0.07$ to 0.33, and $S_\nu = 0.02$ to 0.08, respectively (see Figures 4.7(c) and (d)).

At the inlet velocity of $U_o = 0.1$ m/s, a similar pattern is observed for the particle trajectory, where the particle entrainment is enhanced with the reduction of MP size. This again can be attributed to the reduction of the settling parameter in small particle sizes. However, increasing turbulent intensity, k, also enhances particle entrainment. As shown in Figures 4.7(b) for inlet velocities of $U_o = 0.025$ m/s and 0.1 m/s, S3 particles' mixing with turbulent flow increases with the flow velocity. At the inlet velocity of $U_o = 0.4$ m/s, the turbulent intensity is vigorous, and it overcomes the effect of the particles' buoyancy, even at the largest size of S4. This can be observed in Figure 4.7(a) at $U_o = 0.4$ m/s, where PS and PE particles are entrained in the turbulent flow with a settling parameter of $S_\nu = 0.43$. In the PET-S4 case, the particle is visibly entrained with the flow but ultimately settles to the

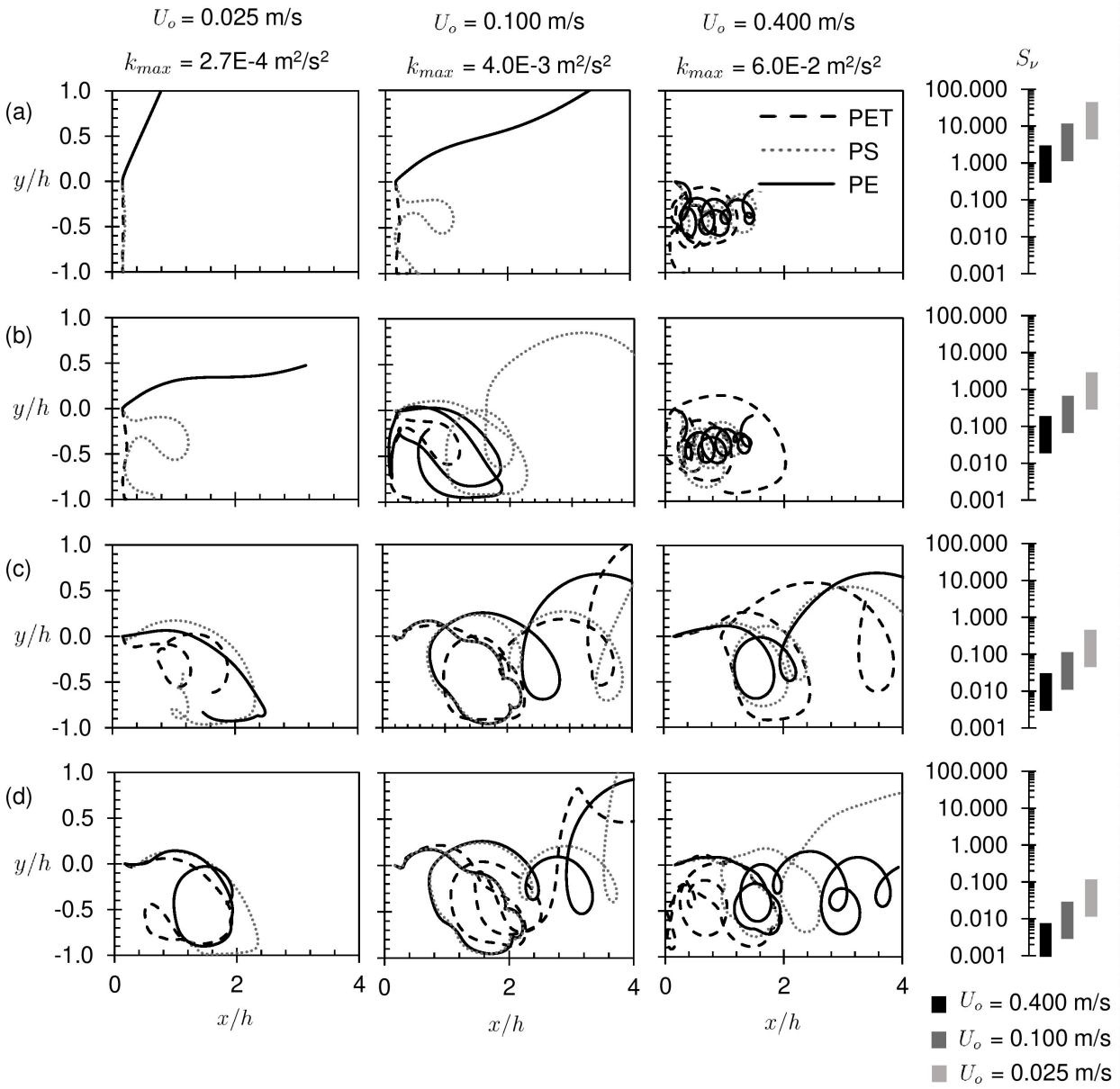

Figure 4.7: Selected particle trajectories for cases demonstrated in Table 4.1. (a), (b), (c), and (d) associate with S4, S3, S2, and S1 MP sizes, respectively. Particle trajectories are demonstrated for a duration of T for the inlet velocities of $U_o = 0.1$ and 0.4 m/s (centre and right columns), and $T/2$ for the inlet velocity of $U_o = 0.025$ m/s (left column). The corresponding range of settling parameters is demonstrated on the right-hand side.

bed. This particle possesses a higher marginal density compared to PE and PS and therefore has a higher settling parameter of $S_\nu = 2.08$. Similar to the other two inlet velocities, the size reduction increases the level of entrainment at the inlet velocity of $U_o = 0.4$ m/s. The superposition of size refinement and turbulent intensity creates the most entrained case, as shown in Figure 4.7(d) for S1 particles at the inlet velocity of $U_o = 0.4$ m/s. In this case, the settling parameter is within the lowest range of $S_\nu = 0.001$ to 0.005, and all three MPs follow a similar pathway, regardless of their densities.

Evidently, the particle's settling parameter, S_ν, can describe the combined effect of MP size and density in turbulent motion. The settling parameter of $S_\nu < 1.0$ corresponds to small particles and/or very vigorous turbulent motion. For the inlet velocity of $U_o = 0.4$ m/s, most particles, regardless of their densities and sizes, possess settling parameters below 1 (except for PET-S4). Similarly, for fine MPs of S1 and S2 sizes, at the inlet velocities of $U_o = 0.025$ m/s and 0.1 m/s, the settling parameter was reportedly smaller than 1. All these particles have shown entrainment with the flow, and over one (or half a) period of oscillation, T, they remain entrained.

On the contrary, $S_\nu > 1.0$ associates with the movement of heavy large MPs and/or weak turbulent flow. This is evidently the case for S4 particles of the largest diameter in weak turbulent flow generated behind the BFS of $U_o = 0.025$ m/s. Finally, when a particle's settling parameter is $S_\nu \approx 1.0$ or is in the order of 1, particles mainly rise or settle due to gravity and buoyancy, while their trajectories may somewhat be affected by turbulent motion. This is observed for PE-S3 and PS-S3 in $U_o = 0.025$ m/s ($S_\nu = 0.43$) and for PE-S4 and PS-S4 in $U_o = 0.1$ m/s ($S_\nu = 1.71$), among other cases.

In the current BFS study, small particles of S2 and S1 with diameters of $d_P = 0.2$ and 0.1 mm, are all entrained in turbulent ambient flow of all intensities from the weakest turbulent flow at $U_o = 0.025$ m/s to the flow of inlet velocity of $U_o = 0.4$ m/s, which exhibited the strongest turbulent intensities. For such small sizes of MPs, buoyancy has a minimal effect, and these particles are mainly dispersed by the turbulent ambient flow. This behaviour is also

in effect for PET with the highest marginal density in this study, as shown in Figures 4.7(c) and (d).

4.4.4 Microplastic's response to instantaneous flow features

To illustrate the response of MPs to the instantaneous features of a turbulent flow, particles are injected at an interval of 10 s to the flow. In Figure 4.8, we have identified the number of particles in each of the twelve PET cases that settled after a full period of oscillation, T. PET particles possess the highest marginal density among polymers selected for this study and exhibit a higher relaxation time compared to PS and PE. Since PET particles have the highest tendency to gravitational settling/rising, they have been selected for this analysis.

As expected, for inlet velocities of $U_o = 0.025$ and 0.1 m/s, the vertical movement of all PET particles with a diameter of $d_p = 2$ mm is dominated by their buoyancy, and they all settle after a period of T. Gradually, with a decrease in size, the percentage of settled particles drops. For MPs with a diameter of $d_p = 0.1$ mm at inlet velocities of $U_o = 0.025$ and 0.1 m/s, the percentage of settled particles reduces to 36.67 and 10%, respectively. Moreover, this ratio also declines with increasing inlet velocity. This demonstrates that, although the response of individual MPs to instantaneous features of the flow may vary, their overall entrainment and vertical diffusion are highly dependent on particle size and turbulent intensity.

4.5 General discussion and conclusion

Deposition and distribution of aquatic Microplastics (MPs) are the culmination of many factors including source vicinity, exposure to weathering, as well as ambient flow hydrodynamics. Turbulent mixing is often considered the dominant component of dispersion in freshwater and marine environments [261], and similar to sediments and other contaminants, it is critical to investigate turbulent induced mixing and transport of MPs. Here, we explored the interaction of MPs with the turbulent ambient flow, while focusing on particle's size combined with density. This is particularly important, as a size-selective distribution of MPs has been

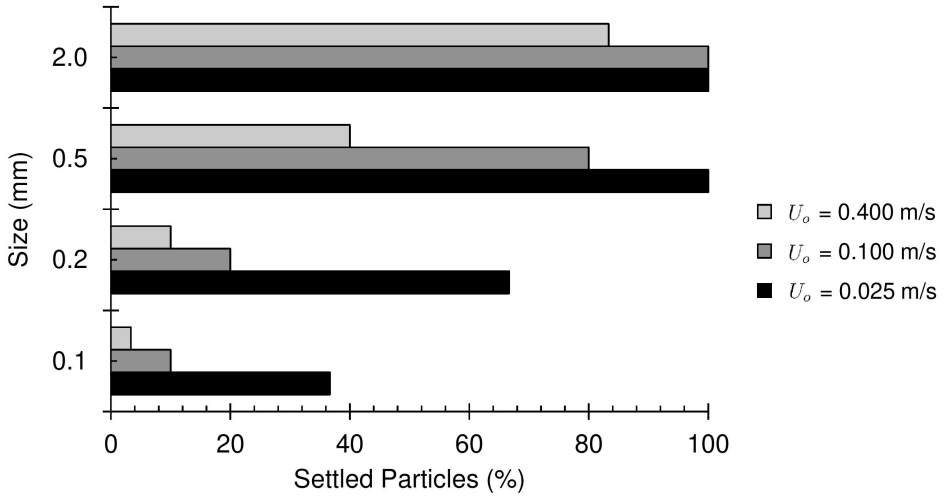

Figure 4.8: Percentage of settled particles in twelve PET cases. This percentage is obtained using the trajectories of thirty particles after a full period of oscillation, T.

repeatedly reported in the literature [200]. For instance, studies observed the absence of MP particles with dimensions of 1 mm and smaller in the ocean surface layers [34], while others reported the abundance of fine MPs in remote deep-sea sediments [40].

Here, MPs' mixing and entrainment in the coherent turbulent structure induced over a backward-facing step is investigated using MPs' analogy with sediment particles. We described MPs' entrainment with the ambient turbulent flow using the settling parameter, as defined in Eq. 4.16. The settling parameter integrates the effects of particle size and density with the ambient turbulent flow intensity. This parameter may vary several orders of magnitude in the same ambient flow based on MPs' characteristics. Our results indicate that large dimensions of MP particles and/or weak turbulent flow correspond to settling parameters above unity, which leads to their gravitational settling/rising. On the other hand, small MPs and/or vigorous flow indicate settling parameters below unity, which results in MPs mixing and entrainment with the ambient turbulent flow.

Furthermore, in the present study, we observed that for fine MPs the impact of density on particle motion is not significant. In other words, for MPs sized 0.1 and 0.2 mm, all particles, regardless of their densities, were mixed with the ambient flow. In such small sizes, MPs'

vertical motion is mainly dominated by turbulent dispersion, and the density has a minimal effect on their dispersal. This is also evident in the definition of the settling parameter (Eq. 4.16), where particle size has an exponent of two, which signifies the role of size in their mixing. Additionally, such small MPs are mobile and transported with the vortical structures far from their source of injection.

MPs' motion and dispersion cannot be solely described by their density and buoyancy. Mixing induced by turbulent flow can lead to entrainment and transport of particles to distances far from their source. Fine MPs are more responsive to turbulent induced mixing, which leads to their transport to remote areas or deep-sea sediments. This research sheds light on the importance of plastic size on their dispersal and vertical motion, which along with biofouling can explain the absence of fine microplastics in marine water surface, as reported in literature. The present study does not incorporate the effect of shape, as there is no generalized formula for drag coefficient for MPs with complex shapes [262]. Therefore, further work is required to investigate the impact of shape on MPs' entrainment and behaviour in turbulent flow.

4.6 Appendix A: Numerical convergence and verification

Herein, we present convergence studies, conducted for numerical simulations to estimate the error associated with the results. PE-S1 case, with the density of $\rho_p = 940$ kg/m^3 and the size of $d_p = 0.1$ mm, at the inlet velocity of 0.1 m/s is selected as the pilot simulation for convergence tests. As shown in the manuscript, these particles are fully entrained with the flow. Both the Eulerian and Lagrangian phases of the pilot simulation are conducted at three grid sizes with a refinement ratio of $r = 2$. Here we used the normalized vertical position, measured from the bottom of the channel, at y/h = -1, to evaluate the error convergence and accuracy of the model. For each of the three simulations, thirty different particles' trajectories are recorded during a full period after each particle's injection, T (see appendix B), with an

Table 4.3: Percentiles, fractional error, and order of convergence after two levels of refinement for $r = 2$.

Percentile (%)	Δx (m)	$(y+h)/h$	P_k	$PR_{\Delta x \to 0}$	FE (%)	N
	2.500	1.286			18.188	120
85	1.250	1.107	3.345	1.088	1.790	240
	0.625	1.090			0.176	480
	2.500	1.384			18.382	120
90	1.250	1.217	2.154	1.169	4.131	240
	0.625	1.180			0.928	480
	2.500	1.510			11.019	120
95	1.250	1.381	2.829	1.360	1.551	240
	0.625	1.363			0.218	480

interval of 1 s after being injected into the ambient flow. Then 85, 90, and 95 percentiles (PR) are calculated for vertical locations in each of the simulations. The order of convergence, P_k, is defined by Karimpour Ghannadi and Chu [260] as:

$$P_k = \frac{1}{\ln r} \ln\left(\frac{PR_k - PR_{k-1}}{PR_{k+1} - PR_k}\right) \tag{4.17}$$

where PR is the percentile rank, $k-1$, k, and $k+1$ are the simulation results obtained from the sequential refinement of the grid as k is the original grid size. The estimated 'exact' value, $PR_{\Delta x \to 0}$, is extrapolated and the fractional computational error, FE, for each of the three simulations is defined accordingly:

$$PR_{\Delta x \to 0} = \frac{r^{P_k} PR_{k+1} - PR_k}{r^{P_k} - 1} \tag{4.18}$$

$$FE_n = \frac{PR_n - PR_{\Delta x \to 0}}{PR_{\Delta x \to 0}} 100 \tag{4.19}$$

where n in Equation 4.19 is the corresponding percentile. Table 4.3 reports the properties as well as the convergence parameters for each of the three cases.

As demonstrated in Figure 4.9, simulation results confirm the convergence of the fractional computational error with the grid refinement. The horizontal axis, N, represents the number

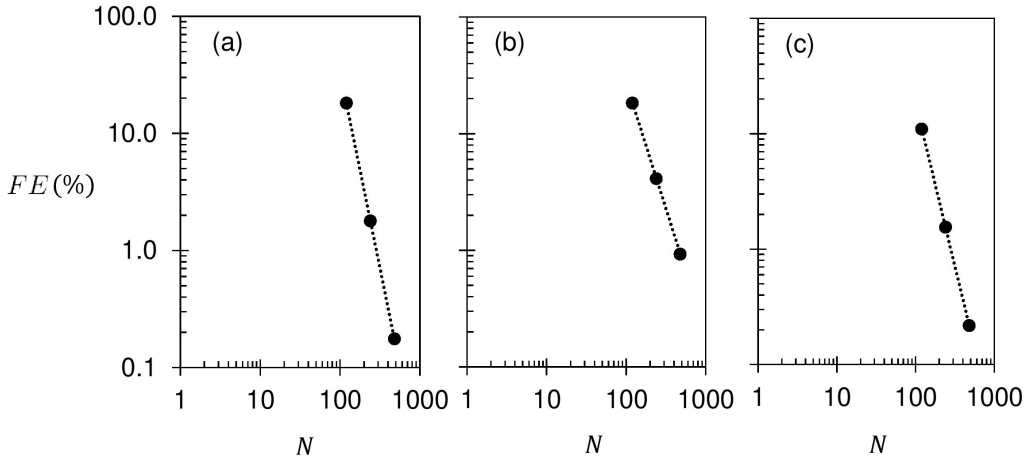

Figure 4.9: Fractional computational error, FE, convergence for three grid sizes; (a), (b), and (c) correspond to 85, 90, and 95 percentiles, respectively.

of grids along the step height, h. The fractional error in all cases reduces with grid size. Results presented in the manuscript are based on $N = 240$. As demonstrated in Table 4.3, the fractional error for this level of refinement remains below 4.1%, which verifies the presented results. Furthermore, in all grid sizes, the entertainment depth, $(y + h)/h$, progressively increases from 85 to 90, and ultimately 95 percentile. For instance, in the finest grid size simulation where $N = 480$, over one period of T, 85% of particles remain at positions lower than $y/h = 0.090$ and 95% of particles are positioned lower than $y/h = 0.363$.

4.7 Appendix B: Frequency analysis of flow behind backward-facing steps

The detachment and reattachment of turbulent flow is an important process and has a large number of applications in areas such as channels with sudden expansions, diffusers, airfoils, and combustors. Among two-dimensional turbulent structures, flow over a Backward-Facing Step (BFS) is an established benchmark to study such intermittent flow behaviours. This flow has features such as shear layer development, formation of recirculating zone, and separation

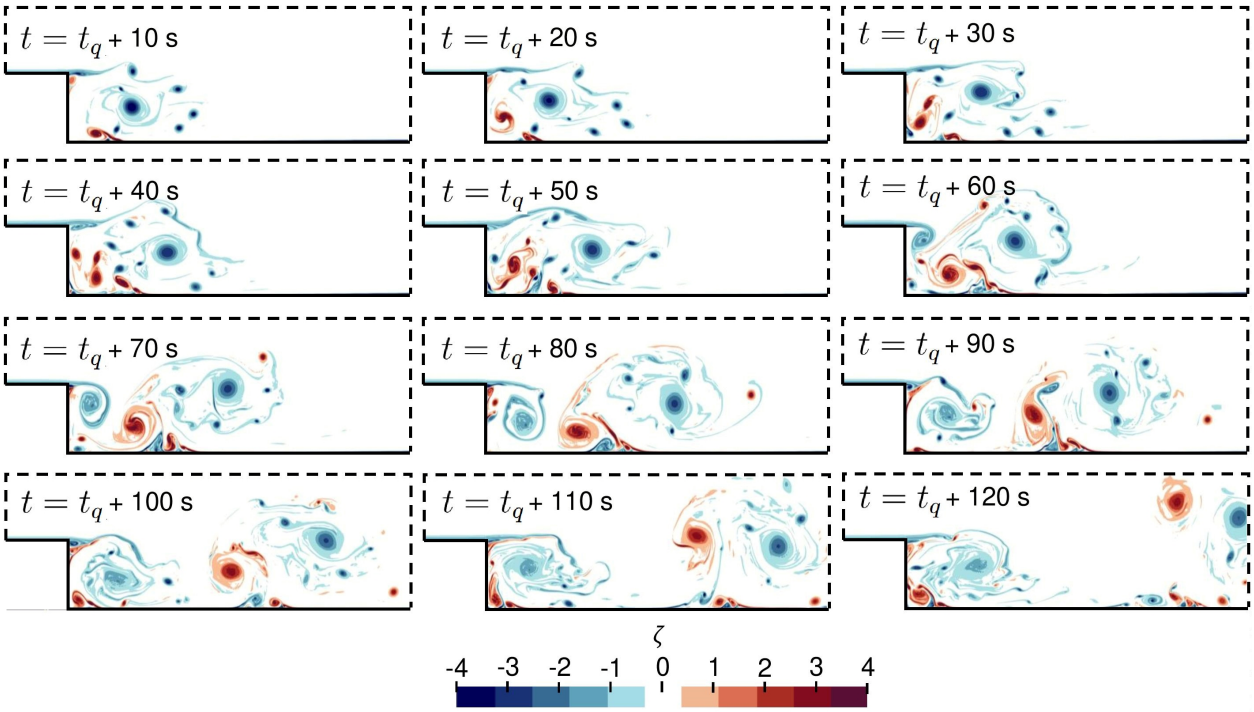

Figure 4.10: Detachment and reattachment of the vortices behind the BFS for the inlet velocity of $U_o = 0.4$ m/s. The spanwise vorticity in the z-direction, $\zeta = \frac{\partial v}{\partial x} - \frac{\partial u}{\partial y}$, is demonstrated for a full period of detachment, that is 120 s.

and reattachment of vortical structures. Figure 4.10 shows the detachment and reattachment process behind the BFS in one of the present simulations. A shear layer is initiated from the corner of the step and expands towards the recirculating zone behind the step. The vortical structures interact with the recirculating zone, gradually detach from the step corner, and subsequently are replaced by a new recirculating zone and shear layer.

Here, an existing experimental study is used to validate the hydrodynamics of turbulent flow over BFS [252]. Strouhal number characterizes the dominant oscillation frequency, and therefore, is used to investigate such intermittent behaviour. The Strouhal number, Str, is defined as:

$$Str = f\frac{h}{U_o} \tag{4.20}$$

where f is the frequency, h is the step height, and U_o is the inlet velocity. To obtain the

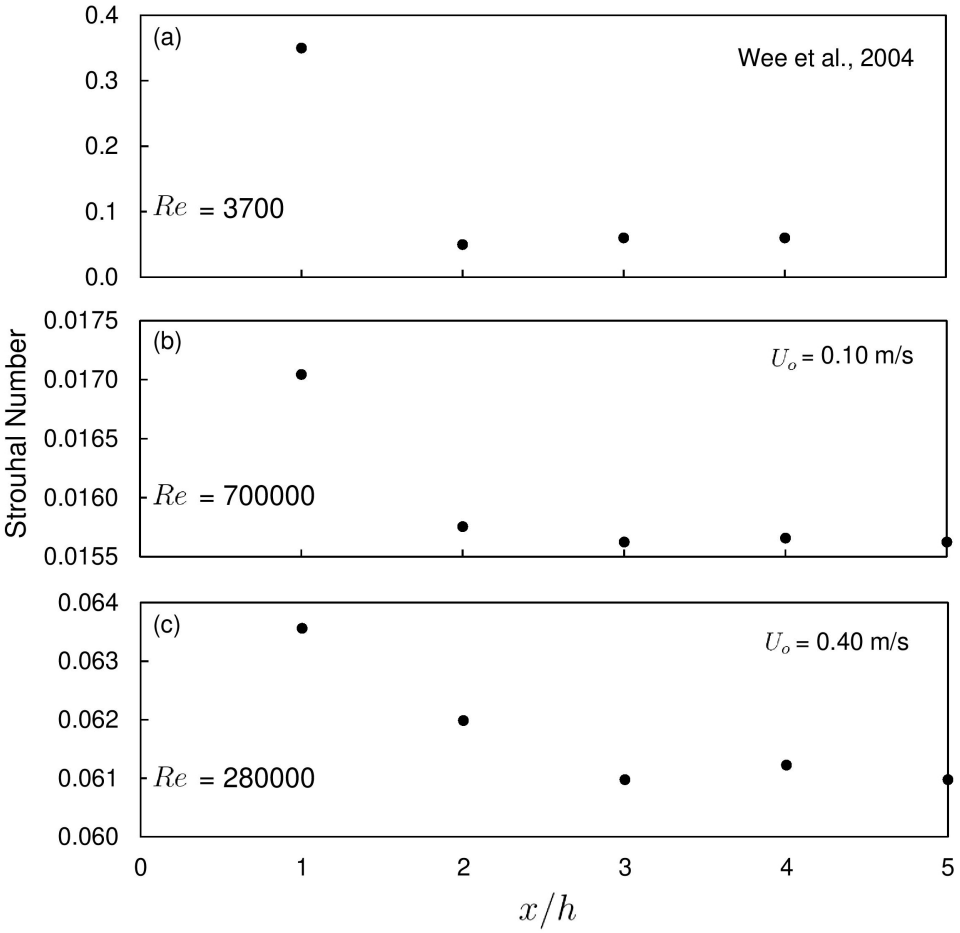

Figure 4.11: The change of Strouhal number with distance from the corner, x/h, for (a) Wee et al. (2004), (b) $U_o = 0.1$ m/s, and (c) $U_o = 0.4$ m/s.

frequency, Fourier analysis is conducted on the x component of the velocity adjacent to the wall. Figure 4.11 shows the change in Strouhal number against distance from the step corner. The top figure demonstrates results by Wee et al. [252] reported for turbulent flow with a low Reynolds number. As shown by Wee et al. [252], the Strouhal number gradually decreases behind the step and reaches an almost constant value at $x/h = 2$. Here Reynolds number, Re, is defined as:

$$Re = \frac{U_o h}{\nu} \tag{4.21}$$

where ν is the kinematic viscosity of the ambient flow. Figures 4.11(b) and (c) demonstrate

the change of Strouhal number for two inlet velocities of $U_o = 0.1$ and 0.4 m/s, respectively. The Re number in this study is significantly higher than the value reported by Wee et al. [252]. However, we have observed a similar trend in the change of Strouhal number behind the step. The Strouhal number reaches an approximately constant value at $x/h = 2$ and 3 for inlet velocities of $U_o = 0.1$ and 0.4 m/s, respectively.

Chapter 5

Microplastics Entrainment in Turbulent Flow: A Numerical Study on the Effect of Shape and Other Physical Particle Properties

A. Shamskhany & S. Karimpour, Microplastics Entrainment in Turbulent Flow: A Numerical Study on the Effect of Shape and Other Physical Particle Properties, Submitted, 2024.

5.1 Abstract

Diversity in microplastics' (MPs) characteristics, including shape, size, and density, significantly affects their transport and distribution in aquatic systems. Turbulence-induced mixing plays a crucial role in shaping the dispersion of sediments and contaminants in marine and freshwater environments. This study investigates how MP shape, density, and size influence their entrainment in turbulent flows using computational fluid dynamics and sediment analogy. Results show that MPs with lower density differences with the ambient flow, smaller sizes, and non-spherical shapes exhibit higher entrainment levels, while larger, denser, and spherical particles align more with gravitational behaviour. MPs with low Stokes numbers, such as fine, non-spherical particles, tend to follow fluid trajectories and become entrained in smaller vortices. In contrast, MPs with higher Stokes numbers deviate from flow paths, avoiding

smaller flow perturbations. These findings provide insight into the varying abundance of MPs, particularly the prevalence of smaller, non-spherical MPs in remote aquatic regions.

5.2 Introduction

Over the last decades, the presence of non-biodegradable plastic waste has surged due to the increasing demand for plastic polymers, valued for their durability, versatility, and low cost [6]. Plastic pollution severely impacts the aquatic ecosystem, with microplastics (MPs) being one of the contributors. MPs, usually defined as pieces of polymer smaller than 5 mm, enter aquatic environments through various sources, including rivers, wastewater treatment discharge, tidal waves, and stormwater runoff. Since the first report of MP abundance in 1972 by Carpenter et al. [13], their presence in aquatic environments has been increasingly reported, in different environmental matrices and corners of the aquatic system, from deep-sea sediments to polar regions [200]. MPs pose a significant threat to aquatic ecosystems, with numerous studies documenting their ingestion by aquatic species and marine birds [16]. Understanding the transport and fate of MPs is an undeniable prerequisite for mitigating their adverse impacts.

The mobility, distribution, and fate of aquatic MPs are dominated by their physical properties and the dynamics of the surrounding flow [200]. The multifaceted nature of MPs creates innumerable combinations of physical characteristics, making their transport and distribution challenging to comprehend. MPs are composed of different polymers with densities ranging from 0.88 to 2.30 g/cm^3, as recorded in various aquatic compartments [35, 200]. Additionally, biofouling—the accumulation of microorganisms and algae on particles—can alter the densities of MPs [133]. MPs also vary widely in size, ranging from 10 µm to 5 mm, with smaller particles being barely visible and larger ones comparable to small gravels [200]. Particle size is crucial in determining the gravitational and drag forces, playing a significant role in the transport of MPs. Previous studies have extensively discussed the effects of particle size and density on the transport and fate of MPs in induced turbulent structures [249]. Furthermore,

MPs exhibit a wide variety of shapes, from spheres and isometric forms for manufactured primary MPs to irregular shapes like fragments and fibres resulting from the degradation of larger particles through various weathering processes [42]. The shape of the particle is known to impact its drag coefficient. Among the different physical characteristics of MPs, understanding the effect of their diverse shapes, especially irregular shapes, on drag coefficient calculation remains a challenging question that has not been clearly answered [47, 48].

In recent years, multiple experimental and numerical studies have investigated the effect of the physical properties of MPs—primarily density, size, and shape—on their vertical transport in quiescent conditions [47, 89, 133]. In such conditions, the vertical movement of a suspended particle is dictated by its physical properties, which is to either rise to the surface for positively buoyant particles or sink to the bottom for negatively buoyant particles. However, in aquatic environments, the transport and distribution of MPs depend on particle properties as well as the dynamics of the carrier flow. Turbulence, a common phenomenon in aquatic environments arising from temperature or velocity gradient or topography changes, can interfere with the natural rising/sinking behaviour of MPs and entrain these particles. Under the effect of turbulence, MPs' vertical movements might differ from their behaviour under quiescent conditions. The absence of the majority of MPs from the surface layers of aquatic environments, despite most being buoyant, as Schwarz et al. [35] reported, is an indicator of the effect of flow dynamics and particle entrainment within the flow [34, 44].

Variations in the properties of aquatic MPs result in complex interactions with the surrounding flow, many aspects of which remain poorly understood. The irregular shapes of MPs, combined with a wide range of sizes and densities, cause them to behave differently in turbulent flows, with their instantaneous settling velocities often deviating significantly from those observed in quiescent conditions [49]. Natural suspended particles, which also exhibit a broad spectrum of physical properties, have been extensively studied over the years. Decades of research on natural particle transport have yielded a deep understanding of particle entrainment and the key factors involved. The effect of non-spherical shapes on the drag coefficient of particles has been widely studied in the context of sediments and other natural particles [88, 263]. Moreover,

the impact of turbulence on the entrainment of natural suspended particles has been explored through various mechanisms, including the effects of nonlinear drag, vortex trapping, and loitering on accelerated/decelerated settling, as well as the preferential transport and mixing of heavy particles of different characteristics [154, 160, 161]. Despite the significant differences between the characteristics of MPs and natural particles, the sediment analogy remains a valuable framework for investigating the effects of MPs' physical properties in combination with turbulent flow on particle entrainment. Multiple recent studies have applied the sediment analogy to describe the behaviour of MPs in both quiescent and dynamic ambient conditions [133, 217, 264].

Here, we conducted several numerical experiments to investigate the effect of particle physical characteristics on turbulent-induced mixing and transport, with a particular focus on particle shape. Our experiments included the densities of commonly encountered polymers as reported in the literature [35]. We tested a broad range of particle sizes and shapes, including both spherical and non-spherical forms. These particles were subjected to a fully developed two-dimensional (2D) turbulent structure to observe their entrainment and transport behaviours. To understand the overall and instantaneous entrainment behaviours of MPs in turbulent flow, we used established hydrodynamic and sediment transport parameters, such as the Particle Reynolds number, relaxation time, settling parameter, Stokes number, and the radius of eddy trapping, to quantify the combined effects of particle properties and flow dynamics. Our results revealed a wide range of Particle Reynolds numbers, spanning both the Stokesian and transient regimes, highlighting the diverse effects of drag on MPs' transport in flow. Based on our findings, particle size and shape can significantly influence the drag force, with smaller sizes and non-spherical shapes associated with higher drag coefficients. The results of this study demonstrate that reducing the particle size, sphericity, and density difference with the ambient fluid can increase the effect of the drag force, potentially surpassing the effect of gravity.

5.3 Methodology

Numerical experiments in this study are conducted using Open Source Field Operation and Manipulation (OpenFOAM-v6), an open-source computational fluid dynamics tool. To induce turbulence and mixing, a Backward Facing Step (BFS) geometry is selected in this study, where the passage of the approaching flow over the edge leads to the formation of a shear layer (spreading from the edge) and a recirculating region which is confined between the shear layer and the lower wall [265]. This geometry is paramount to hydraulics as it applies to numerous natural and artificial geometrical configurations, such as downstream areas of weirs and gates, estuaries, and continental slopes, where sudden change in depth or bathymetry is expected. In this study, we employed a single-phase Eulerian approach to compute the flow configuration over the BFS and a Lagrangian model to simulate MP particle movement in a fully developed turbulent flow. Here we employed Newton's second law for Lagrangian particle tracking, without the prior assumption that the particle's terminal velocity is valid under turbulent conditions. This assumption has been shown not to be valid in several studies on the movement of other particulates under turbulent conditions [154, 161].

5.3.1 Eulerian and Lagrangian Solvers

Herein, the turbulent model utilized is the Large Eddy Simulation (LES), where the governing equations are derived from the filtered Navier-Stokes equations:

$$\frac{\partial u_i}{\partial x_i} = 0 \tag{5.1}$$

$$\frac{\partial u_i}{\partial t} + \frac{\partial (u_i u_j)}{\partial x_j} = -\frac{1}{\rho_f}\frac{\partial p}{\partial x_i} + \nu \frac{\partial^2 u_i}{\partial x_j \partial x_j} + \frac{1}{\rho_f}\frac{\partial \tau_{ij}^R}{\partial x_j} \tag{5.2}$$

where, ρ_f represents the density of the ambient flow, which is assumed as 1020 kg/m^3 (density of seawater) and ν represents the kinematic viscosity of the fluid [266]. u and p denote the

LES resolved velocity and pressure, respectively, where the index notation is used to specify Cartesian coordinates. Additionally, τ_{ij}^R accounts for residual LES stresses. To model the subgrid scale motions, k-equation is employed [267].

$$\tau_{ij}^R = -2\nu_t S_{ij} + \frac{1}{3}\tau_{kk}^R \delta_{ij} \tag{5.3}$$

$$S_{ij} = \frac{1}{2}\left(\frac{\partial u_i}{\partial x_j} + \frac{\partial u_j}{\partial x_i}\right) \tag{5.4}$$

$$\nu_t = C_k \Delta^2 \sqrt{k_R} \tag{5.5}$$

$$\frac{\partial(\rho_f k_R)}{\partial t} + \frac{\partial(\rho_f u_i k_R)}{\partial x_i} = \frac{\partial}{\partial x_i}[(\mu + \mu_t)\frac{\partial k_R}{\partial x_i}] - \rho_f \tau_{ij}^R S_{ij} - C_e \frac{\rho_f k_R^{3/2}}{\Delta} \tag{5.6}$$

where k_R represents the residual turbulent kinetic energy, δ_{ij} is the Kronecker delta tensor, ν_t and μ_t are the kinematic and dynamic eddy viscosity of the subgrid scale motions, respectively, μ represents the dynamic viscosity of the fluid, $\Delta = \sqrt{(dxdy)}$ is the filter size, and C_e and C_k are constant coefficients equal to 1.05 and 0.094, respectively.

The interaction between particles and turbulent flow can be categorized into three groups—one-way, two-way, and four-way coupling—based on the volume concentration of particles in the flow [178]. The reported concentration of MPs, defined as the ratio of MPs' volume to the sampled flow volume, never exceeds 10^{-6} in various marine compartments [34]. This concentration falls within the recommended range for dilute suspensions, as proposed by Elghobashi [178], where particles are not expected to influence the turbulent structure or interact with each other. Therefore, a one-way coupling scheme is adopted to elucidate the interaction between particles and the ambient flow. In this system, only the ambient flow influences the behaviour and trajectories of particles, and any collision among MPs, along with their impact on the surrounding flow, is considered negligible. The instantaneous

velocity of the particle is calculated based on Newton's second law:

$$m_p \frac{Du_p}{Dt} = F_D + F_{VM} + F_G + F_B \tag{5.7}$$

where m_p is the particle's mass and u_p is the particle's instantaneous velocity in vertical direction. Here, drag, F_D, virtual mass, F_{VM}, gravity, F_G, and buoyancy , F_B, are considered as active forces on MP particles and are defined as:

$$F_D = \frac{1}{2}\rho_f C_D A_{prj} |u - u_p|(u - u_p) \tag{5.8}$$

$$F_{VM} = -C_m \rho_f V_p (\frac{du_p}{dt} - \frac{du}{dt}) \tag{5.9}$$

$$F_G + F_B = gV_p(-\rho_p + \rho_f) \tag{5.10}$$

A_{prj} is the projected area of the equivalent sphere with an identical volume, u_i is the ambient flow instantaneous velocity in the vertical direction, ρ_p is the density of the particle, C_D is the drag coefficient, C_m is the virtual mass coefficient derived based on the particle's shape [268], and V_p is the volume of the particle. To capture the response of particles to instantaneous turbulent flow features, multiple particles are injected sequentially into the flow at two-second intervals. As discussed in the results section, this time interval is selected due to the period of intermittent separation and replacement of eddies from the corner of the step in the current BFS set-up.

5.3.2 Drag coefficient of the spherical and non-spherical particles

The Drag Coefficient, C_D, versus particle Reynolds, Re_p, relationship presented by Putnam [170] for spherical particles:

$$C_D = \begin{cases} \frac{24}{Re_p}(1 + \frac{1}{6}Re_p^{\frac{2}{3}}), & Re_p \leq 1000 \\ 0.424, & Re_p > 1000 \end{cases} \tag{5.11}$$

$$Re_p = \frac{d_p|u - u_p|}{\nu} \tag{5.12}$$

where d_p is the particle diameter. The Haider and Levenspiel [175] (1988) method is implemented, where drag coefficient, C_D, in addition to Re_P, is also a function of geometric properties of the particle based on the ratio of the area of an equivalent sphere with the same volume to the particle's surface area, ϕ.

$$C_D = \frac{24}{Re_p}(1 + ARe_p^B) + (CRe_p)/(D + Re_p) \tag{5.13}$$

$$A = \exp(2.3288 - 6.4581\phi + 2.4486\phi^2) \tag{5.14}$$

$$B = 0.0964 + 0.5565\phi \tag{5.15}$$

$$C = \exp(4.9050 - 13.8944\phi + 18.4222\phi^2 - 10.2599\phi^3) \tag{5.16}$$

$$D = \exp(1.4681 + 12.2584\phi - 20.7322\phi^2 + 15.8855\phi^3) \tag{5.17}$$

In Equations 5.14 to 5.17, ϕ is particle sphericity, defined as $\phi = S_{sph}/S$, which S is the surface area of the particle, and S_{sph} is the surface area of the equivalent sphere with the same volume.

5.3.3 Numerical set-up and modelling

The temporal discretization method is the second order backward scheme and implicit. This method is conditionally stable and therefore, we use a Courant stability condition for temporal discretization. Spatial discretization of the advection flux in the momentum equation, Eq. 5.2,

and the subgrid-scale turbulent kinetic energy flux in the k-equation, Eq. 5.6, is performed using a limited linear divergence scheme, a second order accurate method, which leans towards upwind in regions with a rapidly changing gradient. Other non-advective terms are discretized using Gauss integration with linear interpolation.

Figure 5.1 illustrates the current BFS set-up, where the domain has an inlet water depth of d, a step height of h, and lengths L_1 and L_2 before and after the step, respectively. A uniform flow boundary condition is applied at the upstream inlet boundary (A-B) with an inlet velocity of U_o, while the outlet and free surface boundaries (C-D and B-C, respectively) have zero-gradient and symmetry conditions. The lower wall boundary (A-F-E-D) has a no-slip condition. A structured, orthogonal, square mesh is employed, where the size of the base mesh is $dx = dy = 5$ cm and in the refinement zone, grid size is reduced to $dx = dy = 1.25$ cm. These grid sizes were chosen to reliably capture the energy-containing scales of turbulence in the LES model. Based on an analysis of the LES model's quality, it was determined that the ratio of resolved to total turbulent kinetic energy exceeds 80%, in accordance with the guidelines suggested by Pope [255]. Further details can be found in the supplementary file.

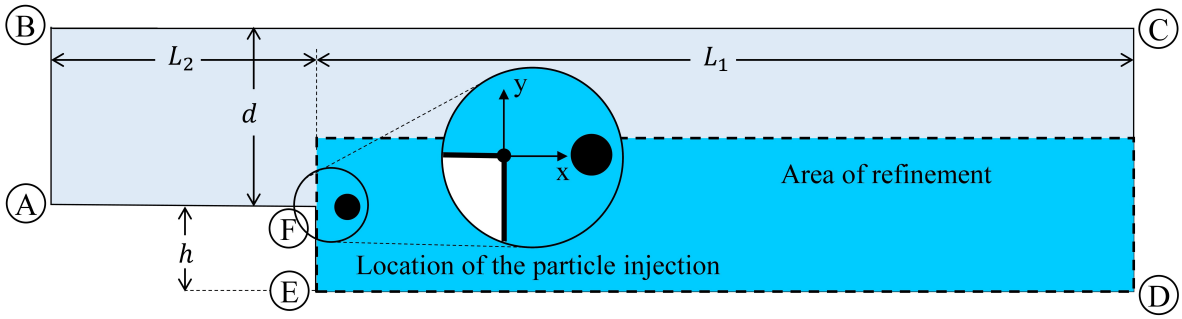

Figure 5.1: Geometry of the BFS; $L_1 = 20$, $L_2 = 30$, $d = 7$, and $h = 3$ m; Coordinates of the injection point = (0.5 m, 0.0 m). The coordinate system is located at the corner of the BFS.

The injection of MPs starts once the turbulent flow attains a fully developed quasi-steady state. As illustrated in Figure 5.1, this injection point remains consistent across all simulations and is situated at a sufficient distance from the boundaries and the step edge. Particles are periodically released in the domain with zero initial momentum and velocity. The injection site is selected within a region where there is a greater probability of the injected MP being

entrained by the vortices emanating from the corner of the step. This injection site creates an opportunity for MP particles to get exposed to a varying range of turbulent scales.

5.3.4 Particle properties

Two categories of density are selected based on the abundance of the related polymer reported in both sediments and water in aquatic environment, both negatively buoyant. Polystyrene (PS), with densities ranging from 1040 to 1100 kg/m^3, is a polymer commonly identified in bed sediments in the form of fibres and filaments [200]. Another polymer considered here is Polyethylene Terephthalate (PET), with a reported density range of 1370 to 1455 kg/m^3, similar to the range of density for Polyvinyl Chloride. Additionally, four size classes, ranging from a spherical equivalent diameter of 2 mm to 100 µm are considered. These size ranges were selected based on the prevalence of MPs in various aquatic compartments, spanning from surface waters to bed sediments [34, 200].

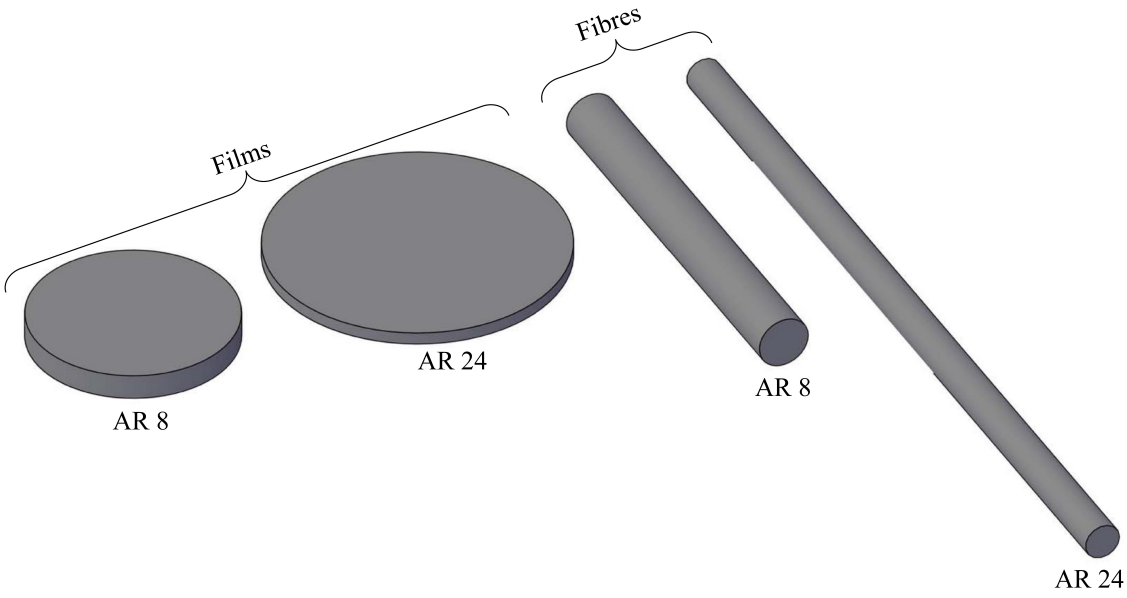

Figure 5.2: Cylindrical shapes in the present study for non-spherical cases presented in Table 5.1 ; (a) and (b) represent elongated and flattened cylinders resembling MP fibres and films, respectively, with two different aspect ratios of 8 and 24.

The study of shape effects presents challenges, particularly because there are uncertainties

Table 5.1: MP particles properties and IDs. All cases are studied at the inlet velocity of $U_o = 0.4$ m/s. For non-spherical cases, E1/F1 and E2/F2 are associated with the aspect ratios of $AR = 8$ and 24, respectively.

	PS:1100 (kg/m^3)	PET:1410 (kg/m^3)		
Size (mm)	Sphere	Sphere	Fibre (E)	Film (F)
0.1	S1-B	S1-B	S1-E1/E2	S1-F1/F2
0.2	S2-B	S2-B		
0.5	S3-B	S3-B	S3-E1/E2	S3-F1/F2
2.0	S4-B	S4-B		

reported for the drag coefficient for spherical and irregularly shaped MPs. Kowalski et al. [89] documented a notable inconsistency between the observed sinking speed of irregularly shaped MPs and the theoretical projections proposed by Dietrich (1982), which rely on the assumption of a perfect sphere with an equivalent diameter. This incongruity has prompted ongoing investigations into determining the terminal velocity, V_T, and drag coefficient, C_D, for non-spherical MPs [47]. Herein, to leverage the existing relationship developed for drag by Haider and Levenspiel [175], fibres and films are described as elongated or flattened cylindrical shapes, respectively. As illustrated in Figure 5.2, four cylindrical shapes are selected, in addition to spherical particles, to represent non-spherical MPs. Elongated cylinders resemble fibres, while flattened ones resemble films. The two non-spherical shapes are categorized into two different Aspect Ratios (AR), defined as the ratio between the longest and shortest dimensions. Aspect ratios are selected to resemble the characteristics of the MP fibres most commonly reported in the aquatic environment [96]. This decision facilitates a more thorough investigation into the impact of the particle surface area-to-volume ratio on drag.

Table 5.1 compiles the simulation IDs, considering the particle density, size, and shape. Each row corresponds to a specific size, ensuring that all cases within the same row share equal volumes (V) and equivalent diameters (d_{eq}), but different shapes and ARs. Cylindrical shapes are employed for specific PET sizes, which include both entrained and deposited particles (discussed further in section 5.4.4). These combinations facilitate an investigation into the combined impact of size and shape on particle entrainment within the ambient flow.

Table 5.2: Characteristics of the non-spherical shapes with $AR = 8$, in SI units, a, b, and c are the longest, the intermediate, and shortest axes.

PET	S1-E1	S3-E1	S4-E1	S1-F1	S3-F1	S4-F1
d_{eq} (mm)	0.10	0.50	2.00	0.10	0.50	2.00
a (mm)	0.35	1.75	6.99	0.17	0.87	3.49
b (mm)	0.04	0.22	0.87	0.17	0.87	3.49
c (mm)	0.04	0.22	0.87	0.02	0.11	0.44
$V * 10^2$ (mm^3)	0.05	6.54	418.88	0.05	6.54	418.88
S (mm^2)	0.05	1.27	20.38	0.06	1.50	23.97
S/V (mm^{-1})	97.30	19.46	4.87	114.47	22.89	5.72
S_{sph} (mm^2)	0.03	0.79	12.57	0.03	0.79	12.57
ϕ	0.62	0.62	0.62	0.52	0.52	0.52

Table 5.3: Characteristics of the non-spherical shapes with $AR = 24$, in SI units, a, b, and c are the longest, the intermediate, and shortest axes.

PET	S1-E2	S3-E2	S1-F2	S3-F2
d_{eq} (mm)	0.10	0.50	0.10	0.50
a (mm)	0.73	3.63	0.25	1.26
b (mm)	0.03	0.15	0.25	1.26
c (mm)	0.03	0.15	0.01	0.05
$V * 10^2$ (mm^3)	0.05	6.54	0.05	6.54
S (mm^2)	0.07	1.76	0.11	2.70
S/V (mm^{-1})	134.83	26.97	206.36	41.27
S_{sph} (mm^2)	0.03	0.79	0.03	0.79
ϕ	0.45	0.45	0.29	0.29

Tables 5.2 and 5.3 present a detailed overview of characteristics of non-spherical particles for aspect ratios of $AR = 8$ and 24, respectively.

5.4 Results and discussion

5.4.1 Hydrodynamics of the backward facing step

The flow over the BFS exhibits intermittent behaviour, characterized by turbulent eddies generated from the corner of the step, detaching after a period, and advecting downstream, while new eddies are generated at the corner. Here we applied the Fourier transform

analysis previously established in our publications to determine the dominant frequency and associated period, $T = 120$ s, of the self-sustained intermittent oscillations behind the BFS [249]. Figure 5.3 depicts the normalized mean velocity profiles and Reynolds stress components of the BFS prototype used in this study. All parameters presented in Figure 5.3 are averaged over three periods of intermittency, T. This ensemble averaging is conducted after a fully developed flow and when the quasi-steady state was reached.

Figures 5.3 (a) and (b) illustrate the normalized resolved mean streamwise, $\overline{U}$, and depthwise, $\overline{V}$, velocity profiles across the BFS, respectively, enabling assessment of the flow impact on MP transport in these directions. Additionally, Figures 5.3 (c), (d), and (e) show the normalized streamwise, $\overline{u'^2}$, depthwise, $\overline{v'^2}$, and shear Reynolds, $-\overline{u'v'}$, stresses behind the step, providing insights into the overall intensity of turbulence affecting particle transport. These Reynolds stress components only represent the resolved components.

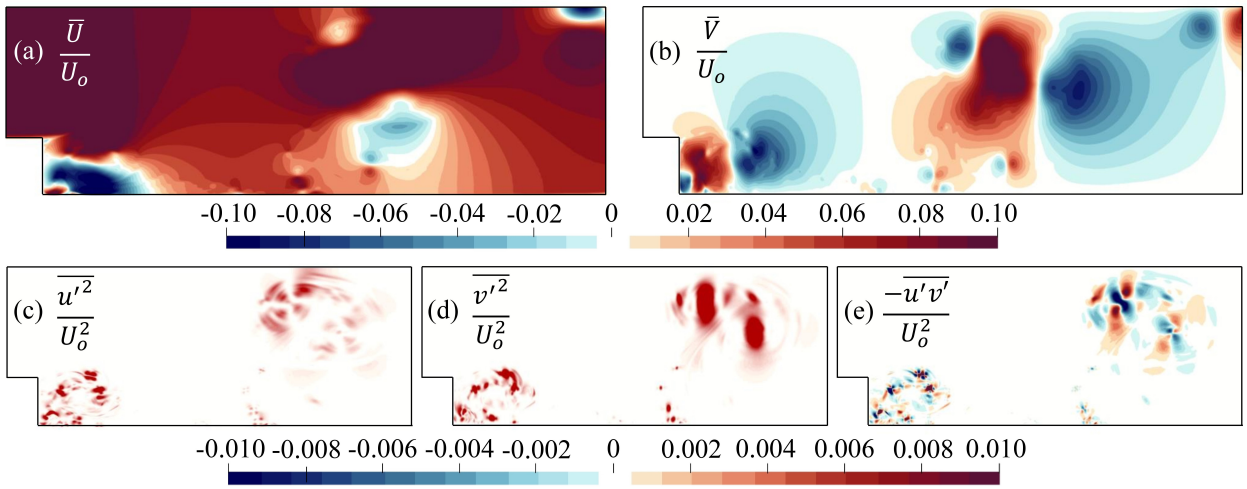

Figure 5.3: (a) Normalized streamwise mean velocity profile, (b) normalized depthwise mean velocity profile, (c) normalized streamwise Reynolds stress, (d) normalized depthwise Reynolds stress, (e) normalized shear Reynolds stress.

The instantaneous dynamic of the flow significantly affects the trajectories and fate of suspended particles. To maintain consistency in ambient flow turbulent structures, the same onset of injection and injection interval are applied across all cases. Results in the upcoming sections present instantaneous and averaged response of particles of different

physical characteristics to this ambient flow.

5.4.2 A glance at the regimes of MPs motion

This study includes a broad spectrum of particle Reynolds numbers, Re_p (See Eq. 5.12), from Stokesian regimes, $Re_p < 1$, to transitional regimes where $1 < Re_p < 1000$. Figure 5.4 (a) and (b) depict the range of drag coefficient, C_D, plotted against the particle Reynolds numbers, Re_p, for spherical and non-spherical particles, respectively. Discrete points indicate the terminal particle Reynolds numbers, calculated based on Putnam [170] for spherical particles and Haider and Levenspiel [175] for non-spherical particles. These points are aligned with the reference curves provided by Putnam [170] and Flemmer and Banks [171].

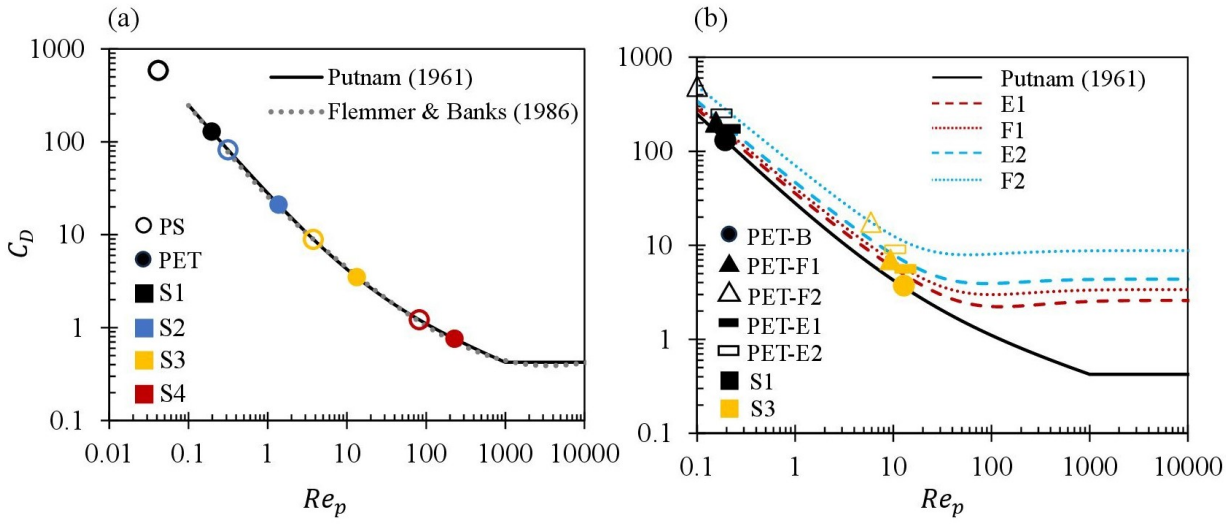

Figure 5.4: Drag coefficient as a function of particle Reynolds number; comparison of present case studies calculated based on the equations of Putnam (1961) for spherical shape (a), and Haider and Levenspiel (1988) for non-spherical ones (b), with Flemmer and Banks (1986) correlations.

The size of the particles has a direct impact on the particle Reynolds number, Re_p , as indicated by Eq. 5.12. Figure 5.4 (a) demonstrates that, as the particle size increases from the smallest size in this study, $d_p = 100$ μm, to the largest size, $d_p = 2.0$ mm, the particle Reynolds number changes from Stokesian to transitional regime, leading to reduction in drag

coefficient. Additionally, the shape of the particle plays a fundamental role on particles' regime and drag coefficient. As shown in Figure 5.4 (b), for MPs with the same equivalent diameter, increasing the surface area-to-volume ratio leads to a decrease in the particle Reynolds number and an increase in the drag coefficient. This can be achieved by altering the shape from sphere to film and fibre or by increasing the aspect ratio from $AR = 8$ to $AR = 24$ for non-spherical shapes. As an example, the terminal particle Reynolds numbers for PET-S1-F2 and PET-S1-B are $Re_p = 0.10$ and 0.20, with associated drag coefficients of $C_D = 493.20$ and 130.46, respectively. Therefore, for the same equivalent diameter, d_{eq}, transitioning from a sphere to the most flattened film results in an almost fourfold increase in the drag coefficient, while the terminal particle Reynolds number is halved. Notably, the PET-S1-E2 case, i.e., the smallest d_{eq} and most elongated fibre, and the PET-S1-F2 case, i.e., the smallest d_{eq} and most flattened film, are associated with the highest drag coefficient amongst all case studies.

5.4.3 MP particles entrainment with the ambient flow

Settling parameter, defined as the ratio of the particle velocity-scale to the flow velocity-scale, functions as a key metric in sediments and heavy particles' transport and entrainment with turbulent flow [154, 161]. Settling parameter is defined based on the particle relaxation time as indicated in Eq. 5.18 [161]:

$$S_\nu = \frac{\tau_p g}{\sigma_f} \tag{5.18}$$

where g is the gravitational acceleration, σ_f is the velocity-scale of the ambient flow, τ_p is the particle relaxation time, and μ is the dynamic viscosity of the ambient flow. The derivation of particle relaxation time relies on the particle's terminal velocity under Stokesian conditions, that is $V_T = (|\rho_p - \rho_f| d_p^2 g)/(18\mu)$. However, our study includes a wide range of particle Reynolds numbers, spanning from Stokesian to transitional regimes (see Figure 5.4). Furthermore, the definition of the particle relaxation time only accounts for the equivalent diameter of the particles, and thus, neglects the particle shape as a factor contributing to the

response of MP particles. To address these limitations, and in accordance with the original derivation, here we re-defined particle relaxation time, τ_p, as:

$$\tau_p = \frac{V_T}{g} \tag{5.19}$$

where V_T is the particle terminal velocity across all particle regimes, from laminar to turbulent. The updated definition of the relaxation time also integrates the effect of particle shape for non-spherical particles. Consequently, the definition of the settling parameter will be updated as Eq. 5.20. Here, we consider the flow velocity scale to be the inlet velocity, U_o.

$$S_\nu = \frac{\tau_p g}{\sigma_f} = \frac{V_T}{U_o} \tag{5.20}$$

The settling parameter governs the interplay between particle entrainment with the ambient flow and adherence to their terminal sinking behaviour. When the settling parameter is low and the particle terminal velocity is considerably smaller than the ambient flow velocity, depthwise particle trajectory becomes heavily affected by the ambient flow. Conversely, when the settling parameter is relatively high, particles are predominantly influenced by terminal sinking, experiencing minimal entrainment with the turbulent flow. However, as stated in Eq. 5.20, in this study settling parameter does not incorporate the instantaneous features of the ambient flow.

Stokes number, defined as the ratio of the particle time-scale, τ_p, to the flow time-scale, τ_l, is another commonly used parameter in sediment transport [154, 161]. In this study we have leveraged this parameter to capture the time-dependant response of the particles to the instantaneous flow features. The flow time-scale in this parameter is defined using the ratio of the step height to the instantaneous depthwise velocity of the flow at the location of particle, h/v_f:

$$St = \frac{\tau_p}{\tau_l} = \frac{V_T v_f}{gh} \tag{5.21}$$

The Stokes number serves as an indicator of the particle's instantaneous ability to adjust to fluctuations in the surrounding turbulent flow, as it represents the ratio of particle and flow time-scales. In other words, lower Stokes values indicate a higher potential for the MP particle to adapt to the velocity changes of the ambient flow, while MPs associated with higher Stokes number may not have sufficient time to adjust to the oscillations in the ambient flow.

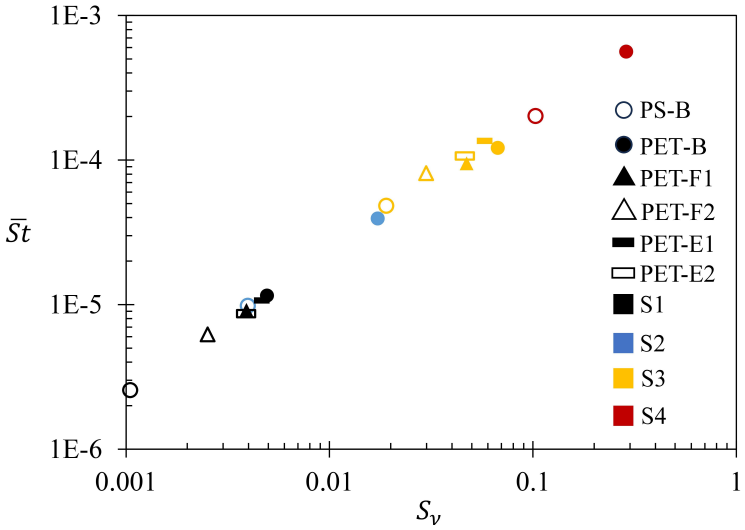

Figure 5.5: The average Stokes number, $\overline{St} = (1/n)\sum_1^n St$, versus settling parameter for case studies outlined in Table 5.1.

Figure 5.5 illustrates the averaged Stokes number, $\overline{St}$, over a period, T, plotted against the associated settling parameter for cases presented in Table 5.1. The PS-S1-B and PET-S1-F2 cases exhibit the minimum settling parameter and Stokes numbers, as shown in Figure 5.5. These two cases also demonstrate the lowest Reynolds numbers and the highest drag coefficients, as depicted in Figure 5.4 (a) and (b). Therefore, when the particle equivalent diameter, d_{eq}, and/or sphericity, ϕ, decrease, the settling parameter and the Stokes number decrease. This indicates that these particles can adjust to changes in the ambient flow immediately. Moreover, the PS-S1-B exhibits a lower Stokes number and settling parameter compared to the corresponding PET particle. Therefore, reducing the marginal density between the particle and the fluid leads to increased drag coefficient and higher levels of

particle entrainment. A more comprehensive discussion on the impact of the particle's marginal density on entrainment and mixing with the ambient flow has been presented in a previous publication [249].

On the other hand, the PS-S4-B and PET-S4-B cases are associated with the maximum settling parameter and Stokes numbers, as depicted in Figure 5.5. Thus, when the particle size or sphericity increases, particles are more influenced by their terminal sinking, and consequently, they skip smaller-scale features of the turbulent flow as discussed in section 5.4.6.

5.4.4 The instantaneous effect of drag on entrained MPs

To further develop the discussion surrounding the instantaneous effect of drag on particle entrainment, the instantaneous Reynolds numbers of selected particles for each case are plotted in Figure 5.6. For a more effective comparison across different cases, all selected particles in Figure 5.6 are injected into the flow simultaneously, and their instantaneous velocity and trajectory are recorded over a period of T.

The top row in Figures 5.6 (a) and (b) represent the size-dependent comparison of instantaneous particle Reynolds numbers of PS and PET beads, respectively. For smaller particles of sizes of S1 and S2, the instantaneous particle Reynolds number remains within the Stokesian regime, $Re_p < 1$. Therefore, these small particles are associated with a higher range of drag coefficients. However, as particle size increases to sizes of S3 and S4, particles' movement become more aligned with their terminal sinking behaviour. For PS-S4-B and PET-S4-B cases, this trend continues until they are fully deposited on the bed, as demonstrated in Figure 5.6 (a) and (b).

Figures 5.6 (c) and (d) in the top row depict the shape-dependent comparison of the instantaneous particle Reynolds number for cases presented in Table 5.1. Similar to the PET-S1-B, the instantaneous particle Reynolds number of the PET-S1 fibre (E1 and E2) and film (F1 and F2) particles also falls within the laminar Stokesian regime, $Re_p < 1$. However, it is evident from Figures 5.6 (c) and (d) that among the PET-S3 cases of different shapes, the

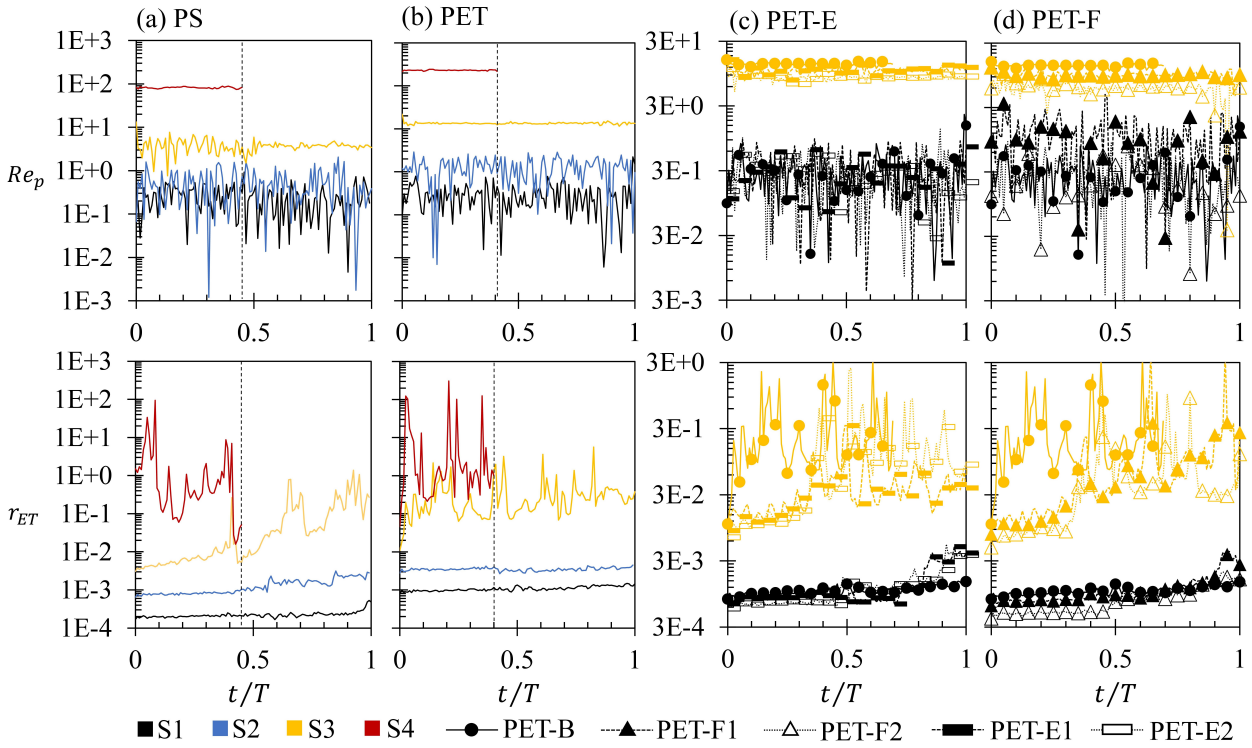

Figure 5.6: Instantaneous behaviour of selected MPs particles. Columns (a) and (b) correspond to PS and PET beads, respectively. Columns (c) and (d) compare spherical and non-spherical particles of equivalent sizes, illustrating fibre and film particles, respectively. The top and bottom rows represent the instantaneous particle Reynolds number, Re_p, and the radius of eddy trapping, r_{ET}, within a period of T. The vertical dashed lines in columns (a) and (b) demonstrate the full deposition of particles.

PET-S3-E2 and PET-S3-F2 demonstrate lower instantaneous Reynolds numbers and a higher effect of drag. Therefore, for a constant equivalent diameter, as the sphericity decreases from $\phi = 1$ (a perfect sphere) to $\phi = 0.29$ (films with an aspect ratio of 24), the range of the instantaneous particle Reynolds numbers also decreases. Nevertheless, as observed in the top row of Figure 5.6, the ranges of instantaneous particle Reynolds numbers are very similar for PET-S1 particles of different shapes, making it challenging to build a distinct discussion around the effect of shape at smaller sizes of S1 and S2.

Vortex trapping is the process by which vortices in the turbulent flow entrain and carry

particles. The eddy trapping process can be measured by a radius defined by [160]:

$$r_{ET} = \frac{V_T}{\Omega_z} \tag{5.22}$$

In this definition, it is assumed that a particle's depthwise velocity is the summation of its terminal velocity, V_T, and the depthwise velocity of the flow at the particle's instantaneous location [160]. When the radius of eddy trapping is small, particles closely follow the trajectory of adjacent fluid parcels, whereas, when the radius of eddy trapping is large, particles deviate from the movement of the adjacent fluid parcels, and potentially escape the nearby vortices.

Figure 5.6 bottom row demonstrates the radius of eddy trapping, r_{ET}, for the same selected particles. The bottom row of columns (a) and (b) in Figure 5.6 compares different sizes of PS and PET beads, respectively. As the size of the particle increases, the radius of eddy trapping also increases and therefore, larger particles are deviating more from the fluid parcel trajectories. This was also supported by higher Stokes numbers and settling parameters for these particles. The bottom row of Figures 5.6 (c) and (d) compares the radius of eddy trapping for PET-S1 and PET-S3 cases listed in Table 5.1, focusing on the effect of shape. As evident from these panels, the radius of eddy trapping decreases as the sphericity decreases. Building on the earlier discussion regarding the influence of particle size on the radius of eddy trapping, it is notable that the PET-S1-E2 and PET-S1-F2 cases are associated with the lowest values of radius of eddy trapping among all cases considered in this study.

5.4.5 Comparison of instantaneous and terminal settling velocities of MPs

Figure 5.7 illustrates the instantaneous settling velocity of 100 particles, each recorded over a period of T, versus their associated settling parameters across different case studies. The top row of Figure 5.7 displays the ratio of average settling velocity to terminal velocity, $\overline{V_{sm}}/V_T$. The left column compares different sizes of PS and PET beads, while the right

column compares PET-S1 and S3 cases of different shapes. In quiescent ambient conditions, the instantaneous settling velocity of a particle equals its terminal velocity, resulting in $\overline{V_{sm}}/V_T \approx 1$. As demonstrated in the top row of Figure 5.7, when the settling parameter increases with size and sphericity, the ratio of average settling velocity to terminal velocity approaches unity. Therefore, particles with higher settling parameters are minimally affected by the turbulent ambient flow, and their instantaneous settling velocity closely matches their terminal velocity.

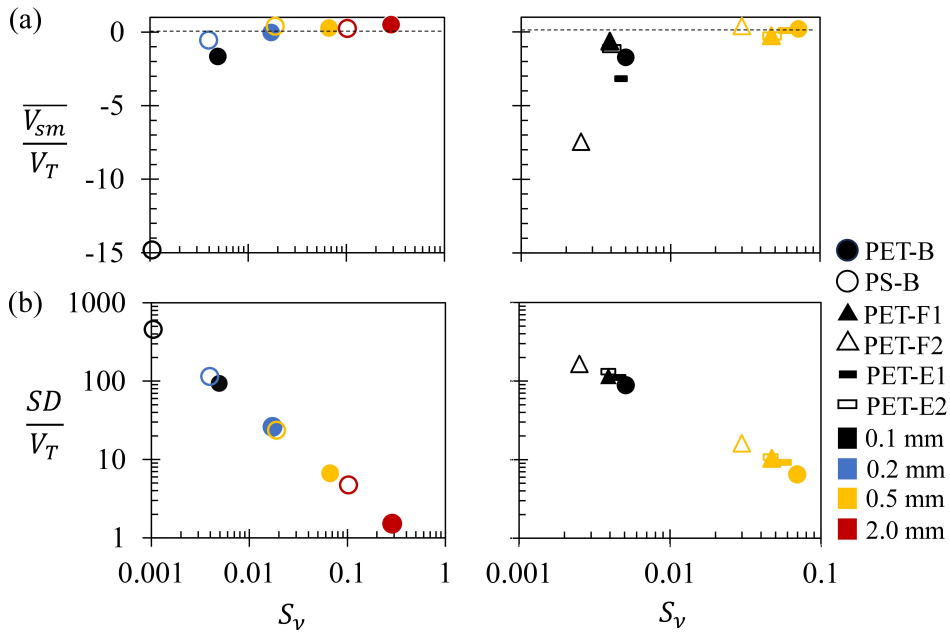

Figure 5.7: Relative settling velocity of MPs. (a) The ratio of average settling velocity to the terminal velocity. (b) The ratio of the settling velocity standard deviation to the terminal velocity. The first and second columns from the left represent spherical and non-spherical particles, respectively. The dashed-lines in the top row demonstrate $\overline{V_{sm}}/V_T = 0$.

On the other hand, physical characteristics that correspond to lower settling parameters cause greater deviations in the instantaneous settling velocity of particles from their terminal velocity. For the smallest particle size of 0.1 mm, $\overline{V_{sm}}$ is nearly 15 times the particle's terminal velocity, indicating a significant impact of the coherent structures on in-depth movement of these particles. Similarly, for PET-F2 particles (films with $AR = 24$), this value is 7 times that of the terminal velocity. This illustrates the importance of in-depth turbulent motion

for particles of small size and low sphericity. Additionally, for spherical particles (left column of Figure 5.7) with low settling parameters of $S_\nu < 0.02$, this ratio, $\overline{V_{sm}}/V_T$, is negative, indicating that the particle's in-depth motion on average is upwards. For non-spherical particles (right column of Figure 5.7), those with $0.03 < S_\nu < 0.05$, are positioned in the vicinity of the $\overline{V_{sm}}/V_T = 0$ line, while for smaller settling parameters, this ratio becomes negative. To further illustrate this dependency, the standard deviation, defined in Eq. 5.23, is used:

$$SD = \sqrt{\frac{\sum_{i=1}^{n}(v_{sm} - \overline{v_{sm}})^2}{n}} \tag{5.23}$$

where V_{sm} is the instantaneous settling velocity, $\overline{V_{sm}}$ is the ensemble averaged settling velocity, and n is the total number of instantaneous data recordings, $n = 12000$, in each case.

The bottom row of Figure 5.7 illustrates the ratio of the settling velocity standard deviation, SD, to the terminal velocity, V_T, plotted against the settling parameter, S_ν. This parameter exhibits an inverse relationship with the settling parameter, S_ν, where relative standard deviation decreases with an increase in the settling parameter. This indicates that characteristics that result in smaller settling parameters—such as reduction in size, lower marginal density, and lower sphericity—would experience a wide range of in-depth particle velocities. In contrast, those particles with higher settling parameters exhibit a lower normalized standard deviation, indicating the dominance of terminal velocity on their in-depth motion.

5.4.6 Entrainment of particles across different turbulent flow scales

Figure 5.8 shows the normalized velocity of the ambient flow at the instantaneous location of selected particles from the cases presented in Table 5.1, each over a period of T. Rows (a) and (b) in Figure 5.8 demonstrate the size-dependent comparison of flow velocity fluctuations adjacent to a selected bead particle in the PS-B and PET-B cases of different sizes, respectively. It can be observed from Figures 5.8 (a) and (b) that the frequency of perturbations for smaller sizes, S1 and S2, as shown in the left column of each row, is higher compared to

Table 5.4: Integral length scale of turbulent eddies, l, across the shear layer evolved from the corner at $y = h = 3$ m

x/h	0.5	1	2	4
l (m)	1.05	1.11	1.65	2.10

that of the larger sizes, S3 and S4, which are shown in the right column. The fluctuations in the normalized local flow velocity, evident in Figure 5.8, indicates particle entrainment with varying scales of the flow, where the smaller periods associate with smaller temporal and spatial scale of the flow while larger periods in Figure 5.8 present larger scale flow features. To illustrate the varying scale of the turbulent flow in the current 2D BFS set-up, Table 5.4 presents the integral length scale of turbulent eddies across the shear layer. In the current 2D simulation set-up, an inverse energy cascade is expected with the growing scale of eddies, moving from the corner in the downstream direction. This trend is clearly evident in results presented in Table 5.4.

In Figures 5.8 (a) and (b), one clear observation is the entrainment of S1 and S2 in smaller scale motion for $t/T < 0.4$ and then engagement with both small scale and larger scale motions after $t/T > 0.4$. This is consistent with the scale of motion reported in Table 5.4. Additionally, the general pattern and the scales of perturbation are similar for PS and PET smaller cases, S1 and S2. However, as the particle size increases to S3, the effect of density becomes more prominent. In row (a) right column, the PS-S3-B is entrained by some smaller-scale perturbations at the beginning of the period, while the equivalent PET case in row (b) right column skips these small scales, as we no longer see the smaller fluctuations in the velocity. For the largest size, S4, both PS and PET beads escape the smaller scale motions at the beginning of the period and end up being fully deposited on the bed before mid-period.

Rows (c) and (d) in Figure 5.8 compare the flow velocity fluctuations adjacent to the trajectories of selected spherical and non-spherical PET particles of sizes S1 (left column) and S3 (right column). Row (c) refers to fibres, while row (d) refers to films. For the smallest S1

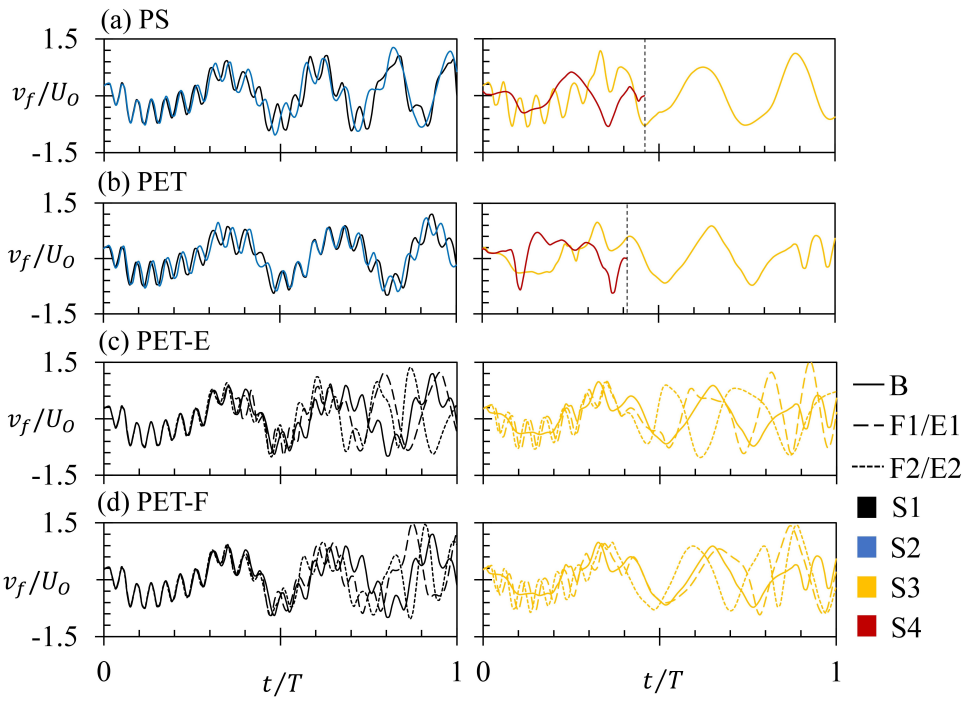

Figure 5.8: Ambient flow velocity at the location of particles. Rows (a) and (b) correspond to spherical PS and PET particles, respectively. Rows (c) and (d) compare spherical and non-spherical particles of equivalent sizes, illustrating fibres and films, respectively. The vertical dashed lines in panels (a) and (b) demonstrate the full deposition of particles.

cases, all spherical and non-spherical particle trajectories coincide before the mid-period when particles are entrained with smaller eddies close to the source of injection, near the corner of the BFS. On the other hand, in the right columns of rows (c) and (d), the PET-S3-B particle escapes the smaller-scale motion at the beginning of the period, while all non-spherical cases of equivalent size get entrained in the smaller-scale eddies close to the corner.

The difference between the trajectories of spherical and non-spherical MPs of equivalent sizes can be explained by the associated radius of trapping, r_{ET} in each case. For fibres and films with low sphericity, the radius of eddy trapping decreases, leading to particle engagement with all flow scales, whereas beads with $\phi = 1$, comparatively, have higher r_{ET}, illustrating selective entrainment. Therefore, the PET-S1-E2 and PET-S1-F2 cases, with the lowest sphericity values in rows (c) and (d), respectively, are entrained with small to large scales. Similarly, the radius of trapping, r_{ET}, is smaller for small sized particles, S1 and S2, and

therefore, these compared to S3 and S4 are engaged more actively with varying scale of the flow in the domain.

5.5 Conclusion

Over the past decade, microplastic (MP) pollution has surged drastically, causing severe impacts on aquatic ecosystems. The transport and fate of MPs are influenced by their physical properties—density, size, and shape—as well as the dynamics of the ambient flow. These factors complicate predictions of MPs' behaviour in water systems compared to natural particles like sediments. While previous studies have examined the effects of particle size and density on MP transport in turbulent flows, the role of particle shape has been less explored.

This research delved into the effect of particle shape—in conjunction with density and size—on the transport and fate of MPs in turbulent flow using computational fluid dynamics. We conducted several numerical experiments to study the mixing and entrainment of MPs with varying physical properties in a two-dimensional coherent turbulent structure induced over a backward-facing step. Our study spanned a wide range of particle Reynolds numbers, from Stokesian to transient regimes. We redefined the particle relaxation time, initially based on Stokesian terminal velocity, to be applicable to transient regimes and included the effect of particle shape in this updated definition. We described the MPs' entrainment using parameters such as the settling parameter, Stokes number, and radius of eddy trapping, which integrate particle characteristics with flow dynamics. Consequently, these parameters can vary by several orders of magnitude within a consistent ambient flow structure, depending on the MPs' characteristics.

Our results indicate that characteristics leading to relatively lower settling parameters and Stokes numbers—such as reducing the density difference between the particles and the flow, decreasing particle size, or lowering particle sphericity—result in higher levels of MP entrainment with the ambient flow. In contrast, larger and heavier particles and those with spherical shapes exhibit higher settling parameters and Stokes numbers and tend toward their

natural sinking behaviour. Additionally, the radius of eddy trapping, which measures how particles deviate from adjacent fluid parcels, showed that smaller, non-spherical particles follow nearby fluid trajectories more closely and become entrained in smaller vortices. Conversely, larger spherical MPs that are entrained with the flow have a larger radius of eddy trapping, causing them to deviate more from fluid parcels and settle more readily.

The transport and distribution of MPs are dominated based on both their diverse physical properties and the dynamics of the ambient flow. Turbulence-induced mixing can lead to the entrainment and transport of MPs over significant distances from their source. MPs of smaller sizes and non-spherical shapes exhibit higher drag coefficients and greater entrainment, which leads to their transport to remote areas or deep-sea sediments [200]. However, the effect of shape becomes less pronounced for very fine MPs. Specifically, for MPs with sizes equal to or smaller than 100 µm, the distinct impacts of shape and density on their entrainment and mixing behaviour become difficult to distinguish.

5.6 Appendix: The resolution of the LES model

To assess the effectiveness and quality of a Large Eddy Simulation (LES) model, it is essential that the majority of turbulent kinetic energy is resolved explicitly, with only a minimal amount modelled according to residual stresses. Pope [255] introduced a widely accepted criterion for evaluating the quality of LES models, suggesting that the resolved turbulent kinetic energy, k_{res}, should represent at least 80% of the total turbulent kinetic energy. This benchmark helps ensure that the LES model provides a sufficiently accurate resolution of the turbulence. The resolved turbulent kinetic energy, k_{res}, can be calculated as:

$$k_{res} = \frac{1}{2}(\overline{u'u'} + \overline{v'v'}) \tag{5.24}$$

where $\overline{u'u'}$, and $\overline{v'v'}$ are the diagonal components of the Reynolds stress tensor, referred to as the normal Reynolds stresses. Here we used the k-equation to model the subgrid scale

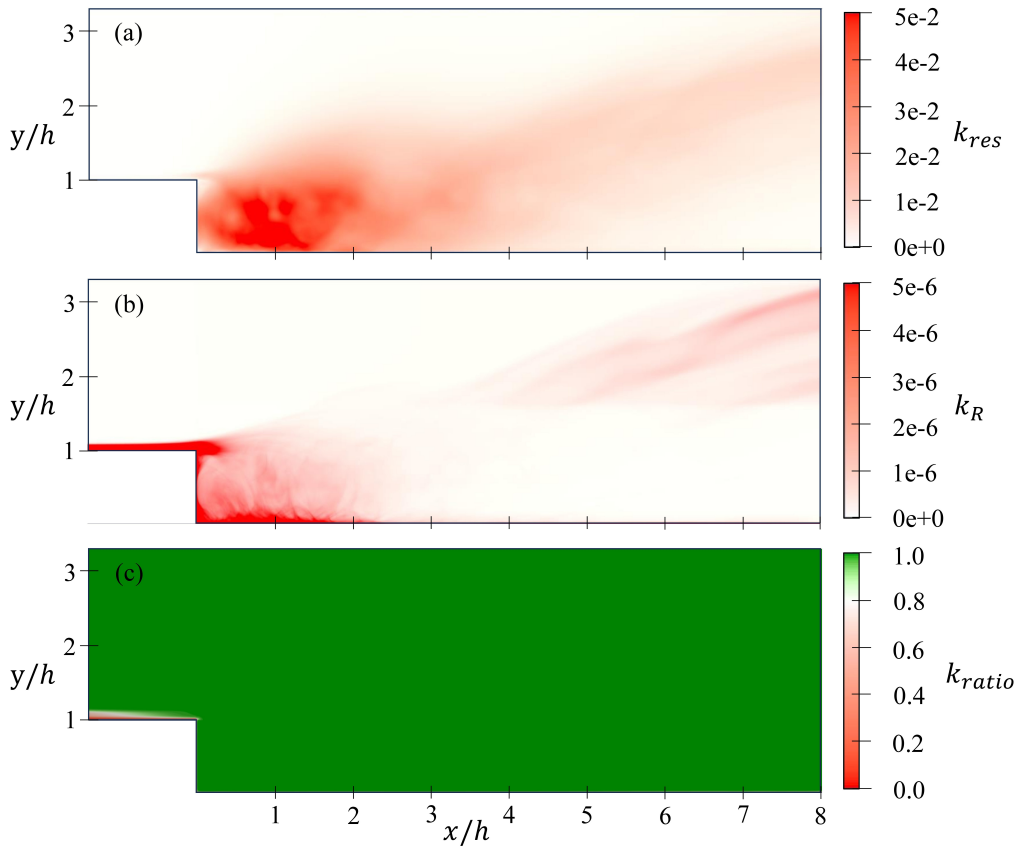

Figure 5.9: The resolution of the LES model. (a) The ensemble averaged resolved turbulent kinetic energy, k_{res}. (b) The ensemble averaged residual turbulent kinetic energy, k_R. (c) The ratio of the quality of the LES model, k_{ratio}, with a threshold of 80%, as suggested by Pope (2000).

motions of the turbulent flow, as stated in Section 5.3.1 of the paper. Therefore, the ratio of the quality of the LES model is calculated as:

$$k_{ratio} = \frac{k_{res}}{k_{res} + k_R} \tag{5.25}$$

where k_R is the residual turbulent kinetic energy, modelled using the k-equation.

Figure 5.9 illustrates the resolution of the LES model used in this study, based on ensemble averaging over two periods of T. As shown in Figure 5.9 (a), the majority of the large-scale, energy-containing eddies are concentrated in the recirculating region behind the step. To

enhance the accuracy of the LES model in this area, two levels of grid refinement were applied to better capture these energy-containing turbulent motions (for more details, see section 5.3.3 of the paper). Conversely, as depicted in Figure 5.9 (b), the residual turbulent kinetic energy in the recirculating region is nearly four orders of magnitude smaller than the resolved turbulent kinetic energy shown in Figure 5.9 (a). As a result, the quality ratio of the LES model, k_{ratio}, which is presented in Figure 5.9 (c), consistently exceeds 90% in the recirculating region and downstream of the step. This confirms that the LES model resolution is sufficient to resolve more than 80% of the turbulent kinetic energy, as recommended by Pope [255]. It is noteworthy that, in the vicinity of the lower wall upstream of the step, where the boundary layer is present, there are some red regions in Figure 5.9 (c) where k_{ratio} falls below 80%. However, since the focus of these simulations is on the downstream region, where the turbulent structures are of primary interest, grid refinement was not applied to the upstream boundary layer, as this area has minimal impact on the downstream turbulence.

Chapter 6

Experimental Investigation of Microplastics Transport in Grid-Generated Turbulence: Effect of Size and Shape

A. Shamskhany & S. Karimpour, Experimental Investigation of Microplastics Transport in Grid-Generated Turbulence: Effect of Size and Shape, Submitted, 2024.

6.1 Abstract

Microplastic (MP) pollution has surged dramatically over the past decade, severely impacting aquatic ecosystems. This study investigates the combined effects of MP size and shape on their behaviour and long-range transport in turbulent flow, within an experimental flume. A series of laboratory experiments in a grid-generated turbulent flow are conducted to evaluate how particle properties and flow dynamics influence MP settling and entrainment, with accumulation measured at two downstream stations. Our results indicate that smaller, non-spherical MPs exhibit higher accumulation rates on downstream capturing nets compared to larger or spherical particles. These MPs settle more slowly and remain entrained in the flow for longer periods, resulting in farther transport from their injection point. This research underscores the significant role of particle characteristics, such as size and shape, as well as flow dynamics, in MP mixing behaviour and long-distance transport.

6.2 Introduction

Global plastic production, and consequently the input of plastics into aquatic environments, is expected to increase significantly over the next decade [6]. Mismanaged plastic waste can enter aquatic systems through various pathways, such as waste water treatment sludge, stormwater runoff, and rivers. Despite the versatility and benefits of plastics, their adverse impact on aquatic environments, particularly through microplastic (MP) pollution, is a growing concern. MPs, defined as plastic particles ranging from a few micrometers to 5 mm, originate either as manufactured particles or from the degradation of larger plastic debris. MPs exhibit a diverse range of densities, sizes, and shapes compared to natural particles, leading to their complex hydrodynamics in aquatic systems [35, 42, 200].

Recent research has documented the abundance and widespread distribution of MPs in various aquatic compartments, including surface waters, bed sediments, and the water column, and linked their physical properties to their environmental distribution [30, 31, 34, 200]. Turbulence, which is generated by various flow processes such as wind, tides, temperature gradients, and sudden bathymetrical changes, plays a crucial role in the mixing and entrainment, suspension, and long-range transport of MPs across aquatic environments. Studies have shown that turbulence can significantly alter particle trajectories, enhancing the vertical and horizontal mixing of MPs [122, 150, 167]. Understanding how turbulence interacts with MPs is therefore critical for predicting their mobility and fate in aquatic systems.

Shape, as one of the most important particle characteristics, directly affects the drag coefficient and, therefore, MP transport. MPs exhibit a wide range of shapes, from regular spheres to irregular fragments, which complicates their interaction with the flow. For instance, the settling velocity of particles varies significantly with particle shape, as demonstrated in the laboratory experiments of Khatmullina and Isachenko [47]. Laboratory experiments by Bagaev et al. [122] showed that the sinking behaviour of small MP fibres varies significantly

based on their random curvature during the settling in the flow. Similarly, Wang et al. [49] investigated the settling trajectories of MPs with irregular shapes under both static and dynamic flow conditions, highlighting the complexities of MP movement in natural waters. While these studies provide valuable insights into the settling behaviour of non-spherical MPs, the role of turbulence in the transport and mixing of these particles remains poorly understood.

Field observations have revealed that turbulence not only impacts MP settling but also plays a key role in long-range transport, often displacing MPs from surface layers to deeper waters [269]. Morét-Ferguson et al. [82] reported that small fragments are the most abundant particles in the surface layers of the North Atlantic Ocean. According to observations by Cózar et al. [31], both shape and size play significant roles in the distant transport of MPs, with smaller non-spherical shapes more likely to be found in distant and deep layers of the aquatic environment. This observation challenges the conventional assumptions that low-density polymers remain suspended in surface waters and suggests that MPs may be transported significant distances from their source [34, 43, 44], due to turbulence-driven mixing and entrainment.

This study aims to build upon the effect of turbulence on MP mixing and long-range transport by presenting an experimental investigation into the response of MP particles of varying sizes and shapes to turbulent flow. We investigate the entrainment and long-range transport of MPs of diverse properties in an experimental flume subjected to grid-generated turbulence. Previous studies have investigated the longitudinal transport and dispersion of buoyant MPs in an open channel flow using fluorescent dyes, with behaviour similar to Rhodamine particles [270]. In this study, we applied a similar approach to investigate the transport and mobility of negatively buoyant MPs. By exposing MPs to turbulent flows of varying intensities, we assess their behaviour in terms of settling prohibition and long-distance transport. This research provides new criteria for understanding how particle properties and turbulence affect the mobility and fate of MPs in aquatic environments.

6.3 Methodology

Experiments are conducted in a Gunt HM 162 experimental recirculating flume with a length of 5 m, a width of 0.309 m, and a maximum depth of 0.45 m. The flume has a tank capacity of approximately 1.1 m^3 and an adjustable inclination slope ranging from -0.5% to 2.5%. The flow rate in the setup can be adjusted between 5 and 100 m^3/hr.

Our experiments are carried out within a confined test section of the flume, spanning a length of 1.9 m. This section is isolated by installing two portable Plexiglas boxes—one at the upstream end and the other at the downstream end of the measurement area—to separate it from the rest of the flume. These Plexiglas boxes are designed to facilitate the installation of a turbulence generator grid at the upstream end, where the flow enters the test section, and a particle-capturing net at the downstream end. The mesh size of the net is adjusted according to the particle dimensions used in each experiment. Figure 6.1 demonstrates the location of the upstream turbulence-generating grid and the downstream capturing nets. The channel is levelled to a zero slope, and the water depth is maintained using a sharp-crested weir positioned at the downstream end of the experimental flume. The weir angle is adjusted based on the flow rates to maintain a consistent water depth of 20 cm within the test section.

The shape and dimensions of the grid significantly affect the turbulence structure downstream of the grid [271]. To reduce inhomogeneity and avoid secondary circulations, a grid solidity of less than 40% is recommended De Silva and Fernando [272]. Grid solidity refers to the proportion of the area of solid bars to the total area of the grid and is defined as $\sigma = (d/M)(2 - d/M)$, where M is the size of the grid opening and d is the width of the solid gap between openings. The turbulence-generating grid used in this study features square openings with $M = 2$ cm and solid gaps of $d = 0.4$ cm, resulting in a grid solidity of 36%. These dimensions are selected to ensure a homogeneous turbulent structure downstream of the grid, based on previous similar studies [271, 273, 274]. We utilized four different flow rates in the range of the flume discharge range: $Q_1 = 6.30 \times 10^{-3}$, $Q_2 = 1.23 \times 10^{-2}$,

$Q_3 = 1.89 \times 10^{-2}$, and $Q_4 = 2.52 \times 10^{-2}$ m^3/s, to investigate the effect of varying turbulence intensities on the advective transport, turbulent mixing and settling of MPs with different properties.

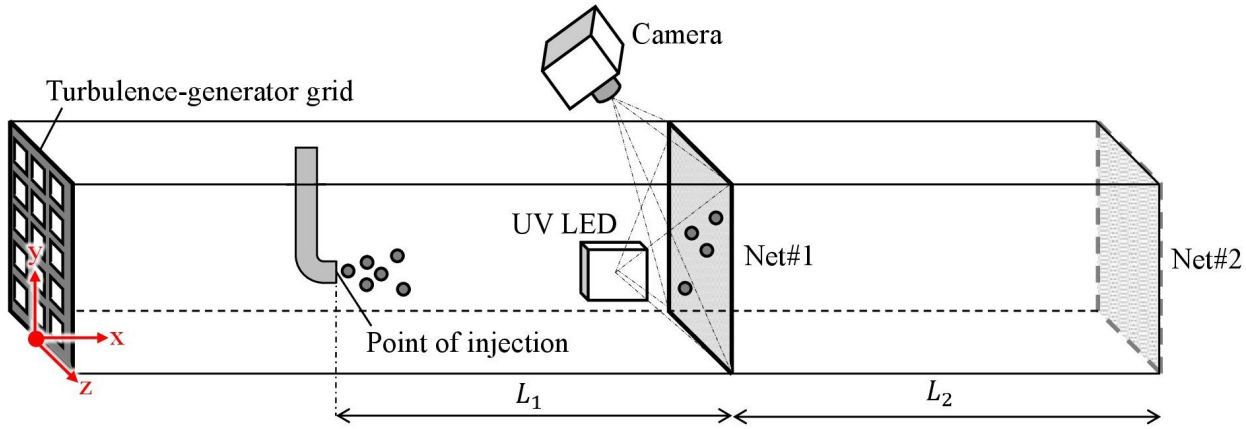

Figure 6.1: Sketch of the experimental setup. The origin of the coordinate system is located at the turbulence generator grid, where x is the stream-wise, y is the depth-wise, and z is the span-wise direction. The injection point of MPs is approximately located at (50, 15, 0) cm. The first and second capturing nets are located at $L_1 = 115$ and $L_2 = 190$ cm, respectively.

6.3.1 Particles: injection to net capturing

This study involves experiments with three distinct particle shapes: spheres, elongated cylinders resembling fibres, and flattened cylinders resembling films, all fabricated using a ProJet MJP 3600 3D printer. The material used for printing the MPs is M3 Crystal (MJP), with a density of 1.22 g/cm^3 after solidification through exposure to ultraviolet light. Figure 6.2 presents a sample of the MPs used in this study. Selected MP shapes are tested in three different equivalent diameters: $d_{eq} = 5.0$, 3.0, and 1.0 mm. The two non-spherical shapes are characterized by an aspect ratio (AR) of 8, representing the ratio between the longest and shortest dimensions. This value is selected based on the prevalent characteristics of MP fibres commonly reported in aquatic environments [96, 100]. In the design of these particles, the smallest dimensions are selected according to the printing limit of the available 3D printer. Table 6.1 provides the characteristics of the MPs used in our experiments along with their corresponding IDs. In this table, ϕ represents the sphericity of the particle defined

as $\phi = S_{sph}/S$, where S is the surface area of the particle, and S_{sph} is the surface area of the equivalent sphere with the same volume.

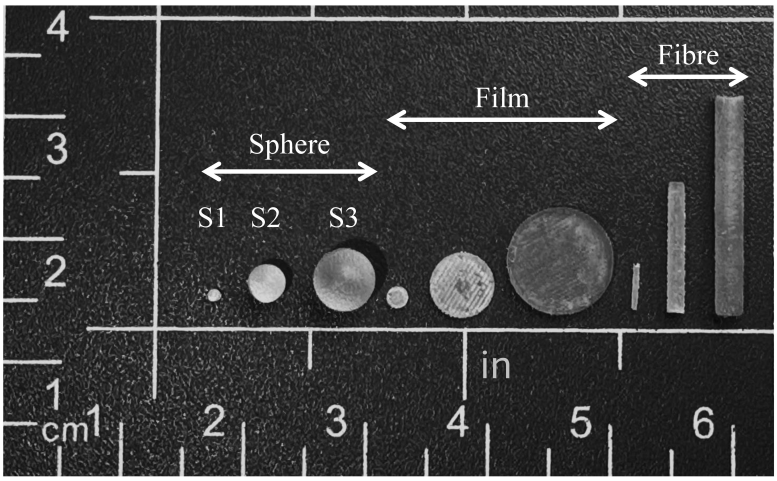

Figure 6.2: 3D printed particles. From left to right: spherical particles (Beads): S1-B, S2-B, S3-B; Flattened cylinders to represent films: S1-F, S2-F, S3-F; Elongated cylinders to represent fibres: S1-E, S2-E, S3-E.

Table 6.1: Characteristics of the MPs. Non-spherical shapes are defined by an aspect ratio of AR = 8. The terms a, b, and c refer to the longest, intermediate, and shortest axes, respectively.

d_{eq} (mm)		S1=1.0			S2=3.0			S3=5.0	
Shape	Sphere	Fibre	Film	Sphere	Fibre	Film	Sphere	Fibre	Film
ID	S1-B	S1-E	S1-F	S2-B	S2-E	S2-F	S3-B	S3-E	S3-F
a (mm)	1.00	3.49	1.75	3.00	10.48	5.24	5.00	17.47	8.74
b (mm)	1.00	0.44	1.75	3.00	1.31	5.24	5.00	2.18	8.74
c (mm)	1.00	0.44	0.22	3.00	1.31	0.66	5.00	2.18	1.09
$S/V*$ (mm^{-1})	600.00	973.01	1144.71	200.00	324.34	381.57	120.00	194.60	228.94
ϕ	1.000	0.617	0.524	1.000	0.617	0.524	1.000	0.617	0.524
V_T (mm/s)	36.27	28.94	25.51	104.66	58.54	50.45	157.80	73.49	63.62

$*$ S/V represents the ratio of the surface area to the volume

The literature on grid-generated turbulence indicates a near-field decay region extending approximately 15 times the grid opening size, where turbulence energy decays more rapidly. This region, typically found within the range of $15 < x/M < 60$, has been widely documented

for its inhomogeneous turbulence, which transitions into a more homogeneous and approximately isotropic far-field turbulence downstream [274, 275]. In our study, we selected an upstream position at x/M within this range to avoid the highly inhomogeneous near-field turbulence and to ensure a fully developed, more homogeneous turbulence regime for the particle entrainment experiments. Particles are injected at around $x = 25M$ downstream of the turbulence generator grid, as shown in Figure 6.1. Thirty particles of identical size and shape are introduced into the fully-developed turbulent flow at varying flow rates. To ensure the particles do not stick to each other and have minimal interaction once released into the flow, they are first mixed with a dilute solution of water-soluble surfactant and then released into the turbulent flow using a large syringe. The particles are subsequently captured using a net with a grid size corresponding to the minimum dimension of particles with an equivalent diameter, ensuring that all particles are collected. The net is positioned at specific stations downstream in the flume, as shown in Figure 6.1.

Two particle-capturing locations are examined to assess the mixing levels and transport distances of MPs with different characteristics in grid-generated turbulent flows at varying flow rates. Each experiment is repeated once, and the results reported here represent the average of these two trials. A camera records the total number of particles accumulating behind the net over time, enabling the comparison of MP accumulation across different cases. The position of the recording camera is shown in Figure 6.1. We employed Ultra-Violet Induced Visible Fluorescence (UVIVF) photography, using a UV LED as the sole light source in a dark room. To enhance the glow from energy re-emission, our 3D-printed MPs are dyed with fluorescent, non-toxic paint and coated with UV varnish. This approach enables the recording of the arrival and trapping time of individual particles throughout each experiment. Manual particle counting is implemented to determine MP accumulation over time on the downstream capturing nets. The UV LED light and camera angles are adjusted to ensure full coverage of the wetted surface of the capturing net.

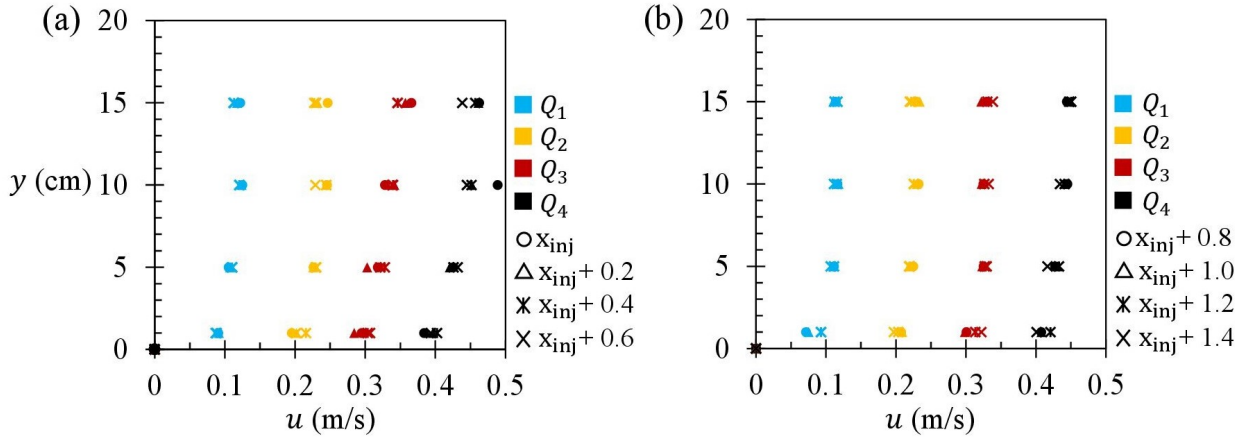

Figure 6.3: In-depth flow velocity measurements at eight stations between the injection point and the second capturing net for various flow rate. (a) and (b) depict the first and second sets of four stations upstream and downstream of the first capturing net, respectively.

6.4 Results and discussion

The flow velocity is measured in the stream-wise (x) and depth-wise (y) directions, as shown in Figure 6.1 using a Flow Tracker Handheld Acoustic Doppler Velocimeter (ADV). This device is capable of measuring velocities from 0.001 m/s to 4.5 m/s at a small measurement point located 10 cm from the acoustic transmitter. The ADV records velocity data at one-second intervals over the selected measurement duration, with the values subsequently averaged to compute the mean flow velocity. Eight longitudinal stations are selected along the $x-y$ plane between the injection point and the second capturing net, with intervals of 20 cm. Thus, the first station is located at the injection point, and the last station is positioned at the second net. Flow velocity components, u and v, are measured at four in-depth elevations of $y = 1$, 5, 10, and 15 cm at each station. Figure 6.3 presents the profiles of the flow velocity in the $x-$direction at each station for different inlet discharges. The corresponding Froude number for each inlet discharge, shown in Figure 6.3, indicates sub-critical flow in the measurement section for all tests conducted in this study. We used the weighted average stream-wise velocity based on depth, defined as U_{avg}, to report the Reynolds number, Re, and the Froude

number, Fr, for different flow rates, as presented in Table 6.2.

$$Fr = \frac{U_{avg}}{\sqrt{gh}} \, . \tag{6.1}$$

$$Re = \frac{U_{avg} h}{\nu} \, . \tag{6.2}$$

where U_{avg} is the weighted depth-averaged u-velocity, $h = 20$ cm is the water depth, and ν is the dynamic viscosity of water, assumed as 10^{-6} at room temperature. In calculation of the weighted average stream-wise velocity based on depth, it is assumed that the flow velocity at the water surface is equivalent to the velocity at the highest measured point of $y = 15$ cm for each station, with a no-slip boundary assumption at the bed, $u_0 = 0$.

Table 6.2: Froude number, Fr, and Reynolds number, Re, for different flow rates.

Q (m^3/s)	Q_1 =6.30E-3	Q_2 =1.23E-2	Q_3 =1.89E-2	Q_4 =2.52E-2
U_{avg}	0.108	0.221	0.322	0.428
Fr	0.079	0.162	0.234	0.313
Re	2.16E4	4.42E4	6.44E4	8.56E4

6.4.1 Regimes of particle motion

In this study, the drag coefficient, C_D, and particle Reynolds number, Re_p, are calculated using the equations from Putnam [170] for spherical particles and Haider and Levenspiel [175] for non-spherical particles. The particle Reynolds numbers range from 25 to 800 that fall within the transitional regime, with drag coefficients spanning from 0.5 to 4.0. Figure 6.4 illustrates the relationship between the drag coefficient, C_D, and particle Reynolds number, Re_p, for each of the distinct particle shapes examined in this study. The discrete data points in Figure 6.4 demonstrate the unique drag coefficients and particle Reynolds numbers associated with each case study.

Sphericity plays a critical role in determining the drag force on particles, with spheres having a sphericity, ϕ, of one, fibres having an intermediate value of 0.617, and films the lowest value

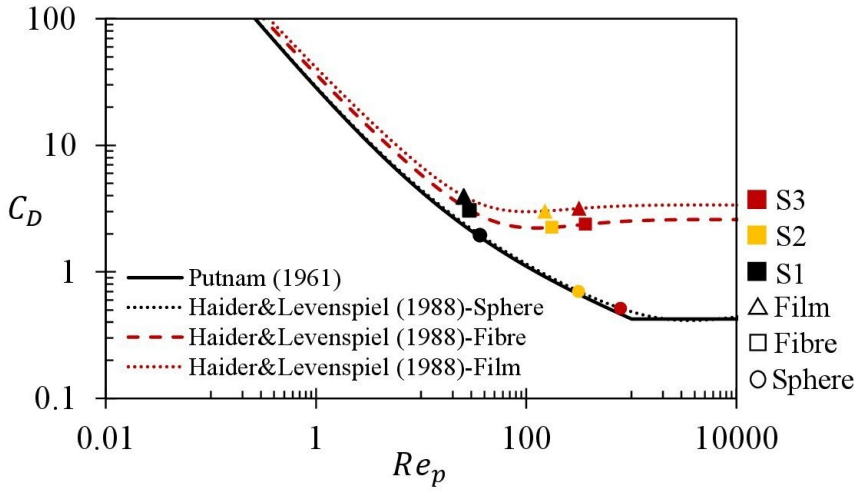

Figure 6.4: Drag coefficient as a function of particle Reynolds number. The markers demonstrate the anticipated drag coefficient, C_D and particle Reynolds number, Re, for the particles listed in Table 6.1 using expressions by Haider and Levenspiel (1989).

at 0.524, as shown in Table 6.1. Sphericity inversely relates to the surface area-to-volume ratio of a particle, therefore, for a given equivalent diameter, films and fibres have higher surface areas compared to spheres. As demonstrated in Figure 6.4, smaller equivalent diameters, d_{eq}, and higher surface area-to-volume ratios, S/V, lead to increased drag coefficients, C_D, and lower particle Reynolds numbers, Re_p. This correlation between drag coefficients and particle Reynolds numbers with surface area-to-volume ratio can partly explain the transport and deposition of MPs in turbulent flow. Smaller, non-spherical particles experience greater drag, making them more susceptible to entrainment and long-range transport in turbulent flow. These findings are consistent with the accumulation patterns and mobility of MPs observed in our study, which will be discussed in the following sections.

6.4.2 MPs' net accumulation in time

Figure 6.5 illustrates the percentage of MPs' accumulation, Π, on each capturing net over time. Fully deposited particles are excluded from net accumulation, even if they reach the net by slithering along the bed. From left to right, it is evident that increasing the flow discharge, from Q_1 to Q_4, proportionally increases the percentage of MPs captured by the nets, Π.

Additionally, the dashed lines, representing MP accumulation on the second downstream net, are visible only for the smaller particle sizes (S1 and S2) and at higher discharges (Q_3 and Q_4). This observation suggests that smaller particles, due to their lower terminal velocities, are less prone to immediate near-source deposition. They are, therefore, more likely to be transported farther from the injection source compared to larger MPs.

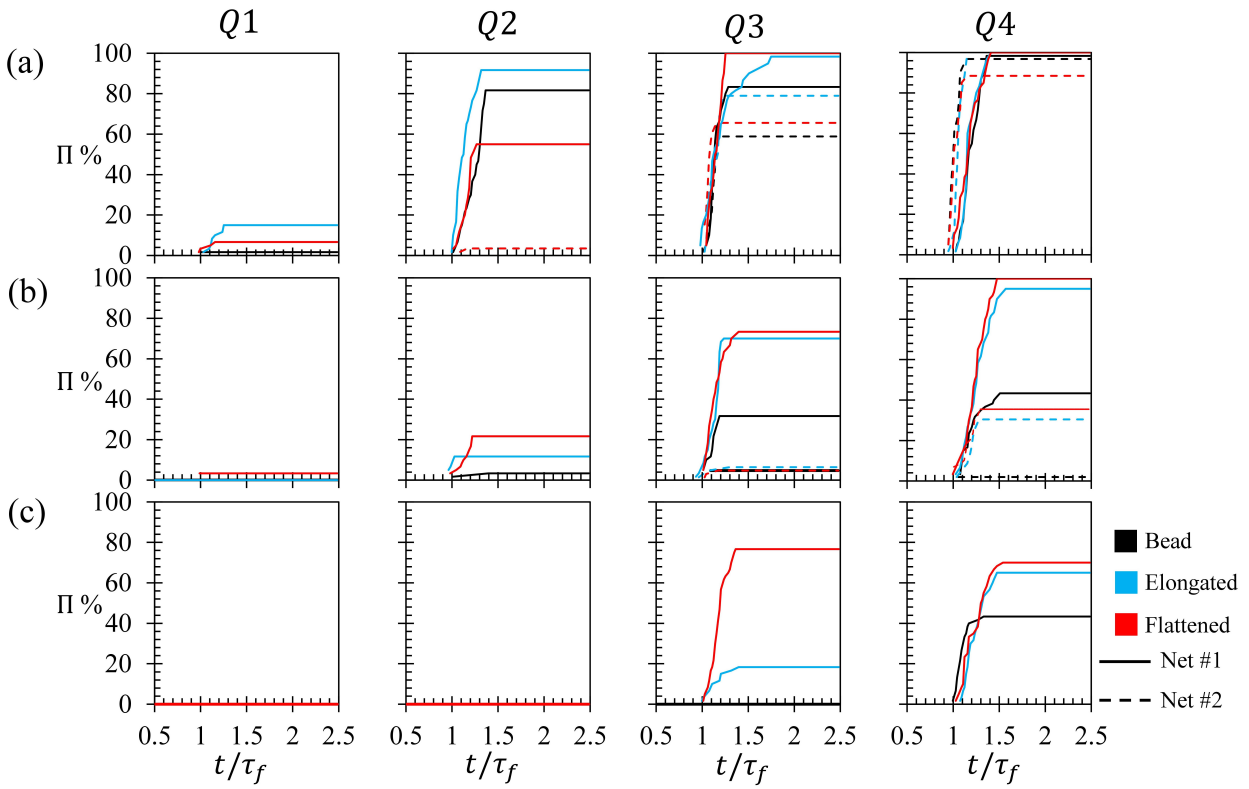

Figure 6.5: Percentage of particles captured on Net#1 and 2, over time. (a), (b), and (c) correspond to size S1, S2, and S3, respectively.

Turbulent entrainment plays a significant role in preventing settling and enabling the long-range transport of MPs, with particle size and shape further influencing particle interactions with the flow. Based on the reported size distribution of MPs across different aquatic regions, smaller particles are the most prevalent in the water columns of remote areas and sediment samples [79, 200]. This suggests an inverse relationship between particle size and suspension, flow mixing, and long-range transport. Furthermore, previous numerical investigations demonstrated a direct relationship between particle size and the proportion of fully deposited

particles in sustained turbulent structures [249]. A similar trend is also reflected in our experimental results. As demonstrated in Figure 6.5, moving from row (a) to row (c), it is evident that increasing particle size results in a lower percentage of accumulation on the nets, indicating that larger MPs are more prone to deposition, and they are associated with lower mixing levels with the turbulent flow.

Moreover, our results show that a decrease in sphericity leads to an increase in net accumulation, Π. This trend can be observed in Figure 6.5 rows (b) and (c), by comparing the black lines—representing spherical shapes—with the blue and red lines—which correspond to fibres and films, respectively. However, for the smallest particle size, S1, as shown in Figure 6.5 row (a), particularly at higher discharges of Q_2, Q_3, and Q_4, the effect of particle shape on net accumulation and long-range transport is less pronounced.

6.4.3 Assessment of MPs' interaction with the ambient turbulent flow

Various dynamic processes contribute to the long-range transport of MP particles, including terminal settling, resuspension, and turbulence-induced mobility. Additionally, the physical properties of MPs—such as density, size, and shape—play a significant role in governing their transport and mobility in the ambient flow by influencing particle-flow interactions. For instance, as demonstrated by the results of this study, the size, and sphericity of MPs have an inverse relationship with their tendency to deposit, and therefore a direct relationship with their long-range transport. In addition to size and shape, the marginal density of MPs—the difference between the particle's density and that of the ambient flow—is also a crucial factor in governing their turbulent mixing, as demonstrated by previous numerical investigations [249]. Based on the sediment analogy, marginal density and size are the dominant factors influencing the deposition and transport of particles. Both size and density are directly related to a particle's terminal velocity, meaning that larger or heavier MPs sink more rapidly compared to those with smaller sizes or lower densities.

Similarly, the resuspension of fully deposited particles also depends on their size and marginal density. A deposited particle will begin to move when the forces exerted by the flow, such as drag, exceed the resistance by the particle's gravitational forces. This relationship, first described by Shields (1936), is expressed as a function of the Boundary Reynolds number, Re_*, and the Shields parameter, θ, which is defined as:

$$\theta = \frac{\tau_0}{|\rho_p - \rho_f| g d_{eq}} \tag{6.3}$$

where τ_0 is the critical shear stress, ρ_p is the particle density, ρ_f is the flow density, and d_{eq} is the equivalent diameter. In the Shield's diagram, for a given Boundary Reynolds number, values of the Shields parameter higher than the threshold are associated with the incipient motion of the particle, whereas lower values below the threshold indicate that particles remain deposited. Based on Eq. 6.3, particle resuspension has an inverse relationship with the marginal density and size of the particle. This relationship is further supported by multiple experimental studies, which have demonstrated that reducing the size of MPs enhances their incipient motion in turbulent flow [85, 276]. MP behaviour differs from that of sediment particles, so commonly used sediment threshold motion correlations may introduce errors when applied to predict MP movability and incipient motion [262]. Waldschlager and Schuttrumpf [276] found that smaller particle sizes, non-spherical shapes, and lower densities are associated with higher Shields parameters, making these particles more prone to resuspension and flow mixing. In fact, such physical characteristics increase the sensitivity of particles to changes in the dynamics of the ambient flow and reduce the time needed for particles to respond to these updates.

Particle relaxation time represents the time required for a particle to respond to changes in the ambient flow dynamics and adjust its velocity accordingly. Similar to the Shields parameter, the definition of particle relaxation time, based on the Stokesian terminal velocity,

also takes into account particle size and marginal density:

$$\tau_p = \frac{|\rho_p - \rho_f| d_{eq}^2}{18\mu}. \tag{6.4}$$

where μ is the dynamic viscosity of the flow. In contrast to the Shields parameter, relaxation time has a direct relationship to particle size and marginal density, meaning that larger and denser particles are associated with longer relaxation times. Consequently, smaller MPs and those with lower marginal densities respond more quickly to ambient flow dynamics, increasing their likelihood of deviating from natural settling and remaining suspended in the flow. As evident from Eq. 6.3, such MPs are also associated with higher Shields parameters, making them more likely to become resuspended in turbulent flow. This tendency can also be explained by the notion of the particle relaxation time, as a shorter relaxation time increases the likelihood of MPs being resuspended, entrained, and transported in the turbulent flow [277].

The original definition of particle relaxation time is derived from the ratio of a particle's terminal velocity in the Stokesian regime to gravitational acceleration. However, our study examines a broader range of particle Reynolds numbers within the transitional regime (see Figure 6.4). Additionally, as demonstrated in Eq. 6.4, the conventional definition of particle relaxation time applies only to spherical and isometric shapes, as it is solely based on the equivalent diameter, d_{eq}. To address these limitations, we revised the definition of particle relaxation time to represent the ratio of particle terminal velocity, in any regime, to the gravitational acceleration:

$$\tau_p = \frac{V_T}{g} \tag{6.5}$$

This inclusive definition accounts for MPs with varying physical characteristics, while preserving consistency with the original derivation. Particle relaxation time only accounts for the physical properties of MPs and the ambient flow. To incorporate the effect of ambient turbulent flow on MP mobility and transport, we leveraged a dimensionless parameter,

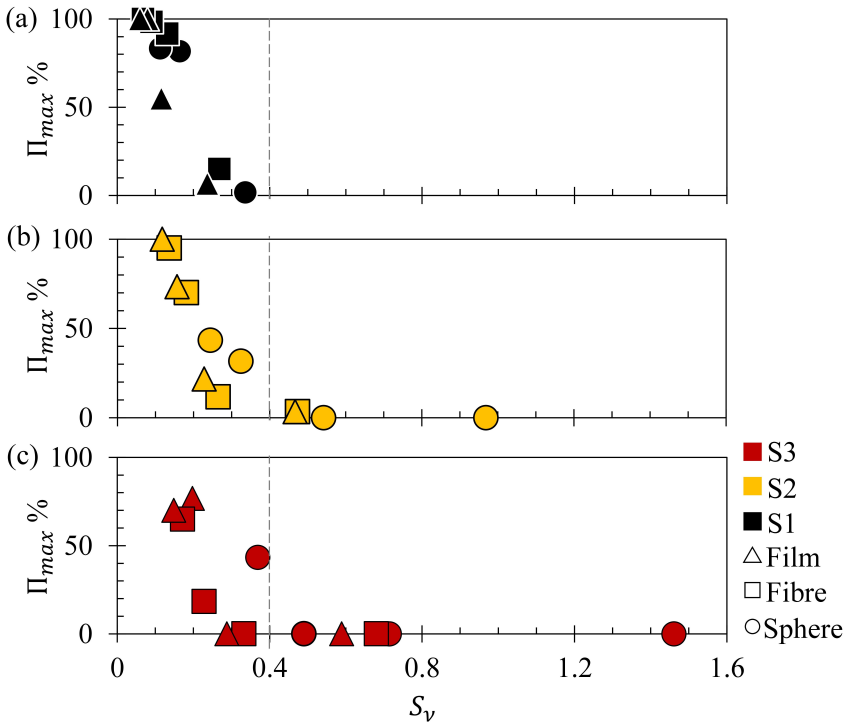

Figure 6.6: Percentage of the fully deposited particles versus the associated settling parameters for each of the case studies. (a), (b), and (c) are associated with sizes S1, S2, and S3, respectively.

combining relaxation time and flow velocity. This dimensionless number, known as Settling Parameter, is widely recognized as a metric for assessing the mixing and entrainment of heavy particles in turbulent flow [154, 161]. Settling parameter is the ratio of the particle velocity scale to the flow velocity scale. The particle velocity scale is determined by the product of the particle relaxation time, τ_p, and gravitational acceleration, g. This parameter, based on Eq. 6.5, is defined as:

$$S_\nu = \frac{\tau_p g}{\sigma_f} = \frac{V_T}{U_{avg}} \,. \tag{6.6}$$

The settling parameter quantifies the balance between a particle's natural tendency to sink in still conditions and the influence of turbulent flow on its movement. At low settling parameters, where the particle's terminal velocity is significantly lower than the flow velocity scale, the particle's vertical motion is predominantly controlled by the flow, often inhibiting its sinking. Figures 6.6 (a), (b), and (c) display the maximum percentage of accumulated

particles on the first capturing net, Π_{max} along with their corresponding settling parameters for MPs of sizes S1, S2, and S3, respectively. As shown in all three panels, for settling parameters below 0.1, all particles remain suspended in the flow and accumulate on the net. However, as the settling parameter increases to a threshold value of $S_\nu = 0.4$, the particles' natural tendency to deposit surpasses the influence of the flow, resulting in full deposition before reaching the capturing net, as seen in Figures 6.6 (a), (b), and (c).

Figures 6.6 (a) to (c) illustrate a direct correlation between the size of MPs and their corresponding settling parameters. Thus, as particle size increases, the settling parameter also rises, resulting in a higher percentage of fully deposited particles and a reduced likelihood of reaching the net. Consequently, particles of size S1, as shown in Figure 6.6 (a), exhibit the highest percentage of net capture and are more likely to remain suspended in the flow, making them more prone to being transported to farther downstream locations. This behaviour is further highlighted in Figure 6.5 (a), where MPs of size S1 exhibit the highest accumulation on the second net, suggesting a greater potential for long-range transport of smaller sizes of MPs from their source of injection. Furthermore, for particles of consistent equivalent diameters, non-spherical shapes (triangles and squares) are associated with lower settling parameters and higher percentages of accumulation on the first capturing net, Π_{max}, compared to spherical shapes. Therefore, physical characteristics that result in lower settling parameters, such as lower marginal density or, as investigated in this study, smaller sizes and sphericities, enhance particle entrainment with turbulent flow and inhibit natural settling and deposition. Consequently, MPs with these properties are more likely to remain in the flow and be transported farther from their injection source.

6.5 Conclusion

Microplastic (MP) pollution has significantly increased over the past decade, causing severe disruptions to aquatic ecosystems. The transport and fate of MPs are influenced by their physical properties as well as the dynamics of ambient flow, which collectively shape the

transport and distribution of MPs. Despite numerous studies on MPs' sinking behaviour and vertical motion, the effects of particle characteristics, particularly shape, on MPs' turbulent mixing and transport remain inadequately addressed.

This research involved a series of laboratory experiments designed to evaluate the combined effects of particle shape and size on the long-range transport and turbulent mixing of MPs. We investigated the downstream transport and net accumulation of MPs with varying sizes and shapes in different grid-generated turbulent structures within an experimental flume. The study encompasses a wide range of particle Reynolds numbers in transitional regimes. Our findings show that MPs with lower particle Reynolds numbers and higher drag coefficients, non-spherical MPs, or smaller sizes, exhibit a lower terminal velocity and higher engagement with the flow. Therefore, they are less likely to be deposited near their source, enabling their long-range transport. Results can also be explained by the potential resuspension mechanism of deposited particles, where MPs with higher Shields parameters, such as smaller or less dense particles, are more likely to resuspend in turbulent flow.

The settling parameter, defined as the ratio of a particle's terminal settling velocity to the ambient flow velocity, is used to assess MPs' mobility and long-range transport in turbulent flow. This parameter incorporates particle size, shape, and marginal density, all of which are critical factors influencing settling, turbulent entrainment, and resuspension. The results of this study revealed that size and sphericity directly correlate with the settling, mixing, and long-range transport of MPs in turbulent flow, with larger and spherical MPs indicating the highest settling parameters as well as the highest tendency toward their natural sinking behaviour and deposition on the bed. On the other hand, smaller non-spherical fibres and films, which are associated with lower settling parameters skip the deposition and remain suspended in the flow for a longer duration. Additionally, the plot of the accumulation rate against the settling parameter indicates that this parameter effectively unifies the results of the current experiment, capturing the key physical processes responsible for long-range transport.

Overall, the transport and fate of MPs are influenced by both their physical properties, such as size and shape and the dynamics of the ambient flow. MP characteristics associated with lower particle Reynolds numbers and higher drag coefficients, such as smaller sizes and non-spherical shapes, lead to long-term suspension and potential entrainment in the turbulent flow, facilitating their transport to remote areas or deep-sea sediments [200]. Furthermore, such characteristics potentially result in enhanced resuspension and re-entrainment of MPs with the turbulent flow. However, for very fine MPs, the effects of shape become less pronounced, making it difficult to distinguish the impact of shape on their entrainment and mixing behaviour.

Chapter 7

Microplastic Response to Turbulent Flow in a Backward-Facing Step: A Numerical Investigation

A. Shamskhany & S. Karimpour, Microplastic Response to Turbulent Flow in a Backward-Facing Step: A Numerical Investigation, Draft for submission, 2024.

7.1 Abstract

Microplastic (MP) pollution is a ubiquitous threat to the aquatic environment. Understanding the transport and mobility of MPs in the aquatic environment and the effective factors, such as different transport mechanisms and physical properties, is a crucial step toward future mitigation. This paper implements an Eulerian-Lagrangian numerical model to simulate the three-dimensional transport and mixing of MPs with various properties in turbulent flow over a backward-facing step geometry. The Lagrangian particle-tracking submodel is based on Newton's second law and follows a dynamic approach, allowing for the calculation of instantaneous acceleration of different MPs and, consequently, the incorporation of the virtual mass force. The results of this study indicate that the vertical slip velocity of MPs can deviate from their terminal velocity in quiescent fluid, especially when their physical properties correspond to low particle relaxation times. MPs with smaller sizes, non-spherical shapes with high aspect ratios, and low marginal densities relative to the ambient flow exhibit a

considerable range of particle acceleration. Consequently, the common assumption of vertical forces equilibrium used in kinematic Lagrangian modelling studies, may be inaccurate for such particle properties. This paper also investigate the effects of various physical properties on the mobility and distribution of MPs within the simulation domain. MPs associated with higher ranges of slip velocity and acceleration are more likely to remain entrained in the turbulent structure and to be transported to regions farther from their source.

7.2 Introduction

Access to clean water is essential for human health and well-being, as emphasized by the United Nations' 6th Sustainable Development Goal [1]. In recent decades, global plastic production has surged notably, driven by the low cost, durability, and versatility of plastic polymers [6, 76], resulting in a proportional increase in global plastic pollution. Microplastics (MPs)-plastic particles smaller than 5 mm—have become a major concern in aquatic environments. MPs enter water bodies through various pathways, including rivers, wastewater discharge, stormwater runoff, and coastal waste [10, 11]. MPs are widely distributed across aquatic environments and have been detected in locations ranging from surface waters and estuaries to deep-sea sediments and polar regions [30, 34, 200]. The abundance and distribution of MPs in these systems are influenced by their physical properties—such as size, density, and shape—as well as the dynamics of the ambient flow, which determine their transport, mixing, and distribution patterns [200]. MPs can have ecological impacts, including ingestion by marine species and transferring of additives, such as antibiotics and toxic chemicals, into their bodies [18, 20]. A clear understanding of the transport and behaviour of MPs is essential for predicting their accumulation and distribution in aquatic systems and for informing strategies to mitigate potential risks to ecosystem health [17].

In aquatic environments, flow is often turbulent induced by temperature and density gradient or sudden changes in bathymetry [147, 148, 149]. Turbulence can entrain the suspended particles and prohibit their natural gravitational motions due to vortex trapping and loitering

[159, 160, 161]. On the other hand, it can enhance the settling behaviour of particles and sweep them in the downdraft regions [154, 158]. Another important role of turbulence based on the sediment transport studies is sliding such particles on the bed,, or in case of adequate turbulence intensity, the resuspension of deposited particles [277]. Multiple recent studies, emphasized on the the significant effect of flow dynamics on particle entrainment [109, 110, 146, 150].

The interplay between particle physical characteristics and ambient turbulence governs the transport and mobility of the particles. MPs are associated with diverse physical characteristics, such as polymer density [35], size [200], and shapes [79], which make their behaviour in the flow distinct from that of sediments and other natural particles which have comparably narrower ranges of physical properties. Still, sedimentology provides valuable insights into the complex interactions between MPs and the ambient flow. Similar to sediment particles, size is a key factor in determination of the settling and mixing behaviour of MPs. MPs span in a vast range of sizes, from 10 μm (invisible to the naked eye) to 5 mm (small gravel). The size of MP significantly affects its sensitivity to the ambient turbulent flow perturbations, and in the identical flow regimes, the motions and trajectories of MPs of different sizes are significantly different [249].

Moreover, MPs exhibit a range of shapes, from spherical and isometric forms to irregular shapes like fragments and fibres. These diverse shapes of MPs affect the drag force magnitude, and therefore, their settling and transport behaviours. The impact of non-spherical shapes on the settling patterns of sediment particles has been underscored in several studies, such as Willmarth et al. [118] and Jayaweera and Mason [119], who reported the oscillatory and complex settling dynamics of non-spherical particles across various particle Reynolds numbers. Studying the effect of MP shape presents additional complexity, as these particles often have highly irregular shapes, making drag calculation challenging and not yet fully understood [47, 49]. Kowalski et al. [89] reported a significant discrepancy between the observed sinking rates of irregular MPs and the theoretical estimates based on sediment correlations. This inconsistency has prompted ongoing research into accurately determining the terminal velocity

(V_T) and drag coefficient (C_D) for non-spherical MPs [47, 48, 49, 124]. However, the persistent tumbling and rotation of non-spherical shapes constantly changes their drag, and all existing empirically developed correlations for the drag coefficient calculation of non-spherical particles are associate with considerable errors [89, 124].

In addition to various sizes and shapes, MPs are initially associated with a wide range of polymer densities, both positively and negatively buoyant. The density of the particle, primarily, dictates its gravitational/buoyant settling behaviours. However, the combination of the effect of density with different sizes and shapes results in significantly different motions and settling/rising trajectories based on recent experimental and numerical investigations [120, 249]. Thus, further investigations are required to examine different factors affecting MPs transport, such as various physical properties, as well as less explored transport mechanisms, such as turbulent dispersion.

Within the past decades, several numerical investigations used a Lagrangian particle-tracking model with a kinematic approach to model the transport and fate of MPs in aquatic environments. A kinematic Lagrangian model calculates the displacement of the particles as the superposition of displacements due to different transport mechanisms. This modelling framework has been used widely in recent years to simulate the transport of MPs in different aquatic compartments, from coastal regions to sediment currents [51, 52, 150, 152]. In a kinematic modelling approach, the slip velocity of a particle is assumed to match its terminal velocity in quiescent fluid. However, this assumption may not be suitable under turbulent conditions or for particles with specific physical properties, such as smaller sizes, lower marginal densities relative to the ambient flow, and non-spherical shapes. Additionally, kinematic models neglect particle acceleration resulting from active forces and the associated nonlinear effects on particle motion. Based on the sediment analogy, when the size of a particle is relatively small compared to the flow scales, it becomes more responsive to turbulent perturbations and often exhibits higher acceleration in turbulent flow [278, 279]. Therefore, the assumption of dynamic equilibrium and zero acceleration may be inaccurate for MPs influenced by turbulence.

A dynamic Lagrangian particle-tracking model, on the other hand, accounts for active force equilibrium and calculates the instantaneous trajectory of individual particles based on their accelerations. This paper examines the effects of shape, density, and size on the mobility, mixing, and transport of MPs in turbulent flow, using a three-dimensional (3D) hybrid Eulerian-Lagrangian numerical model. This model implements a dynamic Lagrangian particle-tracking framework to assess the instantaneous hydrodynamics of MPs, focusing on particle Reynolds number, slip velocity, and acceleration. The numerical experiments in this study incorporate a wide range of MPs physical properties, extending beyond the common characteristics of MPs in aquatic environments, and provide a thorough understanding of how these physical properties influence the transport and behaviour of MPs. The results of this study reveal a broad range of particle Reynolds numbers within the Stokesian and low transitional regimes, highlighting the impact of particle properties on their interactions with the ambient turbulent flow. The findings of this study indicate that MP particles with smaller sizes, lower marginal densities, and non-spherical shapes are associated with considerable ranges of particle accelerations. These properties also lead to deviation of particle's slip velocity from terminal velocity. The following sections will outline the methods employed in this study and present the results, including validation analysis, regimes of the particles motion, slip velocity of MPs, particle acceleration, and the distribution and distant transport of MPs within the domain.

7.3 Methodology

The numerical simulations in this study were performed using OpenFOAM version 6, an open-source computational fluid dynamics software. A 3D Backward Facing Step (BFS) geometry was employed to generate turbulent mixing. In this setup, a shear layer forms and extends downstream of the step as the flow passes over its edge. Consequently, a re-circulation region develops between the shear layer and the lower wall [265]. This geometry is fundamental in hydraulics, as it applies to various natural and artificial configurations, such

as downstream regions of weirs and gates, spillways, channel expansions, river confluences, and estuaries, where sudden changes in bed elevation or underwater topography occur. To simulate the flow configuration over the BFS and the movement and entrainment of MPs in fully developed turbulent flow, a hybrid Eulerian-Lagrangian model is used.. For Lagrangian particle tracking, Newton's second law was employed, incorporating the active force terms on MPs in a dynamic modelling approach. Additionally, this study employed a Large Eddy Simulation (LES) model to capture the larger, energy-containing motions of the turbulent flow, while smaller-scale motions were modelled using a subgrid-scale viscosity equation.

7.3.1 Governing equations of the hybrid model

The LES model in the Eulerian sub-model is based on the filtered incompressible Navier-Stokes equations.

$$\frac{\partial u_i}{\partial x_i} = 0 \tag{7.1}$$

$$\frac{\partial u_i}{\partial t} + \frac{\partial}{\partial x_j}(u_i u_j) = -\frac{1}{\rho_f}\frac{\partial P}{\partial x_i} + 2\nu\frac{\partial}{\partial x_j}S_{ij} + \frac{1}{\rho_f}\frac{\partial \tau_{ij}^{SGS}}{\partial x_j} \tag{7.2}$$

where, ρ_f represents the density of the ambient flow, which is assumed as 1020 kg/m^3 (density of seawater) and ν represents the kinematic viscosity of the fluid [266]. u and P denote the filtered resolved velocity and pressure fields, respectively, where the index notation is used to specify Cartesian coordinates. S_{ij} is the filtered strain rate, calculated as $S_{ij} = 1/2\,(\partial u_i/\partial x_j + \partial u_j/\partial x_i)$, and τ_{ij}^{SGS} accounts for sub-grid scale viscose stresses, which is calculated using the k-equation model [267].

$$\tau_{ij}^{SGS} = -2\rho_f \nu_{SGS} S_{ij} + \frac{2}{3}k_{SGS}\delta_{ij} \tag{7.3}$$

$$\nu_{SGS} = C_k \Delta^2 \sqrt{k_{SGS}} \tag{7.4}$$

$$\frac{\partial(k_{SGS})}{\partial t} + \frac{\partial(u_i k_{SGS})}{\partial x_i} = \frac{\partial}{\partial x_i}[(\nu + \nu_{SGS})\frac{\partial k_{SGS}}{\partial x_i}] \\ -\tau_{ij}^{SGS} S_{ij} - C_e \frac{k_{SGS}^{3/2}}{\Delta} \tag{7.5}$$

where k_{SGS} represents the sub-grid scale turbulent kinetic energy, δ_{ij} is the Kronecker delta tensor, ν_{SGS} is the sub-grid scale eddy viscosity, C_e and C_k are constant coefficients equal to 1.05 and 0.094, respectively, and $\Delta = \sqrt[3]{V_{Cell}}$ is the filter size, where V_{Cell} is the cell volume.

The instantaneous velocity of each particle is then calculated using Newton's second law:

$$m_p \frac{Du_p}{Dt} = F_D + F_{VM} + F_G + F_B \tag{7.6}$$

$$F_D = \frac{1}{2}\rho_f C_D A_p |u_f - u_p|(u_f - u_p) \tag{7.7}$$

$$F_{VM} = -C_m \rho_f V_p (\frac{du_p}{dt} - \frac{du_f}{dt}) \tag{7.8}$$

$$F_G = g V_p \rho_p \tag{7.9}$$

$$F_B = g V_p \rho_f \tag{7.10}$$

where m_p is the particle's mass, u_p is the particle's instantaneous velocity, F_D is the drag, F_{VM} is the virtual mass, F_G is the gravity, and F_B is the buoyancy. A_p is the projected area assumed as that of the equivalent sphere with an identical volume, u_f is the ambient flow velocity at the location of the particle (local velocity), ρ_p is the density of the particle, C_D is the drag coefficient, C_m is the virtual mass coefficient derived based on the particle's shape [268], and V_p is the volume of the particle.

The reported concentration of MPs, defined as the ratio of MPs' volume to the sampled flow volume, has not been reported to exceed 10^{-6} in various marine compartments [34, 179, 180]. This concentration level aligns with the recommended range for dilute suspensions, as proposed by Elghobashi [178], indicating that MPs do not significantly influence the flow or interact with each other. Consequently, a one-way coupling scheme is adopted, where only

the ambient flow affects particle behaviour and trajectories.

Drag Coefficient Correlations for MPs of Different Shapes

The Lagrangian sub-model in this study applies the equations of Putnam [170] (Eq. 7.11) and Haider and Levenspiel [175] (Eq. 7.12), to calculate the drag coefficient, C_D, as a function of the particle Reynolds number, Re_p, for spherical and non-spherical MPs, respectively:

$$C_D = \begin{cases} \frac{24}{Re_p}(1 + \frac{1}{6}Re_p^{\frac{2}{3}}), & Re_p \leq 1000 \\ 0.424, & Re_p > 1000 \end{cases} \tag{7.11}$$

$$C_D = \frac{24}{Re_p}(1 + ARe_p^B) + (CRe_p)/(D + Re_p) \tag{7.12}$$

In the equation of Haider and Levenspiel [175], A, B, C, and D are equation coefficients, which depend on the sphericity, ϕ, defined as the ratio of the surface area of an equivalent sphere, having the same volume, to the surface area of the non-spherical particle [87]. The definition of these coefficients is provided in Appendix C.

In both correlations for spherical and non-spherical shapes, the particle Reynolds number is defined as:

$$Re_p = \frac{d_{eq}|u_f - u_p|}{\nu} \tag{7.13}$$

where d_{eq} is the equivalent diameter of a sphere with the same volume as the particle.

7.3.2 Modelling setup and computational schemes

In this study, the single-phase solver for incompressible flow, pimpleFoam, is employed to simulate the turbulent ambient flow in the Eulerian sub-model. The pre-existing solver is adapted to handle the transport of MPs through the integration of a Lagrangian particle

tracking scheme, which includes injection models, dispersion models, and active forces [280]. The temporal discretization method used in this model is the second-order implicit backward scheme. This method is conditionally stable, and a Courant stability condition is applied for the temporal discretization. Spatial discretization of the convection terms is performed using the Gauss limited linear divergence scheme, a second order accurate method, which leans towards upwind in regions with a rapidly changing gradient. Other non-advective terms are discretized using Gauss integration with linear interpolation.

The sizes of the MPs in this study are significantly small in comparison to the dimensions of the BFS geometry. As a result, the computational grid size is considerably larger than the particle size. Therefore, the time step associated with the Eulerian LES sub-model can lead to substantial changes in the particle's position and velocity, potentially causing the omission of intermediate movements of MPs during each time step. To address this, two distinct time steps are employed for the Eulerian and Lagrangian sub-models. The Lagrangian time step represents the time required for a particle to exit its containing cell and is a fraction of the Eulerian time step. Therefore, the Lagrangian time step is smaller than or equal to the Eulerian time step, which governs the Eulerian turbulent flow.

Figure 7.1 presents the 3D geometry of the BFS, consisting of an inlet water depth of d, a step height of h, a width of w, and lengths L_1 and L_2 corresponding to the upstream and downstream regions of the step, respectively. At the upstream inlet boundary (ABCD), a uniform flow boundary condition with an inlet velocity of U_o is applied. For the outlet (EFGH) and free surface (BCGF) boundaries, zero-gradient and symmetry conditions are imposed, respectively. Here we use a cyclic boundary condition for the front and back patches (ABFEIJ and DCGHLK), to transform the flow field between these two coupled faces [281]. The lower wall boundary (ADKJ, IJKL, and ILHE) has a no-slip condition. In order to find the suitable width dimension for our simulations we conducted a sensitivity analysis, as presented in Appendix B.

A structured, orthogonal square mesh is implemented with a base mesh size of $dx = dy = dz =$

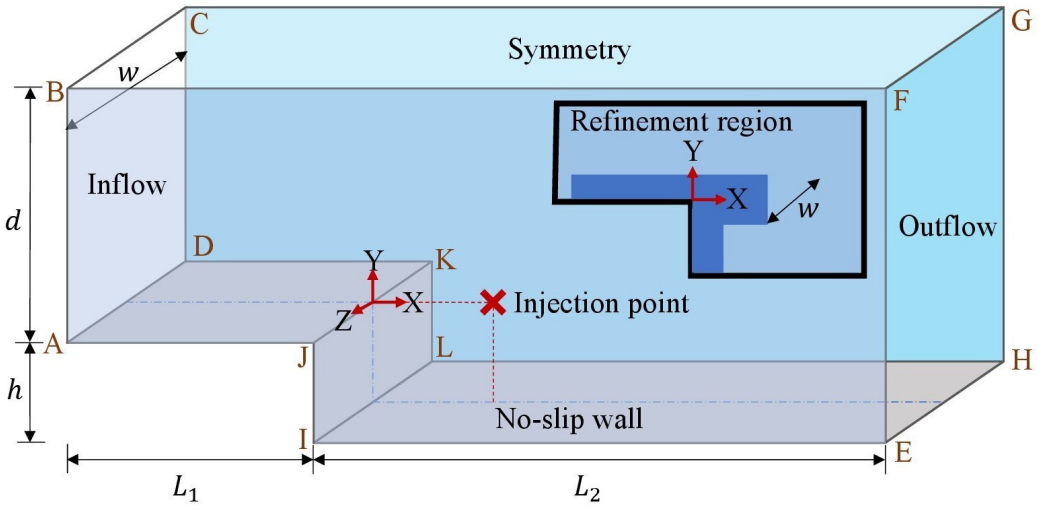

Figure 7.1: Geometry of the BFS; $L_1 = 3$, $L_2 = 5$, $d = 1.5$, $h = 0.5$, and $w = 0.75$ m; X is the streamwise direction, Y is the depth-wise direction, and Z is span-wise direction; The injection point is located at (1.0, 0.0, 0.0) m.

1 cm. To capture the smaller scales of turbulence, grid refinement is applied near the wall boundary and in proximity to the step corner, where the bed elevation drops and the velocity gradient initiates the formation of the shear layer. In this refined zone, which is located between $x = -0.8h$ to $h/2$, y =0.00 to $1.25h$, and $z = -0.75h$ to $0.75h$ (as demonstrated in Figure 7.1), the grid resolution is increased by reducing the mesh size to $dx = dy = dz = 0.5$ cm. These grid dimensions were selected to adequately capture the energy-containing scales of turbulence in the LES model. An analysis of the model's performance showed that the resolved turbulent kinetic energy accounted for more than 80% of the total, in line with the recommendations of Pope [255]. Further details can be found in the Appendix C.

The injection of MPs commences once the turbulent flow has reached a fully developed, quasi-steady state. As depicted in Figure 7.1, the injection point remains consistent across all simulations and is situated at an adequate distance from both the boundaries and the step edge. To effectively capture the effect of the transient features of the turbulent flow on MPs, multiple particles are periodically injected with zero initial momentum. The injection location is strategically selected in a region where the probability of MPs becoming entrained

Table 7.1: MP particles properties and IDs. All cases are studied at the inlet velocity of U_o = 0.4 m/s. For non-spherical cases, E represent fibres (Elongated cylinders) and F represent films (Flattened cylinders). E1/F1 and E2/F2 are associated with the aspect ratios of AR = 8 and 24, respectively.

	PS:1100 (kg/m^3)	PET:1410 (kg/m^3)		
Size (mm)	Sphere	Sphere	Fibre (E)	Film (F)
0.1	S1-B	S1-B	S1-E1/E2	S1-F1/F2
0.5	S2-B	S2-B	S2-E1/E2	S2-F1/F2

by vortices generated near the step corner is intensified. This placement ensures that the injected MPs are exposed to a broad spectrum of turbulent scales.

7.3.3 MPs properties

Table 7.1 lists the simulation IDs, organised by particle density, size, and shape. Two categories of MP density are selected, based on the reported prevalence of related polymers in aquatic environments, both of which are negatively buoyant. The first polymer, Polystyrene (PS), with a density ranging from 1040 to 1100 kg/m^3, is commonly found in bed sediments, particularly in the form of fibres and filaments [46, 200]. The second polymer, Polyethylene Terephthalate (PET), has a density range of 1370 to 1455 kg/m^3, similar to that of Polyvinyl Chloride (PVC), another abundant polymer type found in deep-sea sediments and water columns [35].

Four cylindrical shapes are considered to represent non-spherical MPs, in addition to spherical particles. Elongated cylinders are used to simulate fibres (E), while flattened cylinders represent films (F). These shapes are further classified by two different aspect ratios (AR), defined as the ratio of the longest to the shortest dimension. The AR values are selected to reflect the characteristics of MP fibres commonly found in aquatic environments [30, 96, 100, 102], enabling a deeper understanding of the behaviour of typical aquatic MPs in turbulent flow. The shapes correspond to two size classes, with spherical equivalent diameters ranging from 0.5 mm to 100 μm. These size ranges are chosen based on the widespread abundance

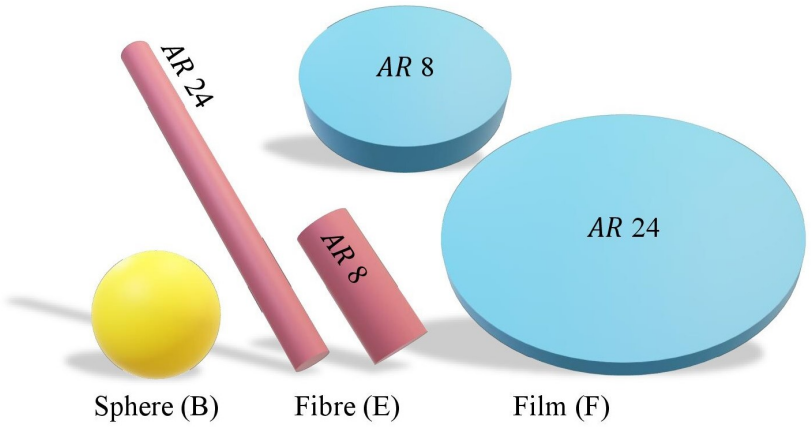

Figure 7.2: Cylindrical shapes in the present study for non-spherical cases presented in Table 7.1.

of MPs across various aquatic compartments, from surface waters to bed sediments [200]. Notably, the dimensions of non-spherical MPs, such as fibres, commonly reported in water column and sediment samples fall within the size range selected for this study, as shown in Table 7.2.

Table 7.2: Characteristics of the non-spherical shapes with AR = 8 (E1 and F1) and 24 (E2 and F2), in SI units, a, b, and c are the longest, the intermediate, and shortest axes.

PET	S1-E1	S2-E1	S1-F1	S2-F1	S1-E2	S2-E2	S1-F2	S2-F2
d_{eq} (mm)	0.100	0.500	0.100	0.500	0.100	0.500	0.100	0.500
a (mm)	0.349	1.747	0.175	0.874	0.727	3.634	0.252	1.260
b (mm)	0.044	0.218	0.175	0.874	0.030	0.151	0.252	1.260
c (mm)	0.044	0.218	0.022	0.109	0.030	0.151	0.010	0.052
$V \times 10^2$ (mm^3)	0.052	6.545	0.052	6.545	0.052	6.545	0.052	6.545
S (mm^2)	0.051	1.274	0.060	1.498	0.071	1.765	0.108	2.701
S/V (mm^{-1})	97.301	19.460	114.471	22.894	134.829	26.966	206.362	41.272
S_{sph} (mm^2)	0.031	0.785	0.031	0.785	0.031	0.785	0.031	0.785
ϕ	0.617	0.617	0.524	0.524	0.445	0.445	0.291	0.291

The particle dimensions associated with the selected aspect ratios in this study extend the threshold for the dimensions of abundant non-spherical MPs, allowing for a comparison of the effects of size and shape. These particle properties are chosen to enable a comprehensive

investigation into the interactions between abundant MPs and the ambient flow in aquatic environments.

7.4 Results and discussion

7.4.1 Validation of the LES model

To validate the LES model in this study, we replicated the experimental study conducted by Nakagawa and Nezu [282] on a BFS geometry. The vertical distributions of the mean streamwise velocity profiles, $\bar{U}$, were compared at eight longitudinal stations between the numerical model and the experimental results, as illustrated in Figure 7.3. In this figure, the x and y values are normalized by the step height based on the experimental configuration, $h = 0.02$ m, and the mean $\bar{U}$ velocities are normalized by the maximum mean velocity, $U_{\max} = 0.409$ m/s, at the station approaching the BFS at $x = 0$ m. Figure 7.3 reveals minimal differences between the numerical simulation results and the experimental data, indicating that the LES model accurately captures the flow configuration observed in the experiment. The root mean square deviation for these mean velocity profiles is limited to 4.6%. Additionally, we calculated the re-circulation length based on the zero stream-function, defined as $\psi = \int_0^y \bar{U} dy$, to evaluate the error between the LES results and the experimental study by Nakagawa and Nezu [282]. The discrepancy between the re-circulation length calculated by the LES model and that obtained from the experimental data was 0.743%, indicating that the LES model closely aligns with the experimental results from Nakagawa and Nezu [282]. It is important to note that studies on sediment transport in the BFS configuration are very limited, and to the best of our knowledge, currently no experimental data is available on the transport of MPs in turbulent flow over BFS. Consequently, the results of the particle tracking module could not be calibrated against experimental tests. However, we employed alternative verification methods, including numerical error convergence analysis, which is detailed in Appendix D.

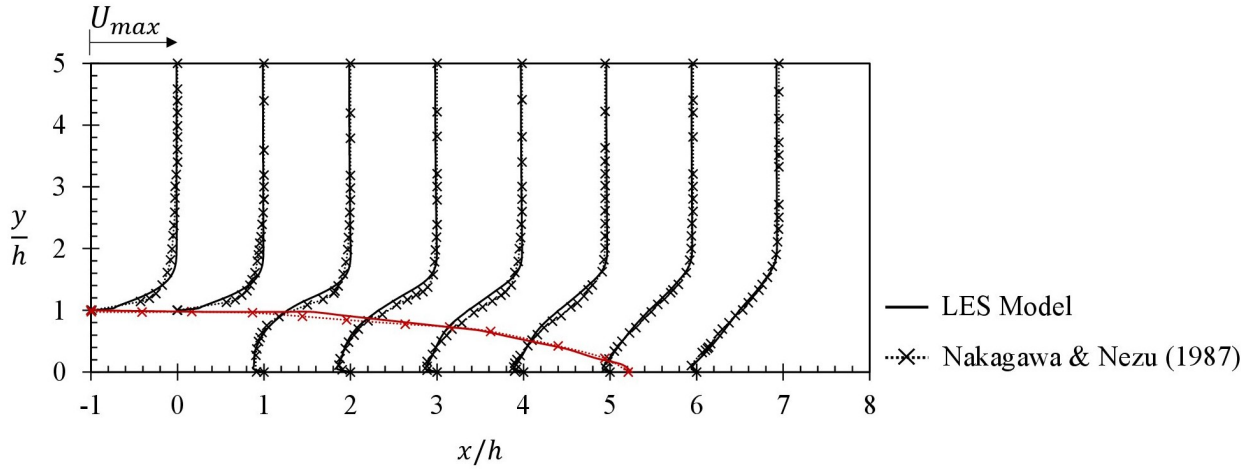

Figure 7.3: Comparison of the mean velocity profiles, U/U_{max} (black), and the length of the re-circulation, $\psi = \int_0^y \bar{U} dy = 0$ (red), between LES model and the experimental values reported by Nakagawa and Nezu (1987).

7.4.2 Particle Reynolds number

The selected particle properties in this study, such as density, size, shape, and aspect ratio as discussed in Section 7.3.3, result in a wide range of particle Reynolds numbers, Re_p, from Stokesian regimes, $Re_p < 1$, to transitional regimes where $1 < Re_p < 1000$. Figures 7.4 (a), (b), and (c) show the range of drag coefficient, C_D, of MPs plotted against the particle Reynolds numbers, Re_p, for spherical and non-spherical particles, respectively. The drag coefficient in panel (a) of Figure 7.4 is calculated based on the terminal particle Reynolds numbers (under quiescent conditions) with the equation of Putnam [170] for spherical particles, and Haider and Levenspiel [175] for non-spherical particles (See Section 7.3.1).Figures 7.4 (b) and (c) represent the range of instantaneous drag coefficient, C_D, and particle Reynolds numbers, Re_p, based on the result of the LES simulations. This range encompasses the values between the 10th and 90th percentiles of the instantaneous data for each simulation. The C_D and Re_p bars for each case intersect at their 50th percentile (median). Similar to Figure 7.4 (a), the discrete markers in panels (b) and (c) represent the terminal values in quiescent conditions.

A comparison between the range of Re_p associated with the size of S1= 100 μm in Figure 7.4 (b) and those of the size of S2= 500 μm in Figure 7.4 (c) demonstrates that as the size of the

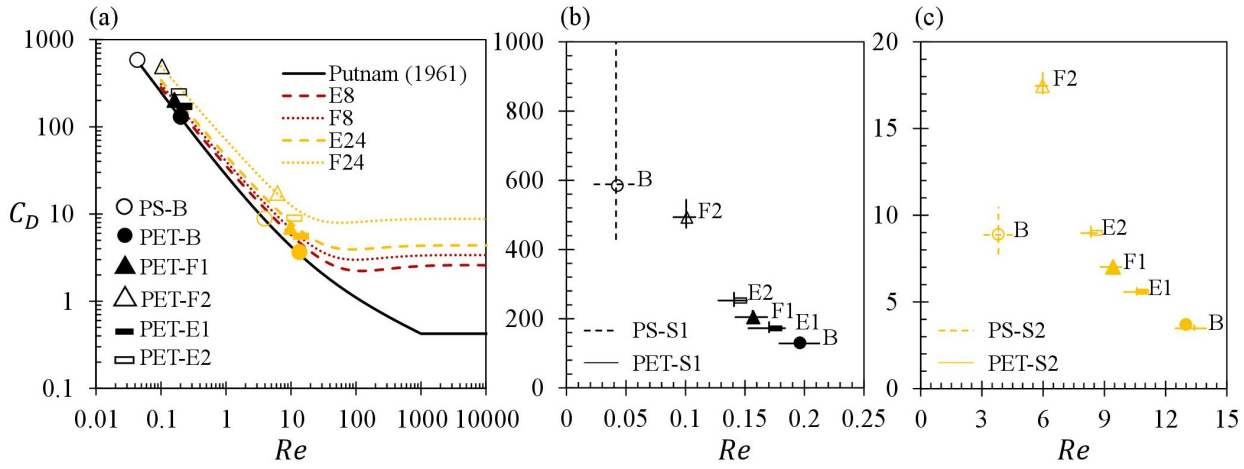

Figure 7.4: Drag coefficient as a function of particle Reynolds number; (a) comparison of terminal values at still fluid for present case studies based on the equations of Putnam (1961) for spherical shape, and Haider and Levenspie (1988) for non-spherical ones, with Flemmer and Banks (1986) correlations; (b) and (c) represent the range of transient values based on the result of the LES simulations for sizes of S1 (black) and S2 (yellow), respectively.

particle increase, the range of particle Reynolds number moves from Stokesian regimes toward transitional regimes. Conversely, the range of drag coefficient significantly decreases with the size increase. Furthermore, the shape of the particle plays a fundamental role on particles' regime and drag coefficient. As depicted in Figures 7.4 (b) and (c), for each of the sizes S1 and S2, reducing the sphericity, moving from beads (B) to films of AR= 24 (F2), results in decreased particle Reynolds numbers and increased drag coefficient. This means that reducing the size and sphericity increases the effect of drag force on MPs. Notably, among PET case studies, the S1-E2 (the smallest d_{eq} and most elongated fibre) and the S1-F2 (the smallest d_{eq} and most flattened film) are associated with the highest drag coefficient. However, reducing the marginal density can intensify the effect of drag on MPs as a result of lower gravitational forces on particles. It can be observed in Figure 7.4 (b) that for MP beads of size S1, reducing the density from PET to PS, increases the range of transient drag coefficients and consequently reduces the particle Reynolds numbers by almost an order of magnitude.

7.4.3 Slip velocity of the MPs

In a kinematic modelling approach, based on the assumption of vertical forces equilibrium, the relative velocity of the particle with respect to the ambient flow (slip velocity) is considered equal to the particle's terminal velocity in quiescent conditions. In other words, this approach assumes that the vertical mobility of MPs is the result of combined displacements from various transport mechanisms, such as vertical advection, turbulent dispersion, and the particle's terminal sinking. However, in a dynamic modelling approach, where active force terms govern the particle's instantaneous motion, MPs can accelerate or decelerate within the flow field, accounting for the effect of the virtual mass force and causing their slip velocity to deviate from the terminal velocity. The ratio of the slip velocity, $v_{Slip} = v_p - v_f$, to the terminal velocity, V_T, is used in this study to assess the extent of the deviation between the particle's actual instantaneous behaviour and its conjectural terminal behaviour, and thus, to evaluate the importance of a dynamic modelling approach for MPs with different properties. Figures 7.5 (a) and (b) show the range of v_{Slip}/V_T versus the ratio of the flow local velocity to the inlet velocity, v_f/U_o, for PS-B, PET-B, and PET-F2 MPs of size S1 and S2, respectively. These ratios are calculated based on instantaneous settling velocity and local velocity of 80 particles, each recorded over a period of $T = 40$ s, for each case. Fully deposited particles are excluded from these records.

A comparison of the range of local flow velocity to the inlet velocity, v_f/U_o, between the two panels in Figure 7.5, demonstrates an almost consistent range between -0.5 and 0.5. This consistency implies that the range of local flow velocity based on the MPs' instantaneous trajectories are similar for all cases. Therefore, all cases demonstrate the potential for entrainment and transport within various parts of the domain. However, the range of the v_{Slip}/V_T is very different across different cases, which means the slip velocity of the MPs depends on their physical characteristics. To investigate the effect of MPs size, density, and shape, on their slip velocity and the deviation of their instantaneous behaviour from their terminal settling, particle relaxation time is utilized in this study, defined as the time required

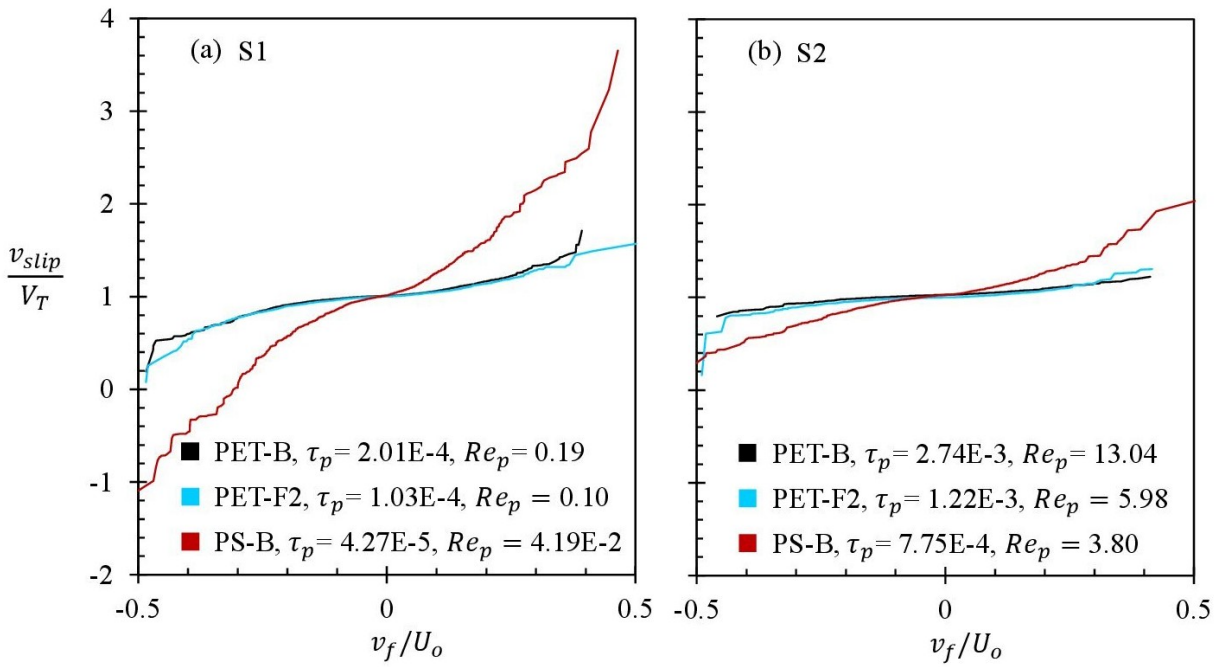

Figure 7.5: The range of slip velocity, $v_{slip} = v_p - v_f$, for different MPs outlined in Table 7.1; (a) and (b) represent sizes S1 and S2, respectively. Particle relaxation time, τ_p (in seconds), and particle Reynolds number, Re_p, are indicated in the legend.

for a particle to respond to updates in the ambient flow dynamics.

$$\tau_{po} = \frac{|\rho_p - \rho_f| d_{eq}^2}{18\mu} \tag{7.14}$$

The classical definition of particle relaxation time is formulated using the particle's terminal velocity in the Stokes regime relative to gravitational acceleration. However, our research expands the scope to include a broader range of particle Reynolds numbers, particularly within the transitional regime (see Figure 7.4). Additionally, as outlined in Eq. 7.14, the classical definition is applicable to spherical and isometric particles, relying on the equivalent diameter, d_{eq}. However, this study aims to investigate he effect of particle shape on behaviour of MPs in the turbulent flow. Therefore, here the definition of the particle relaxation time is

updated to address the mentioned constraints:

$$\tau_p = \frac{V_T}{g} \tag{7.15}$$

The relaxation time, τ_p, associated with size S1 is nearly an order of magnitude smaller than that for the corresponding cases of size S2. This leads to greater mixing with the ambient flow for smaller MPs and causes significant deviations in their vertical mobility from their terminal sinking behaviour under quiescent conditions. As shown in Figures 7.5 (a) and (b), the range of v_{Slip}/V_T almost doubles when comparing size S2 MPs in panel (b) to size S1 MPs in panel (a). This indicates that smaller MPs deviate more from their terminal behaviour than larger ones. For example, the ratio of v_{Slip}/V_T varies between approximately 0.4 and 1.8 for PS-S2-B, while for PS-S1-B, the same ratio fluctuates between -1.0 and 3.6. A similar trend for v_{Slip}/V_T is observed when comparing PET-B and PET-F2 particles as the size decreases from S2 to S1.

Reducing the marginal density of a particle relative to the ambient flow also decreases its relaxation time, enabling MPs to adjust more quickly to changes in ambient flow velocity. This leads to a significant deviation of the slip velocity, v_{Slip}, from the terminal velocity, V_T. The impact of reducing marginal density on this deviation is illustrated in Figure 7.5 (a), where the range of v_{Slip}/V_T expands from (0.2, 1.7) to (-1.2, 3.6)—a 3.2-fold increase—when comparing PET-B (black line) to PS-B (red line). Similarly, in Figure 7.5 (b), the range increases from (0.8, 1.2) to (0.3, 2.1), a 4.5-fold increase between PET-B (black line) and PS-B (red line). Additionally, a comparison between Figures 7.5 (a) and (b) reveals that as particle size decreases, the effect of marginal density becomes less pronounced, with the ratio of the range increase between red and black lines decreasing from 4.5 for size S2 in panel (b) to 3.2 for size S1 in panel (a).

In addition to size and density, decreasing the sphericity of MPs from PET-B cases to PET-F2 cases (film with the highest aspect ratio) of the same equivalent diameter also reduces their particle relaxation time. As shown in the legend of Figures 7.5 (a) and (b), the relaxation

times for PET-B (2.01E-4 for size S1 and 2.74E-3 for S2) are nearly double those of PET-F2 (1.03E-4 for S1 and 1.22E-3 for S2). This reduction in sphericity enhances the particles' mixing with the ambient flow and increases the range of v_{Slip}/V_T, giving non-spherical MPs a higher likelihood of deviating from their terminal sinking behaviour compared to spherical shapes. This is evident in Figure 7.5 (b), where the range expands from (0.8, 1.2) for PET-S2-B to (0.2, 1.3) for PET-S2-F2. However, the effect of shape becomes less distinguishable for the smaller size S1, suggesting that particle size plays the most significant role in determining relaxation time (See Eq. 7.14), while the influence of density and shape becomes less pronounced for smaller MPs.

7.4.4 The instantaneous acceleration of MPs in turbulent flow

The range of vertical accelerations of MPs highlights the importance of a dynamic modelling approach, which accounts for the active forces in MP transport. When a particle's vertical acceleration approaches zero, the net force in the y-direction is negligible, and the particle's slip velocity approaches its terminal velocity. However, our results show that the vertical acceleration of MPs can deviate from zero, suggesting a non-equilibrium state. Figures 7.6 (a) and (b) present the distribution of particles' vertical acceleration, a_y, across different particle characteristics. The diagrams in Figures 7.6 (a) and (b) are based on the instantaneous vertical acceleration of 80 particles in each case, recorded over a period of $T = 40$ s.

A comparison between Figures 7.6 (a) and (b) reveals the significant influence of particle size on the vertical acceleration of MPs. Specifically, the range of normalized vertical acceleration, a_y/g, for MPs of size S1 varies considerably, spanning from -15 to 15, as depicted in Figures 7.6 (a). In contrast, most S2 particles exhibit near-zero vertical acceleration, as shown in Figure 7.6 (b). The same trend regarding the effect of particle size on acceleration in turbulent flow is reported in the literature. Smaller particles, relative to flow scales, generally exhibit higher acceleration in turbulent flow compared to larger particles, which are less responsive to smaller-scale turbulent fluctuations [278, 279, 283].

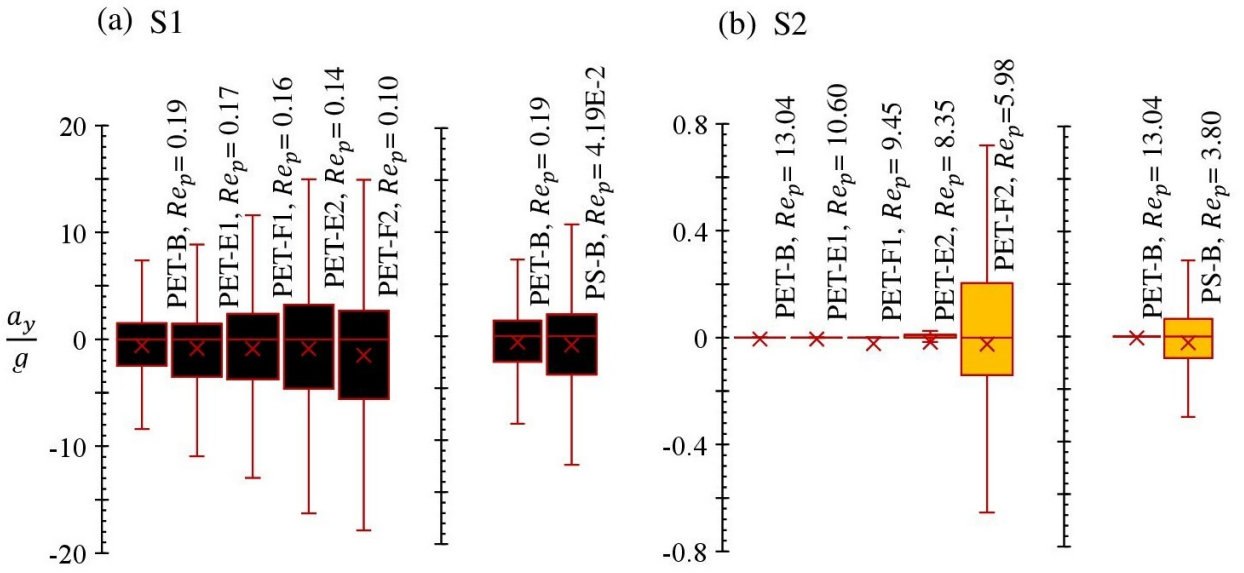

Figure 7.6: The range of normalized particle vertical acceleration, a_y/g, for different MPs outlined in Table 7.1; (a) and (b) correspond to the size S1 and S2 across different shapes and densities, respectively.

Among the larger-sized MPs, the PET-S2-F2 and PS-S2-B cases show a notable deviation in a_y/g compared to other cases of the same equivalent size. This highlights the significant role of particle shape in influencing MPs' acceleration. As previously discussed, particle shape is a critical factor in determining the particle Reynolds number and relaxation time. Non-spherical particles, characterized by lower sphericity and higher aspect ratios, exhibit significantly higher drag coefficients and reduced relaxation times, as outlined in Sections 7.4.2 and 7.4.3. PET-S2-F2, which has the lowest sphericity among the PET-S2 cases, corresponds to drag coefficients nearly four times higher than those of the equivalent bead particle, PET-B, as shown in Figure 7.6(b). A similar trend is observed in Figure 7.6 (a), where reduced sphericity (from B to F2) results in a greater range of vertical acceleration, a_y/g, and deviation from vertical force equilibrium. This variability in vertical acceleration for non-spherical MPs can be attributed to their shorter relaxation times and greater sensitivity to ambient turbulent flow fluctuations.

Moreover, reducing the marginal density of MPs leads to a significant increase in the range

of particle vertical acceleration, a_y/g, as shown in Figures 7.6 (a) and (b), right panels. A comparison between PET-B and PS-B particles of size S1 in Figure 7.6 (a) shows a higher range of vertical acceleration for the PS case, which has lower density. Similarly, in Figure 7.6 (b), PS-B particles of size S2 exhibit vertical accelerations ranging from -0.4 to 0.4, while PET-B particles of the same size are associated with negligible, near-zero values. Overall, particle characteristics that reduce the particle Reynolds number—such as smaller size, lower sphericity, and reduced marginal density—lead to a reduced response time to fluctuations in the turbulent ambient flow and increased vertical acceleration. Consequently, vertical acceleration, and the effect of virtual mass force, cannot be ignored for MPs with particle Reynolds numbers in the Stokesian regime or low transitional regimes of $Re_p < 10$, as the assumptions of dynamic equilibrium and terminal sinking may be inaccurate in such cases.

7.4.5 Particle mobility

In this section, we examined the distribution of MPs in both the streamwise and in-depth directions to investigate the effects of physical properties, including density, size, and shape, on their distribution and long-distance transport in turbulent flow. Understanding these effects is essential, as many studies have documented the selective presence of MPs based on their density [35, 46, 79], size [79, 82, 200], and shape [79, 82, 100, 107] in different aquatic compartments. Figures 7.7 (a) and (b) represent the in-depth and streamwise proportional distribution of suspended MPs in the turbulent flow, respectively, while Figure 7.7 (c) illustrates the streamwise proportional distribution of deposited MPs. These graphs are based on the instantaneous trajectories of 80 particles over a period of $T/2 = 40$ s after injection. This period was chosen to allow sufficient time for MPs to undergo turbulent mixing and transport within the simulation domain. To distinguish fully deposited particles from suspended ones, a vertical position filter with a threshold of $\Delta x = 0.01$ m above the bed was applied. The proportional breakdown reported for each bar in Figures 7.7 (a) to (c) is based solely on MPs present within the specific spatially constrained region. In these

graphs, the results from all cases—with varying densities, sizes, and shapes—are combined, and the percentage presented in each bar represents the ratio of mobile particles within that specific region of the simulation domain.

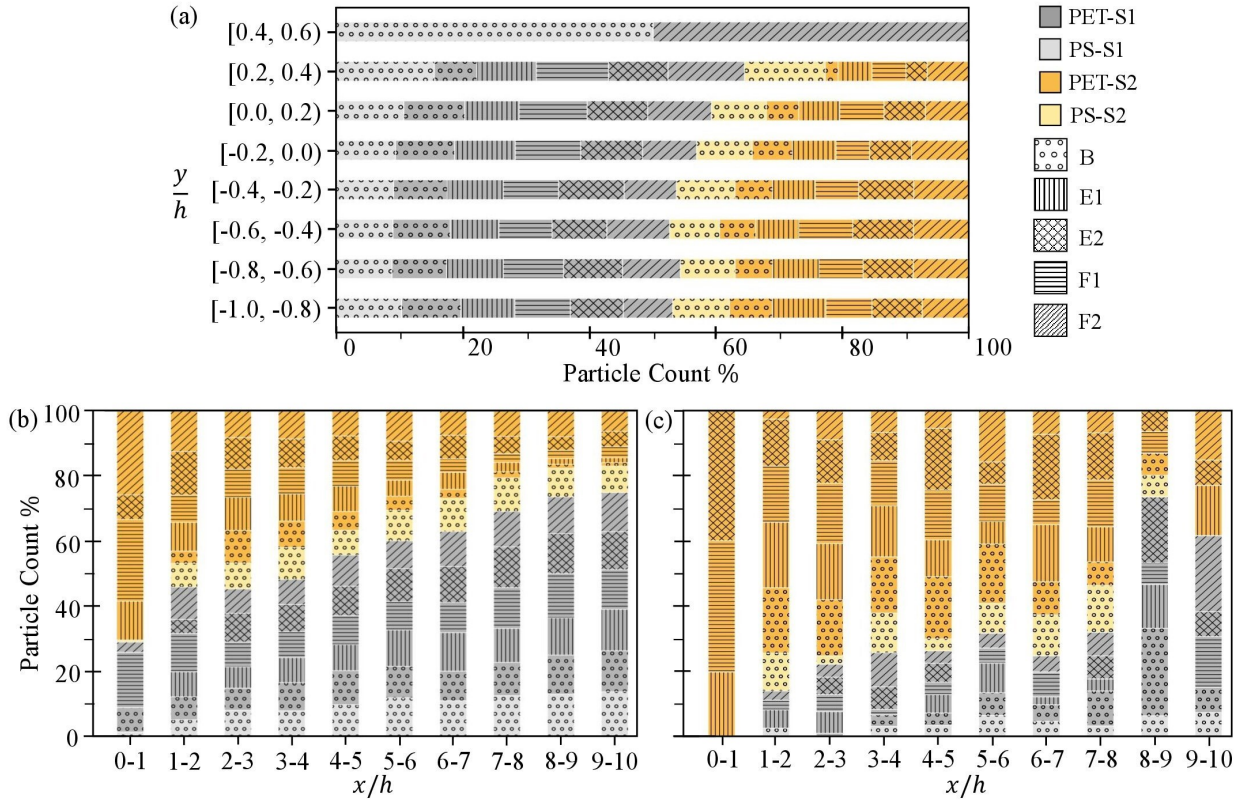

Figure 7.7: MPs proportional distribution behind the step for different cases outlined in Table 7.1; (a) in-depth distribution of suspended MPs in y-direction; (b) longitudinal streamwise distribution of suspended particles; (c) longitudinal streamwise distribution of deposited particles.

The effect of size on the in-depth and longitudinal distribution of MPs, as well as their distant transport, is shown in Figures 7.7 (a) to (c), based on the comparison of the gray and yellow colours. As seen in Figure 7.7 (a), particles of size S1 make up more than 50% of the particles at all elevations, and S1 is the only abundant size at the highest elevation of $0.4 < y/h < 0.6$. This indicates that smaller MPs are less prone to deposition and tend to remain suspended in the turbulent flow. This is further supported by Figure 7.7 (c), where the cumulative proportion of S1-sized particles (gray) is significantly lower than that of larger particles of

size S2. The influence of debris size on vertical distribution and sustained suspension has also been reported in field studies, which observed fine MPs present at various depths, from surface layers to sediments [79, 200].

Moreover, smaller MPs of size S1 are transported to farther distances in the domain compared to MPs of size S2. This trend is evident in Figure 7.7 (b), where the proportion of gray colours increases with distance from the corner of the step, while the proportion of yellow colours decreases in the same direction. Even among fully deposited particles, as shown in Figure 7.7 (c), at the two farthest stations, $8 < x/h < 10$, deposited MPs of size S1 become more prevalent than larger particles. This indicates that most of the deposited particles corresponding to the smaller size S1 are transported toward the end of the simulation domain. The presence of fine MP fragments and fibres in remote Arctic and Antarctic regions further confirms the impact of size refinement on enhancing long-range transport [30, 200]. These reports also highlight the influence of sphericity and shape on MPs' mixing and transport.

Based on Figure 7.7 (a), reducing marginal density, from PET-B to PS-B for both sizes, increases MPs' mixing with the turbulent ambient flow and raises the likelihood of their presence at different depths. It is evident in Figure 7.7 (a) that the proportion of PET-B MPs of both S1 and S2 sizes decreases above an elevation of $y/h = 0.2$ from the bed. In contrast, the proportional distribution of PS-B particles of size S2 remains nearly consistent at various depths, despite these particles naturally sinking, and even increases at the higher elevation of $0.2< y/h <0.4$. Furthermore, for PS-B MPs of size S1, the particles are almost evenly distributed across the water column, while in the highest elevation bin, $0.4< y/h < 0.6$, half of the abundant particles belong to this case. A similar trend is observed in global reviews of aquatic MPs, which document the widespread presence of polymers such as PE, PP, and PS—characterized by lower marginal densities—throughout marine environments, from surface layers to water columns and deep-sea sediments [35, 46, 79].

In addition to the vertical distribution, decreasing the marginal density of MPs also enhances their distant transport with the ambient flow. This behaviour is evident in Figure 7.7 (b),

as the proportion of PS-B MPs of size S2 increases with distance from the injection point, $x/h = 1$, up to $x/h = 4$ and maintains a semi-consistent value after this location. Moreover, Figure 7.7 (c) shows that deposited PS-B particles of size S2 are thoroughly dispersed behind the step, while the overall number of deposited PS-S2 beads is notably less than PET-S2 beads. This means that these larger spherical particles of the lower marginal density still have a great chance to be mixed and transported with the ambient turbulent flow. On the other hand, the abundance of PET-B MP of the size of S2 continuously decreases with distancing from the injection point, $x/h = 1$, as evident in Figure 7.7 (b). Similarly, based on Figure 7.7 (c), these MPs are mostly deposited immediately after injection and within a short distance from the injection point, $1 < x/h < 5$. However, the effect of marginal density on the streamwise distribution of MPs of the smaller size of S1 is less evident, as both PET-B and PS-B MPs of size S1 are quite dispersed behind the BFS and abundant in remote regions of the domain, as evident in Figures 7.7 (b), and (c).

The effect of particle shape on the vertical distribution of larger MPs of size S2 is evident in Figures 7.7 (a), where among yellow colours, the proportion of PET-B (polka-dot) decreases with elevation increase, while the proportion of non-spherical shapes, especially E2 (horizontal lines) and F2 (diagonal lines) with the highest aspect ratios, is almost consistent at different elevations. Figures 7.7 (b) and (c) also demonstrate the effect of particle shape on MPs' turbulent-mixing and longitudinal transport. For suspended MPs, as shown in Figure 7.7 (b), non-spherical shapes of PET-S2 are associated with higher proportions of distant transport (particularly $x/h >4$) compared to spherical shapes. A comparison between Figures 7.7 (b) and (c) indicates that PET-S2-B (orange polka-dot) has the lowest proportion of suspended particles (Figure 7.7 (b)) among MPs of the equivalent size of S2. Most of these larger and heavier spherical particles are fully deposited within the the distance $1< x/h <7$, as demonstrated in Figure 7.7 (c), and only a few of them are suspended after $x/h = 5$.

On the other hand, as shown in Figure 7.7 (b), four non-spherical shapes of PET-S2 are recorded as suspended behind the injection point, $x/h <1$. These particles are influenced by the smaller-scale recirculation close to the bed and are pushed in the negative direction

by these vortices located right behind the step and adjacent to the bed. Conversely, PET-B particles of size S2 bypass these smaller-scale eddies and are absent from this region behind the injection point. Moreover, among the non-spherical MPs of size, S2, PET-S2-F2 (diagonal lines) particles avoid deposition close to the injection point, and remain entrained in the turbulent flow, settling at farther locations, as demonstrated in Figure 7.7 (c). This underscores the effect of higher aspect ratios in the enhanced mixing and long-range transport of non-spherical MPs. In other words, reduced sphericity enhances entrainment and prolongs the period of mixing with the turbulent flow. However, the effect of shape becomes less pronounced for smaller MPs of size S1, making it more challenging to distinguish the behaviour of non-spherical shapes of smaller sizes in turbulent flow.

Based on the results of this study, the physical properties of MPs significantly affect their transport and distribution, both vertical and longitudinal. This is due to the effect of particle properties on their settling tendency versus their flow mixing and entrainment. Reducing particle size, marginal density, and sphericity reduces the particle relaxation time and enhances the flow mixing. Therefore, MPs that are associated with lower relaxation times are associated with higher levels of mixing with the ambient flow, which prohibits their natural tendency of settling and increases the likelihood of their transport to farther distances from the source of injection. This explains the reason for the abundance of small non-spherical MPs of polymers with lower marginal densities, such as Polystyrene and Polypropylene, in remote aquatic regions and bed sediments [46, 100, 200].

7.5 Conclusion

The widespread presence of microplastics (MPs) in aquatic environments is recognized as a major threat to ecosystem health. The dynamics of the flow play a crucial role in the distribution and transport of MPs. Similar to sediment transport, the physical properties of MPs—such as density, size, and shape—strongly influence their mobility within the ambient flow. However, due to the vast range of physical properties among MPs, their behaviour in

aquatic systems is significantly more varied than that of sediments. In particular, the diverse shapes of MPs greatly impact their turbulent mixing and settling behaviours, which remain complex, with many aspects still not fully understood.

This study investigates the influence of density, size, and shape on the turbulent entrainment and distribution of sinking MPs (densities higher than that of the surrounding fluid) within a three-dimensional (3D) backward-facing step (BFS) geometry. A hybrid Eulerian-Lagrangian model is employed, where the hydrodynamics of the ambient turbulent flow are simulated using a 3D LES model, while the Lagrangian particle-tracking sub-model adopts a dynamic modelling approach. This dynamic approach, which accounts for active forces and particle acceleration, allows the model to evaluate the relative motion of particles with respect to the flow and, consequently, the effect of the virtual mass force. As a result, the dynamic model employed here quantifies the deviation of different MPs' settling and mixing behaviours from their natural terminal sinking.

The MPs considered in this study exhibit diverse physical properties, including both spherical and non-spherical shapes, with varying aspect ratios. The results show that MPs' motion spans a wide range of regimes, from Stokesian to transient, resulting in variations in their drag coefficients. Particle size has the most significant effect on the drag coefficient, followed by density and shape. The effect of shape in this study is incorporated using a combination of equivalent diameter (of the sphere of the same volume) and the sphericity factor. A reduction in particle size, marginal density with respect to the ambient flow, and sphericity leads to lower particle Reynolds numbers and an increase in drag coefficients. A comparison of the instantaneous slip velocities of MPs with different properties reveals that reducing size, marginal density, and sphericity also causes a deviation in slip velocity from the terminal velocity observed in quiescent conditions. This suggests that the relative motion of MPs with respect to the ambient flow can considerably deviate from their natural gravitational tendency, as turbulent entrainment may accelerate or decelerate their settling behaviour. Furthermore, based on the associated ranges of instantaneous particle acceleration for MPs with varying characteristics, those with low particle Reynolds numbers are significantly

influenced by velocity fluctuations in the ambient turbulent flow. As a result, the assumption of vertical force equilibrium may be insufficient for accurately modelling the transport of smaller, non-spherical MPs with high aspect ratios, such as small fibres and films.

This study also examines the distribution and mobility of different MPs within the geometry, based on their recorded instantaneous positions during a uniform entrainment period. The results indicate that particles experiencing higher levels of entrainment and mixing with the flow are more likely to deviate from their natural settling behaviour. Instead, they tend to be more prevalent in regions farther from their injection point, both vertically and longitudinally. Small fibres and films with the higher aspect ratio, as well as those with the lower marginal density relative to the ambient flow, constitute the majority of MPs found in the most remote regions of the geometry from their injection source. Furthermore, while most deposited MPs are larger spherical particles or non-spherical shapes with lower the aspect ratio, even among fully deposited MPs, those with smaller size, lower sphericity, and lower marginal density tend to settle farther from their injection point compared to others.

Based on the results of this study, among the various characteristics of MPs, size and marginal density have the most significant effect on particle entrainment in turbulent flow. While the findings indicate that shape plays a notable role in enhancing the entrainment level for larger MPs (above 500 μm), the impact of shape on the transport and entrainment behaviour of smaller MPs is not quite distinguishable. This suggests that the effects of size and marginal density may surpass those of shape for MPs below a certain threshold size. However, further investigations are needed to explore the effect of particle shape, using different shape parameters, in conjunction with other physical properties.

7.6 Appendix A: The Haider and Levenspiel (1989) drag coefficient correlation parameters

$$A = \exp(2.3288 - 6.4581\phi + 2.4486\phi^2) \tag{7.16}$$

$$B = 0.0964 + 0.5565\phi \tag{7.17}$$

$$C = \exp(4.9050 - 13.8944\phi + 18.4222\phi^2 - 10.2599\phi^3) \tag{7.18}$$

$$D = \exp(1.4681 + 12.2584\phi - 20.7322\phi^2 + 15.8855\phi^3) \tag{7.19}$$

7.7 Appendix B: Analysis of the suitable lateral dimension

In this 3D model, a periodic boundary condition is applied between the front and back faces of the geometry in the spanwise, z, direction. This spatially periodic boundary condition reintegrates the flow field exiting along the spanwise direction back into the domain. To establish a fully developed and statistically homogeneous turbulent structure, the width of the periodic domain must be sufficiently larger than the largest flow scale present in the system [284]. To determine the appropriate width for the 3D geometry that effectively captures all turbulent scales, we tested various spanwise dimensions and assessed their influence on the development of turbulence in the BFS geometry by comparing mean velocity profiles (both temporally and laterally), $\bar{U}$, in the streamwise direction across the BFS.

To achieve this, the domain width, w, was adjusted incrementally using four fractions of the step height: $h/2$, h, $1.5h$, and $2h$. Figure 7.8 presents the ensemble-averaged and transverse-averaged velocity profiles, $\bar{U}$, for the different widths. The $\bar{U}$ profiles were normalized based on $U_{\max}$, which represents the maximum $\bar{U}$ value along the line at $x/h = 0$, located at the corner of the step. Ensemble averaging for all widths was conducted over a 150 s period after an initial time of $t = 40$ s, when the turbulent structure had reached a fully developed quasi-steady state, as indicated by the averaged vorticity and reattachment length. The

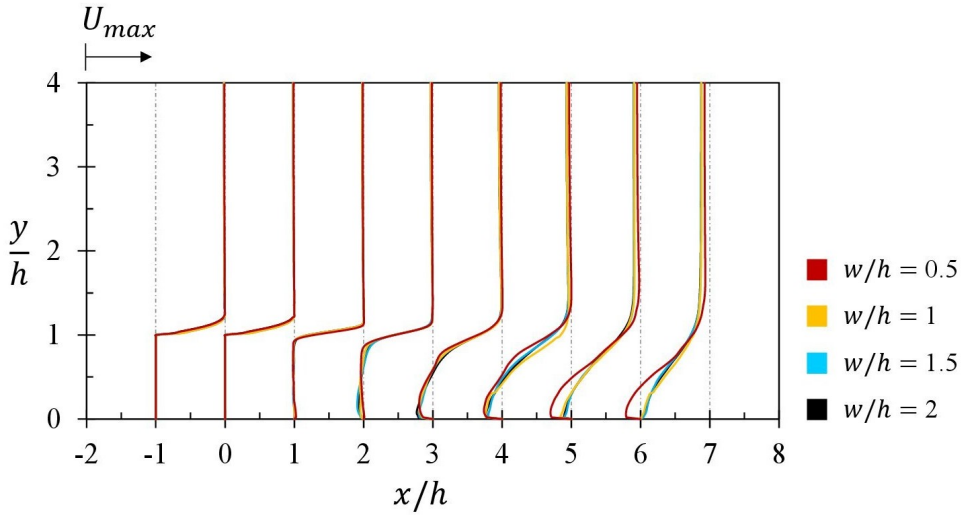

Figure 7.8: Mean velocity profiles (ensemble- and spanwise-averaged), $\bar{U}$, for different widths over a period of 150 s after the quasi steady-state

150 s averaging period was sufficient to capture all turbulent scales and reflect the average behaviour of the turbulent flow over the BFS for the different domain widths.

Figure 7.8 shows that the $\bar{U}$ profiles overlap across all widths near the step corner, within the range -1 $< x/h <$1, where the shear flow begins to form. However, as the shear layer progresses downstream, at $x/h > 1$, discrepancies in the $\bar{U}$ profiles become apparent. This discrepancy is particularly noticeable for the narrower width of $w = h/2$ compared to the larger widths, as depicted in Figure 7.8. It is also evident that as the width increases from 25 cm to 100 cm, the $\bar{U}$ profiles gradually converge, with the difference between the profiles at $w = 75$ cm and $w = 100$ cm becoming nearly negligible. Therefore, a width of 75 cm is selected as the optimal dimension in this study to simulate the turbulent structure of the 3D BFS geometry.

7.8 Appendix C: The quality of the LES model

To evaluate the effectiveness and accuracy of a Large Eddy Simulation (LES) model, it is crucial that the majority of turbulent kinetic energy is directly resolved, with only a small

portion modelled through sub-grid scales. In this study, we applied the criterion proposed by Pope [255] to evaluate the quality of our 3D LES model, which specifies that the resolved turbulent kinetic energy, k_{res}, should constitute at least 80% of the total turbulent kinetic energy, $k_{total} = k_{res} + k_{SGS}$, where k_{SGS} is the sub-grid scale turbulent kinetic energy. This benchmark ensures that the LES model achieves an adequately precise representation of the turbulent structure. The resolved turbulent kinetic energy, k_{res}, is calculated as:

$$k_{res} = \frac{1}{2}(\overline{u'u'} + \overline{v'v'} + \overline{w'w'}) \tag{7.20}$$

where $\overline{u'u'}$, $\overline{v'v'}$, and $\overline{w'w'}$ are the diagonal components of the Reynolds stress tensor, referred to as the normal Reynolds stresses. Here we used the k-equation to model the subgrid scale turbulent kinetic energy of the LES simulation, as stated in Section 7.3.1 of the paper.

Figure 7.9 illustrates the quality assessment of the LES model used in this study, based on ensemble averaging over a period of $T = 80$ s and spanwise averaging over the width of the geometry, $w = 0.75$ m. As shown in Figure 7.9 (a), the quality ratio of the LES model, k_{ratio}, remains consistently above 90% in the recirculating region and downstream of the step. This indicates that the LES model resolves more than 80% of the turbulent kinetic energy, as recommended by Pope [255]. Figure 7.9 (b) shows that the majority of large-scale, energy-containing eddies are concentrated in the recirculating region behind the step. To improve the accuracy of the LES model in this area, two levels of grid refinement were applied to better capture these energy-containing turbulent motions (for more details, see section 7.3.2 of the paper). Conversely, as represented in Figure 7.9 (c), the residual turbulent kinetic energy in the recirculating region is nearly twenty times smaller than the resolved turbulent kinetic energy presented in Figure 7.9 (b). It is noteworthy that, near the lower wall upstream of the step, where the boundary layer is present, some red regions in Figure 7.9 (a) indicate that k_{ratio} falls below 80%. However, since adding another level of grid refinement for this 3D geometry would significantly increase computational costs, and the numerical verification and error convergence analysis, presented in the following appendix,

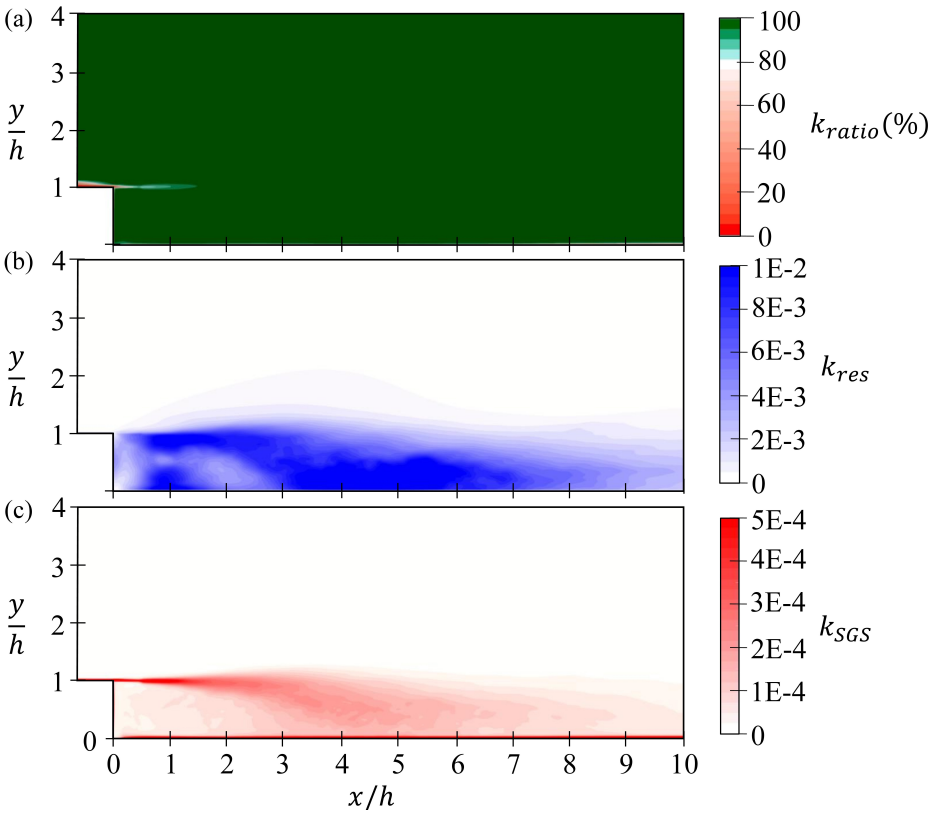

Figure 7.9: The resolution of the LES model. (a) The ratio of the quality of the LES model, k_{ratio}, with a threshold of 80%, as suggested by Pope (2000); (b) The averaged resolved turbulent kinetic energy, k_{res}; (c) The averaged residual turbulent kinetic energy, k_{SGS}.

confirmed the accuracy of the results, this wall boundary region is assumed to have minimal impact on the downstream turbulent structure.

7.9 Appendix D: Numerical convergence and verification

In addition to the validation and LES resolution studies, here we conducted convergence investigations, to estimate the error associated with the results of the 3D LES numerical simulations. PET-S2-B case, with the density of $\rho_p = 14100$ kg/m^3 and the size of $d_p = 0.5$ mm, is selected as the pilot simulation for convergence tests. Both the Eulerian and Lagrangian phases of the pilot simulation are conducted at three grid sizes with a refinement ratio of $r = 1.6$. Here we used two metrics, the length of the recirculation region and the deviation of the averaged transient particle Reynolds number from the terminal one, to evaluate the error convergence and accuracy of the model for both Eulerian and Lagrangian sub-models. For each of the three simulations- associated with the coarsened, normal, and refined grids-the mean $u-$velocity profile as well as the instantaneous velocity of forty different particles' (injected every one second) are recorded during a period of $T = 80$ s after each particle's injection.

The length of the recirculation is calculated based on the zero stream-function, defined as $\psi = \int_0^y \bar{U} dy$, and the averaged particle Reynolds number is calculated as $\bar{Re}_p = 1/nRe_p$, where n is the total number of data recordings for each of the simulations. Then, the order of convergence, P_k, is calculated based on the definition by Karimpour Ghannadi and Chu [260]:

$$P_k = \frac{1}{\ln r} \ln\left(\frac{PR_k - PR_{k-1}}{PR_{k+1} - PR_k}\right) \tag{7.21}$$

where PR is the percentile rank, $k-1$, k, and $k+1$ are the simulation results obtained from the sequential refinement of the grid as k is the original grid size. The estimated 'exact' value, $PR_{\Delta x \to 0}$, is extrapolated and the fractional computational error, FE, for each of the three

Table 7.3: Fractional errors and order of convergence after two levels of refinement for $r = 1.6$, for the length of the recirculation, l_r, and the deviation between the averaged particle Reynolds number, $\bar{Re}_p$, and the terminal particle Reynolds number, Re_T.

Parameter (%)	Δx (m)	values	P_k	$PR_{\Delta x \to 0}$	FE (%)	N
	1.600	4.739			90.895	31
l_r	1.00	5.145	4.381	5.169	4.127	50
	0.625	5.162			0.175	80
	1.600	0.052			98.590	31
$\lvert\bar{Re}_p - Re_T\rvert$	1.000	0.029	4.868	0.026	3.317	50
	0.625	0.026			0.112	80

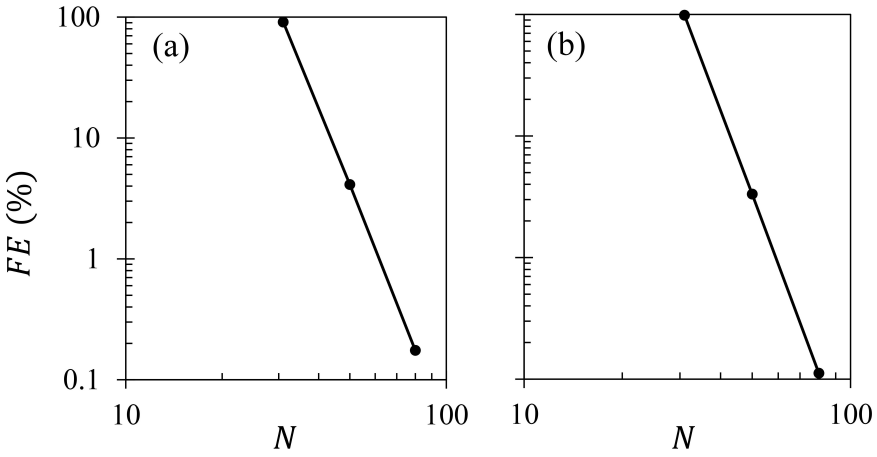

Figure 7.10: Fractional computational error, FE, convergence for three grid sizes; (a) and (b) correspond to the error calculation for the length of the recirculation and particle Reynolds number for the PET-S2-B, respectively.

simulations is defined accordingly:

$$PR_{\Delta x \to 0} = \frac{r^{P_k} PR_{k+1} - PR_k}{r^{P_k} - 1} \tag{7.22}$$

$$FE = \frac{PR - PR_{\Delta x \to 0}}{PR_{\Delta x \to 0}} 100 \tag{7.23}$$

The error is calculated for each of the two parameters, the length of the recirculation, l_r, and the averaged particle Reynolds number, $\bar{Re}_p$. Table 7.3 reports the properties as well as the convergence parameters for each of the three cases.

As demonstrated in Figure 7.10, simulation results confirm the convergence of the fractional computational error with the grid refinement. The horizontal axis, N, represents the number of grids along the step height, h. The fractional error for both parameters reduces with grid size. Results presented in the manuscript are based on $N = 50$. As demonstrated in Table 7.3, the fractional error for this level of refinement remains below 5%.

Chapter 8

Conclusion

The accessibility of clean water is a fundamental need for human health, yet water pollution remains a critical global issue. Pollutants such as chemicals, plastics, and waste materials degrade water quality and negatively impact aquatic ecosystems. Among the major contributors to water pollution, plastic debris accounts for roughly 75% of marine litter and has become a severe environmental problem. A significant portion of mismanaged plastic waste ends up in oceans and seas, where it can persist for centuries, if not millennia. Since the 1950s, the mass production of plastics has increased substantially, leading to heightened levels of plastic pollution in aquatic environments. The issue was further exacerbated during the COVID-19 pandemic, when billions of single-use plastic face masks were discarded daily. Plastic waste is generally categorized into macroplastics, mesoplastics, microplastics (MPs), and nanoplastics, based on the size of the debris. MPs, which range from 10 μm to 5 mm, can either be directly manufactured for industrial purposes (primary MPs) or result from the breakdown of larger plastic items (secondary MPs). Even if the release of larger plastic waste were halted, the abundance of aquatic MPs would still increase exponentially due to the ongoing fragmentation of existing plastic debris in aquatic environments. Over the past few decades, concerns about the adverse impacts of MPs in aquatic ecosystems and their entry into the food chain have remarkably grown.

MPs pose a significant threat to aquatic species and the overall health of marine ecosystems.

Numerous studies have detected and reported the accumulation of MPs in marine animals, birds, and even humans. These small particles can adsorb and transport harmful chemicals, metals, and antibiotics into the bodies of organisms that ingest them. Although recent methods for removing MPs from water bodies have been developed, significant challenges remain. These include the high cost of removal, the difficulty of efficiently filtering very small particles, and the widespread distribution of MPs in aquatic systems. A key step toward developing more effective mitigation strategies is gaining a thorough understanding of MPs' behaviour, transport, and fate in water, along with the associated challenges.

The dynamics of the ambient flow significantly influence the movement and distribution of these particles in aquatic environments. Various transport mechanisms and physical processes, including sinking, advection, turbulent dispersion, biofouling, and fragmentation, affect the transport and distribution of MPs. A key observation is the absence of many MPs from surface layers, despite their buoyant nature, which underscores the impact of transport processes and particle characteristics. Turbulence, a common flow regime in aquatic environments resulting from pressure and velocity gradients due to changes in temperature, density, or topography, can disrupt the natural settling or rising behaviour of MPs in stationary fluid. Among the different mechanisms affecting MP distribution, turbulent entrainment is particularly complex and requires further investigation.

Furthermore, the physical properties of aquatic MPs—such as density, size, and shape—play a dominant role in determining their mobility, flow mixing, and selective distribution and accumulation. MPs are composed of various polymers with a wide range of densities, which primarily influence the gravitational force acting on the particles and, consequently, their natural settling or rising behaviour. Factors such as biofouling and photo-oxidation can further alter polymer densities over time. MPs also vary greatly in size, from barely visible particles to larger ones comparable to small gravels. Particle size plays a crucial role in determining the settling and mixing behaviour of MPs, as it affects forces such as gravity, drag, and virtual mass. In addition to size and density, MPs exhibit a broad spectrum of shapes, ranging from spherical and isometric forms for manufactured primary MPs to irregular shapes like

fragments and fibres, which result from the degradation of larger particles through weathering processes. The shape of MP significantly affects its drag coefficient and, therefore, plays a key role in its settling and transport. Among the various physical characteristics of MPs, understanding the influence of shape—especially irregular shapes—on their transport and fate remains one of the most complex and underexplored areas, particularly when considering the effects of turbulence.

The multifaceted nature of MPs results in countless combinations of physical characteristics, making their transport and distribution more challenging to understand compared to natural particles like sediments. The variations in size, shape, and density of aquatic MPs lead to complex interactions with the ambient flow, many aspects of which remain unclear. However, decades of sediment transport research have yielded a solid understanding of particle and flow entrainment, as well as the key factors involved. This extensive body of knowledge provides a valuable foundation for studying the transport and fate of aquatic MPs. Therefore, despite the significant differences between MPs and natural suspended particles, the sediment analogy remains a useful tool for investigating the effects of particle characteristics and establishing criteria for evaluating the transport and mixing behaviour of MPs.

Numerical modelling and computational fluid dynamics are valuable tools for understanding and predicting the complex behaviour of MPs in aquatic environments, especially in large systems like lakes, seas, and oceans. These methods enhance time and cost efficiency by reducing the need for extensive field investigations, which are often resource-intensive and logistically challenging. Several recent studies have employed Lagrangian particle tracking with a kinematic approach to model MP transport in turbulent flow. While this approach is useful for predicting the long-range transport of MPs based on large-scale circulations, it has limitations in calculating the particle's relative velocity with respect to the ambient flow and accounting for particle acceleration. The effect of particle acceleration can be significant on the behaviour of MPs, depending on their unique characteristics. Moreover, these models are often linked to an averaged large-scale ocean circulation model, which might not adequately capture the effects of smaller-scale flow perturbations. Combining a Large

Eddy Simulation (LES) turbulence model for ambient flow computations with a dynamic Lagrangian particle-tracking model, accounting for active force equilibrium and particle acceleration, can improve the current understanding of MPs' distinct mixing patterns and entrainment in turbulent flow.

8.1 Summary of the key findings

This PhD dissertation investigates various aspects of MPs' behaviour in turbulent flow, including their settling, mixing, long-distance transport, and distribution, with a focus on how their physical properties—such as density, size, and shape—along with flow dynamics, influence their diverse behaviours. The research combines both two-dimensional (2D) and three-dimensional (3D) numerical simulations with preliminary laboratory experiments. The findings aim to deepen the understanding of MPs' transport and distribution in aquatic environments and contribute to the development of more effective mitigation and management strategies. The key findings from each chapter of this study highlight the significant role that MPs' physical properties—size, shape, and density—play in determining their mixing behaviour and transport in turbulent flow conditions.

The review of existing literature revealed that MPs' mobility is not only governed by hydrodynamics of the ambient flow but also by particle properties such as density, shape, and size. Based on the sediment analogy, MP size plays a key role in determining mobility and transport within the flow. MP size influences the magnitude of buoyant and gravitational forces, as well as drag. Smaller MPs respond more readily to changes in the ambient flow and are associated with lower settling velocities. Consequently, these particles experience longer periods of entrainment and mixing and are more likely to be transported to regions distant from their source. Our analysis indicates that smaller MPs are notably absent from offshore surface waters, as they are easily entrained by in-depth circulations and transported to deeper parts of the water column. Furthermore, small MPs are prevalent in sediment samples from remote Arctic regions. In addition to flow mixing, smaller MPs undergo higher

rates of biofouling, which increases their settling velocities and further contributes to their scarcity in surface waters.

The initial phase of 2D numerical simulations focused on the interaction between MPs and turbulent ambient flow, investigating the effects of particle size and density. Using a backward-facing step (BFS) configuration, this phase of the research demonstrated that MPs' entrainment in turbulent flow can be assessed through their settling parameter, which is directly related to particle size and marginal density. Larger and heavier MPs are associated with higher settling parameters, whereas settling parameter decreases as the MP size and marginal density reduce. The results of this study indicate that MPs smaller than a threshold size of 0.2 mm exhibit strong mixing and entrainment with the ambient flow, regardless of their marginal density. These MPs are associated with relatively lower settling parameters and are more prone to deviate from their natural terminal settling or rising behaviour. These findings may explain the absence of fine MPs from surface layers in the aquatic environment, as turbulence entrains and transports smaller MPs with lower settling parameters to deeper parts of the water column.

The second phase of 2D simulations expanded on the previous part, by incorporating the role of particle shape in addition to size and density. The findings indicated that MPs with lower sphericity and reduced size experience higher levels of entrainment, as measured by parameters like the Stokes number and radius of eddy trapping. The study demonstrated that non-spherical MPs are associated with lower radius of eddy trapping and follow fluid trajectories more closely. Thus, non-spherical MPs, especially those with higher aspect ratios, show greater entrainment and lower tendency toward their gravitational behaviour compared to spherical particles. The deviation of instantaneous settling velocity from terminal velocity was substantial for non-spherical MPs with an aspect ratio of 24. Such particles are associated with low settling parameters, and high levels of turbulent entrainment. However, the effect of shape was most pronounced for larger particles, while very small MPs (0.1 mm) exhibited less distinguishable behaviour based on shape, suggesting that size and density have more dominant impacts on fine MPs.

In the laboratory-based study, MPs with varying sizes and shapes were analysed in grid-generated turbulent flow to assess their settling and deposition versus their downstream long-range transport and accumulation on capturing nets. The results confirmed that smaller MPs, particularly non-spherical shapes of fibres and films, remain suspended for longer periods, enabling their transport to distant regions. The experimental findings support the conclusion that MPs with higher drag coefficients and lower settling velocities—due to reduced size or sphericity—are more likely to be transported over long distances. The results of this part of the study also highlighted the probability of resuspension for smaller, less dense, and non-spherical particles in turbulent flows.

The final chapter of this dissertation employed a 3D numerical study of a backward-facing step to explore the effects of particle size, density, and shape on the transport and distribution of sinking MPs in turbulent flow. This chapter investigates the suitability of kinematic versus dynamic modelling approaches for different MP characteristics. The results demonstrated that particle size has the most significant effect on drag coefficients and entrainment, followed by density and shape. Smaller MPs, those with non-spherical shapes of high aspect ratios, and less dense particles exhibited higher deviations from their natural settling behaviour, driven by turbulent fluctuations, suggesting that these particles experience enhanced entrainment and are transported to more distant regions. The slip velocity of such MPs, corresponding to lower particle Reynolds numbers, deviates notably from their terminal velocity. Furthermore, particles with smaller sizes, lower marginal densities, and reduced sphericities exhibit significant ranges of instantaneous accelerations, making the assumptions of dynamic equilibrium and zero acceleration potentially inaccurate under turbulent conditions. The results of this chapter also demonstrated that the effect of shape is more pronounced for larger MPs, whereas for smaller MPs, size and density dominate their turbulent entrainment and transport.

8.2 Research limitations and recommendations for future studies

While the research conducted in this PhD dissertation has provided significant insights into understanding the behaviour, transport, and distribution of MPs in aquatic environments, several limitations remain that suggest directions for future investigations. These limitations arise from both methodological constraints and the inherent complexities of MP transport in turbulent flows:

- Further investigations on the effect of shape:

  The complexities associated with non-spherical and irregular MP shapes leave ample room for future research. The influence of particle shape on drag is well established; however, identifying the most appropriate parameters to quantify the impact of shape, as well as understanding its effect in conjunction with other physical properties, requires further investigation. Additionally, although this research included MPs with both spherical and non-spherical shapes, it did not address the full range of possible MP shapes or the complexity of irregular forms. Based on experimental studies, MPs in natural environments often exhibit irregular and complex shapes, which can substantially affect their drag coefficients and settling behaviour. While this dissertation used regular cylindrical shapes to represent fibres and films, future studies should explore a wider variety of shapes and shape parameters—such as aspect ratios, curvature, and surface roughness—to better capture the diversity of MP behaviour in natural environments. Furthermore, in the Lagrangian numerical model used in this study, the effect of particle's rotation is not incorporated. This omission can potentially impact particle orientation, projected surface area, and consequently, the effect of drag on non-spherical shapes.

- Sediment interactions:

  The interaction between sediment particles and MPs is not considered in the present

study. However, recent studies have highlighted the role of turbidity currents in transporting MPs and distributing them into deeper layers of the aquatic environment, including the sea floor. Collisions and interactions with sediments may influence MPs' trajectories, resuspension potential, settling dynamics, and accumulation. While the analogy used in this research—comparing MPs to sediments—offers valuable insights, further investigation is needed to fully understand how MPs interact with sediments, particularly in environments with high sediment concentrations, such as bottom density currents. Additionally, in this study, the impact of particles on flow development was not considered, as the selected particle dimensions were notably smaller than those of the finest grid cells.

- Biofouling

  Biofouling, the process by which organic materials attach to MPs, is a significant factor influencing their density and settling behaviour. Biofouling can accelerate the sinking of MPs, particularly smaller particles, by increasing their effective density, and it is recognized as a crucial physical process in determining the fate of aquatic MPs. Future studies should account for the biofouling process, especially over realistic time scales, where MPs are exposed to environmental conditions long enough to be significantly impacted by such processes.

- Fragmentation:

  While fragmentation and the breakdown of larger plastic debris into smaller particles is a dominant process affecting all plastic debris, including MPs, and undeniably impacts their transport and entrainment by altering their size and shape, this research does not address this phenomenon. As MPs fragment into smaller pieces, it is expected that their settling rates will decrease, thereby increasing their potential for entrainment in turbulent flows, which in turn influences their long-range transport and distribution in aquatic systems. However, similar to biofouling, fragmentation occurs over a longer time scale, and is therefore not relevant to the current relatively short-scale study. Incorporating fragmentation models into future studies would provide a more

comprehensive understanding of MPs' long-term behaviour.

In summary, this research advances the understanding of MPs' behaviour in turbulent flow and the complex mechanisms governing their transport and fate in aquatic environments. The results of this PhD dissertation underscore the advantages of dynamic modelling over kinematic approaches in simulating the transport of MPs in turbulent flow, bridging critical gaps in the literature and providing new insights into their distribution in aquatic environments. Understanding the hydrodynamics of MPs, based on their physical properties such as density, size, and shape, is essential for developing effective environmental management strategies. The findings presented here provide a robust foundation for future research and practical solutions to address aquatic plastic pollution by highlighting how particle size, shape, and density influence MPs' entrainment and transport in turbulent flow. These findings contribute to the development of predictive tools to assess MPs' fate and can assist in identifying MPs' hotspots in aquatic environments based on their physical properties. This PhD dissertation lays the groundwork for broader efforts to mitigate the impacts of plastic pollution in aquatic environments.

Bibliography

[1] United Nations. *Goal 6: Ensure Availability and Sustainable Management of Water and Sanitation for All*. Accessed: 2024-09-04. 2015. URL: https://sdgs.un.org/goals/goal6.

[2] René P Schwarzenbach, Beate I Escher, Kathrin Fenner, Thomas B Hofstetter, C Annette Johnson, Urs Von Gunten, and Bernhard Wehrli. "The challenge of micropollutants in aquatic systems". In: *Science* 313.5790 (2006), pp. 1072–1077.

[3] United Nations Environment Programme (UNEP). *A Snapshot of the World's Water Quality: Towards a Global Assessment*. Accessed: 2024-09-04. Nairobi: United Nations Environment Programme, 2016. URL: https://www.unep.org/resources/report/snapshot-worlds-water-quality-towards-global-assessment.

[4] Imogen Ellen Napper and Richard C Thompson. "Plastic debris in the marine environment: history and future challenges". In: *Global Challenges* 4.6 (2020), p. 1900081.

[5] PlasticsEurope. *Plastics – The Facts 2019*. Tech. rep. Accessed: 2024-09-04. Avenue E. van Nieuwenhuyse 4/3, 1160 Brussels, Belgium: PlasticsEurope, 2020. URL: https://www.plasticseurope.org/en/resources/market-reports.

[6] Jenna R Jambeck, Roland Geyer, Chris Wilcox, Theodore R Siegler, Miriam Perryman, Anthony Andrady, Ramani Narayan, and Kara Lavender Law. "Plastic waste inputs from land into the ocean". In: *Science* 347.6223 (2015), pp. 768–771.

[7] Nsikak U Benson, David E Bassey, and Thavamani Palanisami. "COVID pollution: impact of COVID-19 pandemic on global plastic waste footprint". In: *Heliyon* 7.2 (2021).

[8] Dirk Xanthos and Tony R Walker. “International policies to reduce plastic marine pollution from single-use plastics (plastic bags and microbeads): A review”. In: *Marine pollution bulletin* 118.1-2 (2017), pp. 17–26.

[9] Alysse Mathalon and Paul Hill. “Microplastic fibers in the intertidal ecosystem surrounding Halifax Harbor, Nova Scotia”. In: *Marine pollution bulletin* 81.1 (2014), pp. 69–79.

[10] Julien Boucher and Damien Friot. *Primary microplastics in the oceans: a global evaluation of sources*. Vol. 43. Iucn Gland, Switzerland, 2017.

[11] Laurent CM Lebreton, Joost Van Der Zwet, Jan-Willem Damsteeg, Boyan Slat, Anthony Andrady, and Julia Reisser. “River plastic emissions to the world’s oceans”. In: *Nature Communications* 8.1 (2017), pp. 1–10.

[12] David KA Barnes, Francois Galgani, Richard C Thompson, and Morton Barlaz. “Accumulation and fragmentation of plastic debris in global environments”. In: *Philosophical Transactions of the Royal Society B: Biological Sciences* 364.1526 (2009), pp. 1985–1998.

[13] Edward J Carpenter, Susan J Anderson, George R Harvey, Helen P Miklas, and Bradford B Peck. “Polystyrene spherules in coastal waters”. In: *Science* 178.4062 (1972), pp. 749–750.

[14] Chibuisi Gideon Alimba and Caterina Faggio. “Microplastics in the marine environment: Current trends in environmental pollution and mechanisms of toxicological profile”. In: *Environmental toxicology and pharmacology* 68 (2019), pp. 61–74.

[15] Peter G Ryan. “Effects of ingested plastic on seabird feeding: evidence from chickens”. In: *Marine pollution bulletin* 19.3 (1988), pp. 125–128.

[16] Kosuke Tanaka and Hideshige Takada. “Microplastic fragments and microbeads in digestive tracts of planktivorous fish from urban coastal waters”. In: *Scientific reports* 6.1 (2016), p. 34351.

[17] Xiang Zhao and Fengqi You. “Microplastic Human Dietary Uptake from 1990 to 2018 Grew across 109 Major Developing and Industrialized Countries but Can Be Halved

by Plastic Debris Removal". In: *Environmental Science & Technology* 58.20 (2024), pp. 8709–8723.

[18] Michelle L. Taylor, Claire Gwinnett, Laura F. Robinson, and Lucy C. Woodall. "Plastic microfibre ingestion by deep-sea organisms". In: *Scientific reports* 6.1 (2016), p. 33997.

[19] Antonio Ragusa, Alessandro Svelato, Criselda Santacroce, Piera Catalano, Valentina Notarstefano, Oliana Carnevali, Fabrizio Papa, Mauro Ciro Antonio Rongioletti, Federico Baiocco, Simonetta Draghi, et al. "Plasticenta: First evidence of microplastics in human placenta". In: *Environment international* 146 (2021), p. 106274.

[20] Emma L Teuten, Jovita M Saquing, Detlef RU Knappe, Morton A Barlaz, Susanne Jonsson, Annika Björn, Steven J Rowland, Richard C Thompson, Tamara S Galloway, Rei Yamashita, et al. "Transport and release of chemicals from plastics to the environment and to wildlife". In: *Philosophical transactions of the royal society B: biological sciences* 364.1526 (2009), pp. 2027–2045.

[21] Chelsea M Rochman, Eunha Hoh, Tomofumi Kurobe, and Swee J Teh. "Ingested plastic transfers hazardous chemicals to fish and induces hepatic stress". In: *Scientific reports* 3.1 (2013), pp. 1–7.

[22] Andrew Turner and Luke A Holmes. "Adsorption of trace metals by microplastic pellets in fresh water". In: *Environmental chemistry* 12.5 (2015), pp. 600–610.

[23] Liming Xing, Haifei Liu, and Diogo Bolster. "Statistical-physical method for simulating the transport of microplastic-antibiotic compound pollutants in typical bay area". In: *Environmental Pollution* 344 (2024), p. 123339.

[24] Francisca Ribeiro, Jake W O'Brien, Tamara Galloway, and Kevin V Thomas. "Accumulation and fate of nano-and micro-plastics and associated contaminants in organisms". In: *TrAC Trends in analytical chemistry* 111 (2019), pp. 139–147.

[25] Paul U Iyare, Sabeha K Ouki, and Tom Bond. "Microplastics removal in wastewater treatment plants: a critical review". In: *Environmental Science: Water Research & Technology* 6.10 (2020), pp. 2664–2675.

[26] Shivika Sharma and Subhankar Chatterjee. “Microplastic pollution, a threat to marine ecosystem and human health: a short review”. In: *Environmental Science and Pollution Research* 24 (2017), pp. 21530–21547.

[27] Chaoran Li, Rosa Busquets, and Luiza C Campos. “Assessment of microplastics in freshwater systems: A review”. In: *Science of the Total Environment* 707 (2020), p. 135578.

[28] Maiju Lehtiniemi, Samuel Hartikainen, Pinja Näkki, Jonna Engström-Öst, Arto Koistinen, and Outi Setälä. “Size matters more than shape: Ingestion of primary and secondary microplastics by small predators”. In: *Food webs* 17 (2018), e00097.

[29] Xiaoyun Qu, Lei Su, Hengxiang Li, Mingzhong Liang, and Huahong Shi. “Assessing the relationship between the abundance and properties of microplastics in water and in mussels”. In: *Science of the total environment* 621 (2018), pp. 679–686.

[30] Kristina Enders, Robin Lenz, Colin A Stedmon, and Torkel G Nielsen. “Abundance, size and polymer composition of marine microplastics 10 μm in the Atlantic Ocean and their modelled vertical distribution”. In: *Marine pollution bulletin* 100.1 (2015), pp. 70–81.

[31] Andrés Cózar, Elisa Martí, Carlos M Duarte, Juan García-de Lomas, Erik Van Sebille, Thomas J Ballatore, Victor M Eguíluz, J Ignacio González-Gordillo, Maria L Pedrotti, Fidel Echevarría, et al. “The Arctic Ocean as a dead end for floating plastics in the North Atlantic branch of the Thermohaline Circulation”. In: *Science advances* 3.4 (2017), e1600582.

[32] Mine B Tekman, Claudia Wekerle, Claudia Lorenz, Sebastian Primpke, Christiane Hasemann, Gunnar Gerdts, and Melanie Bergmann. “Tying up loose ends of microplastic pollution in the Arctic: distribution from the sea surface through the water column to deep-sea sediments at the HAUSGARTEN Observatory”. In: *Environmental Science & Technology* 54.7 (2020), pp. 4079–4090.

[33] Lisbeth Van Cauwenberghe, Ann Vanreusel, Jan Mees, and Colin R Janssen. "Microplastic pollution in deep-sea sediments". In: *Environmental Pollution* 182 (2013), pp. 495–499.

[34] Andrés Cózar, Fidel Echevarría, J Ignacio González-Gordillo, Xabier Irigoien, Bárbara Úbeda, Santiago Hernández-León, Álvaro T Palma, Sandra Navarro, Juan García-de Lomas, Andrea Ruiz, et al. "Plastic debris in the open ocean". In: *Proceedings of the National Academy of Sciences* 111.28 (2014), pp. 10239–10244.

[35] Anna E Schwarz, Tom N Ligthart, Elise Boukris, and T Van Harmelen. "Sources, transport, and accumulation of different types of plastic litter in aquatic environments: a review study". In: *Marine Pollution Bulletin* 143 (2019), pp. 92–100.

[36] Song Ye and Anthony L Andrady. "Fouling of floating plastic debris under Biscayne Bay exposure conditions". In: *Marine Pollution Bulletin* 22.12 (1991), pp. 608–613.

[37] Alvise Vianello, Alfredo Boldrin, Paolo Guerriero, Vanessa Moschino, Rocco Rella, Alberto Sturaro, and Luisa Da Ros. "Microplastic particles in sediments of Lagoon of Venice, Italy: First observations on occurrence, spatial patterns and identification". In: *Estuarine, Coastal and Shelf Science* 130 (2013), pp. 54–61.

[38] Jens H Dekiff, Dominique Remy, Jörg Klasmeier, and Elke Fries. "Occurrence and spatial distribution of microplastics in sediments from Norderney". In: *Environmental Pollution* 186 (2014), pp. 248–256.

[39] Julia Reisser, Boyan Slat, Kimberly Noble, Katherine Du Plessis, Meredith Epp, Maira Proietti, Jan de Sonneville, Thomas Becker, and Charitha Pattiaratchi. "The vertical distribution of buoyant plastics at sea: an observational study in the North Atlantic Gyre". In: *Biogeosciences* 12.4 (2015), pp. 1249–1256.

[40] Melanie Bergmann, Vanessa Wirzberger, Thomas Krumpen, Claudia Lorenz, Sebastian Primpke, Mine B Tekman, and Gunnar Gerdts. "High quantities of microplastic in Arctic deep-sea sediments from the HAUSGARTEN observatory". In: *Environmental Science & Technology* 51.19 (2017), pp. 11000–11010.

[41] Karen Duis and Anja Coors. “Microplastics in the aquatic and terrestrial environment: sources (with a specific focus on personal care products), fate and effects”. In: *Environmental Sciences Europe* 28.1 (2016), p. 2.

[42] Young Kyoung Song, Sang Hee Hong, Mi Jang, Jung-Hoon Kang, Oh Youn Kwon, Gi Myung Han, and Won Joon Shim. “Large accumulation of micro-sized synthetic polymer particles in the sea surface microlayer”. In: *Environmental Science & Technology* 48.16 (2014), pp. 9014–9021.

[43] Richard C Thompson, Ylva Olsen, Richard P Mitchell, Anthony Davis, Steven J Rowland, Anthony WG John, Daniel McGonigle, and Andrea E Russell. “Lost at sea: where is all the plastic?” In: *Science* 304.5672 (2004), pp. 838–838.

[44] Alexandra Ter Halle, Lucie Ladirat, Xavier Gendre, Dominique Goudouneche, Claire Pusineri, Corinne Routaboul, Christophe Tenailleau, Benjamin Duployer, and Emile Perez. “Understanding the fragmentation pattern of marine plastic debris”. In: *Environmental Science & Technology* 50.11 (2016), pp. 5668–5675.

[45] David Keith Alan Barnes and P Milner. “Drifting plastic and its consequences for sessile organism dispersal in the Atlantic Ocean”. In: *Marine Biology* 146 (2005), pp. 815–825.

[46] Gabriel Erni-Cassola, Vinko Zadjelovic, Matthew I Gibson, and Joseph A Christie-Oleza. “Distribution of plastic polymer types in the marine environment; A meta-analysis”. In: *Journal of Hazardous Materials* 369 (2019), pp. 691–698.

[47] Liliya Khatmullina and Igor Isachenko. “Settling velocity of microplastic particles of regular shapes”. In: *Marine Pollution Bulletin* 114.2 (2017), pp. 871–880.

[48] Daria Tatsii, Silvia Bucci, Taraprasad Bhowmick, Johannes Guettler, Lucie Bakels, Gholamhossein Bagheri, and Andreas Stohl. “Shape matters: long-range transport of microplastic fibers in the atmosphere”. In: *Environmental Science & Technology* 58.1 (2023), pp. 671–682.

[49] Zhen Wang, Ming Dou, Pengju Ren, Bin Sun, Ruipeng Jia, and Yuze Zhou. "Settling velocity of irregularly shaped microplastics under steady and dynamic flow conditions". In: *Environmental Science and Pollution Research* (2021), pp. 1–17.

[50] Kara Lavender Law. "Plastics in the marine environment". In: *Annual review of marine science* 9.1 (2017), pp. 205–229.

[51] Isabel Jalón-Rojas, Xiao Hua Wang, and Erick Fredj. "A 3D numerical model to track marine plastic debris (TrackMPD): sensitivity of microplastic trajectories and fates to particle dynamical properties and physical processes". In: *Marine Pollution Bulletin* 141 (2019), pp. 256–272.

[52] Atsuhiko Isobe, Kenta Kubo, Yuka Tamura, Etsuko Nakashima, Naoki Fujii, et al. "Selective transport of microplastics and mesoplastics by drifting in coastal waters". In: *Marine pollution bulletin* 89.1-2 (2014), pp. 324–330.

[53] Nanna B Hartmann, Thorsten Huffer, Richard C Thompson, Martin Hassellov, Anja Verschoor, Anders E Daugaard, Sinja Rist, Therese Karlsson, Nicole Brennholt, Matthew Cole, et al. *Are we speaking the same language? Recommendations for a definition and categorization framework for plastic debris*. 2019.

[54] Rana Zeeshan Habib, Morog Mohammed Salim Abdoon, Reem Mohammed Al Meqbaali, Furtuna Ghebremedhin, Marim Elkashlan, Wajeeh Faris Kittaneh, Nizamudeen Cherupurakal, Abdel-Hamid Ismail Mourad, Thies Thiemann, and Ruwaya Al Kindi. "Analysis of microbeads in cosmetic products in the United Arab Emirates". In: *Environmental Pollution* 258 (2020), p. 113831.

[55] Ella Harvey, Rory Sullivan, and Nicky Amos. "Microplastic pollution: the causes, consequences and issues for investors". In: *First Sentier MUFG Sustainable Investment Institute, Tokyo* (2017).

[56] Beverley Henry, Kirsi Laitala, and Ingun Grimstad Klepp. "Microfibres from apparel and home textiles: Prospects for including microplastics in environmental sustainability assessment". In: *Science of the total environment* 652 (2019), pp. 483–494.

[57] Jing Song, Chunhui Wang, and Gang Li. “Defining Primary and Secondary Microplastics: A Connotation Analysis”. In: *ACS ES&T Water* (2024).

[58] Liqi Cai, Jundong Wang, Jinping Peng, Ziqing Wu, and Xiangling Tan. “Observation of the degradation of three types of plastic pellets exposed to UV irradiation in three different environments”. In: *Science of the Total Environment* 628 (2018), pp. 740–747.

[59] Anthony L Andrady, SH Hamid, X Hu, and Ayako Torikai. “Effects of increased solar ultraviolet radiation on materials”. In: *Journal of photochemistry and photobiology B: Biology* 46.1-3 (1998), pp. 96–103.

[60] Carina Longo, Michele Savaris, Mára Zeni, Rosmary Nichele Brandalise, and Ana Maria Coulon Grisa. “Degradation study of polypropylene (PP) and bioriented polypropylene (BOPP) in the environment”. In: *Materials Research* 14 (2011), pp. 442–448.

[61] Helen Shnada Auta, Chijioke Uche Emenike, B Jayanthi, and Shahul Hamid Fauziah. “Growth kinetics and biodeterioration of polypropylene microplastics by Bacillus sp. and Rhodococcus sp. isolated from mangrove sediment”. In: *Marine pollution bulletin* 127 (2018), pp. 15–21.

[62] Saeed S Sadri and Richard C Thompson. “On the quantity and composition of floating plastic debris entering and leaving the Tamar Estuary, Southwest England”. In: *Marine pollution bulletin* 81.1 (2014), pp. 55–60.

[63] Anthony L Andrady. “Microplastics in the marine environment”. In: *Marine pollution bulletin* 62.8 (2011), pp. 1596–1605.

[64] Chelsea M Rochman. “Microplastics research—from sink to source”. In: *Science* 360.6384 (2018), pp. 28–29.

[65] Carlos Edo, Miguel González-Pleiter, Francisco Leganés, Francisca Fernández-Piñas, and Roberto Rosal. “Fate of microplastics in wastewater treatment plants and their environmental dispersion with effluent and sludge”. In: *Environmental Pollution* 259 (2020), p. 113837.

[66] Zhiqi Zhang and Yinguang Chen. "Effects of microplastics on wastewater and sewage sludge treatment and their removal: a review". In: *Chemical Engineering Journal* 382 (2020), p. 122955.

[67] Kerstin Magnusson and Fredrik Norén. *Screening of microplastic particles in and down-stream a wastewater treatment plant*. 2014.

[68] Erin R. Zylstra. "Accumulation of wind-dispersed trash in desert environments". In: *Journal of arid environments* 89 (2013), pp. 13–15.

[69] James N Hitchcock. "Storm events as key moments of microplastic contamination in aquatic ecosystems". In: *Science of the Total Environment* 734 (2020), p. 139436.

[70] Lydia J Knight, Florence NF Parker-Jurd, Maya Al-Sid-Cheikh, and Richard C Thompson. "Tyre wear particles: an abundant yet widely unreported microplastic?" In: *Environmental Science and Pollution Research* 27 (2020), pp. 18345–18354.

[71] Lapyote Prasittisopin, Wahid Ferdous, and Viroon Kamchoom. "Microplastics in construction and built environment". In: *Developments in the Built Environment* 15 (2023), p. 100188.

[72] Piyush Malaviya and Asha Singh. "Constructed wetlands for management of urban stormwater runoff". In: *Critical Reviews in Environmental Science and Technology* 42.20 (2012), pp. 2153–2214.

[73] Teresita de Jesus Piñon-Colin, Ruben Rodriguez-Jimenez, Eduardo Rogel-Hernandez, Adriana Alvarez-Andrade, and Fernando Toyohiko Wakida. "Microplastics in stormwater runoff in a semiarid region, Tijuana, Mexico". In: *Science of the Total Environment* 704 (2020), p. 135411.

[74] Charles A Harper and Edward M Petrie. *Plastics materials and processes: a concise encyclopedia*. John Wiley & Sons, 2003.

[75] Robert J Young and Peter A Lovell. *Introduction to polymers*. CRC press, 2011.

[76] PlasticsEurope. *Plastics – The Facts 2023*. Tech. rep. Accessed: 2024-09-04. Avenue E. van Nieuwenhuyse 4/3, 1160 Brussels, Belgium: PlasticsEurope, 2023. URL: `https://plasticseurope.org/knowledge-hub/plastics-the-fast-facts-2023/`.

[77] PlasticsEurope. *Plastics – The Facts 2021*. Tech. rep. Accessed: 2024-09-04. Avenue E. van Nieuwenhuyse 4/3, 1160 Brussels, Belgium: PlasticsEurope, 2021. URL: https://plasticseurope.org/knowledge-hub/plastics-the-facts-2021/.

[78] PlasticsEurope. *Plastics – The Facts 2022*. Tech. rep. Accessed: 2024-09-04. Avenue E. van Nieuwenhuyse 4/3, 1160 Brussels, Belgium: PlasticsEurope, 2022. URL: https://plasticseurope.org/knowledge-hub/plastics-the-facts-2022/.

[79] Valeria Hidalgo-Ruz, Lars Gutow, Richard C Thompson, and Martin Thiel. "Microplastics in the marine environment: a review of the methods used for identification and quantification". In: *Environmental science & technology* 46.6 (2012), pp. 3060–3075.

[80] Irina Chubarenko, Elena Esiukova, Andrei Bagaev, Igor Isachenko, Natalia Demchenko, Mikhail Zobkov, Irina Efimova, Margarita Bagaeva, and Lilia Khatmullina. "Behavior of microplastics in coastal zones". In: *Microplastic contamination in aquatic environments*. Elsevier, 2018, pp. 175–223.

[81] Ana L d F Lacerda, Lucas dos S Rodrigues, Erik Van Sebille, Fábio L Rodrigues, Lourenço Ribeiro, Eduardo R Secchi, Felipe Kessler, and Maíra C Proietti. "Plastics in sea surface waters around the Antarctic Peninsula". In: *Scientific reports* 9.1 (2019), pp. 1–12.

[82] Skye Morét-Ferguson, Kara Lavender Law, Giora Proskurowski, Ellen K Murphy, Emily E Peacock, and Christopher M Reddy. "The size, mass, and composition of plastic debris in the western North Atlantic Ocean". In: *Marine pollution bulletin* 60.10 (2010), pp. 1873–1878.

[83] Winnie Courtene-Jones, Brian Quinn, Ciaran Ewins, Stefan F Gary, and Bhavani E Narayanaswamy. "Microplastic accumulation in deep-sea sediments from the Rockall Trough". In: *Marine Pollution Bulletin* 154 (2020), p. 111092.

[84] Bożena Graca, Karolina Szewc, Danuta Zakrzewska, Anna Dołęga, and Magdalena Szczerbowska-Boruchowska. "Sources and fate of microplastics in marine and beach sediments of the Southern Baltic Sea—a preliminary study". In: *Environmental Science and Pollution Research* 24 (2017), pp. 7650–7661.

[85] Irina Chubarenko, Andrei Bagaev, Mikhail Zobkov, and Ekaterina Esiukova. “On some physical and dynamical properties of microplastic particles in marine environment”. In: *Marine Pollution Bulletin* 108.1-2 (2016), pp. 105–112.

[86] Bernard R. Jennings and Kenneth Parslow. “Particle size measurement: the equivalent spherical diameter”. In: *Proceedings of the Royal Society of London. A. Mathematical and Physical Sciences* 419.1856 (1988), pp. 137–149.

[87] Hakon Wadell. “The coefficient of resistance as a function of Reynolds number for solids of various shapes”. In: *Journal of the Franklin Institute* 217.4 (1934), pp. 459–490.

[88] William E Dietrich. “Settling velocity of natural particles”. In: *Water Resources Research* 18.6 (1982), pp. 1615–1626.

[89] Nicole Kowalski, Aurelia M Reichardt, and Joanna J Waniek. “Sinking rates of microplastics and potential implications of their alteration by physical, biological, and chemical factors”. In: *Marine Pollution Bulletin* 109.1 (2016), pp. 310–319.

[90] Roberto Rosal. “Morphological description of microplastic particles for environmental fate studies”. In: *Marine Pollution Bulletin* 171 (2021), p. 112716.

[91] Simon J Blott and Kenneth Pye. “Particle shape: a review and new methods of characterization and classification”. In: *Sedimentology* 55.1 (2008), pp. 31–63.

[92] Walter Hans Graf. *Hydraulics of sediment transport*. Water Resources Publication, 1984.

[93] Arthur T. Corey. “Influence of shape on the fall velocity of sand grains”. In: *Colorado Agricultural and Mechanical College* (1949).

[94] Norman C. Janke. “Effect of shape upon the settling vellocity of regular convex geometric particles”. In: *Journal of Sedimentary Research* 36.2 (1966), pp. 370–376.

[95] Imogen E Napper and Richard C Thompson. “Release of synthetic microplastic plastic fibres from domestic washing machines: Effects of fabric type and washing conditions”. In: *Marine pollution bulletin* 112.1-2 (2016), pp. 39–45.

[96] Abigail PW Barrows, Courtney A Neumann, Michelle L Berger, and Susan D Shaw. "Grab vs. neuston tow net: a microplastic sampling performance comparison and possible advances in the field". In: *Analytical methods* 9.9 (2017), pp. 1446–1453.

[97] Marielis C Zambrano, Joel J Pawlak, Jesse Daystar, Mary Ankeny, Jay J Cheng, and Richard A Venditti. "Microfibers generated from the laundering of cotton, rayon and polyester based fabrics and their aquatic biodegradation". In: *Marine pollution bulletin* 142 (2019), pp. 394–407.

[98] Rose Sinclair. *Textiles and fashion: materials, design and technology*. Elsevier, 2014.

[99] Boniphace Kanyathare, Benjamin O Asamoah, Umair Ishaq, James Amoani, Jukka Räty, and Kai-Erik Peiponen. "Optical transmission spectra study in visible and near-infrared spectral range for identification of rough transparent plastics in aquatic environments". In: *Chemosphere* 248 (2020), p. 126071.

[100] Jean-Pierre W Desforges, Moira Galbraith, Neil Dangerfield, and Peter S Ross. "Widespread distribution of microplastics in subsurface seawater in the NE Pacific Ocean". In: *Marine pollution bulletin* 79.1-2 (2014), pp. 94–99.

[101] Amy L Lusher, Ann Burke, Ian O'Connor, and Rick Officer. "Microplastic pollution in the Northeast Atlantic Ocean: validated and opportunistic sampling". In: *Marine pollution bulletin* 88.1-2 (2014), pp. 325–333.

[102] HARRISON Frost, THOMAS Bond, T Sizmur, and MONICA Felipe-Sotelo. "A review of microplastic fibres: generation, transport, and vectors for metal (loid) s in terrestrial environments". In: *Environmental Science: Processes & Impacts* 24.4 (2022), pp. 504–524.

[103] Penelope K Lindeque, Matthew Cole, Rachel L Coppock, Ceri N Lewis, Rachael Z Miller, Andrew JR Watts, Alice Wilson-McNeal, Stephanie L Wright, and Tamara S Galloway. "Are we underestimating microplastic abundance in the marine environment? A comparison of microplastic capture with nets of different mesh-size". In: *Environmental Pollution* 265 (2020), p. 114721.

[104] Montserrat Filella. “Questions of size and numbers in environmental research on microplastics: methodological and conceptual aspects”. In: *Environmental Chemistry* 12.5 (2015), pp. 527–538.

[105] KIMO Sweden. “Small plastic particles in Coastal Swedish waters”. In: *N. Research Reportcommissioned by KIMO Sweeden (Submitted to BDC)* (2007).

[106] Jingli Mu, Ling Qu, Fei Jin, Shoufeng Zhang, Chao Fang, Xindong Ma, Weiwei Zhang, Cheng Huo, Yi Cong, and Juying Wang. “Abundance and distribution of microplastics in the surface sediments from the northern Bering and Chukchi Seas”. In: *Environmental Pollution* 245 (2019), pp. 122–130.

[107] Pedro M Lourenço, Catarina Serra-Gonçalves, Joana Lia Ferreira, Teresa Catry, and José P Granadeiro. “Plastic and other microfibers in sediments, macroinvertebrates and shorebirds from three intertidal wetlands of southern Europe and west Africa”. In: *Environmental pollution* 231 (2017), pp. 123–133.

[108] Viola Fischer, Nikolaus O Elsner, Nils Brenke, Enrico Schwabe, and Angelika Brandt. “Plastic pollution of the Kuril–Kamchatka Trench area (NW pacific)”. In: *Deep Sea Research Part II: Topical Studies in Oceanography* 111 (2015), pp. 399–405.

[109] Lisbeth Van Cauwenberghe, Lisa Devriese, François Galgani, Johan Robbens, and Colin R Janssen. “Microplastics in sediments: a review of techniques, occurrence and effects”. In: *Marine environmental research* 111 (2015), pp. 5–17.

[110] Michiel Claessens, Steven De Meester, Lieve Van Landuyt, Karen De Clerck, and Colin R Janssen. “Occurrence and distribution of microplastics in marine sediments along the Belgian coast”. In: *Marine pollution bulletin* 62.10 (2011), pp. 2199–2204.

[111] Lucy C Woodall, Anna Sanchez-Vidal, Miquel Canals, Gordon LJ Paterson, Rachel Coppock, Victoria Sleight, Antonio Calafat, Alex D Rogers, Bhavani E Narayanaswamy, and Richard C Thompson. “The deep sea is a major sink for microplastic debris”. In: *Royal Society open science* 1.4 (2014), p. 140317.

[112] Georgia Gatidou, Olga S Arvaniti, and Athanasios S Stasinakis. "Review on the occurrence and fate of microplastics in Sewage Treatment Plants". In: *Journal of hazardous materials* 367 (2019), pp. 504–512.

[113] Muhammad Reza Cordova and AaJ Wahyudi. "Microplastic in the deep-sea sediment of Southwestern Sumatran Waters". In: *Marine Research in Indonesia* 41.1 (2016), pp. 27–35.

[114] Marcus Eriksen, Laurent CM Lebreton, Henry S Carson, Martin Thiel, Charles J Moore, Jose C Borerro, Francois Galgani, Peter G Ryan, and Julia Reisser. "Plastic pollution in the world's oceans: more than 5 trillion plastic pieces weighing over 250,000 tons afloat at sea". In: *PloS one* 9.12 (2014), e111913.

[115] Julia Reisser, Jeremy Shaw, Chris Wilcox, Britta Denise Hardesty, Maira Proietti, Michele Thums, and Charitha Pattiaratchi. "Marine plastic pollution in waters around Australia: characteristics, concentrations, and pathways". In: *PloS one* 8.11 (2013), e80466.

[116] Albert A Koelmans, Merel Kooi, Kara Lavender Law, and Erik Van Sebille. "All is not lost: deriving a top-down mass budget of plastic at sea". In: *Environmental Research Letters* 12.11 (2017), p. 114028.

[117] Kryss Waldschlager and Holger Schuttrumpf. "Effects of particle properties on the settling and rise velocities of microplastics in freshwater under laboratory conditions". In: *Environmental science & technology* 53.4 (2019), pp. 1958–1966.

[118] William W Willmarth, Norman E Hawk, and Robert Laurie Harvey. "Steady and unsteady motions and wakes of freely falling disks". In: (1964).

[119] KOLF Jayaweera and BJ Mason. "The behaviour of freely falling cylinders and cones in a viscous fluid". In: *Journal of Fluid Mechanics* 22.4 (1965), pp. 709–720.

[120] Ge Yang, Zijian Yu, Abul BM Baki, Weiwei Yao, Matthew Ross, Wanqing Chi, and Wenming Zhang. "Settling behaviors of microplastic disks in water". In: *Marine Pollution Bulletin* 188 (2023), p. 114657.

[121] David Kaiser, Arne Estelmann, Nicole Kowalski, Michael Glockzin, and Joanna J Waniek. "Sinking velocity of sub-millimeter microplastic". In: *Marine pollution bulletin* 139 (2019), pp. 214–220.

[122] Andrei Bagaev, Artem Mizyuk, Liliya Khatmullina, Igor Isachenko, and Irina Chubarenko. "Anthropogenic fibres in the Baltic Sea water column: Field data, laboratory and numerical testing of their motion". In: *Science of the Total Environment* 599 (2017), pp. 560–571.

[123] Koray Deniz Goral, Hasan Gokhan Guler, Bjarke Eltard Larsen, Stefan Carstensen, Erik Damgaard Christensen, Nils B Kerpen, Torsten Schlurmann, and David R Fuhrman. "Settling velocity of microplastic particles having regular and irregular shapes". In: *Environmental Research* 228 (2023), p. 115783.

[124] Usama Ijaz, Abul BM Baki, Weiming Wu, and Wenming Zhang. "Settling velocity of microplastics in turbulent open-channel flow". In: *Science of The Total Environment* 946 (2024), p. 174179.

[125] Ali Al-Darraji, Ibukun Oluwoye, Christopher Lagat, Shuhei Tanaka, and Ahmed Barifcani. "Erosion of rigid plastics in turbid (sandy) water: quantitative assessment for marine environments and formation of microplastics". In: *Environmental Science: Processes & Impacts* (2024).

[126] Young Kyoung Song, Sang Hee Hong, Mi Jang, Gi Myung Han, Seung Won Jung, and Won Joon Shim. "Combined effects of UV exposure duration and mechanical abrasion on microplastic fragmentation by polymer type". In: *Environmental science & technology* 51.8 (2017), pp. 4368–4376.

[127] Aurel Blaga. "Deterioration mechanisms in weathering of plastic materials". In: *Durability of Building Materials and Components*. ASTM International, 1980.

[128] Nicolas FA Biber, Andy Foggo, and Richard C Thompson. "Characterising the deterioration of different plastics in air and seawater". In: *Marine pollution bulletin* 141 (2019), pp. 595–602.

[129] Tim O'Brine and Richard C Thompson. "Degradation of plastic carrier bags in the marine environment". In: *Marine pollution bulletin* 60.12 (2010), pp. 2279–2283.

[130] Andrew Fairbrother, Hsiang-Chun Hsueh, Jae Hyun Kim, Deborah Jacobs, Lakesha Perry, David Goodwin, Christopher White, Stephanie Watson, and Li-Piin Sung. "Temperature and light intensity effects on photodegradation of high-density polyethylene". In: *Polymer degradation and stability* 165 (2019), pp. 153–160.

[131] Fèlix Carrasco, Pere Pagès, Sergi Pascual, and Xavier Colom. "Artificial aging of high-density polyethylene by ultraviolet irradiation". In: *European polymer journal* 37.7 (2001), pp. 1457–1464.

[132] Delphine Lobelle and Michael Cunliffe. "Early microbial biofilm formation on marine plastic debris". In: *Marine pollution bulletin* 62.1 (2011), pp. 197–200.

[133] Merel Kooi, Egbert H van Nes, Marten Scheffer, and Albert A Koelmans. "Ups and downs in the ocean: effects of biofouling on vertical transport of microplastics". In: *Environmental Science & Technology* 51.14 (2017), pp. 7963–7971.

[134] Francesca MC Fazey and Peter G Ryan. "Biofouling on buoyant marine plastics: An experimental study into the effect of size on surface longevity". In: *Environmental pollution* 210 (2016), pp. 354–360.

[135] Michiel Van Melkebeke, Colin Janssen, and Steven De Meester. "Characteristics and sinking behavior of typical microplastics including the potential effect of biofouling: implications for remediation". In: *Environmental science & technology* 54.14 (2020), pp. 8668–8680.

[136] Atsuhiko Isobe, Hirofumi Hinata, Shin'ichiro Kako, and Shun Yoshioka. "Formulation of leeway-drift velocities for sea-surface drifting-objects based on a wind-wave flume experiment". In: *Interdisciplinary studies on environmental chemistry-marine environmental modeling and analysis. Terrapub., Tokyo* (2011), pp. 239–249.

[137] Eric Anderson, Anatoly Odulo, and Malcolm L Spaulding. *Modeling of leeway drift.* Tech. rep. 1998.

[138] Bruce Hackett, Øyvind Breivik, and Cecilie Wettre. "Forecasting the drift of objects and substances in the ocean". In: *Ocean weather forecasting: an integrated view of oceanography* (2006), pp. 507–523.

[139] Kara Lavender Law, Skye Morét-Ferguson, Nikolai A Maximenko, Giora Proskurowski, Emily E Peacock, Jan Hafner, and Christopher M Reddy. "Plastic accumulation in the North Atlantic subtropical gyre". In: *Science* 329.5996 (2010), pp. 1185–1188.

[140] Tobias Kukulka, Giora Proskurowski, Skye Morét-Ferguson, Daniel W Meyer, and Kara Lavender Law. "The effect of wind mixing on the vertical distribution of buoyant plastic debris". In: *Geophysical research letters* 39.7 (2012).

[141] Kayla C Brignac, Melissa R Jung, Cheryl King, Sarah-Jeanne Royer, Lauren Blickley, Megan R Lamson, James T Potemra, and Jennifer M Lynch. "Marine debris polymers on main Hawaiian island beaches, sea surface, and seafloor". In: *Environmental science & technology* 53.21 (2019), pp. 12218–12226.

[142] Maria Luiza Pedrotti, Stéphanie Petit, Amanda Elineau, Stéphane Bruzaud, Jean-Claude Crebassa, Bruno Dumontet, Elisa Martí, Gabriel Gorsky, and Andrés Cózar. "Changes in the floating plastic pollution of the Mediterranean Sea in relation to the distance to land". In: *PloS one* 11.8 (2016), e0161581.

[143] Laura Thornton and Nancy L Jackson. "Spatial and temporal variations in debris accumulation and composition on an estuarine shoreline, Cliffwood Beach, New Jersey, USA". In: *Marine Pollution Bulletin* 36.9 (1998), pp. 705–711.

[144] Juan P. Le Roux. "Grains in motion: A review". In: *Sedimentary Geology* 178.3-4 (2005), pp. 285–313.

[145] Hua Zhang. "Transport of microplastics in coastal seas". In: *Estuarine, Coastal and Shelf Science* 199 (2017), pp. 74–86.

[146] Mark A Browne, Tamara S Galloway, and Richard C Thompson. "Spatial patterns of plastic debris along estuarine shorelines". In: *Environmental science & technology* 44.9 (2010), pp. 3404–3409.

[147] Michael C Gregg. “The study of mixing in the ocean: A brief history”. In: *Oceanography* 4.1 (1991), pp. 39–45.

[148] David Tolmazin and David Tolmazin. “Turbulence and rotation of waters in oceans and seas”. In: *Elements of Dynamic Oceanography* (1985), pp. 70–88.

[149] Nanacy A. Bray. “Thermohaline circulation in the Gulf of California”. In: *Journal of Geophysical Research: Oceans* 93.C5 (1988), pp. 4993–5020.

[150] Ian A Kane, Michael A Clare, Elda Miramontes, Roy Wogelius, James J Rothwell, Pierre Garreau, and Florian Pohl. “Seafloor microplastic hotspots controlled by deep-sea circulation”. In: *Science* 368.6495 (2020), pp. 1140–1145.

[151] Tobias Kukulka, Kara L Law, and Giora Proskurowski. “Evidence for the influence of surface heat fluxes on turbulent mixing of microplastic marine debris”. In: *Journal of Physical Oceanography* 46.3 (2016), pp. 809–815.

[152] Anika Ballent, Autun Purser, Pedro de Jesus Mendes, S Pando, and Laurenz Thomsen. “Physical transport properties of marine microplastic pollution.” In: *Biogeosciences Discussions* 9.12 (2012).

[153] Henry Stommel. “Trajectories of small bodies sinking slowly through convection cells”. In: *J. mar. Res* 8.11 (1949), pp. 24–29.

[154] John E. Stout, S. Pal Arya, and Eugene L. Genikhovich. “The effect of nonlinear drag on the motion and settling velocity of heavy particles”. In: *Journal of Atmospheric Sciences* 52.22 (1995), pp. 3836–3848.

[155] Chao-Yang Yang and Uichiro Lei. “The role of the turbulent scales in the settling velocity of heavy particles in homogeneous isotropic turbulence”. In: *Journal of Fluid Mechanics* 371 (1998), pp. 179–205.

[156] Alberto Aliseda, Alain Cartellier, F Hainaux, and Juan C Lasheras. “Effect of preferential concentration on the settling velocity of heavy particles in homogeneous isotropic turbulence”. In: *Journal of Fluid Mechanics* 468 (2002), pp. 77–105.

[157] Thorsten Bosse, Leonhard Kleiser, and Eckart Meiburg. “Small particles in homogeneous turbulence: settling velocity enhancement by two-way coupling”. In: *Physics of Fluids* 18.2 (2006).

[158] Yixiang Wang, Kit Ming Lam, and Yi Lu. “Settling velocity of fine heavy particles in turbulent open channel flow”. In: *Physics of Fluids* 30.9 (2018), p. 095106.

[159] Peter Nielsen. “On the motion of suspended sand particles”. In: *Journal of Geophysical Research: Oceans* 89.C1 (1984), pp. 616–626.

[160] Subhasish Dey, Sk Zeeshan Ali, and Ellora Padhi. “Terminal fall velocity: the legacy of Stokes from the perspective of fluvial hydraulics”. In: *Proceedings of the Royal Society A* 475.2228 (2019), p. 20190277.

[161] Gordon H. Good, Sergey Gerashchenko, and Zellman Warhaft. “Intermittency and inertial particle entrainment at a turbulent interface: the effect of the large-scale eddies”. In: *Journal of Fluid Mechanics* 694 (2012), pp. 371–398.

[162] Gordon H. Good, P. J. Ireland, Gregory P. Bewley, Eberhard Bodenschatz, Lance R. Collins, and Zellman Warhaft. “Settling regimes of inertial particles in isotropic turbulence”. In: *Journal of Fluid Mechanics* 759 (2014).

[163] Peter Nielsen. “Turbulence effects on the settling of suspended particles”. In: *Journal of Sedimentary Research* 63.5 (1993), pp. 835–838.

[164] Kiyosi Kawanisi and Ryohei Shiozaki. “Turbulent effects on the settling velocity of suspended sediment”. In: *Journal of hydraulic engineering* 134.2 (2008), pp. 261–266.

[165] Stephen P Murray. “Settling velocities and vertical diffusion of particles in turbulent water”. In: *Journal of geophysical research* 75.9 (1970), pp. 1647–1654.

[166] Walter Fornari, Francesco Picano, Gaetano Sardina, and Luca Brandt. “Reduced particle settling speed in turbulence”. In: *Journal of Fluid Mechanics* 808 (2016), pp. 153–167.

[167] Huan Yang and Hosein Foroutan. “Effects of near-bed turbulence on microplastics fate and transport in streams”. In: *Science of The Total Environment* 905 (2023), p. 167173.

[168] Raymond Charles Vaseleski and AB Metzner. “Drag reduction in the turbulent flow of fiber suspensions”. In: *AIChE Journal* 20.2 (1974), pp. 301–306.

[169] Suresh K. Aggarwal and Feng Peng. “A review of droplet dynamics and vaporization modeling for engineering calculations”. In: (1995).

[170] Arthur Putnam. *Integratable form of droplet drag coefficient*. 1961.

[171] Rory LC Flemmer and CL Banks. “On the drag coefficient of a sphere”. In: *Powder Technology* 48.3 (1986), pp. 217–221.

[172] Miroslav Hartman and John G Yates. “Free-fall of solid particles through fluids”. In: *Collection of Czechoslovak chemical communications* 58.5 (1993), pp. 961–982.

[173] Roland Clift, John R Grace, and Martin E Weber. “Bubbles, drops, and particles”. In: (2005).

[174] Eric Loth. “Drag of non-spherical solid particles of regular and irregular shape”. In: *Powder Technology* 182.3 (2008), pp. 342–353.

[175] Amir Haider and Octave Levenspiel. “Drag coefficient and terminal velocity of spherical and nonspherical particles”. In: *Powder technology* 58.1 (1989), pp. 63–70.

[176] Edward K. Marchildon, Abe Clamen, and William H. Gauvin. “Drag and oscillatory motion of freely falling cylindrical particles”. In: *The Canadian Journal of Chemical Engineering* 42.4 (1964), pp. 178–182.

[177] Sabine Tran-Cong, Michael Gay, and Efstathios E Michaelides. “Drag coefficients of irregularly shaped particles”. In: *Powder Technology* 139.1 (2004), pp. 21–32.

[178] Said Elghobashi. “On predicting particle-laden turbulent flows”. In: *Applied Scientific Research* 52.4 (1994), pp. 309–329.

[179] Mirai Sato, Zijiang Yang, Yukiho Katagata, Hiroaki Hamada, Yuta Yamada, and Hisayuki Arakawa. “Microplastic volumes in Tokyo Bay”. In: *Marine Pollution Bulletin* 207 (2024), p. 116871.

[180] Emilia Uurasjärvi, Samuel Hartikainen, Outi Setälä, Maiju Lehtiniemi, and Arto Koistinen. “Microplastic concentrations, size distribution, and polymer types in the

surface waters of a northern European lake". In: *Water Environment Research* 92.1 (2020), pp. 149–156.

[181] Mostafa Bigdeli, Abdolmajid Mohammadian, Abolghasem Pilechi, and Mercedeh Taheri. "Lagrangian modeling of marine microplastics fate and transport: The state of the science". In: *Journal of Marine Science and Engineering* 10.4 (2022), p. 481.

[182] Alethea Sara Mountford and MA Morales Maqueda. "Eulerian modeling of the three-dimensional distribution of seven popular microplastic types in the global ocean". In: *Journal of Geophysical Research: Oceans* 124.12 (2019), pp. 8558–8573.

[183] Federica Guerrini, Lorenzo Mari, and Renato Casagrandi. "The dynamics of microplastics and associated contaminants: data-driven Lagrangian and Eulerian modelling approaches in the Mediterranean Sea". In: *Science of The Total Environment* 777 (2021), p. 145944.

[184] Tor Nordam, Ruben Kristiansen, Raymond Nepstad, Erik van Sebille, and Andy M Booth. "A comparison of Eulerian and Lagrangian methods for vertical particle transport in the water column". In: *Geoscientific Model Development Discussions* 2023 (2023), pp. 1–41.

[185] Peter D Nooteboom, Philippe Delandmeter, Erik van Sebille, Peter K Bijl, Henk A Dijkstra, and Anna S von der Heydt. "Resolution dependency of sinking Lagrangian particles in ocean general circulation models". In: *PloS one* 15.9 (2020), e0238650.

[186] Laurent C.-M. Lebreton, Sarah D. Greer, and Jose Carlos Borrero. "Numerical modelling of floating debris in the world's oceans". In: *Marine Pollution Bulletin* 64.3 (2012), pp. 653–661.

[187] Yousef Alosairi, Saud M. Al-Salem, and Abdullah Al Ragum. "Three-dimensional numerical modelling of transport, fate and distribution of microplastics in the northwestern Arabian/Persian Gulf". In: *Marine pollution bulletin* 161 (2020), p. 111723.

[188] Pouyan Ahmadi, Franz Dichgans, Lisa Jagau, Christian Schmidt, Vadym Aizinger, Benjamin S Gilfedder, and Jan H Fleckenstein. "Systematic CFD-based evaluation of

physical factors influencing the spatiotemporal distribution patterns of microplastic particles in lakes". In: *Science of the Total Environment* 917 (2024), p. 170218.

[189] Kay Critchell and Jonathan Lambrechts. "Modelling accumulation of marine plastics in the coastal zone; what are the dominant physical processes?" In: *Estuarine, Coastal and Shelf Science* 171 (2016), pp. 111–122.

[190] Gholamreza Shiravani, Dennis Oberrecht, Lena Roscher, Sebastian Kernchen, Michael Halbach, Maren Gerriets, Barbara M. Scholz-Böttcher, Gunnar Gerdts, Thomas H. Badewien, and Andreas Wurpts. "Numerical modeling of microplastic interaction with fine sediment under estuarine conditions". In: *Water Research* 231 (2023), p. 119564.

[191] Abolghasem Pilechi, Abdolmajid Mohammadian, and Enda Murphy. "A numerical framework for modeling fate and transport of microplastics in inland and coastal waters". In: *Marine Pollution Bulletin* 184 (2022), p. 114119.

[192] Pouyan Ahmadi, Hassan Elagami, Franz Dichgans, Christian Schmidt, Benjamin S Gilfedder, Sven Frei, Stefan Peiffer, and Jan H Fleckenstein. "Systematic evaluation of physical parameters affecting the terminal settling velocity of microplastic particles in lakes using CFD". In: *Frontiers in Environmental Science* 10 (2022), p. 875220.

[193] Robin Jérémy, Latessa Pablo Gaston, and Manousos Valyrakis. "Coupled CFD-DEM modelling to assess settlement velocity and drag coefficient of microplastics". In: *EGU General Assembly 2020* (2020).

[194] Jinfeng Zhang, Chaoqun Ji, Guangwei Liu, Qinghe Zhang, and Enbo Xing. "Settling processes of cylindrical microplastics in quiescent water: A fully resolved numerical simulation study". In: *Marine Pollution Bulletin* 194 (2023), p. 115438.

[195] Le Duc Quyen, Young-Gyu Park, In-cheol Lee, and Jun Myoung Choi. "CFD Analysis of Microplastic Transport over the Slopes". In: *Journal of Marine Science and Engineering* 12.1 (2024), p. 145.

[196] Mohammadreza Fatahi, Guven Akdogan, Christie Dorfling, and Petrie Van Wyk. "Numerical study of microplastic dispersal in simulated coastal waters using cfd approach". In: *Water* 13.23 (2021), p. 3432.

[197] Le Duc Quyen, Jun Myoung Choi, et al. “Accumulation and dispersion of microplastics near a submerged structure: basic study using a numerical wave tank”. In: *Journal of Marine Science and Engineering* 10.12 (2022), p. 1934.

[198] Mohammad Nabi, Huib J. De Vriend, Erik Mosselman, Cees J. Sloff, and Yasuyuki Shimizu. “Detailed simulation of morphodynamics: 2. Sediment pickup, transport, and deposition”. In: *Water resources research* 49.8 (2013), pp. 4775–4791.

[199] Mingyang Wang, Eldad Avital, Qingsheng Chen, John Williams, Shuo Mi, and Qiancheng Xie. “A numerical study on suspended sediment transport in a partially vegetated channel flow”. In: *Journal of Hydrology* 599 (2021), p. 126335.

[200] Arefeh Shamkhany, Zhuoran Li, Preet Patel, and Shooka Karimpour. “Evidence of Microplastic Size Impact on Mobility and Transport in the Marine Environment: A Review and Synthesis of Recent Research”. In: *Frontiers in Marine Science* 8 (2021), p. 1869.

[201] Matthew Cole, Pennie Lindeque, Elaine Fileman, Claudia Halsband, Rhys Goodhead, Julian Moger, and Tamara S Galloway. “Microplastic ingestion by zooplankton”. In: *Environmental science & technology* 47.12 (2013), pp. 6646–6655.

[202] Maria Cristina Fossi, Cristina Panti, Cristiana Guerranti, Daniele Coppola, Matteo Giannetti, Letizia Marsili, and Roberta Minutoli. “Are baleen whales exposed to the threat of microplastics? A case study of the Mediterranean fin whale (Balaenoptera physalus)”. In: *Marine pollution bulletin* 64.11 (2012), pp. 2374–2379.

[203] Amy Lusher. “Microplastics in the marine environment: distribution, interactions and effects”. In: *Marine anthropogenic litter* (2015), pp. 245–307.

[204] Fionn Murphy, Ciaran Ewins, Frederic Carbonnier, and Brian Quinn. “Wastewater treatment works (WwTW) as a source of microplastics in the aquatic environment”. In: *Environmental science & technology* 50.11 (2016), pp. 5800–5808.

[205] Tatenda Dalu, Thabiso Banda, Thendo Mutshekwa, Linton F Munyai, and Ross N Cuthbert. “Effects of urbanisation and a wastewater treatment plant on microplastic

densities along a subtropical river system". In: *Environmental Science and Pollution Research* 28 (2021), pp. 36102–36111.

[206] Aimee Huntington, Patricia L Corcoran, Liisa Jantunen, Clara Thaysen, Sarah Bernstein, Gary A Stern, and Chelsea M Rochman. "A first assessment of microplastics and other anthropogenic particles in Hudson Bay and the surrounding eastern Canadian Arctic waters of Nunavut". In: *Facets* 5.1 (2020), pp. 432–454.

[207] Trishan Naidoo, David Glassom, and Albertus J Smit. "Plastic pollution in five urban estuaries of KwaZulu-Natal, South Africa". In: *Marine pollution bulletin* 101.1 (2015), pp. 473–480.

[208] Peter G Ryan. "Does size and buoyancy affect the long-distance transport of floating debris?" In: *Environmental Research Letters* 10.8 (2015), p. 084019.

[209] Austin K Baldwin, Steven R Corsi, and Sherri A Mason. "Plastic debris in 29 Great Lakes tributaries: relations to watershed attributes and hydrology". In: *Environmental science & technology* 50.19 (2016), pp. 10377–10385.

[210] Erik Van Sebille, Stefano Aliani, Kara Lavender Law, Nikolai Maximenko, José M Alsina, Andrei Bagaev, Melanie Bergmann, Bertrand Chapron, Irina Chubarenko, Andrés Cózar, et al. "The physical oceanography of the transport of floating marine debris". In: *Environmental Research Letters* 15.2 (2020), p. 023003.

[211] Fabienne Lagarde, Ophélie Olivier, Marie Zanella, Philippe Daniel, Sophie Hiard, and Aurore Caruso. "Microplastic interactions with freshwater microalgae: hetero-aggregation and changes in plastic density appear strongly dependent on polymer type". In: *Environmental pollution* 215 (2016), pp. 331–339.

[212] Marc Long, Brivaëla Moriceau, Morgane Gallinari, Christophe Lambert, Arnaud Huvet, Jean Raffray, and Philippe Soudant. "Interactions between microplastics and phytoplankton aggregates: impact on their respective fates". In: *Marine Chemistry* 175 (2015), pp. 39–46.

[213] Giuseppe Suaria, Carlo G Avio, Annabella Mineo, Gwendolyn L Lattin, Marcello G Magaldi, Genuario Belmonte, Charles J Moore, Francesco Regoli, and Stefano Aliani.

"The Mediterranean Plastic Soup: synthetic polymers in Mediterranean surface waters". In: *Scientific reports* 6.1 (2016), p. 37551.

[214] Mingxiao Di and Jun Wang. "Microplastics in surface waters and sediments of the Three Gorges Reservoir, China". In: *Science of the Total Environment* 616 (2018), pp. 1620–1627.

[215] Kryss Waldschläger, Maximilian Born, Win Cowger, Andrew Gray, and Holger Schüttrumpf. "Settling and rising velocities of environmentally weathered micro-and macroplastic particles". In: *Environmental Research* 191 (2020), p. 110192.

[216] Emma L Teuten, Steven J Rowland, Tamara S Galloway, and Richard C Thompson. "Potential for plastics to transport hydrophobic contaminants". In: *Environmental science & technology* 41.22 (2007), pp. 7759–7764.

[217] Ian A Kane and Michael A Clare. "Dispersion, accumulation, and the ultimate fate of microplastics in deep-marine environments: a review and future directions". In: *Frontiers in earth science* 7 (2019), p. 80.

[218] Hui Yang and Changxing Shi. "Sediment grain-size characteristics and its sources of ten wind-water coupled erosion tributaries (the Ten Kongduis) in the Upper Yellow River". In: *Water* 11.1 (2019), p. 115.

[219] Franklin T Heitmuller and Paul F Hudson. "Downstream trends in sediment size and composition of channel-bed, bar, and bank deposits related to hydrologic and lithologic controls in the Llano River watershed, central Texas, USA". In: *Geomorphology* 112.3-4 (2009), pp. 246–260.

[220] Lian-Ping Wang and Martin R Maxey. "Settling velocity and concentration distribution of heavy particles in homogeneous isotropic turbulence". In: *Journal of fluid mechanics* 256 (1993), pp. 27–68.

[221] Shooka Karimpour, Tao Wang, and Vincent H Chu. "The exchanges between the mainstream in an open channel and a recirculating flow on its side at large Froude numbers". In: *Journal of Fluid Mechanics* 920 (2021), A8.

[222] Shooka Karimpour and Vincent H Chu. "The role of waves on mixing in shallow waters". In: *Canadian Journal of Civil Engineering* 46.2 (2019), pp. 134–147.

[223] Mikhael Gorokhovski and Rémi Zamansky. "Modeling the effects of small turbulent scales on the drag force for particles below and above the Kolmogorov scale". In: *Physical Review Fluids* 3.3 (2018), p. 034602.

[224] Eoghan M Cunningham, Sonja M Ehlers, Jaimie TA Dick, Julia D Sigwart, Katrin Linse, Jon J Dick, and Konstadinos Kiriakoulakis. "High abundances of microplastic pollution in deep-sea sediments: evidence from Antarctica and the Southern Ocean". In: *Environmental Science & Technology* 54.21 (2020), pp. 13661–13671.

[225] Ronald Clift, John Grace, and Martin Weber. "Nonspherical rigid particles at higher Reynolds numbers". In: *Bubbles, Drops, and Particles; Academic Press: New York, NY, USA* (1978), pp. 142–168.

[226] David Kaiser, Nicole Kowalski, and Joanna J Waniek. "Effects of biofouling on the sinking behavior of microplastics". In: *Environmental research letters* 12.12 (2017), p. 124003.

[227] Trishul Artham, M Sudhakar, R Venkatesan, C Madhavan Nair, KVGK Murty, and Mukesh Doble. "Biofouling and stability of synthetic polymers in sea water". In: *International Biodeterioration & Biodegradation* 63.7 (2009), pp. 884–890.

[228] Christoph D Rummel, Annika Jahnke, Elena Gorokhova, Dana Kuhnel, and Mechthild Schmitt-Jansen. "Impacts of biofilm formation on the fate and potential effects of microplastic in the aquatic environment". In: *Environmental science & technology letters* 4.7 (2017), pp. 258–267.

[229] Anika Ballent, Patricia L Corcoran, Odile Madden, Paul A Helm, and Fred J Longstaffe. "Sources and sinks of microplastics in Canadian Lake Ontario nearshore, tributary and beach sediments". In: *Marine Pollution Bulletin* 110.1 (2016), pp. 383–395.

[230] Feng Xiao, Xiaoyan Li, Kitming Lam, and Dongsheng Wang. "Investigation of the hydrodynamic behavior of diatom aggregates using particle image velocimetry". In: *Journal of Environmental Sciences* 24.7 (2012), pp. 1157–1164.

[231] Mark C. Miller, Ian N. McCave, and Paul D. Komar. “Threshold of sediment motion under unidirectional currents”. In: *Sedimentology* 24.4 (1977), pp. 507–527.

[232] Douglas L Inman and Patricia M Masters. “Coastal sediment transport concepts and mechanisms”. In: (1991).

[233] Douglas L. Inman and Ralph A. Bagnold. “Beach and nearshore processes. Part II. Littoral processes”. In: *The Sea: Ideas and Observations* 3 (1963), pp. 529–553.

[234] Justin R Finn, Ming Li, and Sourabh V Apte. “Particle based modelling and simulation of natural sand dynamics in the wave bottom boundary layer”. In: *Journal of Fluid Mechanics* 796 (2016), pp. 340–385.

[235] Xiaoyun Qu, Lei Su, Hengxiang Li, Mingzhong Liang, and Huahong Shi. “Assessing the relationship between the abundance and properties of microplastics in water and in mussels”. In: *Science of the total environment* 621 (2018), pp. 679–686.

[236] Nao Sagawa, Keiyu Kawaai, and Hirofumi Hinata. “Abundance and size of microplastics in a coastal sea: comparison among bottom sediment, beach sediment, and surface water”. In: *Marine pollution bulletin* 133 (2018), pp. 532–542.

[237] Doo-Hyeon Chae, In-Sung Kim, Seung-Kyu Kim, Young Kyoung Song, and Won Joon Shim. “Abundance and distribution characteristics of microplastics in surface seawaters of the Incheon/Kyeonggi coastal region”. In: *Archives of environmental contamination and toxicology* 69.3 (2015), pp. 269–278.

[238] Charles J Moore, Shelly L Moore, Molly K Leecaster, and Stephen B Weisberg. “A comparison of plastic and plankton in the North Pacific central gyre”. In: *Marine pollution bulletin* 42.12 (2001), pp. 1297–1300.

[239] Dongdong Zhang, Xidan Liu, Wei Huang, Jingjing Li, Chunsheng Wang, Dongsheng Zhang, and Chunfang Zhang. “Microplastic pollution in deep-sea sediments and organisms of the Western Pacific Ocean”. In: *Environmental Pollution* 259 (2020), p. 113948.

[240] James R Clark, Matthew Cole, Penelope K Lindeque, Elaine Fileman, Jeremy Blackford, Ceri Lewis, Timothy M Lenton, and Tamara S Galloway. “Marine microplastic

debris: a targeted plan for understanding and quantifying interactions with marine life". In: *Frontiers in Ecology and the Environment* 14.6 (2016), pp. 317–324.

[241] Julie C Anderson, Bradley J Park, and Vince P Palace. "Microplastics in aquatic environments: implications for Canadian ecosystems". In: *Environmental Pollution* 218 (2016), pp. 269–280.

[242] Sanae Chiba, Hideaki Saito, Ruth Fletcher, Takayuki Yogi, Makino Kayo, Shin Miyagi, Moritaka Ogido, and Katsunori Fujikura. "Human footprint in the abyss: 30 year records of deep-sea plastic debris". In: *Marine Policy* 96 (2018), pp. 204–212.

[243] Justine Barrett, Zanna Chase, Jing Zhang, Mark M Banaszak Holl, Kathryn Willis, Alan Williams, Britta D Hardesty, and Chris Wilcox. "Microplastic pollution in deep-sea sediments from the Great Australian Bight". In: *Frontiers in Marine Science* 7 (2020), p. 576170.

[244] Jennifer K Adams, Bethany Y Dean, Samantha N Athey, Liisa M Jantunen, Sarah Bernstein, Gary Stern, Miriam L Diamond, and Sarah A Finkelstein. "Anthropogenic particles (including microfibers and microplastics) in marine sediments of the Canadian Arctic". In: *Science of the Total Environment* 784 (2021), p. 147155.

[245] Michele Rebesco, F Javier Hernández-Molina, David Van Rooij, and Anna Wåhlin. "Contourites and associated sediments controlled by deep-water circulation processes: State-of-the-art and future considerations". In: *Marine Geology* 352 (2014), pp. 111–154.

[246] Timour Radko. "Thermohaline-shear instability". In: *Geophysical Research Letters* 46.2 (2019), pp. 822–832.

[247] Irina Efimova, Margarita Bagaeva, Andrei Bagaev, Alexander Kileso, and Irina P Chubarenko. "Secondary microplastics generation in the sea swash zone with coarse bottom sediments: laboratory experiments". In: *Frontiers in Marine Science* 5 (2018), p. 313.

[248] Benoît Camenen. "Simple and general formula for the settling velocity of particles". In: *Journal of Hydraulic Engineering* 133.2 (2007), pp. 229–233.

[249] Arefeh Shamskhany and Shooka Karimpour. "Entrainment and vertical mixing of aquatic microplastics in turbulent flow: The coupled role of particle size and density". In: *Marine Pollution Bulletin* 184 (2022), p. 114160.

[250] Christian Scherer, Nicole Brennholt, Georg Reifferscheid, and Martin Wagner. "Feeding type and development drive the ingestion of microplastics by freshwater invertebrates". In: *Scientific Reports* 7.1 (2017), pp. 1–9.

[251] Evan M Chua, Jeff Shimeta, Dayanthi Nugegoda, Paul D Morrison, and Bradley O Clarke. "Assimilation of polybrominated diphenyl ethers from microplastics by the marine amphipod, Allorchestes compressa". In: *Environmental Science & Technology* 48.14 (2014), pp. 8127–8134.

[252] Daehyun Wee, Tongxun Yi, Anuradha Annaswamy, and Ahmed F Ghoniem. "Self-sustained oscillations and vortex shedding in backward-facing step flows: Simulation and linear instability analysis". In: *Physics of Fluids* 16.9 (2004), pp. 3361–3373.

[253] David M Driver and H Lee Seegmiller. "Features of a reattaching turbulent shear layer in divergent channelflow". In: *AIAA Journal* 23.2 (1985), pp. 163–171.

[254] Jundi Xu, Mahish Mohan, Ebrahim Ghahramani, and Hakan Nilsson. "Modification of stochastic model in Lagrangian tracking method". In: *Chalmers University of Technology: Göteborg, Sweden* (2016).

[255] Stephen B Pope. *Turbulent flows*. Cambridge university press, 2000.

[256] Zhuoran Li, Akash Venkateshwaran, and Shooka Karimpour. "Turbulent Characteristics and Air Entrainment Patterns in Breaking Surge Waves". In: *Fluids* 6.12 (2021), p. 422.

[257] Joseph Smagorinsky. "General circulation experiments with the primitive equations: I. The basic experiment". In: *Monthly Weather Review* 91.3 (1963), pp. 99–164.

[258] MAT Van Hinsberg, HJH Clercx, and F Toschi. "Enhanced settling of nonheavy inertial particles in homogeneous isotropic turbulence: The role of the pressure gradient and the Basset history force". In: *Physical Review E* 95.2 (2017), p. 023106.

[259] Shooka Karimpour, Tao Wang, and Vincent H Chu. “The exchanges between the mainstream in an open channel and a recirculating flow on its side at large Froude numbers”. In: *Journal of Fluid Mechanics* 920 (2021).

[260] Shooka Karimpour Ghannadi and Vincent H Chu. “High-order interpolation schemes for shear instability simulations”. In: *International Journal of Numerical Methods for Heat & Fluid Flow* 25.6 (2015), pp. 1340–1360.

[261] Zhen-Gang Ji. *Hydrodynamics and water quality: modeling rivers, lakes, and estuaries*. John Wiley & Sons, 2017.

[262] Zijian Yu, Weiwei Yao, Mark Loewen, Xiaochen Li, and Wenming Zhang. “Incipient motion of exposed microplastics in an open-channel flow”. In: *Environmental Science & Technology* 56.20 (2022), pp. 14498–14506.

[263] Song Zhiyao, Wu Tingting, Xu Fumin, and Li Ruijie. “A simple formula for predicting settling velocity of sediment particles”. In: *Water Science and Engineering* 1.1 (2008), pp. 37–43.

[264] Kristina Enders, Andrea Käppler, Oliver Biniasch, Peter Feldens, Nicole Stollberg, Xaver Lange, Dieter Fischer, Klaus-Jochen Eichhorn, Falk Pollehne, Sonja Oberbeckmann, et al. “Tracing microplastics in aquatic environments based on sediment analogies”. In: *Scientific Reports* 9.1 (2019), p. 15207.

[265] Xingyu Ma and Andreas Schröder. “Analysis of flapping motion of reattaching shear layer behind a two-dimensional backward-facing step”. In: *Physics of Fluids* 29.11 (2017).

[266] Lawrence Korson, Walter Drost-Hansen, and Frank J Millero. “Viscosity of water at various temperatures”. In: *The Journal of Physical Chemistry* 73.1 (1969), pp. 34–39.

[267] Akira Yoshizawa. “Statistical theory for compressible turbulent shear flows, with the application to subgrid modeling”. In: *The Physics of fluids* 29.7 (1986), pp. 2152–2164.

[268] Nikolay Ivanov Kolev and Nikolay I Kolev. *Multiphase flow dynamics: Fundamentals*. Vol. 1. Springer, 2005.

[269] Kryss Waldschläger, Muriel ZM Brückner, Bethanie Carney Almroth, Christopher R Hackney, Tanveer Mehedi Adyel, Olubukola S Alimi, Sara Lynn Belontz, Win Cowger, Darragh Doyle, Andrew Gray, et al. "Learning from natural sediments to tackle microplastics challenges: A multidisciplinary perspective". In: *Earth-Science Reviews* 228 (2022), p. 104021.

[270] Sarah Cook, Hui-Ling Chan, Soroush Abolfathi, Gary D Bending, Hendrik Schäfer, and Jonathan M Pearson. "Longitudinal dispersion of microplastics in aquatic flows using fluorometric techniques". In: *Water Research* 170 (2020), p. 115337.

[271] Nian-Sheng Cheng and Adrian Wing-Keung Law. "Measurements of turbulence generated by oscillating grid". In: *Journal of Hydraulic Engineering* 127.3 (2001), pp. 201–208.

[272] Indra P. D. De Silva and Harindra J. S. Fernando. "Some aspects of mixing in a stratified turbulent patch". In: *Journal of Fluid Mechanics* 240 (1992), pp. 601–625.

[273] José I. Cardesa, Tim B. Nickels, and James R. Dawson. "2D PIV measurements in the near field of grid turbulence using stitched fields from multiple cameras". In: *Experiments in fluids* 52.6 (2012), pp. 1611–1627.

[274] Haoyu Yao, Linlin Cao, Dazhuan Wu, Yangyang Gao, Shijie Qin, and Faxin Yu. "PIV study on grid-generated turbulence in a free surface flow". In: *Water* 13.7 (2021), p. 909.

[275] Juan C Isaza, Ricardo Salazar, and Zellman Warhaft. "On grid-generated turbulence in the near-and far field regions". In: *Journal of Fluid Mechanics* 753 (2014), pp. 402–426.

[276] Kryss Waldschlager and Holger Schuttrumpf. "Erosion behavior of different microplastic particles in comparison to natural sediments". In: *Environmental science & technology* 53.22 (2019), pp. 13219–13227.

[277] Christophe Henry and Jean-Pierre Minier. "Progress in particle resuspension from rough surfaces by turbulent flows". In: *Progress in Energy and Combustion Science* 45 (2014), pp. 1–53.

[278] Greg A Voth, Arthur La Porta, Alice M Crawford, Jim Alexander, and Eberhard Bodenschatz. “Measurement of particle accelerations in fully developed turbulence”. In: *Journal of Fluid Mechanics* 469 (2002), pp. 121–160.

[279] Luca Brandt and Filippo Coletti. “Particle-laden turbulence: progress and perspectives”. In: *Annual Review of Fluid Mechanics* 54.1 (2022), pp. 159–189.

[280] Robert Kasper. *Particle simulation with openfoam® introduction, fundamentals and applications*. 2017.

[281] Gavin R Tabor and MH Baba-Ahmadi. “Inlet conditions for large eddy simulation: A review”. In: *Computers & Fluids* 39.4 (2010), pp. 553–567.

[282] Hiroji Nakagawa and Iehisa Nezu. “Experimental investigation on turbulent structure of backward-facing step flow in an open channel”. In: *Journal of Hydraulic Research* 25.1 (1987), pp. 67–88.

[283] Federico Toschi and Eberhard Bodenschatz. “Lagrangian properties of particles in turbulence”. In: *Annual review of fluid mechanics* 41.1 (2009), pp. 375–404.

[284] John Kim, Parviz Moin, and Robert Moser. “Turbulence statistics in fully developed channel flow at low Reynolds number”. In: *Journal of fluid mechanics* 177 (1987), pp. 133–166.